A Study on

Azimuthal anisotropic flow of the medium produced in heavy-ion collisions at RHIC

Prabhupada Dixit

A thesis submitted in partial fulfillment of the requirements for the degree of

Doctor of Philosophy

Indian Institute of Science Education and Research (IISER) Berhampur

India

Supervisor: Dr. Md. Nasim

DEPARTMENT OF PHYSICAL SCIENCES
Indian Institute of Science Education and Research (IISER) Berhampur

A Study on
Azimuthal anisotropic flow of the medium produced in heavy-ion collisions at RHIC

A thesis submitted in partial fulfilment of the requirements for the award of the degree of

Doctor of Philosophy

by

Prabhupada Dixit
Registration Number- 1920503

to the

Department of Physical Sciences
Indian Institute of Science Education and Research (IISER) Berhampur
India

December 2024

ACADEMIC INTEGRITY AND COPYRIGHT DISCLAIMER

I hereby declare that this thesis is my own work and, to the best of my knowledge, it contains no materials previously published or written by any other person, or substantial proportions of material which have been accepted for the award of any other degree or diploma at IISER Berhampur or any other educational institution, except where due acknowledgment is made in the thesis.

I certify that all copyrighted material incorporated into this thesis is in compliance with the Indian Copyright (Amendment) Act, 2012 and that I have received written permission from the copyright owners for my use of their work, which is beyond the scope of the law. I agree to indemnify and save harmless IISER Berhampur from any and all claims that may be asserted or that may arise from any copyright violation.

Prabhupada Dixit

SIGNATURE: ______________________________

Prabhupada Dixit

DATE: 31st December, 2024

PLACE: Berhampur, India

CERTIFICATE

The undersigned have examined the Ph.D. thesis entitled:

A study on azimuthal anisotropic flow of the medium produced in heavy-ion collisions at RHIC presented by **Prabhupada Dixit**, a candidate for the degree of Doctor of Philosophy in **department of physical sciences**, and hereby certify that it is worthy of acceptance.

Thesis Supervisor: Dr. Md. Nasim — **Signature:** Md. Nasim 04.04.2025

Convener: Dr. Santanu Bhattacharyya — **Signature:** 04/04/25

Thesis Examiner: Dr. Saikat Biswas — **Signature:** Saikat Biswas. 04.04.2025

डॉ. सैकत बिस्वास / Dr. Saikat Biswas
सह प्राध्यापक / Associate Professor
भौतिकी विज्ञान विभाग / Department of Physical Sciences
बसु विज्ञान मंदिर / BOSE INSTITUTE
ई एन - 80, सेक्टर V, बिधाननगर / EN 80, Sector V, Bidhannagar
कोलकाता / Kolkata-700 091 (भारत / India)

Acknowledgments

First and foremost, I would like to express my deepest gratitude to my thesis supervisor, Dr. Md. Nasim, for his unwavering guidance, insightful feedback, and constant support throughout my PhD journey. His mentorship has been instrumental in shaping my research and academic growth.

I am immensely thankful to Dr. Sandeep Chatterjee, a collaborator and a remarkable teacher, who has also been a member of my thesis committee. His profound insights, constructive suggestions, and dedication to physics have greatly inspired me.

My sincere thanks to Professor Bedangadas Mohanty, a member of my thesis committee, for his motivational guidance and stimulating discussions during various meetings that enriched my understanding of physics.

I would also like to acknowledge Dr. Chitrasen Jena, under whose supervision I completed a one-year project at IISER Tirupati before embarking on my PhD journey. His guidance played a significant role in laying the foundation for my research skills.

My heartfelt thanks to Professor Shusu Shi for inviting me to CCNU, China, to collaborate with his group. The collaborative work with his team has been a profoundly rewarding experience.

I am grateful to Dr. Subhash Singha, with whom I had the privilege of collaborating on one of our research papers, for his valuable insights and contributions.

Special thanks to the Conveners of the FCV group at STAR, whose weekly physics discussions, helpful suggestions, and comments have significantly contributed to the progress of my work.

I am indebted to the ALICE-STAR India collaboration for organizing ALICE-India schools and meetings that provided a platform for helpful discussions and networking within the community.

Among my friends and peers, I am especially thankful to Mr. Tribhuban Parida, a good friend and well-wisher. His thoughtful discussions have often cleared my doubts and provided much-needed clarity.

I deeply value the support of Mr. Aswini Kumar Sahoo, who has been a vital companion during my PhD journey. From traveling together to conferences and meetings to engaging in research discussions, his support has been indispensable. I am grateful for our collaboration on a research paper as well.

A special mention goes to Mr. Nimish Mahapatra for not only serving me delicious meals but also engaging in beautiful mathematics discussions that have expanded my knowledge.

My heartfelt thanks to Mr. Kaiser Shafi, a good friend who has often helped me debug my codes and resolve computer-related issues. I value his friendship and our collaborative research work.

I cherish the moments spent with the IISER Berhampur PhD cricket team, whose camaraderie and love for cricket made for an enjoyable respite from academic pursuits.

I am also grateful to IISER Berhampur for providing me with a fellowship that supported my research endeavors.

My sincere thanks to Mr. Krishan Gopal, whose friendship and research discussions during my project at IISER Tirupati left a lasting impression.

I fondly remember the time spent with Dr. Ashutosh Dash, a senior whose presence at IISER Berhampur made my journey more enjoyable. The picnic to Daringbadi remains a cherished memory.

I am thankful to my junior Mr. Pranjal Barik for providing his computational resources sometimes for my work.

I extend my gratitude to my fellow researchers—Rishab, Sharang, Priyanshi, Sameer, Paban, Abhinash, Suruchee, Mitali, Tapas, Saroj, Amiya, and Bhagyashree—for their camaraderie and support throughout this journey.

I am also thankful to my CCNU friends—Guoping Wang, Zuowen Liu, Xing Wu, and Shuai Zhou—for their company during my time at CCNU.

Lastly, and most importantly, I dedicate this work to my family: To my Father and Mother, for their unconditional love, sacrifices, and encouragement that have always been my source of strength. To my Wife, Pragnya, for her unwavering support, patience, and understanding throughout this journey, and for being my constant source of strength and inspiration. To my Younger Brothers, Balu and Lulu, for their boundless love, humor, and belief in me.

This thesis is as much theirs as it is mine. To all who have touched my life in countless ways—thank you.

Dedication

To my family, friends and teachers…

List of Publications

1. Azimuthal anisotropy measurement of (multi)strange hadrons in Au+Au collisions at $\sqrt{s_{NN}}$ = 54.4 GeV. STAR collaboration, **Phys. Rev. C 107, 024912 (2023)**.

2. Examining the influence of hadronic interactions on the directed flow of identified particles in RHIC Beam Energy Scan energies using UrQMD model. A. Sahoo, P. Dixit, Md. Nasim, S. Singha, **Mod. Phys. Lett. A 39 (2024) 07, 2450015**.

3. Insight from the elliptic flow of identified hadrons measured in relativistic heavy-ion collision. P. Dixit, Md. Nasim, **Int. J. Mod. Phys. E 31 (2022) 06, 2250059**.

Submitted articles

1. Longitudinal flow decorrelation in heavy-ion collision at RHIC energies using a multi-phase transport model, P. Dixit and Md. Nasim, **arXiv:2307.08406 (2023)**.

2. Exploring the flow harmonic correlations via multi-particle symmetric and asymmetric cumulants in Au+Au collisions at $\sqrt{s_{NN}}$ = 200 GeV. K. Shafi, P. Dixit, S.Chatterjee, Md. Nasim, **arXiv: 2405.02245 (2024)**.

Conference Proceedings

1. Anisotropic flow of (multi-)strange hadrons in Au+Au collisions at BES-II energies. P.Dixit (for the STAR collaboration), **PoS ICHEP2022 496, arXiv: 2211.12973 (2022).**

2. STAR Measurements on Azimuthal Anisotropy of ϕ mesons in Au+Au Collisions at $\sqrt{s_{NN}}$ = 27 and 54.4 GeV. P.Dixit (for the STAR collaboration), **Springer Proc.Phys. 277 (2022) 419-422.**

3. Invariant yield and azimuthal anisotropy measurements of strange and multi-strange hadrons in Au+Au collision at $\sqrt{s_{NN}}$ = 27 and 54.4 GeV, P.Dixit (for the STAR collaboration) **PoS CPOD2021 (2022) 006, arXiv: 2111.04674 (2022).**

4. Azimuthal anisotropy measurement of multi-strange hadrons in Au+Au collision at $\sqrt{s_{NN}}$ = 27 and 54.4 GeV at STAR. P.Dixit (for the STAR collaboration), **EPJ Web Conf. 259 (2022) 10012, arXiv: 2111.04743 (2021)**

Abstract

According to the Standard Model of particle physics, the most fundamental constituents of matter are quarks and leptons. In nature, quarks are always found confined inside hadrons, like protons and neutrons. It's believed that after a few microseconds of the Big Bang, the universe existed in a state where quarks and gluons were no longer bound inside hadrons. Heavy-ion collision experiments are tools to recreate such a free state of quarks and gluons in the laboratory, which is known as quark-gluon plasma (QGP).

The STAR experiment at the Relativistic Heavy Ion Collider (RHIC) is one of these experiments where we can create and study the properties of the medium produced from the collision. The lifetime of the QGP state is on the order of 10^{-23} seconds, and its size is on the order of 10^{-15} meters. Therefore, it's not possible to directly observe QGP. There are many signatures or indirect pieces of evidence of the QGP medium in the initial stage of a heavy-ion collision, which can be studied by detecting the final state particles in the STAR detectors. One such signature of QGP is the collective flow of the produced medium where the medium will expand collectively exhibiting a long range correlation among the constituents of the system. Specifically, the number of constituent quark (NCQ) scaling in the collective flow of the final state hadrons from the produced medium is an important signature of the collectivity developed in the partonic phase of the medium.

At top RHIC energy, that is, at a center-of-mass energy $\sqrt{s_{NN}} = 200$ GeV, the presence of NCQ scaling in the collective flow of the final state identified hadrons indicates the formation of QGP in the initial stage. If we continue decreasing the collision energy, the signature of QGP might disappear, indicating a hadronic dominance in the produced medium. One of the primary goals of the STAR experiment is to search for the threshold energy below which QGP signatures will disappear.

In this dissertation work, we will present the measurement of various orders of anisotropies present in the collective flow, such as elliptic (v_2) and triangular (v_3) flow of various identified particle species at $\sqrt{s_{NN}}$, starting from 54.4 GeV down to 7.7 GeV. These anisotropic flow observables are sensitive to the initial state and transport properties of the medium and reveal the nature of the medium created in the collision.

We also present a phenomenological study of longitudinal flow decorrelation using the A Multi-Phase Transport (AMPT) model. This study reveals the longitudinal dynamics in heavy-ion collisions and provides a comprehensive three-dimensional structure of the fireball produced in such collisions.

Table of Contents

List of Figures

List of Tables

List of Acronyms used in this thesis

QGP: Quark Gluon Plasma
QCD: Quantum Chromodynamics
BNL: Brookhaven National Laboratory
RHIC: Relativistic Heavy Ion Collider
STAR: Solenoidal Tracker at RHIC
LHC: Large Hadron Collider
PHENIX: Pioneering High Energy Nuclear Interaction eXperiment
BRAHMS: Broad RAnge Hadron Magnetic Spectrometer
ALICE: A Large Ion Collider Experiment
TPC: Time Projection Chamber
ToF: Time of Flight
VPD: Vertex Position Detector
EBIS: Electron Beam Ion Source
AGS: Alternating Gradient Synchrotron
MRPC: Multi-gap Resistive Plate Chamber
ZDC: Zero Degree Calorimeter
BBC: Beam-Beam Counter
EEMC: End Cap Electromagnetic Calorimeter
BEMC: Barrel Electromagnetic Calorimeter
BES-I: Beam Energy Scan-I
BES-II: Beam Energy Scan-II
DCA: Distance of Closest Approach
KF-Algorithm: Kalman-Filter Algorithm
NCQ: Number of Constituent Quarks
CMW: Chiral Magnetic Waves
AMPT: A Multi-Phase Transport Model

CHAPTER 1

Introduction

1.1 The standard model of particle physics

What are the fundamental building block of matter? This has been a long-standing question in physics, sparking curiosity for centuries. To date the most successful model describing fundamental particles and their interaction is known as the standard model of particle physics. According to this model everything around us is made of quarks and leptons. There are 3 generation of leptons, electron(e), electron-neutrino (ν_e), muon(μ), muon-neutrino(ν_μ), tau(τ), and tau-neutrino(ν_τ). Similarly there are 3 generation of quarks (up(u), down(d)), (charm(c), strange(s)) and (top(t),bottom(b)). The generations are decided based on the mass and stability of the particles. Lighter and more stable particles belong to the first generation where as heavier and lesser stable particles belong to the second and third generation. These fundamental particles interact with each other by fundamental forces. There are four fundamental force namely strong force, electromagnetic force, weak force and gravitational force. The comparison of the relative strength of these fundamental interaction are given by Eq. 1.1.

$$\text{Gravitational} : \text{Weak} : \text{Electromagnetic} : \text{Strong} = 1 : 10^{33} : 10^{36} : 10^{38} \tag{1.1}$$

The standard model of particle physics included only weak, electromagnetic and strong force where as gravity is not a part of the standard model. There are four force carriers, or exchange particles, responsible for mediating these three types of interactions. Gluons are the carriers of the strong interaction, photons mediate the electromagnetic interaction, and the $W^{\pm}$ and Z bosons are responsible for the weak interaction. In the end there is Higgs boson which is responsible for the mass of these fundamental particle. An overview of classification of these fundamental particles are shown in Fig. 1.1.

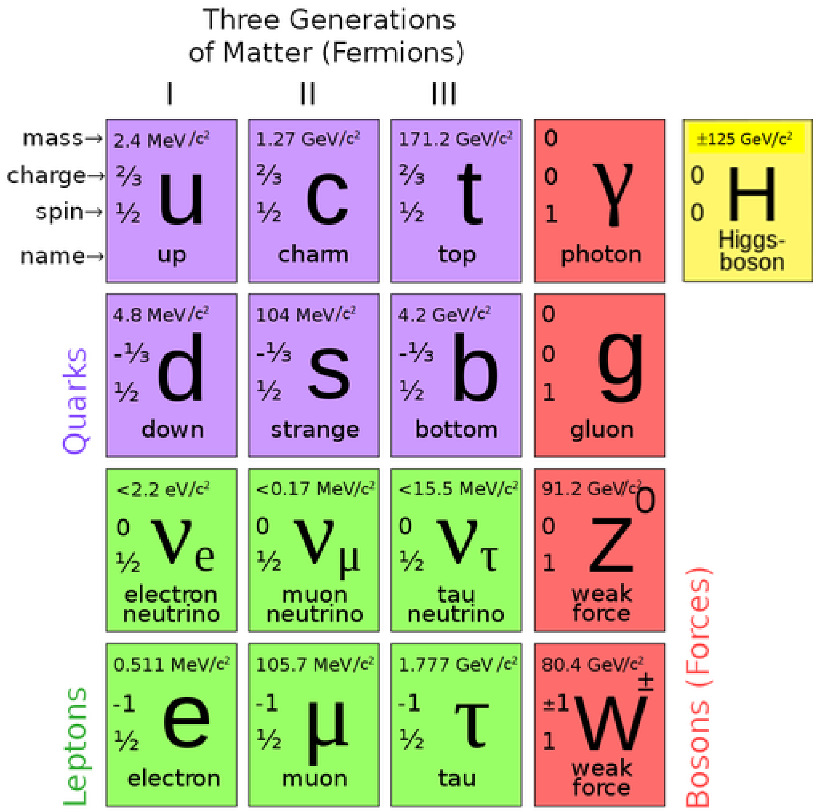

Figure 1.1: Classification of fundamental particle according to the standard model. The figure is taken from Ref. [1].

1.2 The Quark Gluon Plasma (QGP)

In nature, quarks are always found confined within hadrons due to the strong interaction. The strength of this interaction, which binds quarks inside hadrons, is characterized by the coupling constant of the strong force, as expressed in Eq. 1.2.

$$\alpha_s = \frac{12\pi}{(33 - 2N_f)\ln(\frac{Q^2}{\Lambda^2})} \tag{1.2}$$

Where N_f is the number of flavors of partons, Q^2 is the four-momentum transferred, and Λ is a scale parameter known as Quantum Chromo Dynamics (QCD) scale parameter.

Figure 1.2 shows the dependence of α_s as a function of Q. For large value of Q ($Q \gg \Lambda$), the coupling constant approaches to zero. This phenomenon is known as **asymptotic freedom** [2–4]. At this limit the partons are no more bound inside the hadrons instead they behave as free particles. Such free state of quarks and gluons at thermal equilibrium is known as Quark-Gluon-Plasma (QGP). Such an exotic state of matter is believed to be exist during the first few micro seconds of the early universe created in Big-bang. There are also evidences which suggests the presence of such a deconfined state of matter in the core of massive neutron stars [5].

The transition from the ordinary hadron gas phase to QGP phase is represented by conjectured QCD phase diagram as shown in Fig 1.3. The X-axis of the diagram is the baryon chemical potential (μ_B). The baryon chemical potential is defined as the energy required to add or remove one baryon from the system. The baryon chemical potential increases by increasing the net baryon in the system. The Y-axis is the temperature of the system. According to lattice QCD, at very small baryon chemical potential, a transition from hadronic to QGP phase is expected to takes place at temperature about $T = 155$ MeV [6–9]. The transition is a smooth cross over where the fluctuation are smaller than the length scale of QCD. According to QCD based model calculations at high baryon chemical potential the transition from hadronic to QGP phase is expected to be a first order phase transition [10–15]. Under this picture of phase transition from hadronic matter to QGP, there must be a point where the first order phase transition stops and the cross-over transition takes place. That point is known as critical point. The existence of critical point and first order phase transition is still a hypothesis and there are ongoing efforts for its confirmation.

1.3 Relativistic heavy-ion collisions

Heavy-ion collision experiments provide an excellent tool to create and study the QGP medium on a laboratory scale. In these experiments, two heavy nuclei are accelerated to nearly the speed of light in opposite directions and then collided with each other. A schematic diagram illustrating the various stages of a heavy-ion collision is shown in Fig. 1.4. Due to Lorentz contraction, the two heavy nuclei appear as flat disks as they approach each other. During the collision, a large amount of energy is deposited in a small volume. At the top RHIC energy, the temperature of the medium created is approximately 300 MeV, which is sufficient to induce the transition from hadronic matter to the QGP phase. The collision produces a strongly interacting QGP medium that behaves as a nearly perfect fluid. This medium expands over time due to its internal pressure. As the system expands, its tempera-

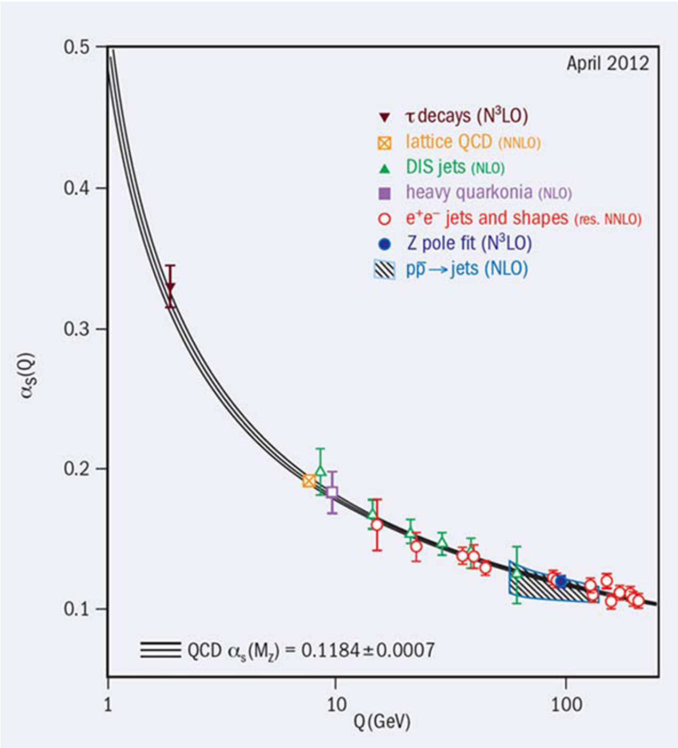

Figure 1.2: The dependence of the strong coupling constant (α_s) as a function of four momentum transferred(Q). The figure is taken from Ref. [16].

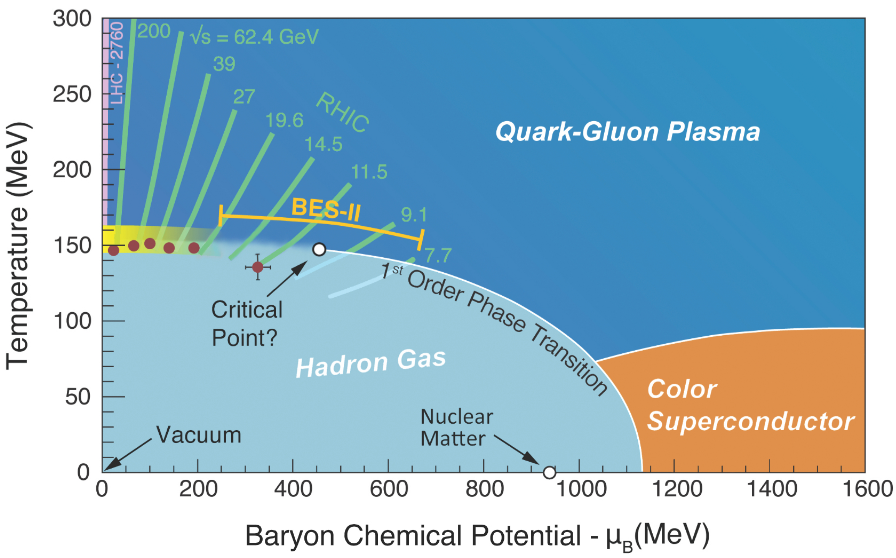

Figure 1.3: The conjectured QCD phase diagram. The picture is taken from Ref. [17].

ture decreases, and the partons begin to confine into various hadronic species. This process of hadron formation is called hadronization. Initially, the hadrons scatter off one another through both elastic and inelastic interactions. As the volume of the system increases, the mean free path between the hadrons grows, causing inelastic scattering to cease first. The surface at which inelastic scattering ends is referred to as the chemical freeze-out surface. After chemical freeze-out, the chemical composition of the medium remains unchanged, although elastic scattering continues. With further expansion, elastic scattering also stops, marking the kinetic freeze-out. At this point, the final-state particles can stream freely outward and are detected in the experimental detectors. The time interval between hadronization and kinetic freeze-out is known as the hadronic phase lifetime..

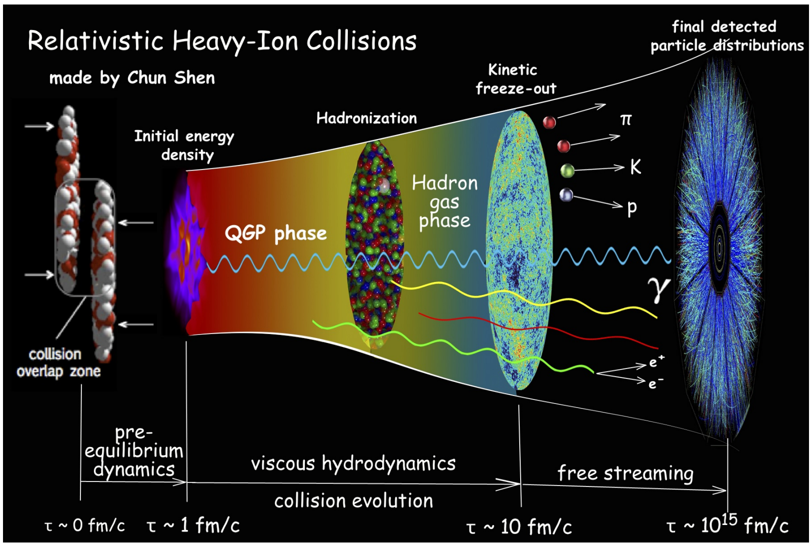

Figure 1.4: Schematic diagram of various stages of heavy-ion collisions. The picture is taken from Ref. [18].

1.4 Signatures of the QGP medium

The produced medium from heavy-ion collision experiment has a life-time of the order of 10^{-23} seconds. Therefore, it's not possible to detect the produced medium directly. There are various experimental evidences or signatures that indicates the presence of such an exotic state of produced matter from the collision. In the following sections we will discuss few of them.

1.4.1 Enhanced production of strange hadrons

The enhanced formation of strange hadrons in heavy-ion collision in comparision with non-QGP medium is proposed as a signature of QGP [19, 20]. The production of strange quark is more favored in QGP medium, the dominant mechanism of formation of s quarks is $gg \rightarrow s\bar{s}$. The other mechanism is $qq \rightarrow s\bar{s}$ although it contributes less than 20% of the total strange quarks [21]. Also it has been studied that the threshold energy needed to produce the strange quark is much smaller in QGP phase compared to hadronic phase. In a study [22], it was pointed out that the production of strange quarks has a smaller characteristic time constant in non-QGP system compared to QGP phase suggesting a high rate of production of strange quark is favorable in QGP compared to hadronic gas phase. All of the above arguments suggest the presence of a QGP medium in the early stage of collision could increase the strange hadron production.

Experimentally, such enhanced production of strange hadron is observed at both Large Hadron Collider (LHC) and RHIC energy. Figure 1.5 shows the ratio of yield (normalized with N_{part}) of strange hadrons in Au+Au and Cu+Cu collisions at 200 GeV to the yield in p+p collision. The ratio shows a clear enhancement in strange hadrons yield in Au+Au and Cu+Cu collisions compared to p+p with increasing N_{part}. The observation aligns with the expectation of the formation of QGP medium at these energies. Interestingly, A Large Ion Collider Experiment (ALICE) collaboration at LHC has reported the strangeness enhancement in high multiplicity p+p collisions which could be the indication of formation of QGP in small collision systems [23].

1.4.2 Jet quenching

Initial hard scattering between partons of colliding nuclei, where the momentum transfer is large could produce a parton with large transverse momentum (p_T). This high p_T parton latter fragments into highly collimated hadrons, known as Jets [25]. Dominant jet production are back to back means each jet has a partner jet moving in opposite direction to conserve momentum. Since jets are produced during the very initial stage of the collision they will sense the whole stage of the system evolution making them good probe for studying the medium. When a jet produced near the edge of the QGP medium one of its partner has to propagate through the QGP medium suffering energy loss and traverse momentum broadening by medium-induced gluon radiation. This phenomena is known as jet quenching [25–28].

Figure 1.6 shows the azimuthal distribution of hadrons with p_T ($p_T > 2.0$ GeV/c) with a

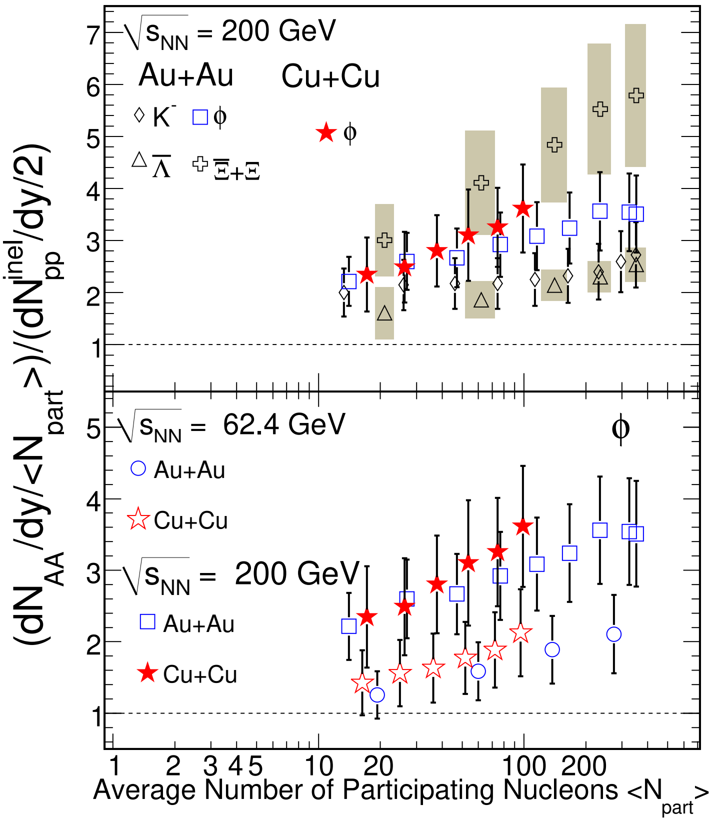

Figure 1.5: The upper panel shows the ratio of the yield of the strange hadrons such as K^-, ϕ, $\bar{\Lambda}$, and $\Xi^- + \bar{\Xi}^+$ normalized with N_{part} in Au+Au and Cu+Cu collisions to the corresponding yield in p+p collision as a function of N_{part} at 200 and 62.4 GeV. The lower panel shows the same for only for ϕ mesons. The figure is taken from the Ref. [24].

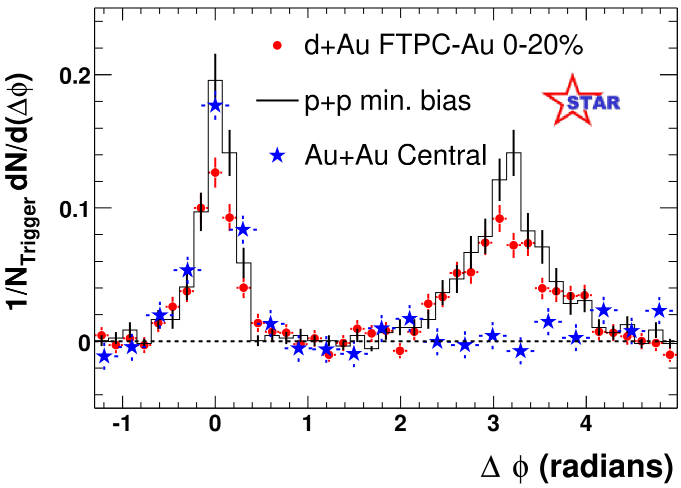

Figure 1.6: STAR measurement of dihadron azimuthal correlation is shown in Au+Au, d+Au and p+p collisions at high p_T. The figure is taken from Ref. [29].

trigger hadron with $p_T^{trig} > 4.0$ GeV/c. An enhanced correlation is observed at $\Delta\phi = 0$ for the two hadrons drawn from a single jet. The correlation is present in all three systems, Au+Au, d+Au and p+p. At $\Delta\phi = \pi$ dihadron correlation is present for both d+Au and p+p where as the correlation is absent for Au+Au collisions indicating the attenuation or quenching of the away side jet. This observation suggest the formation of a medium with colour degree of freedom in Au+Au collisions which is absent in smaller collision system such as in p+p or d+Au.

1.4.3 J/ψ suppression

The J/ψ particle is a bound state of c and $\bar{c}$ quarks. It was simultaneously discovered by two experiments in 1974 [30, 31]. The primary mechanism responsible for J/ψ production involves hard scattering between partons during the initial stages of heavy-ion collisions. In the presence of a hot and dense medium such as the Quark-Gluon Plasma (QGP), the production of the J/ψ state is expected to be suppressed compared to a non-QGP medium. This suppression is attributed to color screening, also known as Debye screening, which weakens the interaction potential between the c and $\bar{c}$ quarks [32].

Various experiments, spanning from SPS to LHC, have reported both the production and suppression of J/ψ [33–40]. Figure 1.7 presents the STAR collaboration's measurement of the nuclear modification factor (R_{AA}) for J/ψ in Au+Au collisions at $\sqrt{s_{NN}} = 200$ GeV [38]. The R_{AA} is defined in Eq. 1.3.

$$R_{AA} = \frac{\left(\frac{d^2N}{2\pi p_T dp_T dy}\right)_{\text{Au+Au}}}{\langle N_{coll}\rangle \times \left(\frac{d^2N}{2\pi p_T dp_T dy}\right)_{\text{p+p}}} \tag{1.3}$$

The R_{AA} denotes the ratio between the invariant yield of J/ψ in Au+Au collisions, normalized by the number of binary collisions, $\langle N_{\text{coll}}\rangle$, to the invariant yield of J/ψ in p+p collisions. In the absence of a QGP medium, the heavy-ion collision system can be viewed as a superposition of many proton-proton collisions. In such a scenario, the $\langle N_{\text{coll}}\rangle$-normalized yield of a particle produced in heavy-ion collisions should be equal to that of a single p+p collision, resulting in $R_{AA} = 1$.

However, the reported R_{AA} in Au+Au collisions is found to be smaller than unity across all centralities, and the ratio decreases with increasing centrality. This observation suggests the suppression of J/ψ production due to the presence of the QGP medium in the initial state.

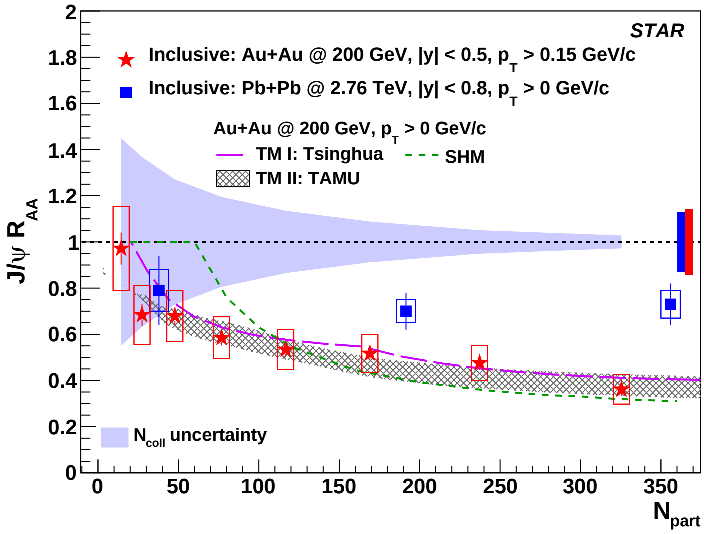

Figure 1.7: The nuclear modification factor R_{AA} for J/ψ is shown as a function of N_{part} in Au+Au collisions at $\sqrt{s_{NN}}$ = 200 GeV. The result is compared with R_{AA} in Pb+Pb collision from LHC experiment [39]. The figure is taken from Ref. [38].

1.4.4 Collective flow

When two heavy nuclei collide, they deposit an immense amount of energy within a small volume. The system formed in the collision undergoes rapid expansion over time. This expanding medium exhibits the properties of a nearly perfect fluid, characterized by an exceptionally low shear viscosity, rather than behaving like a gaseous medium. The constituents of this expanding system do not move independently; instead, they exhibit long-range correlations, resulting in collective behavior. This collective flow of the produced medium is regarded as a key signature of partonic degrees of freedom. The overall flow of the medium can have various orders of azimuthal anisotropy in the momentum space, those anisotropies carry the sensitive information about the produced medium. In the following section, we will delve deeper into the concept of anisotropic flow, providing a comprehensive literature review on the topic.

1.5 Literature review of anisotropic flow

There are various orders of anisotropy present in the momentum distribution of the final particles produced from the collision. The magnitudes of these anisotropies can be studied using a Fourier series expansion of the azimuthal distribution of the final-state particles in momentum space [41], as shown in Eq. 1.4.

$$E\frac{d^3N}{dp^3} = \frac{d^2N}{2\pi p_T dp_T dy}\left(1+\sum_{n=1}^{\infty} 2v_n \cos n(\phi-\Psi_R)\right) \tag{1.4}$$

Here, Ψ_R represents the reaction plane of the system. The reaction plane is the plane that spans the collision axis and the impact parameter between the colliding nuclei, as illustrated in Fig. 1.8. Above and below the reaction plane, the system exhibits reflection symmetry, which causes the sine terms in the Fourier series expansion to vanish. The coefficient v_n quantifies the magnitude of the n^{th}-order azimuthal anisotropy. The n^{th}-order flow coefficient can be determined using Eq. 1.5.

$$v_n = \langle\langle \cos n(\phi-\Psi_R)\rangle\rangle \tag{1.5}$$

In experiments, the impact parameter cannot be measured directly, making it impossible to determine the reaction plane directly from experimental data. Instead, the event plane, Ψ_n, is used as a proxy for the true reaction plane. The event plane can be determined from the distribution of final-state particles in the transverse plane. Since the distribution of final-state particles contains multiple harmonics, the event plane can be obtained independently for each harmonic. In experiments, the n^{th}-order flow coefficient can be expressed as shown in Eq.1.6. The method for determining the event plane from final-state particle distributions is discussed in Chapter 3.

$$v_n = \langle\langle \cos n(\phi-\Psi_n)\rangle\rangle \tag{1.6}$$

Here, the angular brackets represent an average over many particles produced in a single event, followed by an average over many such events. The first-order flow coefficient, v_1, measures the directed flow, which corresponds to the left-right asymmetry in the produced medium. The second-order flow coefficient, v_2, is known as elliptic flow and quantifies the ellipticity present in the momentum distribution of the final-state particles. The third-order flow coefficient, v_3, is referred to as triangular flow, which measures the triangularity in the system. This triangularity arises due to event-by-event fluctuations in the positions of the colliding nucleons within the collision zone. In this thesis, we primarily focus on the elliptic and triangular flow coefficients, which are discussed in detail in the following sections.

1.5.1 Elliptic flow

In a non-central nucleus-nucleus collision the overlap region of the two colliding nuclei looks like an almond as shown in Fig 1.9. In this overlap region the pressure gradient along

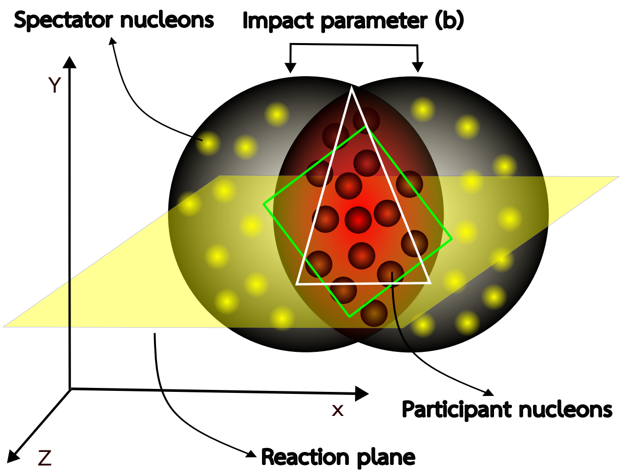

Figure 1.8: Schematic diagram of heavy-ion collision system

x-direction is larger compared to the pressure gradient along y-direction. Due to different magnitude of pressure gradient the system evolve more faster along x-direction compared to y-direction. Such spatial anisotropy generate the momentum isotropy where constituents of the system have large magnitude of momentum along x compared to y. This type of anisotropic flow is call elliptic flow.

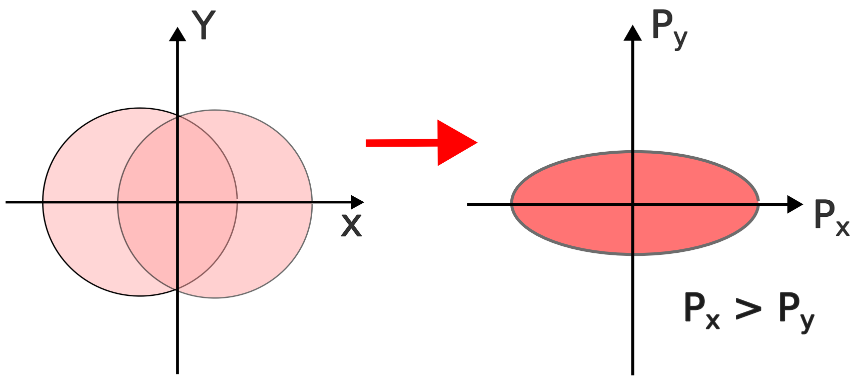

Figure 1.9: Schematic diagram of non-central collision of two heavy-nuclei. The spatial anisotropy will give rise to momentum anisotropy.

Elliptic flow is a widely studied observable in both experimental and phenomenological fields. The first experimental measurement of elliptic flow at RHIC was performed in Au+Au collisions at $\sqrt{s_{NN}}$ = 130 GeV for charged hadrons [42]. The measured v_2 values were found to be in remarkable agreement with hydrodynamic predictions, indicating a high degree of thermalization in the initially produced medium [42]. Later, in Ref.[43], it was demonstrated that hydrodynamics with a finite shear viscosity-to-entropy ratio (η/s) provided a better fit to the v_2 data compared to ideal hydrodynamics with $\eta/s = 0$. Figure1.10 illustrates how the magnitude of v_2 is sensitive to the η/s of the medium, making it a crucial observable for constraining the η/s of the system. Not only different η/s but also choice of different initial state models could change the magnitude of v_2 dramatically as shown in Fig 1.11, where two different model with different initial state produces different magnitude of spatial and momentum anisotropy.

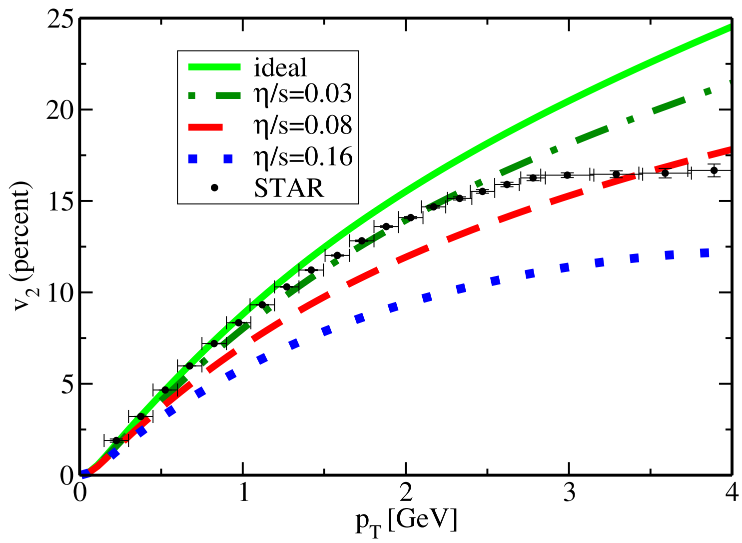

Figure 1.10: $v_2(p_T)$ measured from hydro-dynamics models with different value of η/s is compared with STAR data at 200 GeV. The figure is taken from the Ref. [43].

Therefore, the measurement of elliptic flow is important to constrain the initial state model and transport property such as η/s. The STAR collaboration has also reported the measurement of inclusive charged hadron elliptic flow in Au+Au collisions at lower collision energies, $\sqrt{s_{NN}}$ = 7.7 to 200 GeV [45]. This measurement shows the magnitude of v_2 decreases with decreasing collision energy which could arise due to the change in the medium property at lower collision energies and/or smaller collectivity at lower energies. The explanation of lower collision energy v_2 data demands a 3+1D hydrodynamic model with proper longitudinal dynamics [46].

1.5.2 Triangular flow

The collision geometry fluctuation in the overlap region of the two colliding which could arise due the fluctuation in the participant nucleons position [47]. Such fluctuation can have different order of anisotropy in the spatial space as shown in Fig. 1.8. These type of

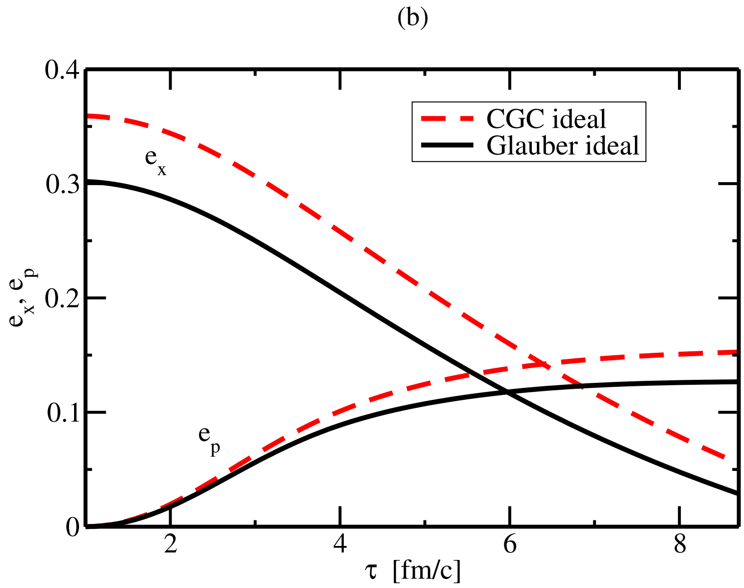

Figure 1.11: Time evolution of eccentricity in spatial and momentum space is shown for two different choice of initial state model. The figure is taken from the Ref. [44].

anisotropic distribution of the participant nucleons due to fluctuation can generate higher order anisotropic flow in the momentum space such as triangular flow, quadrangle flow and so on.

The PHENIX and STAR experiments have reported the presence of non-zero v_3 in Au+Au collision at $\sqrt{s_{NN}}$ = 200 GeV suggesting the presence of an initial geometry fluctuation in the initial state [48, 49]. A hydrodynamical study shown in Fig. 1.12 suggests that the higher order flow coefficients are more sensitive to the change in viscosity of the medium compared to second order v_2 [50]. Therefore, measurement of v_3 is also important to constrain the transport properties of the medium.

1.5.3 Number of constituent quark (NCQ) scaling: Test of partonic collectivity

Assuming the quark coalescence model of hadronization, in which quarks those are close in phase space combine with each other to form hadrons, the v_2 of a hadron at a particular p_T is given by Eq.1.7 [51, 52].

$$v_2^H(p_T) = n_q v_2^q(p_T/n_q) \tag{1.7}$$

Therefore, dividing the v_2^H with number of constituent quarks gives the magnitude of v_2 per quark. Such a study at RHIC top energy that is at $\sqrt{s_{NN}}$ = 200 GeV in Au+Au collisions

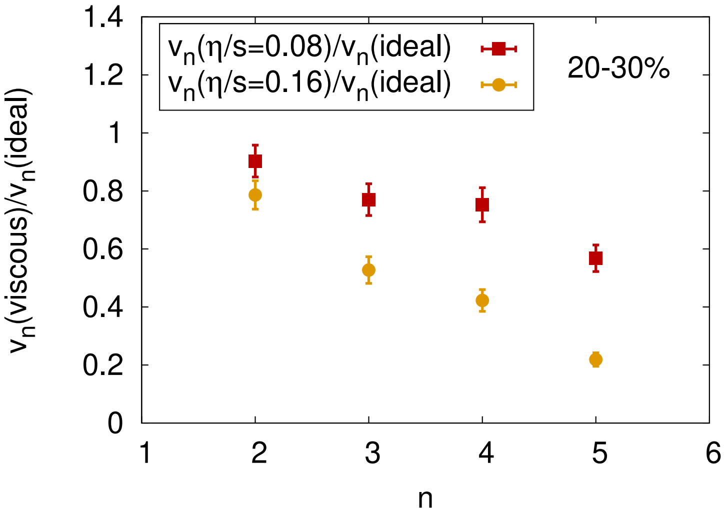

Figure 1.12: The ratio of flow coefficients in viscous to ideal hydro is plotted as function of order of the harmonic in mid-central (20-30% centrality) collisions. The figure is taken from the Ref. [50].

was carried out in Ref. [53]. Figure 1.13 shows the NCQ scaled v_2 plotted as a function of NCQ scaled transverse kinetic energy ($KE_T/n_q = (\sqrt{p_T^2 + m_0^2} - m_0)/n_q$) in Au+Au collisions at $\sqrt{s_{NN}}$ = 200 GeV at STAR. The purpose of studying v_2/n_q as a function of KE_T/n_q instead of p_T/n_q is to eliminate the mass-dependent effects driven by hydrodynamics at low p_T. This approach improves the quality of the scaling behavior [54–56]. The NCQ scaled v_2 measured from various identified particles species show similar magnitude. It was observed at 200 GeV that v_3 follows a modified NCQ scaling as shown in the right panel of Fig 1.13 [54, 55]. The observation of such NCQ scaling in v_2 and v_3 suggests the presence of partonic collectivity in the produced medium at top RHIC energies as well as it supports the quark coalescence model of hadronization.

The STAR collaboration has reported the measurement of v_2 for identified hadrons in Au+Au collisions at $\sqrt{s_{NN}}$ = 7.7–62.4 GeV using data from the first phase of the Beam Energy Scan (BES-I) program [57]. Figure 1.14 shows, at center-of-mass energies $\sqrt{s_{NN}} < 19.6$ GeV, ϕ-mesons exhibit a sudden decrease in v_2, with their magnitude found to be smaller compared to other hadrons, resulting in a breaking of the NCQ scaling. This behavior might suggest that the produced medium at lower collision energies is predominantly hadronic. Since the ϕ-meson has a smaller hadronic interaction cross section and freezes out early from the medium [58–61], it may not interact significantly with the hadronic-dominant medium at these lower energies. Consequently, its v_2 is observed to be smaller than that of other hadrons.

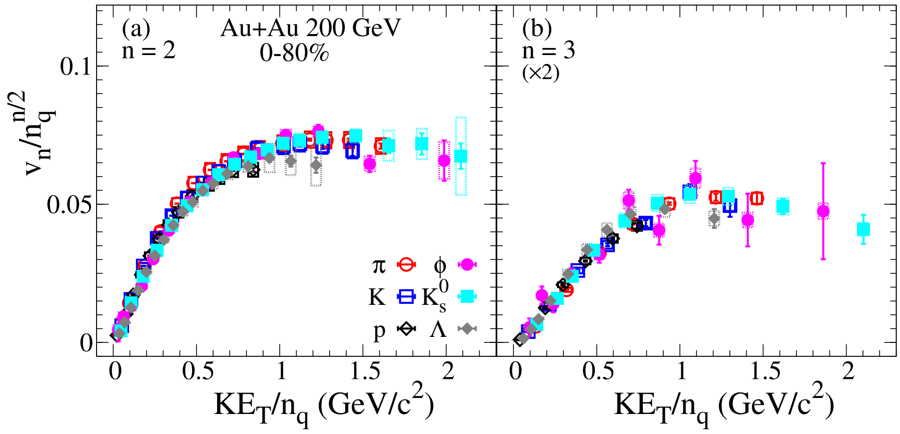

Figure 1.13: Left panel shows the NCQ scaled v_2 from various hadron species is plotted as a function of NCQ scaled transverse kinetic energy (KE_T) for Au+Au collisions at $\sqrt{s_{NN}} = 200$ GeV in 0-80% centrality. Right Panel shows the modified NCQ scaled v_3 as a function of KE_T. The figure is taken from the Ref. [54].

However, definitive conclusions cannot be drawn due to the large statistical uncertainties in the BES-I results. The observed deviation of the ϕ-meson from the NCQ scaling trend could potentially be attributed to statistical fluctuations. Similarly, for other multi-strange baryons and anti-baryons like Ξ^-, $\bar{\Xi}^+$, Ω^-, and $\bar{\Omega}^+$, the measurements lack precision. Therefore, it is crucial to revisit the lower energy regimes with high-statistics data to make any conclusive statements.

1.6 Thesis motivation

The primary goals of STAR collaboration are search for the evidences of first order phase transition, critical point and turn-off signature of QGP. This thesis is mainly focused on the last one that is search for the turn-off signature or disappearance of partonic signatures in the produced medium at lower collision energies. We have scanned the QCD phase diagram by visiting to the high net baryon density region with decreasing collision energy. At these region we have performed precise measurement of v_2 and v_3 and test the NCQ scaling to shed light on the nature of the medium created in these lower energies.

In Chapter 2, we have discussed about the STAR's detector system and the techniques of particle identification. In Chapter 3, we have presented the high precise measurement the strange and multi-strange hadron v_2 and v_3 at $\sqrt{s_{NN}} = 54.4$ GeV. In Chapter 4, We have presented the results for v_2 and v_3 results for identified hadrons using the high statistics BES-II data. The test of NCQ scaling is performed from $\sqrt{s_{NN}} = 19.6$ down to 7.7 GeV to

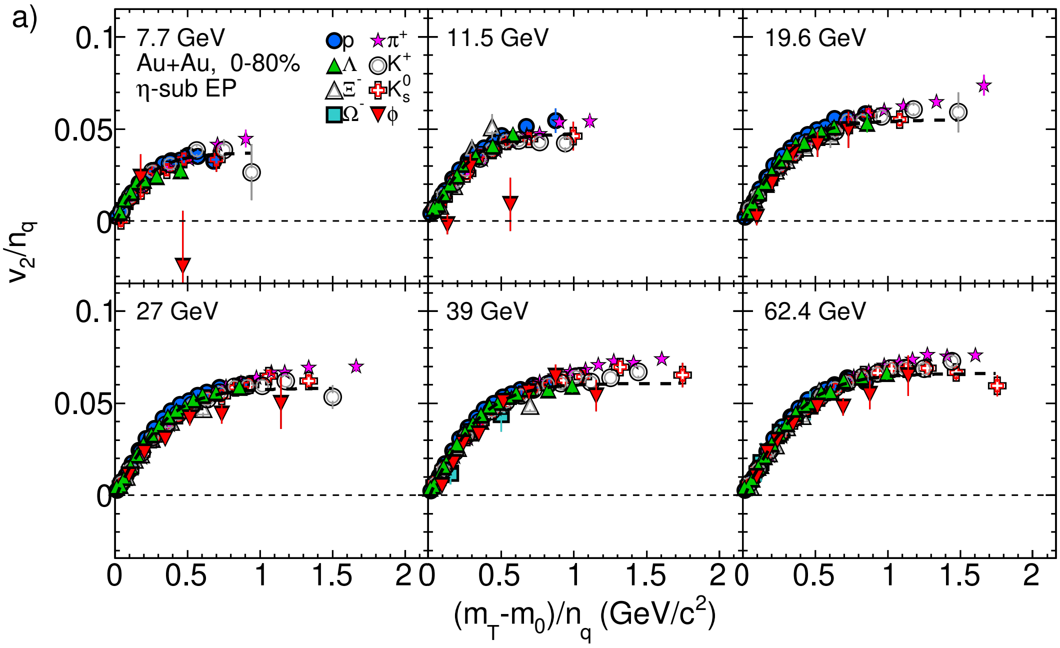

Figure 1.14: BES-I results for NCQ scaling of v_2 in Au+Au collision at $\sqrt{s_{NN}}$ = 7.7 - 200 GeV. The plot is taken from the Ref. [57].

look for the possible presence of hadronic dominance phase at these energies. In Chapter 5, we have discussed about an empirical scaling behavior in v_2 and v_3 of quarks measured from available experimental data for identified hadrons. In Chapter 6, we have also presented A Multi Phase Transport (AMPT) model study of longitudinal flow decorrelation at BES energies which found to be a sensitive observable for η/s.

CHAPTER 2

The STAR experiment at RHIC

2.1 Relativistic Heavy Ion Collider (RHIC)

The Relativistic Heavy Ion Collider (RHIC) is a state-of-the-art particle accelerator located at Brookhaven National Laboratory (BNL) on Long Island, United States. The accelerator has a circumference of approximately 3.8 kilometers. It operates with a variety of key components, as illustrated in Fig. 2.1. Two main ion beam injectors feed ions into the system are the Tandem Van de Graaff (Tandem) and the Electron Beam Ion Source (EBIS). EBIS, a newer and more advanced injector, is currently responsible for injecting ion beams. For instance, gold ion beams injected by EBIS enter the Booster synchrotron with an initial energy of 2 MeV per nucleon and a charge state of Au^{32+}. In the Booster, the ions are accelerated further to 100 MeV per nucleon and their charge is increased to Au^{77+}. The accelerated ions are then fed into the Alternating Gradient Synchrotron (AGS), which is approximately four times the size of the Booster. Within the AGS, the gold ions are accelerated to 8.86 GeV per nucleon and fully stripped of electrons, achieving a charge state of Au^{79+}. Finally, these fully ionized gold ions are transferred to the RHIC storage ring via the AGS-to-RHIC Transfer Line (AtR). RHIC has two rings as blue ring and yellow ring that can accelerate ions in opposite directions with speed of 99.9999% of the speed of light. The highest center of mass energy per nucleon pair ($\sqrt{s_{NN}}$) in a collision achieved in RHIC is 200 GeV. To date, RHIC has accelerated and collided various types of nuclei, including p+p, Au+Au, Cu+Cu, Au+d, Au+Cu, U+U, Zr+Zr, Ru+Ru, and O+O, at collider energies ranging from $\sqrt{s_{NN}}$ = 7.7 to 200 GeV [62].

In the past, RHIC hosted four experiments, each with distinct physics motivations. The Broad RAnge Hadron Magnetic Spectrometers (BRAHMS) [63], located at the 2 o'clock position; the Solenoidal Tracker at RHIC (STAR) [64], located at 6 o'clock; the Pioneering High Energy Nuclear Interaction eXperiment (PHENIX) [65], located at 8 o'clock; and PHOBOS [66], located at 10 o'clock. The BRAHMS experiment began operation in 2000 and concluded in 2006. Similarly, the PHOBOS experiment ran from 1999 to 2005. The PHENIX experiment started in 2000 and continued until 2016. Data-taking at STAR began in 2000, and the experiment is scheduled to continue collecting data through 2025.

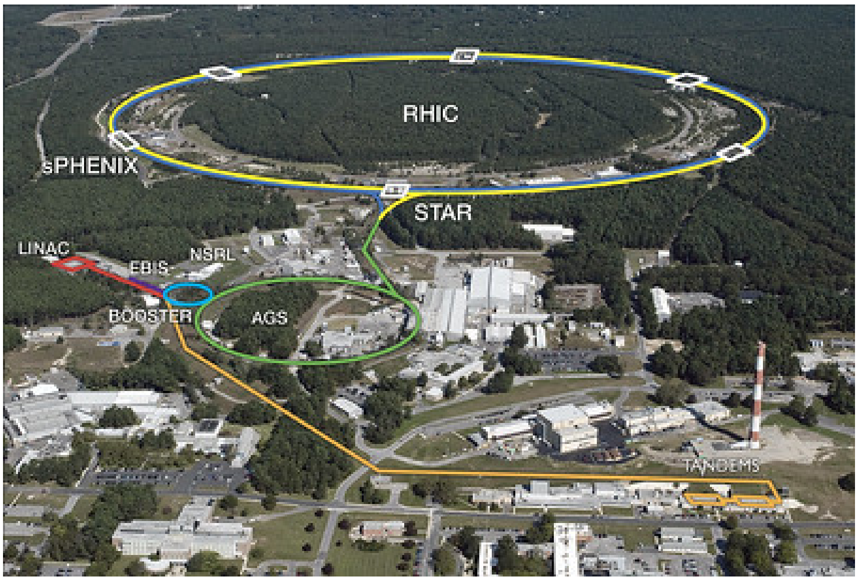

Figure 2.1: A bird-eye view of Relativistic Heavy Ion Collider (RHIC) at Brookhaven National Laboratory (BNL). The picture is taken from [67].

2.2 STAR Experiment

The STAR detector is a cylindrical detector surrounding the beam pipe with full azimuthal coverage and excellent particle identification capability [68]. The detector has many sub components as shown in Fig. 2.2. The large STAR magnet can produce magnetic field of 0.5 T [69]. Some of the detectors and their function are discussed below.

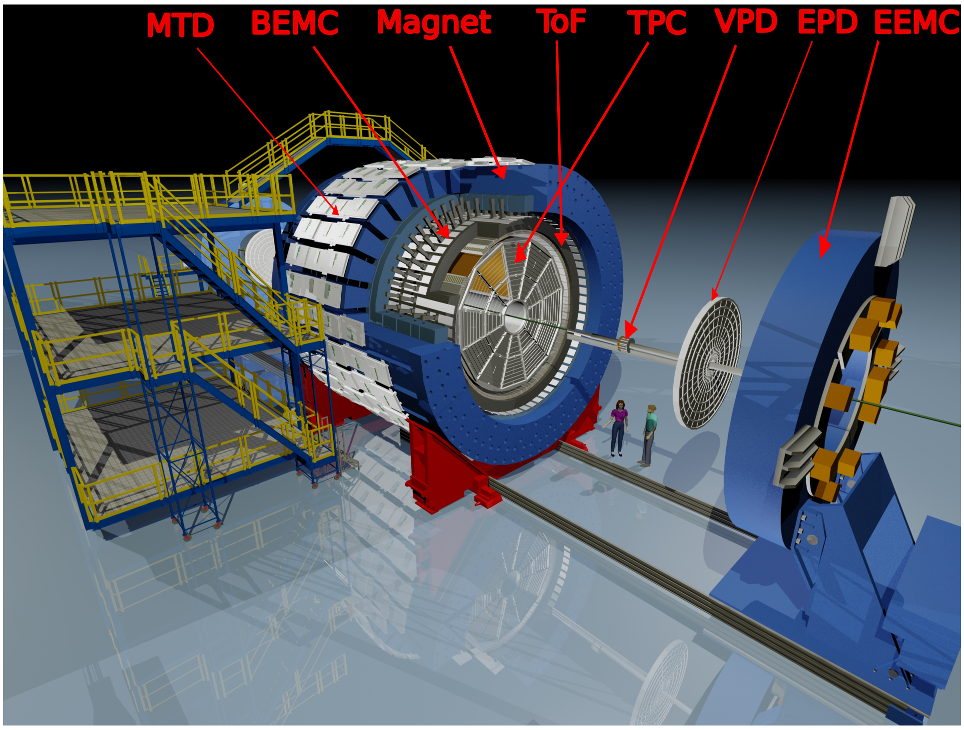

Figure 2.2: A 3D graphical image of the STAR detectors system. The picture is taken from Ref. [70].

2.2.1 Time Projection Chamber (TPC)

2.2.1.1 Construction of TPC

TPC is known as the "heart" of the STAR detector system [71]. It has a full azimuthal coverage and pseudorapidty coverage of -1.5 to 1.5. The pseudorapidity coverage is recently increased from $|\eta| < 1.0$ to $|\eta| < 1.5$ after inner TPC (iTPC) upgrade during Beam Energy Scan Phase-II (BES-II) [72]. TPC is a cylindircal gaseous detector which has length 420 cm. The inner diameter of the TPC is 100 cm. and the outer diameter is 400 cm. A schematic diagram of the TPC is shown in Fig. 2.3. At the center of the TPC, a thin conductive Central Membrane (CM) is kept at voltage 28 kV. The inner valume of the TPC is filled with P10 gas which is a mixture of 90% argon (Ar) and 10% methane (CH_4) [73]. There is a series of equipotential rings that fills the space between the central membrane and the end-cap of the TPC known as inner field cage. The purpose of the field cage is to maintain a constant electric field inside the TPC. The end-cap of the TPC has read-out planes, Multi Wire Proportional Chamber (MWPC) with pad read out mounted on a aluminum support wheel. Each end-cap has 12 such read-out planes which as known as anode planes. A schematic diagram of an anode plane is shown in Fig. 2.4. Each anode plane has two sub-sectors, inner sub-sector and outer sub-sector. The outer sector has 31 pad rows arranged continuously without any space between rows. The inner sector had 13 pad rows earlier before BES-II upgrade now it is changed to 40 [72]. This upgrade increased the η coverage of the TPC as well as brings the low p_T cut-off to 60 MeV. This also enhanced the dE/dx and momentum resolution of the particle tracks.

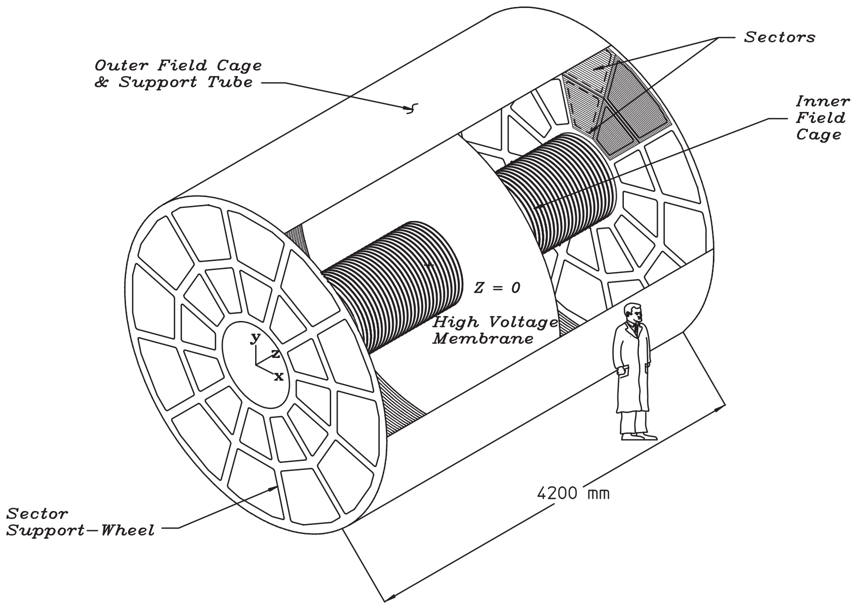

Figure 2.3: A schematic diagram of TPC. The picture is taken from Ref. [71].

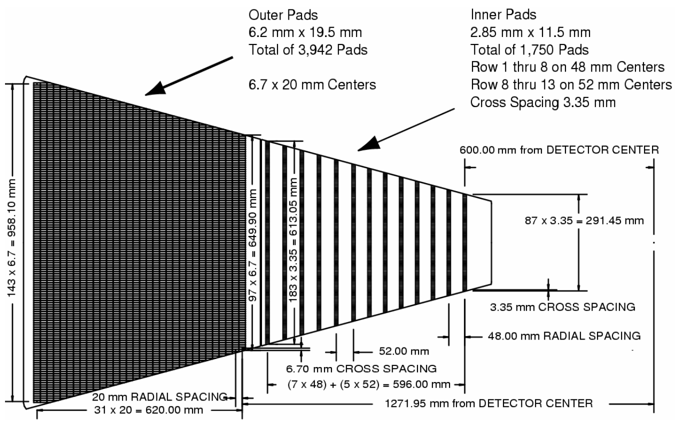

Figure 2.4: A schematic diagram of anode plane. The picture is taken from Ref. [71].

2.2.1.2 Working of TPC

The main purpose of the TPC is track reconstruction and particle identification [74]. After collision of two nuclei, the produced charged hadrons will move in a curve path due to the magnetic field of the TPC. While traversing the length of the TPC, these particles will interact with the gaseous medium of the TPC and ionize the atoms of the gas. The uniform electric field of $\simeq$ 135 V/cm makes the secondary electrons produced from ionization to drift towards the end-cap of the TPC with a typical speed of 5.45 cm/μs. When a secondary electrons hit the end cap of the TPC they will produce a signal in some particular pads, from which the x and y coordinate of the point of ionization can be determined. The z coordinate of a cluster of secondary electrons can be determined by measuring the time taken by the cluster to arrive at the end-cap pad from the point of ionization. When a charged hadron traverse through the volume of the TPC, it will produce secondary ionized electrons from many points by collecting all these electrons from every ionization point one can reconstruct the three dimensional picture of the charged particle.

From the ionization energy loss of a particular charged hadron, one can identify the hadron species since the energy loss depends on the mass of the particle. The energy loss per unit length, specific energy loss by a charged hadron is given by Bethe-Bloch formula 2.1.

$$-\frac{dE}{dx} = Kz^2\frac{Z}{A}\frac{1}{\beta^2}\left(0.5 \times ln\frac{2m_e c^2\beta^2\gamma^2 T_{max}}{I^2} - \beta^2 - \delta(\beta\gamma)/2\right) \tag{2.1}$$

Here, A is the atomic mass of the absorber, K/A = 0.307075 MeV g^{-1} cm^2, z and Z are the atomic number of incident particle and absorber respectively. T_{max} is the maximum kinetic energy transferred during ionization. $\delta(\beta\gamma)$ is the density effect correction to ionization loss. Figure 2.5 shows the dE/dx of particle tracks while traversing the TPC gas medium as a function of rigidity (momentum divided by charge of the track). At a given p, different particle species have different dE/dx. We can select a particular particle species by selecting the tracks close to their theoretical prediction line. The factor that decide closeness of a particular track to its theoretical prediction is defined in Eq. 2.2.

$$n\sigma_x = \frac{1}{R} ln\left(\frac{(dE/dx)_{measured}}{(dE/dx)_{theory}}\right) \tag{2.2}$$

Where R is the dE/dx resolution of TPC. For example, if one put a cut n$\sigma_\pi < 2.0$, that means selecting tracks that are 2 σ away from the theoretical predication for pion. The dE/dx band of pions and kaons merge together at $p \approx 0.6$ GeV/c and proton band merges with kaons at $p \approx 1.1$ GeV/c. Therefore, it's not possible to identify them by using TPC only.

To identify particles with higher momentum we use Time of Flight (ToF) which is described in details in the next section.

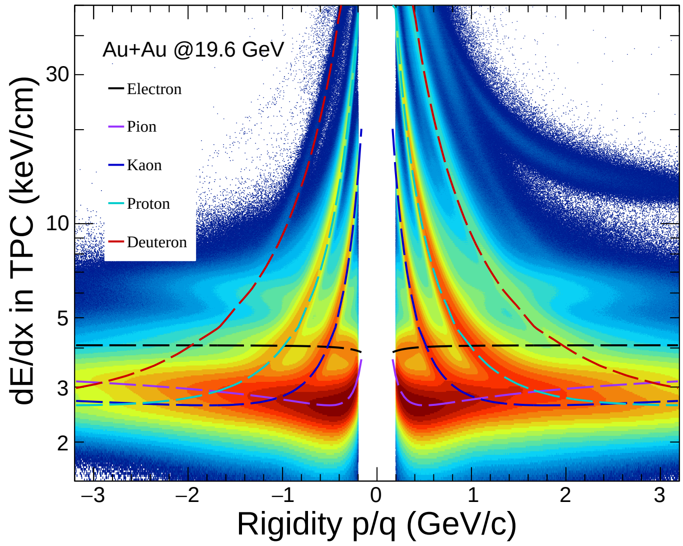

Figure 2.5: Specific energy loss of particle tracks is plotted as function of rigidity (p/q). The dashed lines are the theoretical predication.

2.2.2 Time of Flight (ToF) System

2.2.2.1 Construction of ToF

The STAR Time of Flight (ToF) [75, 76] is a cylindrical detector that surrounds the TPC. It has full azimuthal coverage and η acceptance from -1 to 1. It has two separate sub-detectors for measuring start-time and stop-time of time of flight of a particle track. The detector used for measuring start-time is known as Vertex Position Detector (VPD) [77]. The stop-time is measured by Time of Flight tray. There are two VPDs on either side of the TPC at a distance of 5.7 m from the center of the TPC, close to the beam line as shown in Fig. 2.2. The pseudo-rapidity coverage of the VPDs are $4.24 < \eta < 5.1$ and $-5.1 < \eta < -4.24$ A schematic diagram of side view of a single component or a single detector unit of a VPD is shown in Fig. 2.6. Each detector unit comprises several components: the front "cap" of a magnetic shield, an air gap, a ~0.25 inch thick layer of lead (equivalent to ~1.13 radiation length), a 1 cm thick scintillator, a Hamamatsu R-5946 of 1.5 inch diameter PMT (photomultiplier tube), and a linear resistive base. The lead serves as a photon converter, producing electrons that flood the scintillator layer, resulting in strong PMT signals and excellent start-timing performance. High voltage for the VPD bases is supplied by a LeCroy 1440 HV mainframe located on the platform and delivered to the detectors through RG-59 coaxial cables. Each detector unit weighs approximately 10 lbs, with most of the weight attributed to the magnetic shielding. There are 19 such detector units inside each VPD arranged in two concentric rings like structure. The typical time resolution of the VPD in Au+Au collisions at $\sqrt{s_{NN}}$ = 200 GeV is about 20-30 ps. Where as in p+p collision the resolution degrades to 80 ps.

The STAR Time-of-Flight (ToF) detector is based on Multi-gap Resistive Plate Chamber (MRPC) technology [78, 79]. Figure 2.7 presents both the side and end views of the MRPC modules. The MRPC consists of a stack of 0.54 mm thick resistive float glass plates, separated by uniform gas gaps of 220 μm. The gas mixture used in STAR is composed of 95% R134a and 5% isobutane. Graphite electrodes are applied to the outer surfaces of the outermost glass plates, allowing a high voltage to be applied across them and generating a strong electric field within each gap. When a charged particle traverses the glass stack, it ionizes the gas along its path within the gaps. The strong electric field then amplifies this ionization through avalanche multiplication. The resulting induced signal on the copper readout pads is the cumulative sum of the avalanches generated in each gas gap. There are 32 MRPC modules installed in a single ToF tray, and 120 such trays are placed surrounding the TPC. The STAR ToF detector achieves a typical time resolution of 80–90 ps.

2.2.2.2 Working of ToF

In a collision event, the start-time of the track is provided by the VPD. When the track arrived at the ToF one can get the stop-time. The velocity of the particle is calculated by using the Eq. 2.3.

$$\beta = \frac{v}{c} = \frac{L}{c\Delta t} \tag{2.3}$$

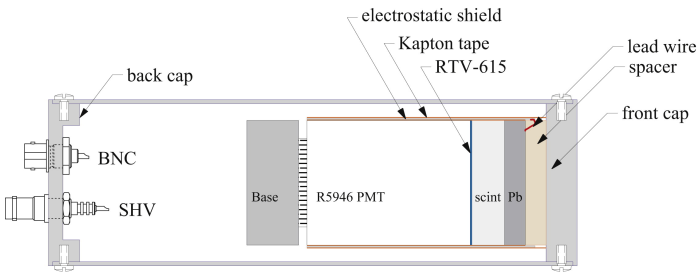

Figure 2.6: A schematic diagram of the side view of the VPD detector. The diagram is taken from the Ref. [77].

Here Δt is time difference between start-time and stop-time. L is the track length of the particle. Once we calculate the β of the track its mass can be calculated using Eq. 2.4.

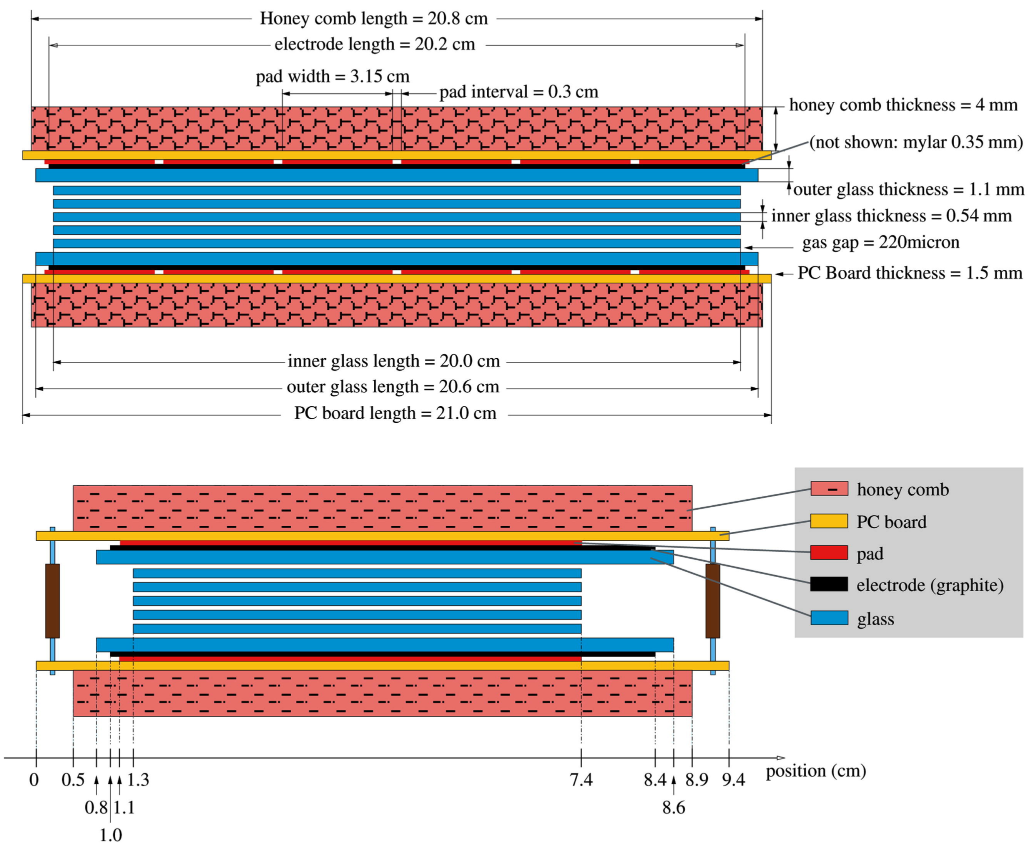

Figure 2.7: A schematic diagram of side and end view of MRPC modules developed for STAR ToF. The figure is taken from the Ref. [78].

$$m^2 = p^2\left(\frac{1}{\beta^2} - 1\right) \tag{2.4}$$

A plot mass m^2 calculated from ToF as a function of momentum is shown in Fig. 2.8.

In ToF, we can identify pions and kaons up to momentum 1.8 GeV/c and protons up to 3 GeV/c.

2.2.3 STAR triggers

In RHIC, collision of heavy-ions take place in form of bunches. Each bunch consists of about 10^9 nuclei. The bunch crossing rate is 9.37 MHz but detectors like TPC operates at much slower rate about 100 Hz. So it's not possible to read all the events by TPC. STAR trigger system consists of a set of fast detectors that read every bunch crossing and activate the slower detectors to read only events of interest [80]. The trigger detectors at forward and backward rapidity window are Zero Degree Calorimeters (ZDC) [81], Vertex Position Detectors (VPD), Beam-Beam Counter (BBC), End Cap Electromagnetic Calorimeter (EEMC).

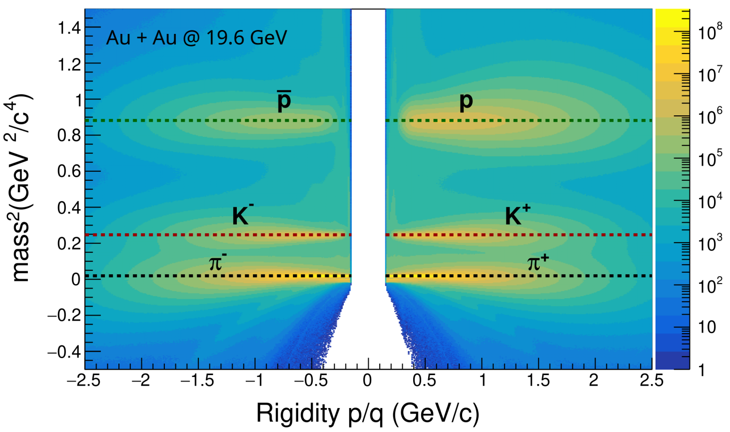

Figure 2.8: m^2 calculated from ToF is plotted as a function of rigidity. The dotted lines indicate the Particle Data Group (PDG) value of the m^2 of π, K, and p.

The trigger detectors at mid rapidity are Barrel Electromagnetic Calorimeter (BEMC) and Time of Flight (ToF).

The ZDCs are place closed to the beam pipe at 18 m away from the center of the TPC. The ZDCs measure the total energy of the spectator neutrons moving along z direction. Minimum biased events are triggered by simultaneous hit at two ZDCs [81]. ZDCs are also used as luminosity monitors [82]. The function of VPDs are already discussed in the previous section. There are two BBC modules mounted on east and west side of TPC at distance of 3.75 m from the center of the TPC [83] covering η acceptance of $3.4 < |\eta| < 5.0$. BBCs are used as minimum bias trigger in proton+proton collisions. The EEMC has η coverage of $1.0 < \eta < 2.0$ and full azimuthal acceptance. The main purpose of the EEMC is to detect photons and particles that decay by electromagnetic interaction such as π^0 and η. It serves as a trigger while detecting high energy electrons and positrons [84]. The BEMC has η acceptance of $-1.0 < \eta < 1.0$ and full azimuthal angle coverage. It's mainly used as a trigger for rare high p_T probes such as Jets, direct photons, heavy quarks etc [85].

2.3 Summary

In this chapter we briefly discussed about the STAR experiment and the detector used for data taking during collision events. The main detectors used for reconstructing particle track after collision and particle identification are TPC and ToF. In our analysis we have used both these detectors.

CHAPTER 3

Azimuthal anisotropic flow measurements of strange and multi-strange hadrons in Au+Au collisions at $\sqrt{s_{NN}}$ = 54.4 GeV

3.1 Chapter introduction

In this chapter, we discuss the measurement of second and third order azimuthal anisotropy parameters (v_2 and v_3) in Au+Au collisions at $\sqrt{s_{NN}}$ = 54.4 GeV at STAR. The measurement is performed for strange and multi-strange hadrons such as K_S^0, Λ, $\bar{\Lambda}$, Ξ^-, $\bar{\Xi}^+$, Ω^-, $\bar{\Omega}^+$, and ϕ mesons. These multi-strange hadrons have smaller hadronic interaction cross-sections and they freeze out earlier from the medium. As a result, the anisotropic flow parameters measured for these particles are less affected by late-stage hadronic interactions, making them valuable for constraining the initial state and transport properties of the medium produced in the collisions [58–61].

3.2 Dataset

In this analysis, we utilized the high-statistics dataset from Au+Au collisions at a center-of-mass energy of $\sqrt{s_{NN}}$ = 54.4 GeV, collected in 2017. We applied the minimum bias triggers, resulting in a total of approximately 600 million events used for this analysis.

3.3 Bad run and pile-up rejection

In heavy-ion collision experiments, a "bad run" refers to a data collection session where the quality of the recorded data is not suitable for analysis due to various issues such as problem in detectors, detector calibration issues, power outages etc. Those runs need to be rejected from the dataset before any analysis. Those bad runs are identified by run-by-run Quality Assurance (QA) checks. In QA analysis, various observable such as event and run average transverse momentum ($\langle p_T \rangle$), pseuorapidity ($\langle \eta \rangle$), azimuthal angle ($\langle \phi \rangle$), reference multiplicity from TPC ($\langle RefMult \rangle$), ZDC coincidence rate ($\langle ZDC_{rate} \rangle$) etc. are calculated. Any run where one or more of these observables deviates by more than 5σ from the overall average is flagged as a bad run and excluded from the analysis. The list of bad runs are given below.
18154039, 18154038, 18154037, 18153063, 18153057, 18157003, 18157011, 18158020, 18158021, 18161005, 18161021, 18164044, 18165039, 18166033, 18166052, 18167014, 18167015, 18167016, 18167017, 18167018, 18167041, 18168015, 18169036, 18170021.

If two collision events happen simultaneously very close to each other then there could be track mixing, where the tracks of one event counted as track of another. These events are called pile-up events. These pileup events are rejected using correlation between $Refmult$ and number of track matched with ToF ($TofMatched$). A linear correlation between $RefMult$ and $TofMatched$ is expected any event with a deviation from this linear correlation is rejected. This task is also performed by using official "StRefMultCorr" class. The correlation plot between "RefMult" and "TofMatched" before and after pile-up rejection is shown in Fig. 3.1.

3.4 Event and track selection

For the analysis, we selected events with the z-coordinate of the collision vertex located within $|V_z| < 30$ cm from the center of the TPC. Inside the beam-pipe, which has a radius of 3.95 cm, collisions with the beam-pipe materials can occur, leading to unwanted events that should be excluded. To reject these undesired collision events, we applied a radial position cut of $V_r < 2.0$ cm. The vertex position distributions are shown in Fig. 3.2.

To select quality tracks for the analysis following track selection criteria is employed. The number of hit points of each track on the endcap of the TPC should be greater than 15. To remove split tracks the total number of TPC hit points of a track should be greater that 52% of the maximum possible hits. A low p_T cut of $p_T > 0.15$ GeV/c is applied since track

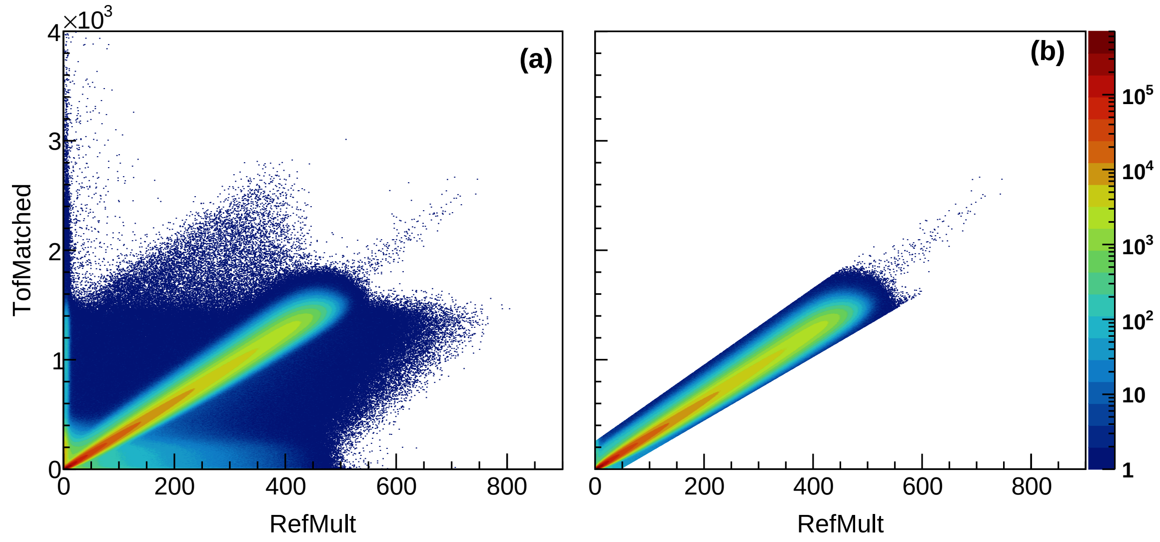

Figure 3.1: Panel(a) shows the RefMult vs. Tofmatched correlation plot before pile-up rejection. Panel(b) shows the same after pile-up rejection.

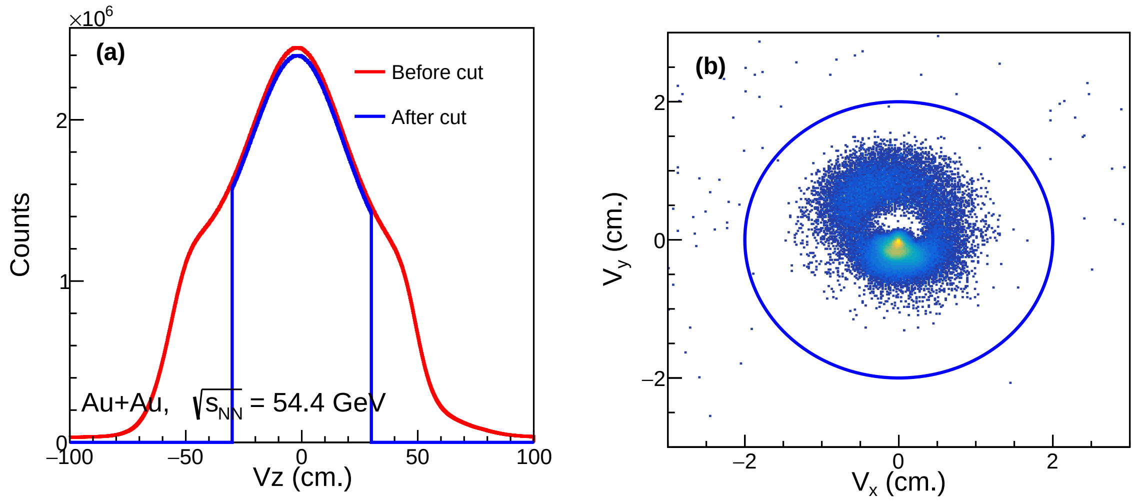

Figure 3.2: Panel(a) shows the distribution of collision vertex position along Z-axis from the center of the TPC. Panel(b) shows the 2D distribution of vertex position along X and Y respectively.

with p_T < 0.15 GeV/c have small momentum resolution. In case we need primary tracks from the collision we have applied a Distance of Closest Approach (DCA) cut on the tracks. Those tracks with DCA < 3.0 cm. from the primary vertex are considered for analysis. A pseudorapidity cut, $|\eta|$ < 1.0 is applied to consider tracks that are within the acceptance range of our detectors. A summary of all the track selection cuts are presented in Table 3.1.

Table 3.1: Track selection cuts used in the analysis of Au+Au collisions at $\sqrt{s_{NN}}$ = 54.4 GeV data.

cuts	values
Nhits	> 15
Nhits/NhitsPoss	> 0.52
p_T	> 0.15 GeV/c
DCA	< 3.0 cm.
$\|\eta\|$	< 1.0

3.5 Centrality determination

The centrality determination has been done using the raw multiplicity (N_{ch}^{raw}) of the charged particle in the mid-rapidity region, -0.5 < η < 0.5. The distribution of N_{ch}^{raw} is shown in Fig. 3.3. The distribution is fitted with a two component Glauber model to account for the vertex finding and trigger inefficiency in the low multiplicity region. The ratio between the Glauber simulation and the raw N_{ch}^{raw} is taken as a weight to correct the distribution at lower multiplicity region. The detail procedure can be found in the Ref. [86, 87]. The weighted distribution then divided in different classes having equal number of events. The first 10% of the highest multiplicity events fall under 0-10% centrality class, the next 10% of under 10-20% and so on.

3.6 Particle identification

The Time Projection Chamber (TPC) and the Time of Flight (ToF) are the two main detectors used for identifying stable charged particles (π, K, p) in this analysis. The detailed operation of these detectors is discussed in Chapter 2. For particle identification in the TPC, we apply a selection criterion of $|n\sigma|$ < 3 based on specific energy loss (dE/dx) informa-

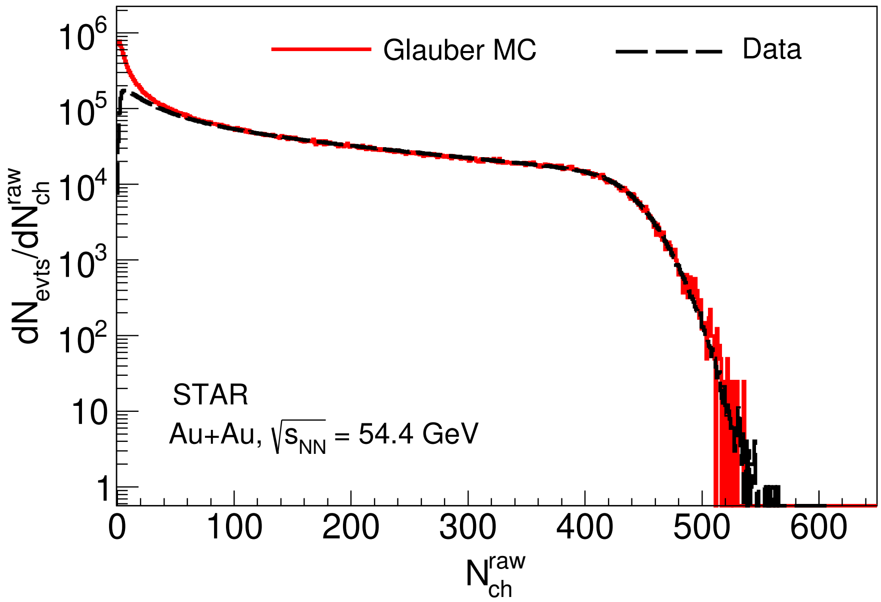

Figure 3.3: The uncorrected multiplicity distribution of reconstructed charged particles in Au+Au collisions at $\sqrt{s_{NN}} = 54.4$ GeV. Glauber Monte Carlo simulation is shown as the solid red curve.

tion. Additionally, for particle tracks with available ToF information, we impose a cut of $|\frac{1}{\beta_{\rm trk}} - \frac{1}{\beta_{\rm pdg}}| < 0.04$ to ensure proper identification.

However, both the TPC and ToF are capable of identifying only stable, long-lived particles that do not decay before reaching the detectors. In our analysis, we are focused on short-lived particles that cannot be directly detected by these detectors. Therefore, we must reconstruct the tracks of these short-lived particles using the information from the detected stable particles. The techniques used for reconstructing these short-lived particles are discussed in the following subsections.

3.6.1 Reconstruction of short lived hadrons

The particle species for which v_2 and v_3 are measured are strange and multi-strange hadrons such as K_S^0, $\Lambda(\bar{\Lambda})$, ϕ, $\Xi^-(\bar{\Xi}^+)$, and $\Omega^-(\bar{\Omega}^+)$. Various useful properties of these particles are listed in table 3.2. These particle have very small lifetime therefore, they can not be directly detected in the detectors. Particle such as K_S^0, $\Lambda(\bar{\Lambda})$, $\Xi^-(\bar{\Xi}^+)$, and $\Omega^-(\bar{\Omega}^+)$ decay by weak interaction whereas ϕ mesons decay by strong interaction. These particles can be reconstructed back using invariant mass technique through their respective hadronic decay channels. When a weakly decaying particle undergoes decay, its daughter particles often form a characteristic V-shaped pattern at the decay vertex, as illustrated in the Fig. 3.4.

Table 3.2: Quark content, lifetime, and major decay mode of the strange and multi-strange hadrons used in this analysis are listed.

Particle	Quark content	Lifetime	Major decay mode
K_S^0	$\frac{1}{\sqrt{2}}(d\bar{s} - s\bar{d})$	0.8954×10^{-10} s	$\pi^+\pi^-$
$\Lambda(\bar{\Lambda})$	uds($\bar{u}\bar{d}\bar{s}$)	2.632×10^{-10} s	pπ^-($\bar{p}\pi^+$)
$\Xi^-(\bar{\Xi}^+)$	dss($\bar{d}\bar{s}\bar{s}$)	1.639×10^{-10} s	$\Lambda\pi^-(\bar{\Lambda}\pi^+)$
$\Omega^-(\bar{\Omega}^+)$	sss($\bar{s}\bar{s}\bar{s}$)	0.821×10^{-10} s	$\Lambda K^-(\bar{\Lambda}K^+)$
ϕ	s$\bar{s}$	40 fm/c (1 fm/c ~ 10^{-23} s)	K^+K^-

These types of particles are known as V_0 particles. In experimental analyses, such decay topologies can be identified during track reconstruction. Instead of combining all produced particles indiscriminately to reconstruct the invariant mass of the parent particle, one could selectively combine only those tracks that most likely originate from these V-shaped topologies. This approach helps to reduce combinatorial background and enhances the significance of the signal. Particles like K_S^0 and Λ decay into stable daughters but Ξ and Ω first decay into a unstable daughter(Λ), which further decays to two grand daughters as shown in lower schematic diagram of Fig. 3.4. To select the possible daughters and/or grand daughters of the V_0 particles, the topological cuts used are summerized in table 3.3.

Table 3.3: Summary of V_0 topology cuts used for selection of daughter and/or grand daughters of weak decay V_0 particles.

cuts/particles	K_S^0	$\Lambda(\bar{\Lambda})$	$\Xi^-(\bar{\Xi}^+)$	$\Omega^-(\bar{\Omega}^+)$
DCA V_0 to PV	< 0.8 cm.	< 0.8 cm.	< 0.8 cm.	< 0.4 cm.
DCA between daughters	< 0.8 cm.	< 0.8 cm.	< 0.8 cm.	< 0.7 cm.
V_0 decay length	> 2.5 cm.	> 3.0 cm.	> 3.4 cm.	> 3.8 cm.
DCA daughter-1 to PV	> 0.7 cm.	> 0.3 cm.	> 0.2 cm.	> 0.5 cm.
DCA daughter-2 to PV	> 0.7 cm.	> 1.0 cm.	> 0.8 cm.	> 0.7 cm.
DCA between grand daughters	-	-	< 0.8 cm.	> 0.7 cm.
daughter-1 decay length	-	-	> 5.0 cm.	> 6.5 cm.
DCA grand daughter-1 to PV	-	-	> 1.0 cm.	> 1.5 cm.
DCA grand daughter-2 to PV	-	-	> 0.5 cm.	0.4 cm.

After selecting the daughter particles from the V_0 decays, the invariant mass is calculated using Eq. 3.1.

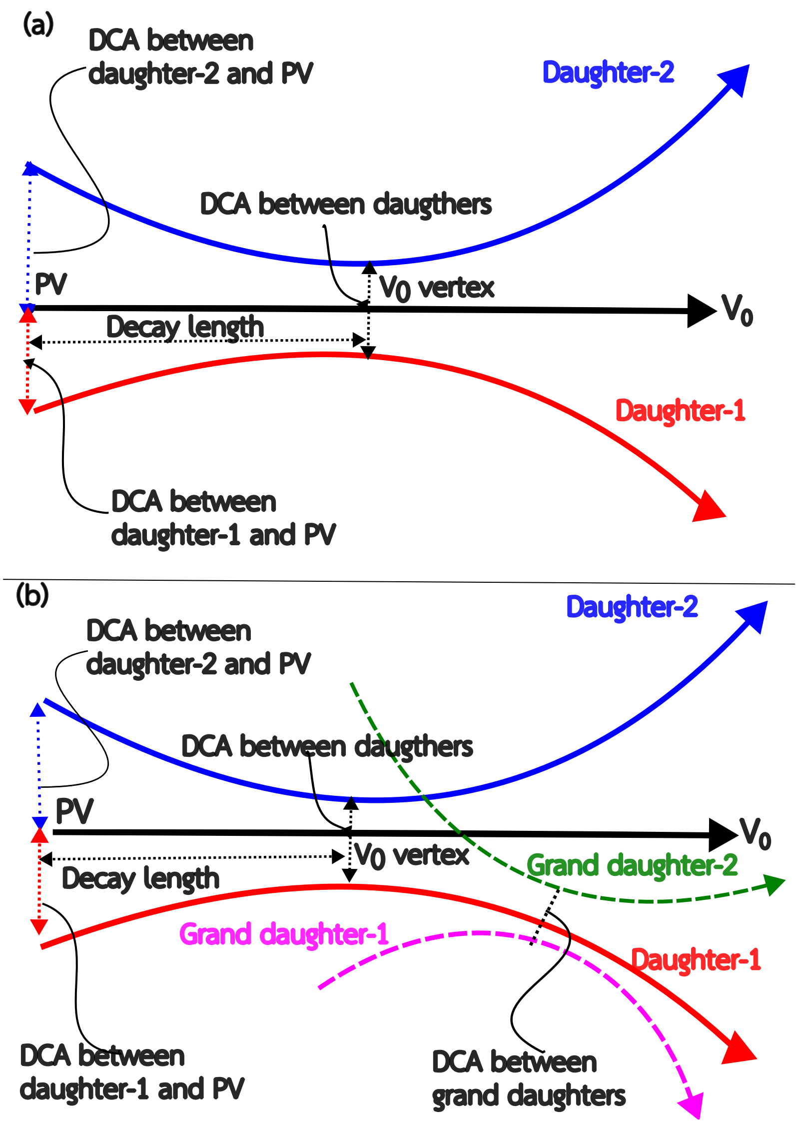

Figure 3.4: The upper figure shows the schematic diagram for decay of K^0_S and Λ. The lower figure shows the same for Ξ and Ω.

$$m_{\text{inv}} = \sqrt{(E_1 + E_2)^2 - \left(\vec{p}_1 + \vec{p}_2\right)^2}. \tag{3.1}$$

Here, $E_{1,2}$ and $\vec{p}_{1,2}$ represent the energy and momentum of the daughter particles, respectively. The invariant mass distributions for the K_S^0, $\Lambda(\bar{\Lambda})$, $\Xi^-(\bar{\Xi}^+)$, $\Omega^-(\bar{\Omega}^+)$, and ϕ mesons are shown in Fig. 3.5.

Unlike weakly decaying particles, topological cuts cannot be applied to ϕ mesons, as they decay via strong interaction much earlier than V_0 particles. To calculate the invariant mass distribution of ϕ mesons, all K^+ candidates in an event are paired with all K^- candidates from the same event. This method results in a relatively larger background for ϕ mesons compared to other particles. To estimate the background for ϕ mesons, we used the mixed event technique. Similarly, for K_S^0 and $\Lambda(\bar{\Lambda})$, the like-sign method was employed for background estimation. For $\Xi^-(\bar{\Xi}^+)$ and $\Omega^-(\bar{\Omega}^+)$, the rotational method was used to estimate the background. Each of these three background estimation methods is described in detail below.

3.6.2 Mixed event techniques for background estimation

This method is used to reconstruct the background of the ϕ mesons [88]. In this method K^+ of one event mixed with K^- of another event. Since there is no correlation between the K^+ and K^- of two different events, the event mixing method can not reproduce the signal of the ϕ meson. The mixed event invariant mass distribution however reproduces the combinatorial background as shown in the panel (e) of Fig. 3.5. In this method, events are first divided in 100 different classes according to there V_z position and centrality. K^+ from one event mixed with 5 different K^- of another events with similar V_z and centrality class.

3.6.3 Like-sign method for background estimation

This method is used to reconstruct the background of K_S^0 and $\Lambda(\bar{\Lambda})$ particles. In this approach, we calculate the invariant mass using daughter particles of the same charge. To reproduce the background of K_S^0, we combine a $\pi^+(\pi^-)$ with another $\pi^+(\pi^-)$ from the same event. Similarly, for $\Lambda(\bar{\Lambda})$, we pair a proton (anti-proton) with another $\pi^+(\pi^-)$ from the same event. Since a parent particle cannot decay into two same-sign daughters due to charge conservation, combining same-sign particles allows us to reproduce the background of the invariant mass distribution. Panel (a), (b) and (f) of Fig 3.5 show the like-sign background for K_S^0, Λ, and $\bar{\Lambda}$ respectively.

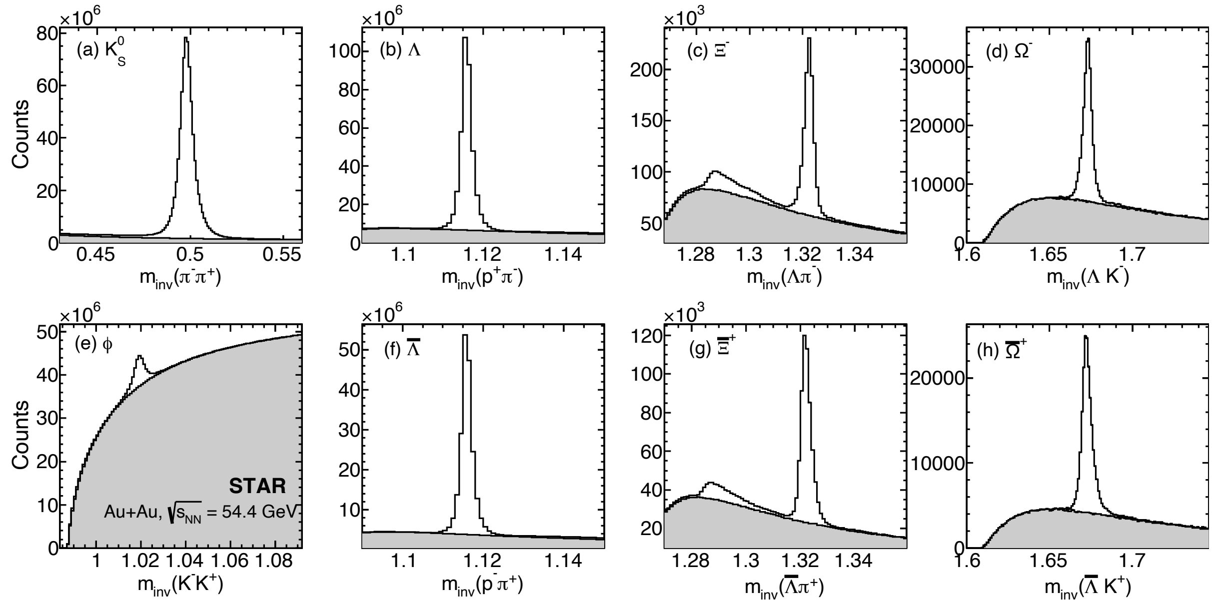

Figure 3.5: Invariant mass distribution of various particle and their antiparticles through their respective decay channel. The gray shaded area shows the distribution of the combinatorial background.

3.6.4 Rotational method for background estimation

This method is used to reconstruct the background of $\Xi^-(\bar{\Xi}^+)$ and $\Omega^-(\bar{\Omega}^+)$. In this method, one of the daughter particle track is rotated by 180° in the transverse plane. This will break the correlation between the two daughter tracks therefore, the invariant mass distribution can not reproduce the signal [89–91]. In case of $\Xi^-(\bar{\Xi}^+)$, the rotated daughter track is $\pi^-(\pi^+)$ and for $\Omega^-(\bar{\Omega}^+)$, the rotated daughter track is $K^-(K^+)$. The rotational background distribution for Ξ^-, Ω^-, $\bar{\Xi}^+$, and $\bar{\Omega}^+$ are shown in panel (c), (d), (g), and (h) of Fig. 3.5 respectively. In case of Ξ, the rotational background can not explain the small bump structure at invariant mass ~1.29 GeV/c^2. This small bump arises due to fake Λ candidates which are reconstructed by pairing the π^- from mother Ξ^- with the proton coming from the real Λ daughter of Ξ^-. This fake Λ candidates are then combined with the π^- from mother Ξ decay to give the bump structure [91, 92]. The effect of this bump on the flow coefficient is discussed in Sec. 3.7.

3.7 Flow measurement methods

3.7.1 Event plane determination and corrections

The n^{th} order flow coefficient from the Fourier series expansion of azimuthal distribution of final state particle yield is given by [41],

$$v_n = \langle\langle \cos n(\phi_i - \Psi_R)\rangle\rangle. \tag{3.2}$$

Where the first angular bracket represents the average over all the tracks in a event and then the second angular bracket represents the average over many such events in a given centrality class. ϕ_i is the azimuthal angle of the i^{th} track of the event. Ψ_R is the reaction plane of the system. Since in experiment, the true reaction plane angle can not be measured. We use event plane (Ψ_n), which is a proxy for the reaction plane, as the reference for v_n measurement. The range of Ψ_n is from zero to $2\pi/n$. Ψ_n of an event can be calculated from the distribution of the final state particles from the event. Ψ_n is given by,

$$\Psi_n = \frac{1}{n} \times \tan^{-1}\left(\frac{Q_{ny}}{Q_{nx}}\right). \tag{3.3}$$

Where Q_{nx} and Q_{ny} are called Q-vectors or flow-vectors along x and y direction respectively. The Q-vectors are calculated from the azimuthal angles of the final state particle using the formula

$$Q_{nx} = \sum_i \cos(n\phi_i) \quad Q_{ny} = \sum_i \sin(n\phi_i) \tag{3.4}$$

The track selection cuts used for event plane determination is almost same as overall track selection criteria as summerized in table 3.1 except one extra high p_T cut of $p_T < 2.0$ GeV/c. This cut is used to avoid inclusion of jets while constructing event plane. In general one would expect the distribution of the event plane is uniform between zero and $2\pi/n$ since every possible orientation of the event plane angle is equi-probable but due to the azimuthal non-uniform detection efficiency of TPC and presence of some dead sectors in the TPC endcap the distribution of event planes become non-uniform as shown in the Fig. 3.6 by the red solid line.

3.7.1.1 ϕ-weight correction

To make the event plane distribution flat we have applied a weight factor which is equal to the inverse of the azimuthal distribution of the detected particles over many events. By appying such weights the azimuthal bin where the particle counts are smaller due to detection problem will get more weight compared to a bin where particle counts are larger. This

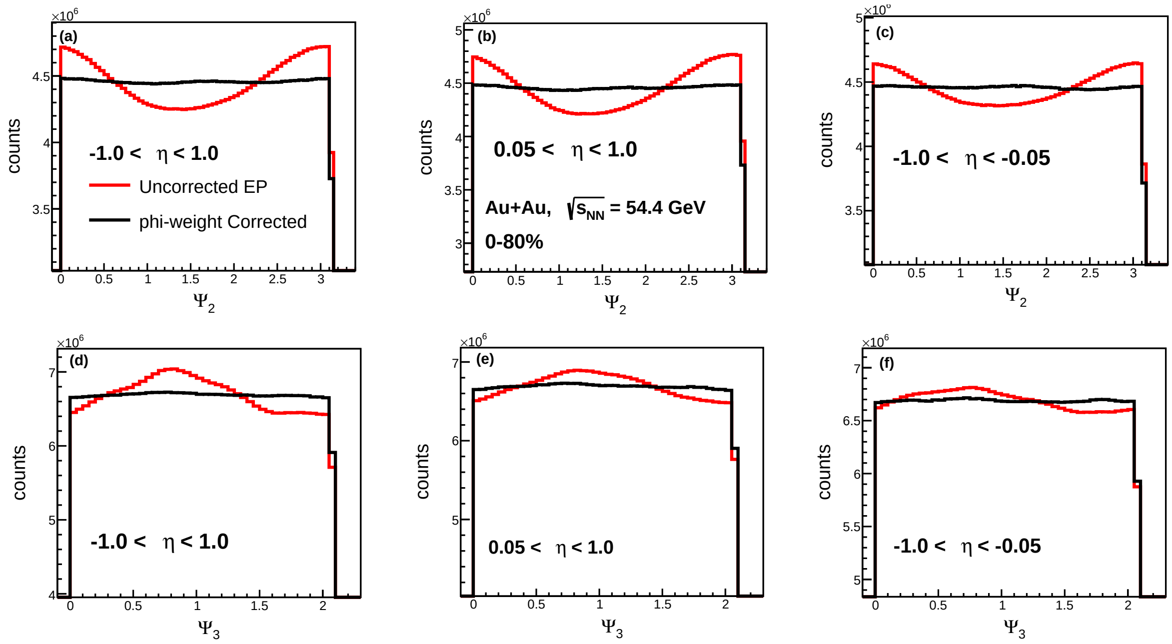

Figure 3.6: Panel(a), (b) and (c) show the distribution of Ψ_2 in three different rapidity window, -1.0 < η < 1.0, 0.05 < η < 1.0, and -1.0 < η < -0.05 respectively. The red solid line is the distribution of the uncorrected Ψ_2 and the black solid line is the distribution of ϕ-weight corrected Ψ_2. Panel(d), (e), and (f) show the same for Ψ_3.

will make the azimuthal distribution of the particle isotropic and consequently we will get a flat distribution of the event plane angles [41]. The ϕ-weight factor is applied while constructing the Q-vectors of an event as shown in the Eq. 3.5.

$$Q_{nx} = \sum_i w_i \cos(n\phi_i) \quad Q_{ny} = \sum_i w_i \sin(n\phi_i) \tag{3.5}$$

Here, w_i = ϕ-weight × p_T. p_T weight will enhance the event plane resolution. The ϕ-weight is calculated separately for different run numbers, centrality classes, V_z positions, and two different η windows (η > 0.05 and η < -0.05). In Fig. 3.6, the black solid line shows the distribution of the event plane angles after ϕ-weight correction. The distribution looks much flatter compared to the uncorrected event plane angles.

3.7.1.2 Event plane resolution

In experiments, the true reaction plane can not be measured directly. Therefore, we measure v_n with respect to the n^{th} order event plane. Due to finite multiplicity of an event, the n^{th} order event plane is not exactly equal to the reaction plane. Let the n^{th} order event plane and the reaction plane are related by Eq. 3.6

$$\Psi_n = \Psi_R + \Delta\Psi_n. \tag{3.6}$$

Where Ψ_R is the reaction plane, Ψ_n is the n^{th} order event plane, and $\Delta\Psi_n$ is the error in the estimation. The measured v_n in an event with respect to Ψ_n is given by

$$v_n^{obs} = \langle \cos n(\phi - \Psi_n)\rangle. \tag{3.7}$$

Here the angular bracket is the average over all the tracks in the event. Substituting Eq. 3.6 in Eq. 3.7, we get

$$\begin{aligned} v_n^{obs} &= \langle \cos n(\phi - (\Psi_R + \Delta\Psi_n))\rangle \\ &= \langle \cos n((\phi - \Psi_R) - \Delta\Psi_n)\rangle \\ &= \langle \cos n(\phi - \Psi_R)\cos(n\Delta\Psi_n)\rangle + \langle \sin n(\phi - \Psi_R)\sin n\Delta\Psi_n\rangle \end{aligned} \tag{3.8}$$

Assuming that the produced particles are distributed symmetrically above and below the reaction plane, the sine term in Eq. 3.9 vanishes. Since Ψ_R and $\Delta\Psi_n$ are uncorrelated we can write

$$v_n^{obs} = \langle \cos n(\phi - \Psi_R)\rangle\langle \cos n\Delta\Psi_n\rangle \tag{3.9}$$

$$= v_n^{true} \times \langle \cos n\Delta\Psi_n\rangle \tag{3.10}$$

Where v_n^{true} is the true flow coefficient measured with respect to the reaction plane Ψ_R. Therefore, the true flow coefficient v_n^{true} is given by

$$\begin{aligned} v_n^{true} &= \frac{v_n^{obs}}{\langle \cos n\Delta\Psi_n\rangle} \\ &= \frac{v_n^{obs}}{\langle \cos n(\Psi_n - \Psi_R)\rangle} \end{aligned} \tag{3.11}$$

The factor in the denominator of Eq. 3.11 is known as the resolution of the n^{th} order event plane which takes the deviation between the reaction plane Ψ_R and the reconstructed event plane Ψ_n into account. The v_2 measured with respect to Ψ_n must be corrected for resolution. In experiments, the resolution is calculated by dividing the full event into two sub-events as shown in Eq. 3.12

$$R_n = \sqrt{\langle \cos n(\Psi_A - \Psi_B)\rangle}. \tag{3.12}$$

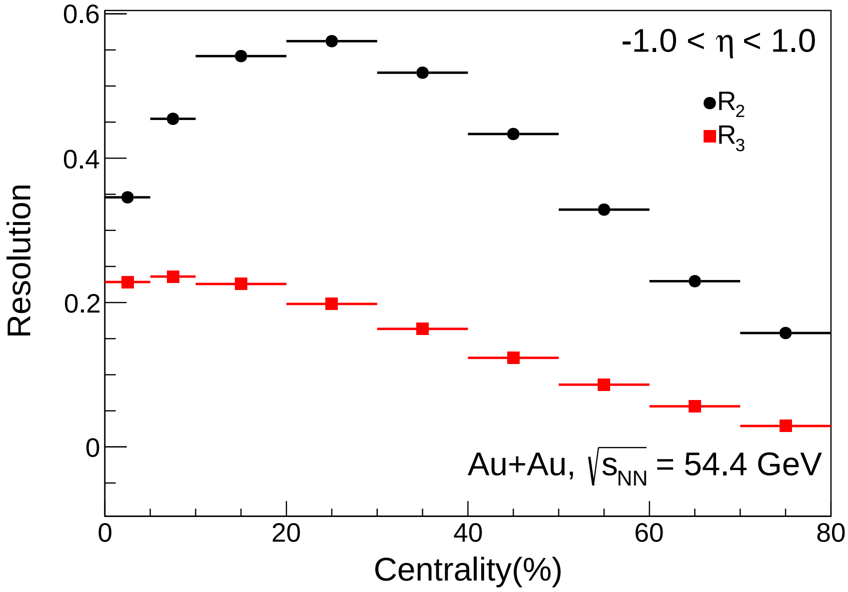

Figure 3.7: The second order event plane resolution (R_2) and the third order event plane resolution (R_3) is plotted as a function of centrality in Au+Au collisions at $\sqrt{s_{NN}}$ = 54.4 GeV.

Here Ψ_A and Ψ_B are two sub-event plane angle in two different rapidity zone. The two sub-events are assumed to be have same multiplicity. In this case the resolution factor obtained is called sub-event plane resolution. In our analysis the rapidity window chosen is -1.0 < η < -0.05 and 0.05 < η < 1.0.

Figure 3.7 shows the second and third order sub-event plane resolutions as a function of centrality. The value of R_2 is the highest in 20-30% centrality collisions and start to decrease towards peripheral collisions due to small multiplicities of the final state particles in the peripheral collisions. It's value also decreases as we move towards more central collisions due to smaller elliptic flow magnitude in central collisions. Similarly, R_3 also decreases from central to peripheral collisions due to smaller multiplicities.

3.7.2 Flow measurement methods for (multi)strange hadrons

The sub-event plane method is used to measure the flow coefficients, v_n, for all particles. In this method, the event plane angle is determined in two separate pseudorapidity (η) regions: $-1.0 < \eta < -0.05$ and $0.05 < \eta < 1.0$, with a gap of 0.1 in η between them. The v_n of a particle in the positive η region is measured with respect to the event plane in the negative η region, and vice versa. This approach helps to remove auto-correlation between the particle of interest and the event plane angle.

To calculate the flow coefficients, v_n, we need the azimuthal angle of the particle of interest. However, in this case, the particles of interest are short-lived, so their azimuthal angle cannot be measured directly. Instead, the v_n of these particles is calculated using the invariant mass method and the $\phi - \Psi$ binning (event plane) method.

3.7.2.1 Invariant mass method

In this method, we first reconstruct the mother particle using the invariant mass distribution of the decay daughters. Then we calculate the v_n as a function of invariant mass of the decay daughter pairs. Taking ϕ meson as an example we show its v_2 measurement method in Fig. 3.8. ϕ meson signal is reconstructed using the invariant mass of the K^+ and K^-. v_2 is calculated as a function of invariant mass. The distribution is shown in the panel (b) of Fig. 3.8. Here the measured v_2 has contribution from both ϕ meson signal and background. To obtain the v_2 of the signal, the distribution is fitted with a function shown in Eq. 3.13. The details about the method can be found in Ref. [93].

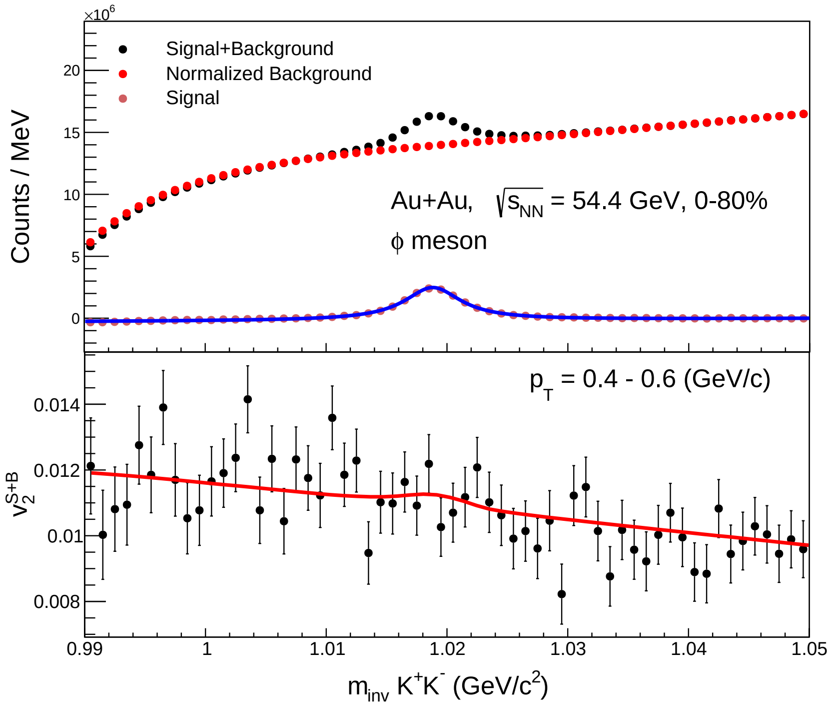

Figure 3.8: Upper panel shows the invariant mass distribution of K^+ and K^- for ϕ meson signal + combinatorial background, normalized mixed event background, and background subtracted signal of ϕ meson in 0-80% centrality class events. Lower panel shows the v_2 of K^+ and K^- pair as a function of their invariant mass. The solid red line is the fitting function mentioned in Eq. 3.13.

$$v_2^{S+B}(m_{inv}) = v_2^S \frac{S}{S+B}(m_{inv}) + v_2^B \frac{B}{S+B}(m_{inv}). \tag{3.13}$$

Here, v_2^{S+B} represents the v_2 of the combined signal and background, v_2^S is the v_2 of the signal, and v_2^B is the v_2 of the background. The symbols S and B denote the signal and background yields, respectively, which are obtained by integrating the invariant mass distributions of the signal and background, as shown in panel (a) of Fig. 3.8. The background v_2^B is approximated by a first-order polynomial function of m_{inv}. The signal v_2^S is treated as a free parameter and is determined through fitting.

Here, resolution correction is applied to the v_2^{S+B} event-by-event in narrow centrality bins. Then the resolution corrected v_2^{S+B} from different centrality bins can be added to get the results for a wide centrality bin. For example, v_2^{S+B} shown in Fig. 3.8 is obtained by adding v_2^{S+B} of centrality bins staring from 0-5% to 70-80%. The v_2^S obtained from the fitting is the resolution corrected v_2. This method is also used to measure v_3, and it applies to all particle species analyzed in the study except Ξ. In case of Ξ we have a bump structure in the residual background. The affect of the bump is taken into consideration by changing the fitting function in Eq. 3.13 to Eq. 3.14.

$$v_2^{S+B}(m_{inv}) = v_2^S \frac{S}{S+B+b}(m_{inv}) + v_2^b \frac{b}{S+B+b}(m_{inv}) + v_2^B \frac{B}{S+B+b}(m_{inv}). \tag{3.14}$$

Here, b is the yield of the residual bump, v_2^b is the v_2 of the residual candidates in the bump region. v_2^b is found to be negligibly small and its affect on the v_2 of Ξ is negligible.

3.7.2.2 $\phi - \Psi$ binning method (Event-plane method)

In this method azimuthal distribution of the yield of particle of interest with respect to event plane is used to calculate v_2 and v_3 [41]. For example, ϕ meson yield is calculated in different $\phi - \Psi_n$ bin as shown in the Fig. 3.9. The distribution is fitted with a function given by R.H.S of Eq. 3.15. From the fitting, we get v_n^{obs} which is resolution uncorrected. In this case the resolution correction is applied in large centrality bins as shown in Eq. 3.16. The average of the resolution inverse in a large centrality bin is calculated using Eq. 3.17 [94].

$$\frac{dN}{d(\phi - \Psi_n)} = \frac{N_0}{2\pi}\left(1 + v_n^{obs}\cos n(\phi - \Psi_n)\right) \tag{3.15}$$

$$v_n = v_n^{obs} \times \left\langle \frac{1}{R_n} \right\rangle \tag{3.16}$$

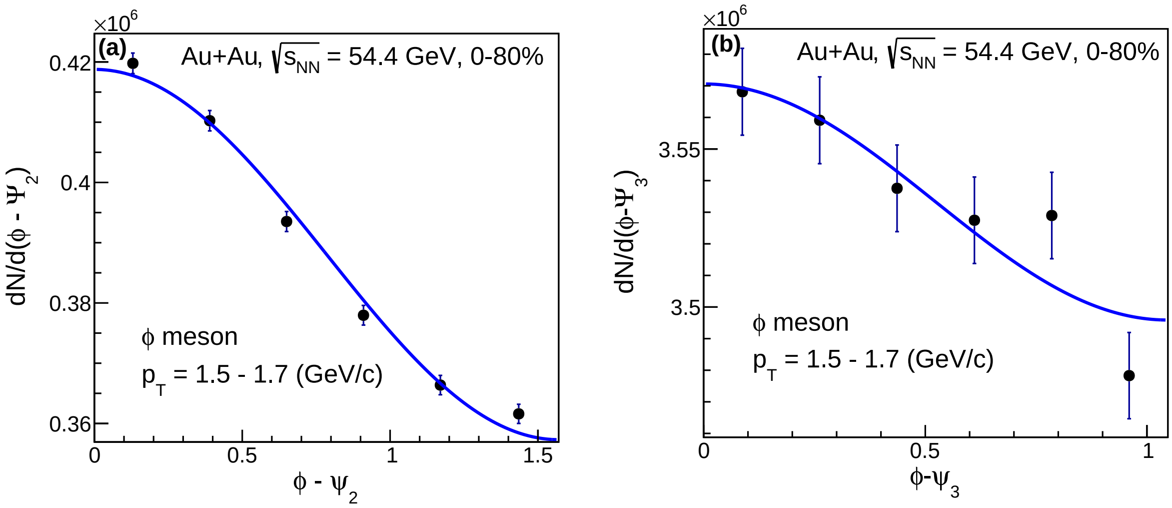

Figure 3.9: Panels (a) and (b) show the raw yield distributions of ϕ mesons in different $\phi-\Psi_2$ and $\phi-\Psi_3$ bins, respectively, for the transverse momentum range $p_T = 1.5-1.7$ GeV/c and 0-80% centrality. The solid blue line represents the fitting function shown in Eq. 3.15.

$$\left\langle \frac{1}{R_n} \right\rangle = \frac{\sum_{i=1}^{n} N_i (1/R_i)}{\sum_{i=1}^{n} N_i} \tag{3.17}$$

Here, R_i is the resolution values in narrow centrality bins, and N_i is the raw yield of the particles in that centrality. The sum is over all the narrow centrality bins.

Figure 3.10 shows the minimum bias results for ϕ meson $v_2(p_T)$. The results from both the methods are in good agreement with each other.

3.8 Systematic uncertainty estimation

The systematic uncertainty in the v_n measurements are evaluated by varying various analysis cuts such as event selection cuts, track selection cuts, PID cuts. A summary of all the systematic variations are listed in Table 3.4. The background for V_0 decay particles are estimated by either like-sign or rotational method as described earlier in Sec. 3.6. These backgrounds are also modeled by polynomial functions and the resulting difference in v_n is added in systematic. The topological cuts used for V_0 particles are also varied by 25% from its default value. Barlow method it applied to calculate the total systematic uncertainty [95]. In this method the data points from various cuts, those are compatible with each other within 1σ are not considered for systematic uncertainty. This method is useful in separating statistical fluctuations from systematic uncertainty. The details about systematic uncertainty calculation using this method is described in details below.

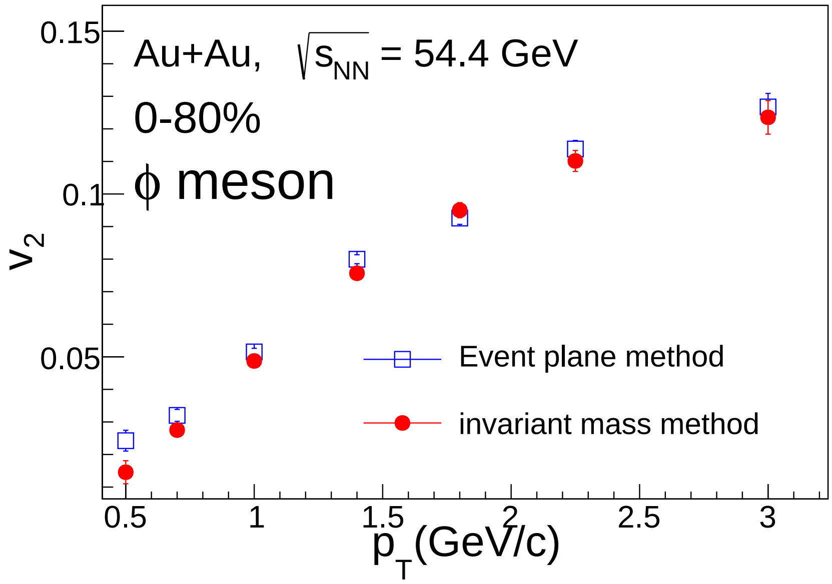

Figure 3.10: A comparison between the results obtained from invariant mass method and $\phi - \psi$ binning method (event plane method) for ϕ mesons in 0-80% centrality for Au+Au collisions at $\sqrt{s_{NN}}$ = 54.4 GeV is shown.

- First the difference between v_n using default cut and a varied cut is calculated.

$$\Delta v_n = |v_n(\text{def}) - v_n(\text{cut})| \tag{3.18}$$

- $\Delta\sigma_{stat}$ which is given by Eq. 3.19 is calculated

$$\Delta\sigma_{stat} = \sqrt{|\Delta\sigma^2_{stat}(\text{cut}) - \Delta\sigma^2_{stat}(\text{def})|} \tag{3.19}$$

  Where $\Delta\sigma^2_{stat}$(cut) and $\Delta\sigma^2_{stat}$(def) are the statistical uncertainties in v_n for varied and default cuts respectively.

- By Barlow condition if $\Delta v_n < \Delta\sigma_{stat}$ then the deviation from the default value is considered as statistical fluctuation and not included in systematic. If $\Delta v_n > \Delta\sigma_{stat}$ then the systematic uncertainty due this particular cut is given by

$$\sigma_{sys} = \sqrt{\Delta v_n^2 - \Delta\sigma^2_{stat}} \tag{3.20}$$

- The total systematic is calculated by quadrature sum of the systematic uncertainties from individual cuts.

$$\sigma_{sys}(\text{tot}) = \sqrt{\sum_i \sigma^2_{sys}(i)} \tag{3.21}$$

  Where $\sigma^2_{sys}(i)$ is the systematic error due to a particular cut.

Table 3.4: Details of the analysis cuts variations for systematic uncertainty estimation.

cuts	default value	variation
$\lvert V_z \rvert$	< 30 cm.	< 25 cm.
V_r	< 2 cm.	< 1 cm.
DCA (for ϕ only)	< 3 cm.	< 2 cm.
Nhits	> 15	> 18
nσ	< 3	< 2

The average systematic uncertainties on v_2 and v_3 calculated for different particles in various centralities are shown in listed in table 3.5 and 3.6 respectively.

Table 3.5: Average systematic uncertainties on v_2 of K_S^0, ϕ, Λ, Ξ and Ω in different centrality bins.

Particle/Centrality	0-10%	10-40%	40-80%	0-80%
K_S^0	2%	2%	2%	2%
ϕ	10%	3%	3%	5%
Λ	2%	2%	2%	2%
Ξ	4%	3%	3%	3%
Ω	22%	6%	15%	8%

Table 3.6: Average systematic uncertainties on v_3 of K_S^0, ϕ, Λ, Ξ and Ω in different centrality bins.

Particle/Centrality	0-10%	10-40%	40-80%	0-80%
K_S^0	3%	3%	3%	3%
ϕ	15%	10%	N.A.	10%
Λ	3%	3%	3%	3%
Ξ	12%	10%	N.A.	8%
Ω	30%	30%	N.A.	30%

3.9 Results

3.9.1 Transverse momentum dependence of the flow coefficients

Figure 3.11 shows the v_2 of (multi)strange hadrons as a function of p_T. Particles and anti-particles are shown separately in two different panels. The v_2 exhibits an increasing trend with p_T for all hadron species until it reaches saturation in the high p_T (p_T > 3.0 GeV/c)

region. In hydrodynamic models, this saturation can be explained by treating the QGP as a viscous fluid with finite η/s [96–99]. In the low p_T region ($p_T < 1.5$ GeV/c), a mass ordering is observed, where lighter particles have a higher flow magnitude compared to heavier particles. This ordering arises due to the radial flow of the produced medium [100, 101].

Figure 3.12 shows the results for mid-rapidity measurements of v_3 of strange and multi-strange hadrons in Au+Au collisions at $\sqrt{s_{NN}}$ = 54.4 GeV for 0-80% centrality. The left and right panel shows the result for particles and anti-particles separately. This is the first measurement of v_3 of multi-strange hadrons like Ξ and Ω. In v_3 results, we also observed a hint of mass ordering in the low p_T region.

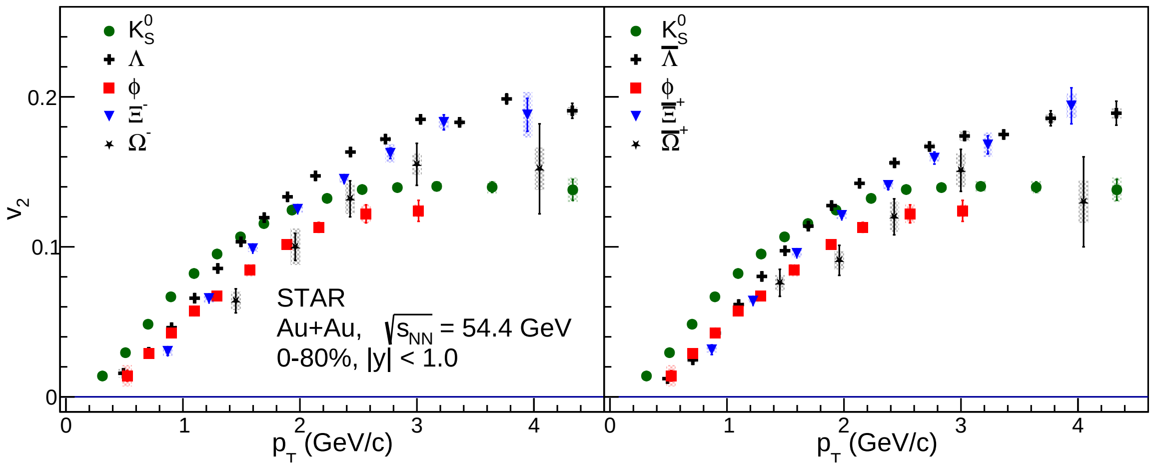

Figure 3.11: Panel (a) shows v_2 of particles as a function of p_T for 0-80% centrality in Au+Au collisions at $\sqrt{s_{NN}}$ = 54.4 GeV in mid-rapidity. Panel (b) shows the same for anti-particles. The vertical lines on the data points shows that statistical errors and the shaded box represents the systematic uncertainty. The data points are taken from our published work [91].

3.9.2 Centrality dependence of the flow coefficient

The centrality dependence of v_2 and v_3 for K^0_S, ϕ, Λ, Ξ^-, Ω^- and their antiparticles has been investigated. Figures 3.13 and 3.14 show v_2 and v_3 as functions of p_T for three wide centrality classes: 0-10%, 10-40%, and 40-80%. Due to limited data, v_3 for ϕ, Ξ, and Ω could not be measured in the 40-80% centrality classes. A pronounced centrality dependence is observed for v_2 across all particles, with the magnitude increasing from central to peripheral collisions. The centrality dependence of v_2 dominantly arises from the initial spatial anisotropy in the overlap region of the colliding nuclei. In peripheral collisions, the spatial anisotropy is more pronounced due to the ellipsoidal shape of the energy deposition,

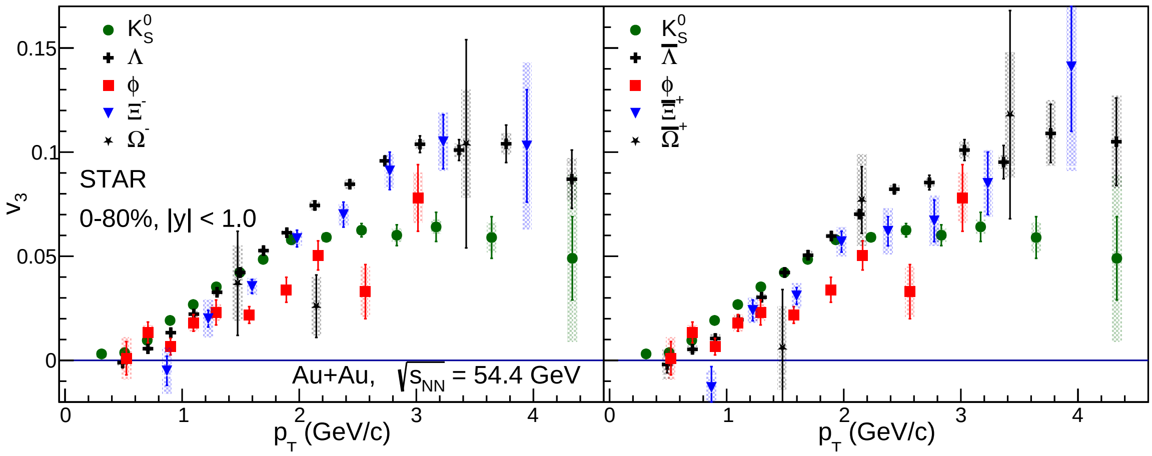

Figure 3.12: Panel (a) shows v_3 of particles as a function of p_T for 0-80% centrality in Au+Au collisions at $\sqrt{s_{NN}}$ = 54.4 GeV in mid-rapidity. Panel (b) shows the same for anti-particles. The vertical lines on the data points show that statistical errors and the shaded box represents the systematic uncertainty. The data points are taken from our published work [91].

whereas in central collisions, the overlap region is more isotropic. Since v_2 is generated by the initial spatial anisotropy, its magnitude is larger in peripheral collisions compared to central ones.

Unlike v_2, v_3 does not show strong centrality dependence as shown in Fig 3.14. The main reason behind the origin of v_3 is the event-by-event fluctuation of the participant nucleons in the overlap zone of the colliding nucleus. Therefore, v_3 shows weak centrality dependence.

3.9.3 Collision energy dependence of flow coefficients

Figure 3.15 shows the v_2 as a function of p_T in 0-80% centrality at $\sqrt{s_{NN}}$ = 200, 54.4, and 39 GeV for K_S^0, $\bar{\Lambda}$, ϕ, $\bar{\Xi}^+$. In order to quantify the energy dependence, in the lower panels ratio of v_2 at $\sqrt{s_{NN}}$ = 54.4 and 39 GeV to 200 GeV fit function is plotted. At intermediate p_T region we observed that the v_2 magnitude is larger for 200 GeV and gradually decreases with decreasing collision. At low p_T region the magnitude of v_2 is found to be larger for 54.4 and 39 GeV compared to 200 GeV and this observation is more profound for heavier particles like $\bar{\Lambda}$ and $\bar{\Xi}^+$. This affect could be due to large radial flow at $\sqrt{s_{NN}}$ = 200 GeV compared to 54.4 and 39 GeV. For particles like ϕ and Ω^-, the statistical error bars are too large to make any conclusion.

The collision energy dependence of v_3 is studied. Figure 3.16 shows the v_3 as function of p_T at $\sqrt{s_{NN}}$ = 200 and 54.4 GeV. The lower panels show the ratio of v_3 data points at

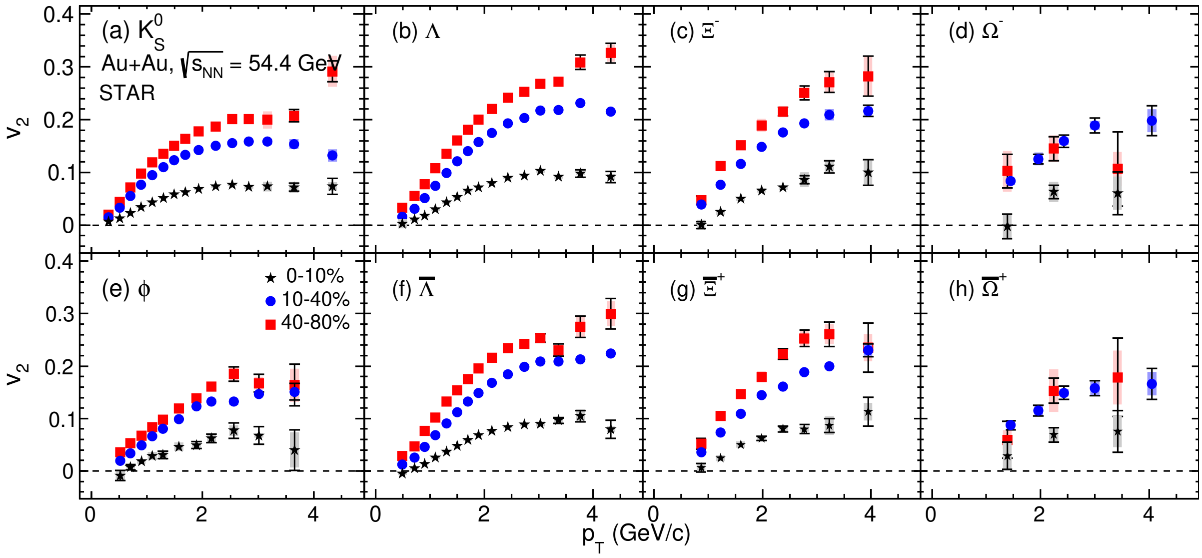

Figure 3.13: The plot of v_2 as a function of p_T is shown for centrality classes of 0-10%, 10-40%, and 40-80%. The vertical lines indicate the statistical error bars, while the shaded bands represent the systematic uncertainties. The figure is taken from our published work [91].

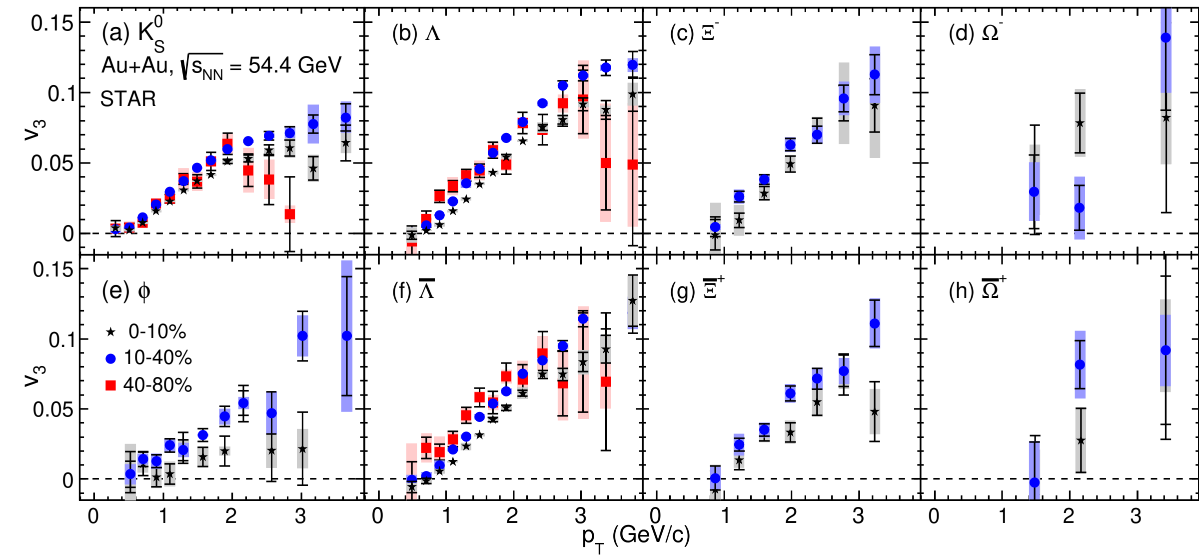

Figure 3.14: The plot of v_3 as a function of p_T is shown for centrality classes of 0-10%, 10-40%, and 40-80%. The vertical lines represent the statistical error bars, and the shaded bands indicate the systematic uncertainties. For the Ξ and Ω particles, data points for the 40-80% centrality class are not shown due to limited statistics. The figure is taken from our published work [91].

$\sqrt{s_{NN}}$ = 54.4 GeV to 200 GeV fit function. Unlike v_2, the v_3 ratios at two different collision energies do not show any strong p_T dependence. The average change in v_2, when the collision energy changes from 200 to 54.4 GeV is about 10% where as the same for v_3 is about 20%. This indicates that v_3 is more sensitive to collision energy compared to v_2.

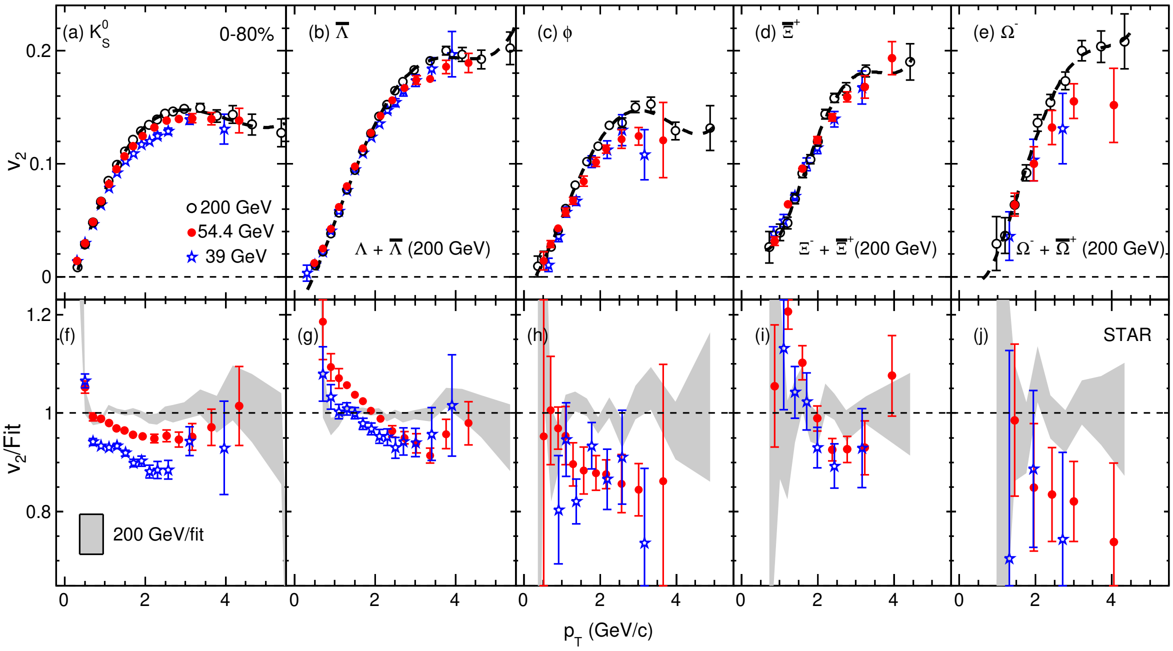

Figure 3.15: The upper panels show the v_2 as a function of p_T is shown for 0-80% centrality at three different collision energies, $\sqrt{s_{NN}}$ = 200, 54.4, and 39 GeV for K^0_S, $\bar{\Lambda}$, ϕ, $\bar{\Xi}^+$, and Ω^-. The 200 and 39 GeV data points are from the Ref. The dotted line represents the polynomial fit function to 200 GeV data. The lower panels show the ratio of v_2 data points at 54.4 and 39 GeV to 200 GeV fit function. The shaded band shows the ratio of 200 GeV data points to the 200 GeV fit function. The figure is taken from our published work [91].

3.9.4 Particle and anti-particle v_n difference

The RHIC BES-I results at lower collision energy regime show a difference between baryons and anti-baryons v_2 [57, 102]. The two possible models that can capture this difference qualitatively are transported quark models and mean-field potentials. Transported quarks are the quarks initially present the colliding nuclei. Those transported quarks can transfer into the particles as a result the v_2 of the particles have a larger magnitude compared to anti-particles which are purely made of produced quarks from the medium. In mean-field potential models, such difference in v_2 could arise due to different nature of mean-field potential for particles and anti-particle [103–105].

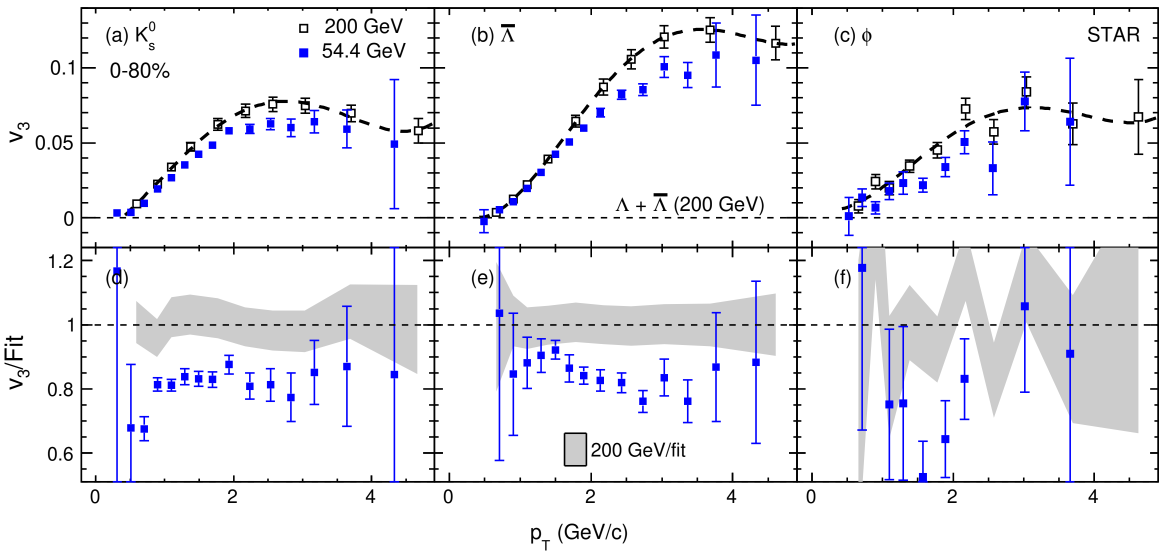

Figure 3.16: The upper panels show the v_3 as a function of p_T is shown for 0-80% centrality at $\sqrt{s_{NN}}$ = 200, and 54.4 for K_S^0, $\bar{\Lambda}$, and ϕ. The dotted line represents the polynomial fit function to 200 GeV data. The lower panels show the ratio of v_3 data points at 54.4 GeV to 200 GeV fit function. The shaded band shows the ratio of 200 GeV data points to the 200 GeV fit function. The 200 GeV data points are from the Ref. [53]. The figure is taken from our published work [91].

A similar study has been conducted in Au+Au collisions at $\sqrt{s_{NN}}$ = 54.4 GeV. In this study we not only observe a difference in v_2 between particle and anti-particles but also for v_3. Figure 3.17 shows the integrated v_n difference between particle and anti-particles as function of mass at $\sqrt{s_{NN}}$ = 54.4 GeV. The v_2 difference result is compared with 62.4 GeV published results [106]. The results from the two collision energies are consistent with each other, however the results at 54.4 GeV are more precise due to large event statistics. The integrated v_n seems to be independent of particle species within the measured uncertainties. The magnitude of integrated v_3 difference is consistent with the integrated v_2 difference.

3.9.5 $v_3/v_2^{3/2}$ ratio

Hydrodynamical models predict that the higher order flow coefficients, v_n is proportional to $v_2^{n/2}$. The proportionality constant, $v_n/v_2^{n/2}$, is independent of p_T and its magnitude is sensitive to the transport coefficient of the medium [107–110]. Such a non-trivial correlation is studied between v_2 and v_3 for strange and multi-strange hadrons at $\sqrt{s_{NN}}$ = 54.4 GeV. Figure 3.18 shows the $v_3/v_2^{3/2}$ ratio in 10-40% centrality. The ratio shows weak p_T dependence in the intermediate p_T region for all the particle species. In case of Ω, the statistics is not sufficient to make any definitive conclusion.

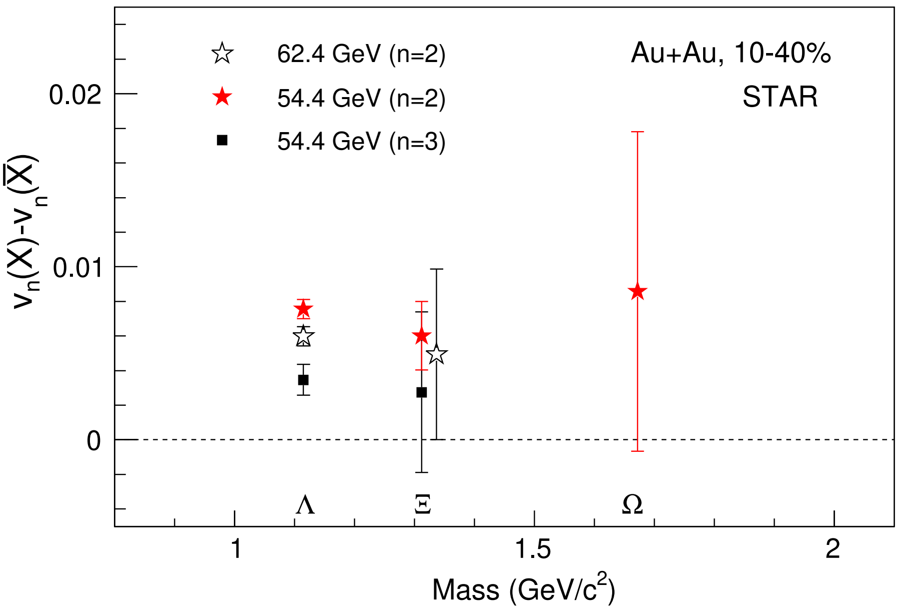

Figure 3.17: Integrated v_2 and v_3 difference between particles and anti-particles in 10-40% centrality is plotted as a function of mass at $\sqrt{s_{NN}}$ = 54.4 and 62.4 GeV. The figure is taken from our published work [91].

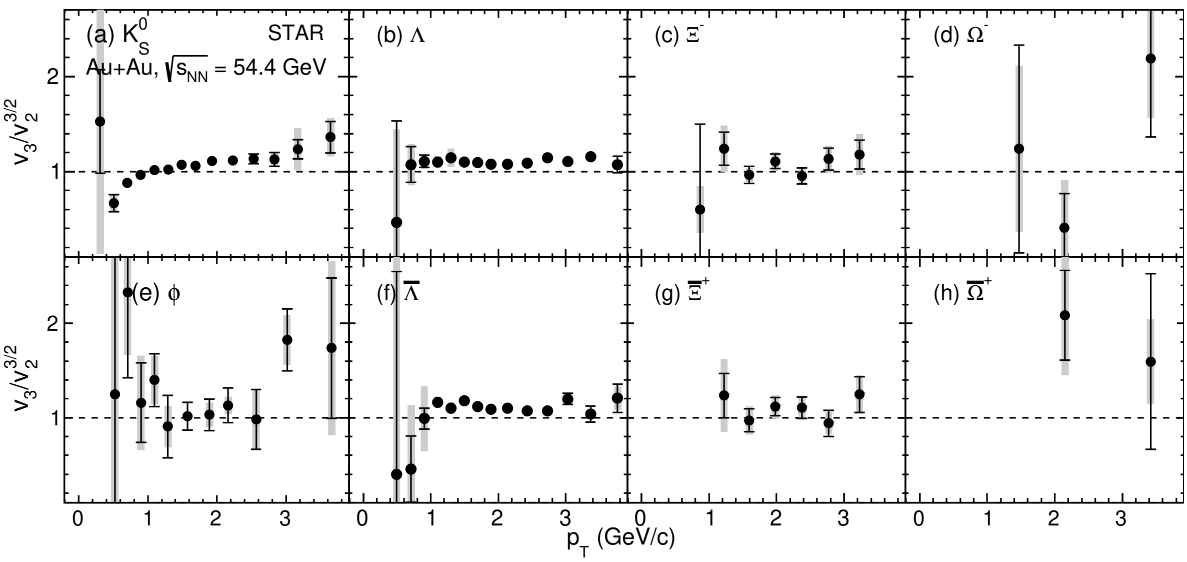

Figure 3.18: Ratio between v_3 and $v_2^{3/2}$ is plotted as a function of p_T for strange and multi-strange hadrons in 10-40% centrality for Au+Au collisions at $\sqrt{s_{NN}}$ = 54.4 GeV. The figure is taken from our published work [91].

3.9.6 Number of constituent quark (NCQ) scaling

The constituent quark scaling of v_2 and v_3 is predicted as a signature of the collective behavior of the medium produced in heavy-ion collisions [111–121]. The assumption in this case is each quark will contribute equally to the overall flow of the hadron. This scaling is usually studied by measuring the magnitude of the flow per constituent quark (v_n/n_q) inside a hadron as a function of transverse kinetic energy, $K_T = m_T - m_0$, where m_T is the transverse mass of the particle given by $m_T = \sqrt{m_0^2 + p_T^2}$, and m_0 is the rest mass of the particle.

Figure 3.19 shows the NCQ scaled v_2 (v_2/n_q) of K_S^0, ϕ, Λ, Ξ^-, Ω^- and their anti-particles as a function of NCQ scaled ($m_T - m_0$). The NCQ-scaled v_2 for all particles and anti-particles aligns along a single line, confirming the adherence to NCQ scaling. To quantify the scaling, the K_S^0 data points are fitted with a polynomial function and the ratio of other data points to K_S^0 fit function is plotted in the lower panels of Fig. 3.19. From the ratio it's clear that the scaling holds within 10% level for both particles and anti-particles. The scaling is also studied for v_3, Fig 3.20 shows the $v_3/n_q^{3/2}$ as a function of $(m_T - m_0)/n_q$. For Λ and $\bar{\Lambda}$, the scaling violates in the low p_T region. For other hadrons the statistical error bars are too large to make any conclusion.

The observed NCQ scaling for v_2 indicates the presence of long range collective behaviour during the partonic phase of the medium at s_{NN} = 54.4 GeV. The scaling also supports the idea of quark recombination model of hadronization [51].

3.9.7 Ratio of $v_2(\phi)/v_2(\bar{p})$

The mass of the ϕ meson is 1019 MeV/c^2 and that of anti-proton is 938 MeV/c^2. Under the assumption of hydrodynamical mass ordering anti-protons should have larger magnitude of v_2 compared to ϕ mesons in the low p_T region. The ratio of $v_2(\phi)/v_2(\bar{p})$ observed to be greater than unity hints a violation in the mass ordering in the low p_T region as shown in Fig. 3.21. Such violation in mass ordering could arise due to the affect of late stage hadronic rescattering on anti-proton whereas the ϕ mesons are less affected by late stage hadronic interaction due to their small scattering cross section. The ratio also shows a centrality dependence being larger for 10-40% compared to 40-80%. In 10-40% central collisions the size of the medium produced is larger than that in 40-80% collisions therefore, there could be more rescattering in 10-40% centrality than 40-80%. The ratio at $\sqrt{s_{NN}}$ = 54.4 GeV is compared to 200 GeV for 0-80% centrality and the two ratios are consistent with each other within uncertainty indicating a similar affect in 200 GeV. At $\sqrt{s_{NN}}$ = 54.4 GeV, we have cho-

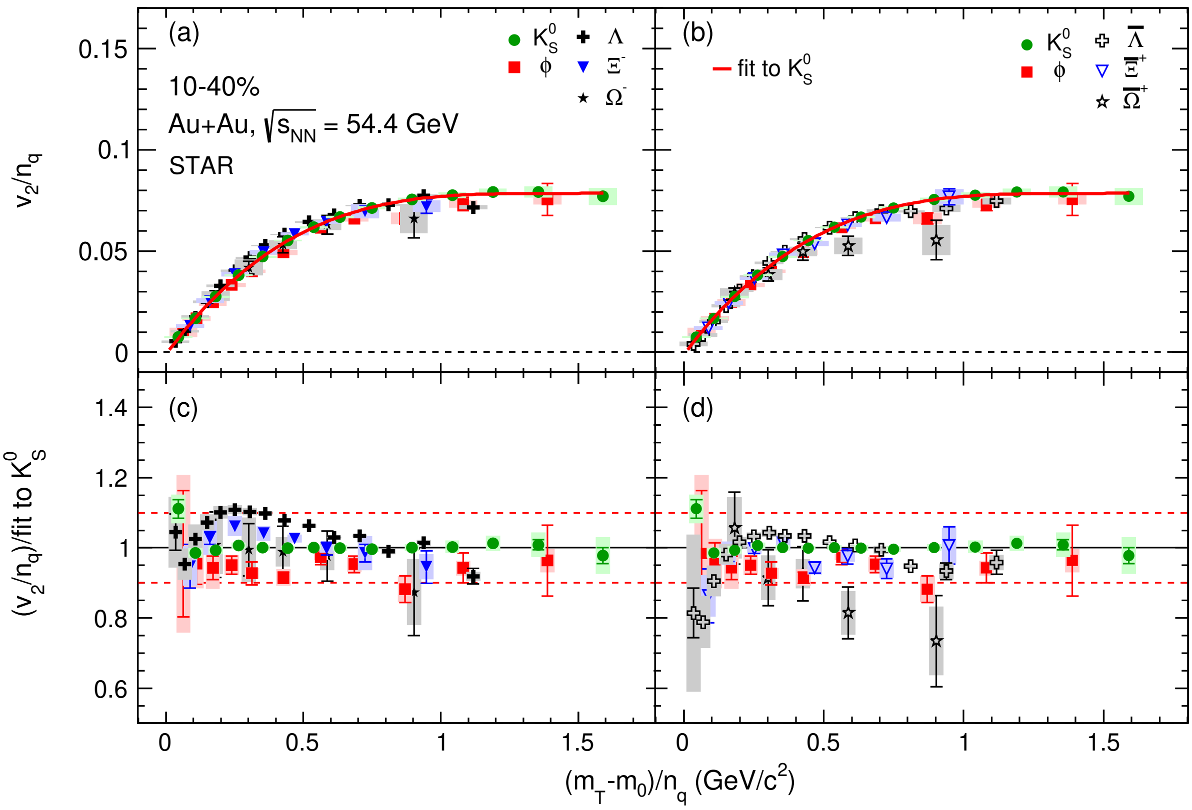

Figure 3.19: Panel (a) and (b) show the NCQ scaled v_2 of (multi)strange hadrons as a function of NCQ scaled transverse kinetic energy for particles and anti-particles respectively. The solid red line is the fit function to the K^0_S data points. Panel (c) and (d) show the ratio of all the data points to the K^0_S fit function. The two dotted red lines show the 10% deviation from the unity. The figure is taken from our published work [91].

sen the anti-proton instead of the proton to calculate the v_2 ratio with the ϕ meson. The reason for this choice is that the anti-proton is composed of produced quarks originating from the medium, whereas the proton can be influenced by transported quarks from the colliding system. This could potentially impact its v_2 magnitude.

3.10 Summary

In this chapter, we discussed the measurement of v_2 and v_3 in Au+Au collisions at $\sqrt{s_{NN}}$ = 54.4 GeV for (multi-)strange hadrons at STAR. We found a hydrodynamical behavior of the produced medium at this energy through the observation of mass ordering in both $v_2(p_T)$ and $v_3(p_T)$. The observed NCQ scaling at $\sqrt{s_{NN}}$ = 54.4 GeV suggests the presence of partonic collectivity in the initial produced medium. The ratio of $v_2(\phi)/v_2(\bar{p})$ provides a hint of

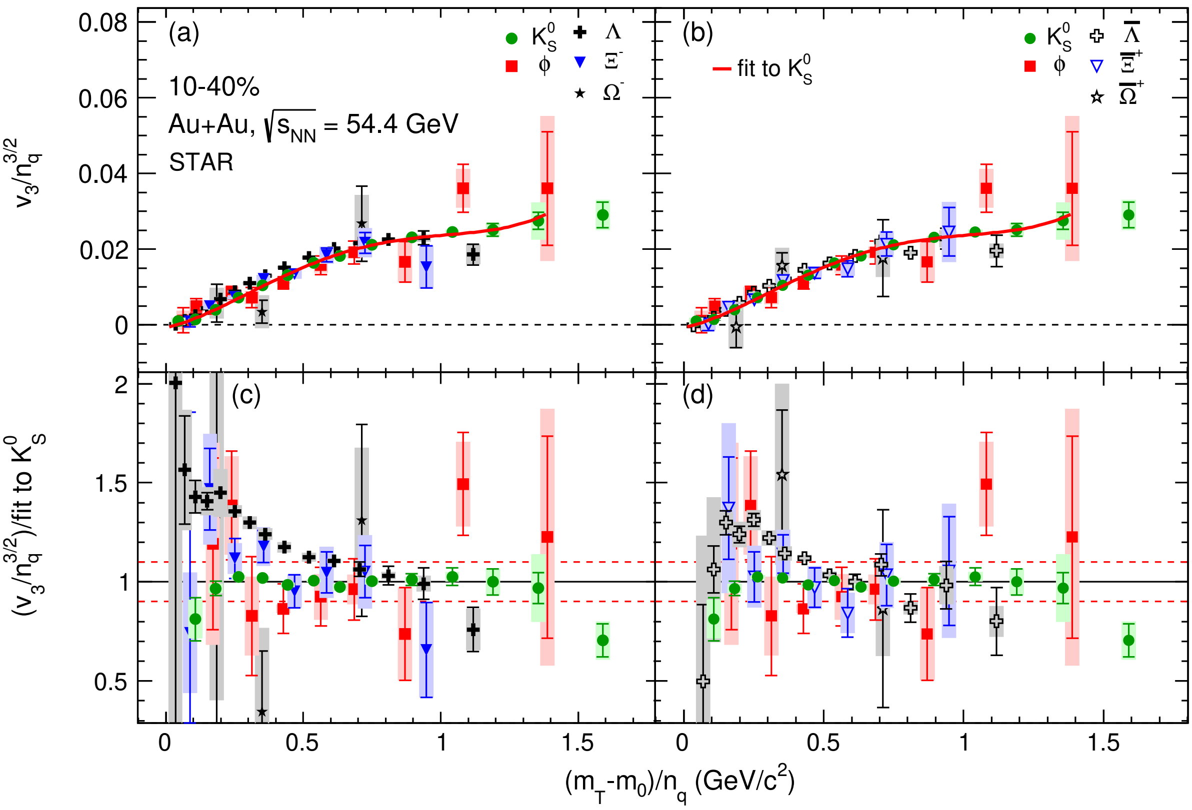

Figure 3.20: Panel (a) and (b) show $v_3/n_q^{3/2}$ of (multi)strange hadrons as a function of NCQ scaled transverse kinetic energy for particles and anti-particles respectively. The solid red line is the fit function to the K_S^0 data points. Panel (c) and (d) show the ratio of all the data points to the K_S^0 fit function. The two dotted red lines show the 10% deviation from the unity. The figure is taken from our published work [91].

violation of mass ordering which could arise due to the larger late stage hadronic rescattering effect on anti-proton v_2 compared to ϕ v_2 considering a smaller hadronic interaction cross section of ϕ mesons.

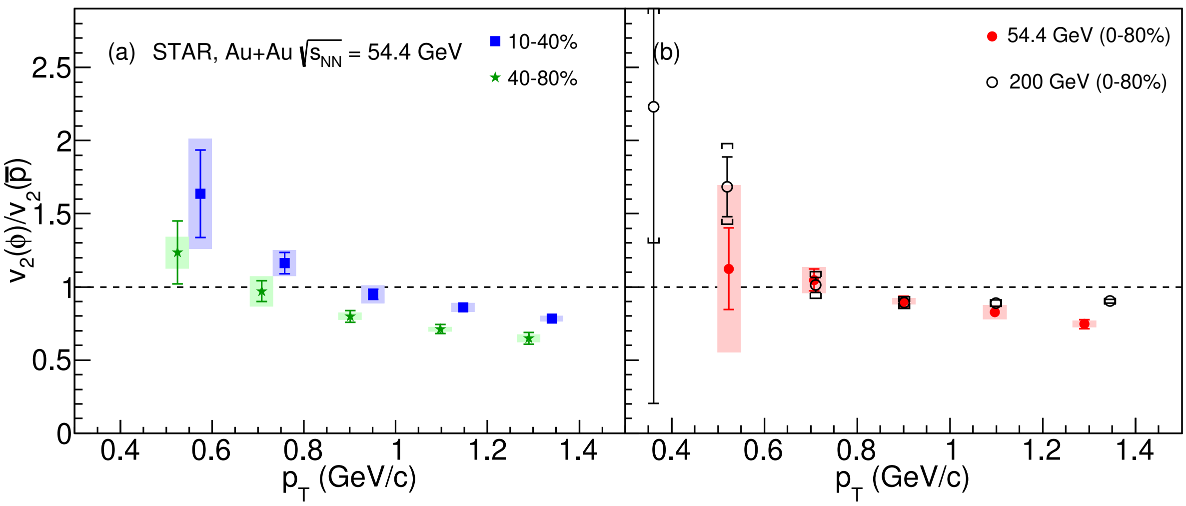

Figure 3.21: Panel (a) shows the ratio of v_2 of ϕ to that of anti-proton as a function of p_T in 10-40% and 40-80% centrality classes. Panel (b) shows the ratio of v_2 of ϕ to that of anti-proton as a function of p_T in 0-80% central collisions at $\sqrt{s_{NN}}$ = 54.4 and 200 GeV. The 200 GeV data points are from the Ref. [53]. The figure is taken from our published work [91].

CHAPTER 4

Elliptic and triangular flow measurement in the second phase of Beam Energy Scan (BES-II) program

4.1 Motivation for collective flow measurements from BES-II

One of the main goals of the STAR experiment at RHIC is to search for the turn-off signature of the Quark-Gluon Plasma (QGP) by exploring the QCD phase diagram. To achieve this, STAR conducted the first phase of the Beam Energy Scan (BES-I) program in 2010-2011. During BES-I, the elliptic flow (v_2) was measured at center-of-mass collision energies ($\sqrt{s_{NN}}$) ranging from 7.7 GeV to 62.4 GeV. The key features of the BES-I results are outlined below, providing hints of hadronic dominance in the medium produced at lower collision energies [106, 122].

- The $v_2(p_T)$ of ϕ mesons at lower collision energies ($\sqrt{s_{NN}}$ = 11.5 and 7.7 GeV) shows a markedly different behavior, with a significant decrease in the energy-dependent trend.
- At $\sqrt{s_{NN}} \leq 11.5$ GeV, the v_2 as a function of reduced transverse mass ($m_T - m_0$) does not exhibit clear baryon-meson splitting at intermediate values of $m_T - m_0$.
- At $\sqrt{s_{NN}} \leq 11.5$ GeV, ϕ mesons are found to violate the NCQ scaling.

If the initial medium at lower collision energies is hadronic dominant then the v_2 of ϕ mesons should be suppressed since ϕ has small hadronic interaction cross section. Although the BES-I data suggests a hadronic dominance of the medium at lower collision energies, no definitive conclusion can be drawn due to the statistical limitations of the results. Therefore, it is crucial to revisit these lower collision energy regimes with the high-statistics data from BES-II, which could provide valuable insights into the nature of the medium in regions of high baryon density.

In this chapter, we have discussed the measurements of v_2 and v_3 of the identified hadrons in Au+Au collisions at BES-II energies ranging from $\sqrt{s_{NN}}$ = 7.7 to 19.6 GeV.

4.2 Datasets

In BES-II, we have used the high-statistics datasets from $\sqrt{s_{NN}}$ = 7.7 to 19.6 GeV. The information about the datasets are summarized in table 4.1.

Table 4.1: Details of the BES-II datasets information used in the analysis.

$\sqrt{s_{NN}}$ (GeV)	Production ID	Production tag	Trigger IDs	Events after cuts (M)
7.7	production_7p7GeV_2021	P22ib	810010, 810020, 810030, 810040	120
9.2	production_9p2GeV_2020b, production_9p2GeV_2020c, production_9p2GeV_2020	P23ia	780010, 780020	200
11.5	production_11p5GeV_2020	P23ia	710000, 710010, 710020	280
14.6	production_14p5GeV_2019	P23id	560000	400
19.6	production_19GeV_2019	P21ic	640001, 640011, 640021, 640031, 640041, 640051	420

Bad runs and piles up are rejected using official StRefMultCorr package. The list of bad runs at $\sqrt{s_{NN}}$ = 7.7-19.6 GeV are given in the Appendix A.

4.3 Analysis cuts

We have used a $|V_Z| < 145$ cm. and $V_r < 2.0$ cm. for all dataset available in BES-II. The track selection cuts are listed in the table 4.2.

Table 4.2: Track selection cuts used in the analysis of Au+Au collisions BES-II energies.

cuts	values
Nhits	> 15
Nhits/NhitsPoss	> 0.52
p_T	> 0.1 GeV/c
DCA	< 3.0 cm.
$\|\eta\|$	< 1.5 (for event plane construction)
$\|\eta\|$	< 1.0 (for PID)

4.4 Particle identification

4.4.1 Identification of pions, kaons, and protons

For the identification of pions, kaons, and protons, we have used their specific energy loss in TPC (dE/dx) and m^2 information from ToF. The protons are identified using a cut m^2 $0.80 < m^2 < 1.10\ GeV/c^2$. To suppress pion and kaon contamination, an additional $|n\sigma_p| < 2$ is also applied. For pions and kaons identification, a new technique is used, which is called the 2D-PID method [122]. In this method, a transformation is performed on the combined $n\sigma_\pi$ and m^2 information. From this transformation a new set of variables x, and y are obtained which are function of $n\sigma_\pi$ and m^2. The distribution of these new variables have a maximum separation between the peaks of pions and kaons. The transformation is given by Eq. 4.1.

$$\begin{bmatrix} x(n\sigma_\pi, m^2) \\ y(n\sigma_\pi, m^2) \end{bmatrix} = \begin{bmatrix} \cos\alpha & -\sin\alpha \\ \sin\alpha & \cos\alpha \end{bmatrix} \begin{bmatrix} x' \\ y' \end{bmatrix} \tag{4.1}$$

where x' and y' are given by Eq. 4.2.

$$\begin{aligned} x' &= \frac{n\sigma_\pi - \mu_\pi(n\sigma_\pi)}{f_{scale}} \\ y' &= m^2 - \mu_\pi(m^2) \end{aligned} \tag{4.2}$$

Here $f_{scale} = \sigma_\pi(n\sigma_\pi)/\sigma_\pi(m^2)$ is a scale factor used to normalize the m^2 axis and $n\sigma$ axis. The generator, α, of the transformation is given by Eq. 4.3.

$$\alpha = -\tanh \frac{\mu_K(m^2) - \mu_\pi(m^2)}{(\mu_K(n\sigma_\pi) - \mu_\pi(n\sigma_\pi))/f_{scale}} \tag{4.3}$$

The parameter $\mu_K(m^2)$ represents the mean of the m^2 distribution for pure kaon tracks, while $\mu_\pi(m^2)$ refers to the mean of the m^2 distribution for pure pion tracks. Similarly, $\mu_K(n\sigma_\pi)$

is the mean of the $n\sigma_\pi$ distribution for pure kaon tracks, and $\mu_\pi(n\sigma_\pi)$ is the mean of the $n\sigma_\pi$ distribution for pure pion tracks. The pure pion tracks are selected from the decay daughters of K_S^0, and the $n\sigma_\pi$ distribution for pure kaon tracks is obtained by applying a strict m^2 cut ($0.242 < m^2 < 0.245$ GeV/c^2). For the m^2 distribution of pure kaon tracks, a cut of $|n\sigma_K| < 2.0$ is used.

The parameters $\mu_\pi(m^2)$, $\mu_K(m^2)$, $\mu_\pi(n\sigma_\pi)$, $\mu_K(n\sigma_\pi)$, $\sigma_\pi(n\sigma_\pi)$, and $\sigma_\pi(m^2)$ are extracted as functions of transverse momentum (p_T), and the results are shown in Fig. 4.1.

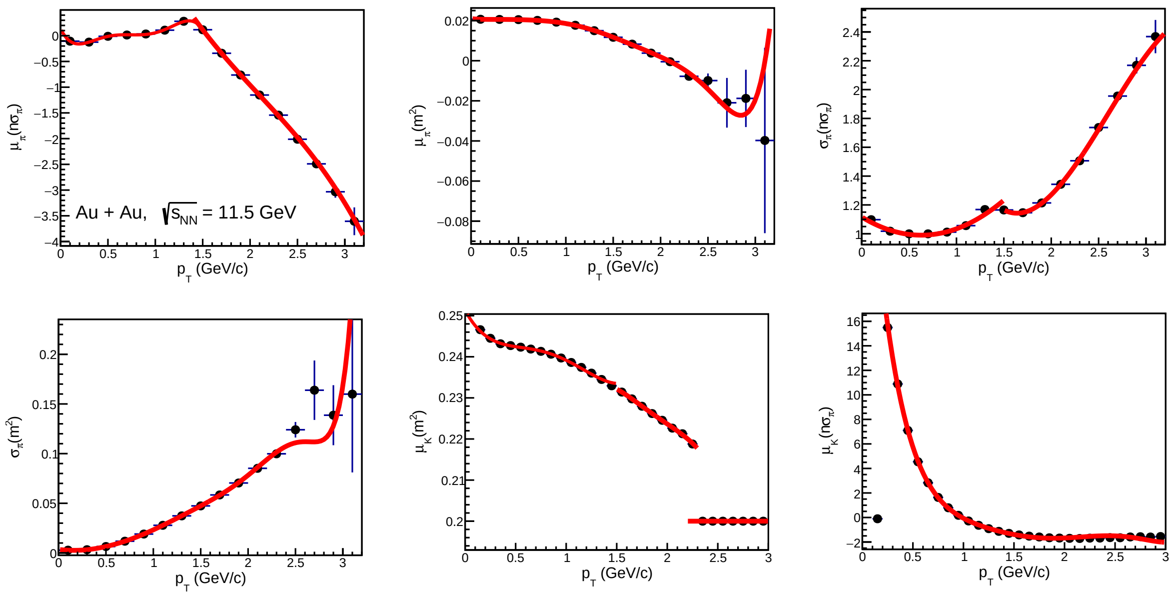

Figure 4.1: The required parameters for the transformation Eq. 4.1, 4.2, 4.3 are plotted as a function of p_T at $\sqrt{s_{NN}}$ = 11.5 GeV. The parameters are fitted with a polynomial function (solid red line) for interpolation purpose.

These parameters are used to perform the transformation. In panel (a) of Fig. 4.2, a 2D distribution of $n\sigma_\pi$ vs. m^2 is presented. The pion and kaon bands overlap, making them difficult to distinguish. In panel (b), the 2D distribution of the transformed variables x and y is shown, where we achieve maximum separation between the pion and kaon tracks. The 2D distribution of x vs. y is projected along the x-axis, revealing distinct peaks for π, K, and p. We subtract the proton peak from the overall distribution to remove proton contamination in the kaons. Finally, the raw yields of π and K are calculated by fitting the student-t function to the distribution of x. The raw yield is calculated in various differential p_T bins as well as in different $\phi - \Psi_n$ bins to calculate v_n.

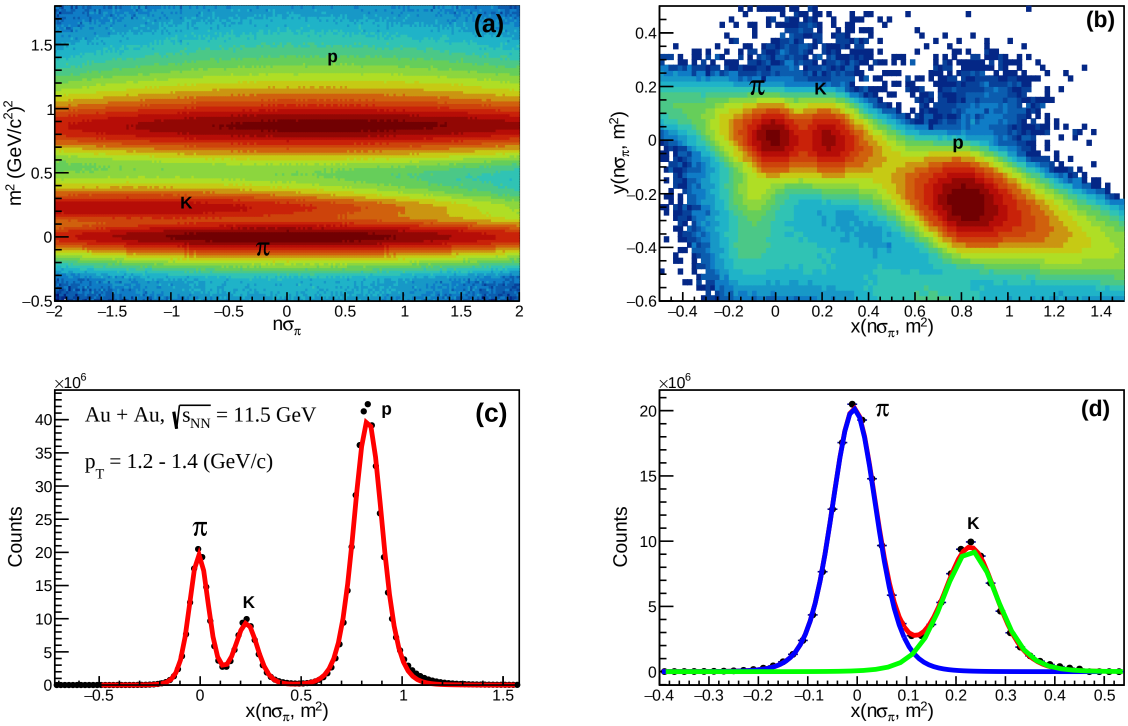

Figure 4.2: Panel (a) shows the 2D distribution of $n\sigma_\pi$ vs. m^2 of particle tracks. Panel (b) shows the 2D distribution of the transformed variables $x(n\sigma_\pi, m^2)$ and $y(n\sigma_\pi$. Panel (c) shows the projection of 2D scatter plot (b) along x axis. The red solid line is student-t fit to the peaks of π, K, and p. Panel(d) shows the same as (c) after subtracting proton's peak. The solid blue and green lines are the student-t functions for π and K respectively.

4.4.2 Reconstruction of strange hadrons

The identification of ϕ mesons and weak decay V_0 particles are already discussed in Chapter 3. The same procedure is also used here to reconstruct V_0 particles and ϕ mesons. Apart from that we have also used available Kalman-Filter (KF) algorithm package to reconstruct weak decay particles. KF algorithm is a recursive algorithm to determine the state of an unknown discrete dynamical system. In this method a particle is described by a state vector with eight parameters (p_x, p_y, p_z, x, y, z, E, s) where E is the energy of the particle in laboratory coordinate system and s is the ratio of the path length traveled by the particle and total momentum. The reconstructed state vector and its correlation matrix has all the information about the particle. The input to the KF particle package are the topological variables in terms of χ^2, which is the probability that a particular particle track satisfies certain topological selection cuts. A detail description of the method can be found in Ref. [123–125]. The selection cuts for various short lived particles are listed in Tab. 4.3.Here χ^2_{topo} is the measure of the DCA between mother particle and primary vertex, χ^2_{prim} is the measure of the DCA between all the daughter and grand daughters and primary vertex, dL is the decay length and dL/σ is decay length normalized by its uncertainty.

Table 4.3: Cuts used for the reconstruction of short lived hadrons using KF particle package

K^0_s	Λ	Ξ	Ω
$\chi^2_{topo} < 4$	$\chi^2_{topo} < 4$	$\chi^2_{topo,\Xi} < 4$	$\chi^2_{topo,\Omega} < 4$
$\chi^2_{prim,\pi_1} > 8$	$\chi^2_{prim,\pi} > 10$	$\chi^2_{prim,\pi_1} > 10$	$\chi^2_{prim,\pi} > 10$
$\chi^2_{prim,\pi_2} > 8$	$\chi^2_{prim,p} > 10$	$\chi^2_{prim,p} > 10$	$\chi^2_{prim,K} > 10$
$dL > 2$ cm.	$dL > 2$ cm.	$\chi^2_{prim,\pi_2} > 10$	$\chi^2_{prim,p} > 10$
$dL/\sigma > 4$	$dL/\sigma > 4$	$dL > 3$	$dL > 3$
		$dL_\Xi > dL_\Lambda$	$dL_\Omega > dL_\Lambda$
		$dL_\Xi/\sigma > 3.0$	$dL_\Omega/\sigma > 3.0$

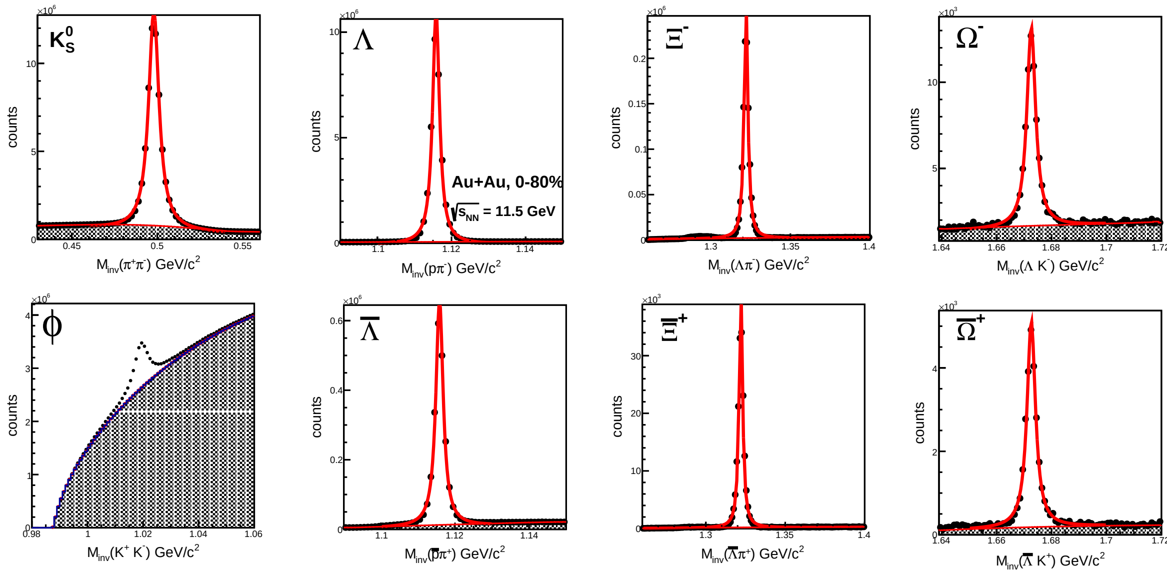

Figure 4.3: Reconstructed signals of strange and multi-strange hadrons in Au+Au collision at $\sqrt{s_{NN}} = 11.5$ GeV.

4.5 Event plane construction

For event plane construction we have used the same method as discussed in Chapter 3. To make the event plane distribution isotropic we have used phi-weight correction and shift correction method. The phi-weight correction method is already discussed in Chapter 3. Shift correction method is used to achieve more flatness in the distribution of the event plane angles. The flatness is achieved by shifting the distribution of the event planes after phi-weight correction by a factor $\Delta\Psi$ as shown in Eq. 4.4.

$$\Psi_n^s = \Psi_n + \sum_n \frac{-2}{n}\langle \sin n\Psi_n\rangle \cos n\Psi_n + \sum_n \frac{2}{n}\langle \cos n\Psi_n\rangle \sin n\Psi_n. \tag{4.4}$$

Where Ψ_s is the event plane angle after shift correction. The derivation of Eq. 4.4 is given in Appendix B.

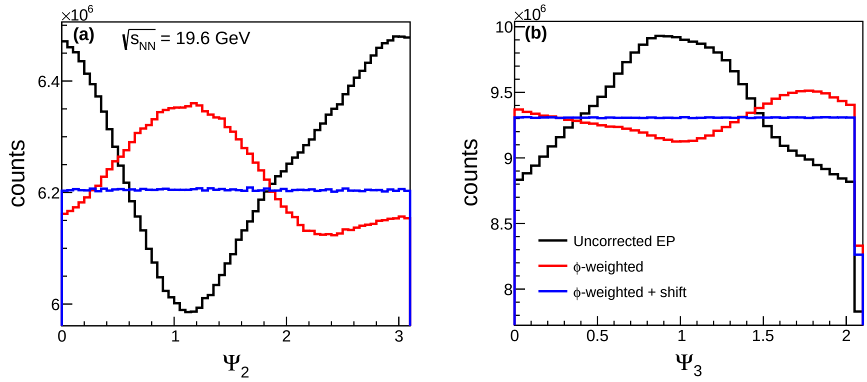

Figure 4.4: Panel (a) shows the distribution of Ψ_2 before correction, after ϕ-weight correction, and after ϕ-weight + shift correction. Panel (b) shows the same for Ψ_3

4.5.1 Event plane resolution

The sub-event plane resolution is measured using the same method described in Chapter 3. Figure 4.5 shows the Ψ_2 and Ψ_3 resolutions as functions of centrality. The resolution value decreases with lower collision energy, as both the multiplicity and flow magnitude decline with decreasing collision energy.

4.6 v_2 and v_3 measurement methods

We have used both event plane and invariant mass method to calculate v_n of the identified particles. The details procedure of these two methods are already discussed in Chapter 3 for strange and multi-strange hadrons. For pions and kaons the raw yield calculated in various $\phi - \Psi_n$ bin after using 2D-PID method is shown in Fig. 4.6. The distribution then fitted with the Eq. 4.5 to calculate v_n of pions and kaons. For protons, we have used the formula

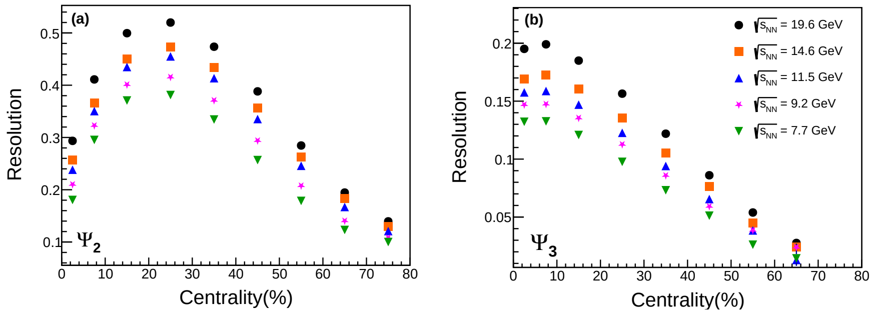

Figure 4.5: Panel (a) shows the Ψ_2 resolution as a function of centrality for collision energy $\sqrt{s_{NN}}$ = 7.7 to 19.6 GeV. Panel (b) shows the same for Ψ_3.

$\langle\langle\cos n(\phi - \Psi_n)\rangle\rangle$ directly after proton's m^2 and $n\sigma_{proton}$ cut to get v_n. The observed v_n in all the cases needs to be resolution corrected in the final step.

$$\frac{dN}{d(\phi - \Psi_n)} = \frac{N_0}{2\pi}\left(1 + v_n^{obs}\cos n(\phi - \Psi_n)\right) \tag{4.5}$$

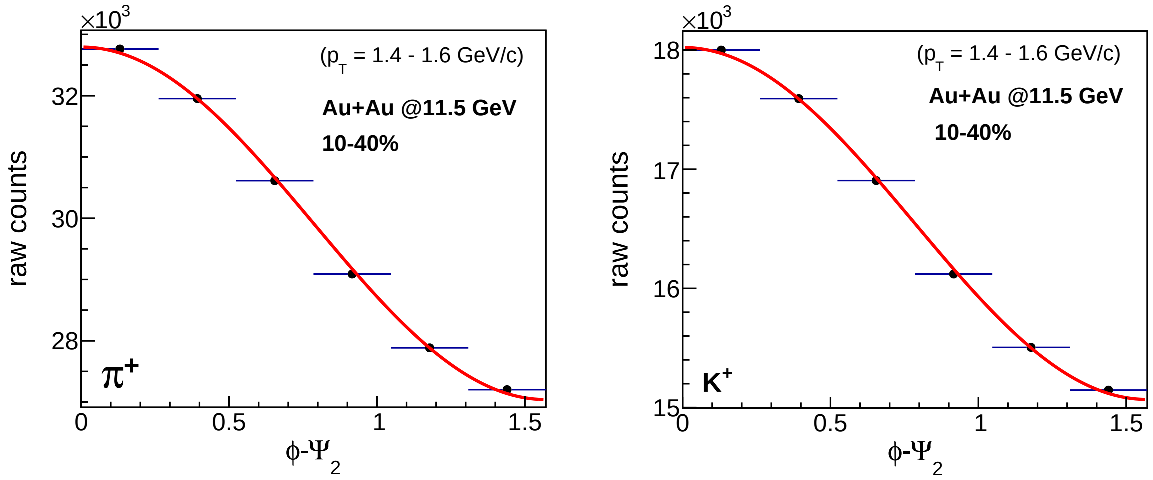

Figure 4.6: Azimuthal distribution of the raw yield of π^+ and K^+ is shown in Au+Au collisions at $\sqrt{s_{NN}}$ =11.5 GeV in 10-40% centrality for p_T bin 1.4-1.6 GeV/c. The distribution is fitted with the Eq. 4.5 to get v_n^{obs}.

4.7 Systematic uncertainty estimation

The systematic uncertainty in the v_2 and v_3 measurements are estimated by varying various event selection and track selection cuts listed in Tab. 4.4. Apart from that a 10% variation is applied to the KF-particle cuts listed in Tab 4.3 for systematic study. Barlow check is applied in the end to exclude statistical fluctuations from systematic uncertainty as discussed in Chapter 3.

Table 4.4: Details of the analysis cuts variations for systematic uncertainty estimation in BES-II measurements

cuts	default value	variation
$\|V_z\|$	< 145 cm.	< 130 cm.
V_r	< 2 cm.	< 1 cm.
DCA (for π, K, p, and ϕ)	< 3 cm.	< 2 cm.
Nhits	> 15	> 20
nσ	< 3	< 2

4.8 Results

4.8.1 v_2 of ϕ mesons

Figure 4.7 shows the v_2 of ϕ mesons as a function of p_T for 0-80% centrality at mid-rapidity, across collision energies $\sqrt{s_{NN}}$ = 7.7 to 19.6 GeV. These results are compared with those from BES-I. In BES-II, we observe more precise measurements of v_2 for ϕ mesons compared to BES-I. At collision energies below $\sqrt{s_{NN}}$ = 14.6 GeV, the v_2 of ϕ mesons follows the usual trend, whereas, in BES-I, data points show a sudden drop after p_T > 1.0 GeV/c which is due to the affect of statistical fluctuation.

4.8.2 $m_T - m_0$ scaling

Figures 4.8 and 4.9 show v_2 as a function of $m_T - m_0$. Plotting against $m_T - m_0$ eliminates the mass dependency of particle species, allowing clearer trends to emerge. A distinct separation between baryons and mesons is observed above $m_T - m_0 > 0.5$ GeV for particles across all collision energies from $\sqrt{s_{NN}}$ = 7.7 to 19.6 GeV. Within each category, baryons display a uniform magnitude of v_2, as do mesons, though at a different level. This baryon-meson v_2 splitting suggests the presence of partonic degrees of freedom in the system's initial state.

For anti-particles, baryon-meson splitting is also observed at $\sqrt{s_{NN}}$ > 9.2 GeV, though the magnitude of this separation is noticeably smaller than for particles. At lower collision energies, specifically $\sqrt{s_{NN}}$ < 11.5 GeV, the baryon-meson splitting for anti-particles vanishes. This occurs because, at these energies, anti-baryons exhibit significantly lower v_2

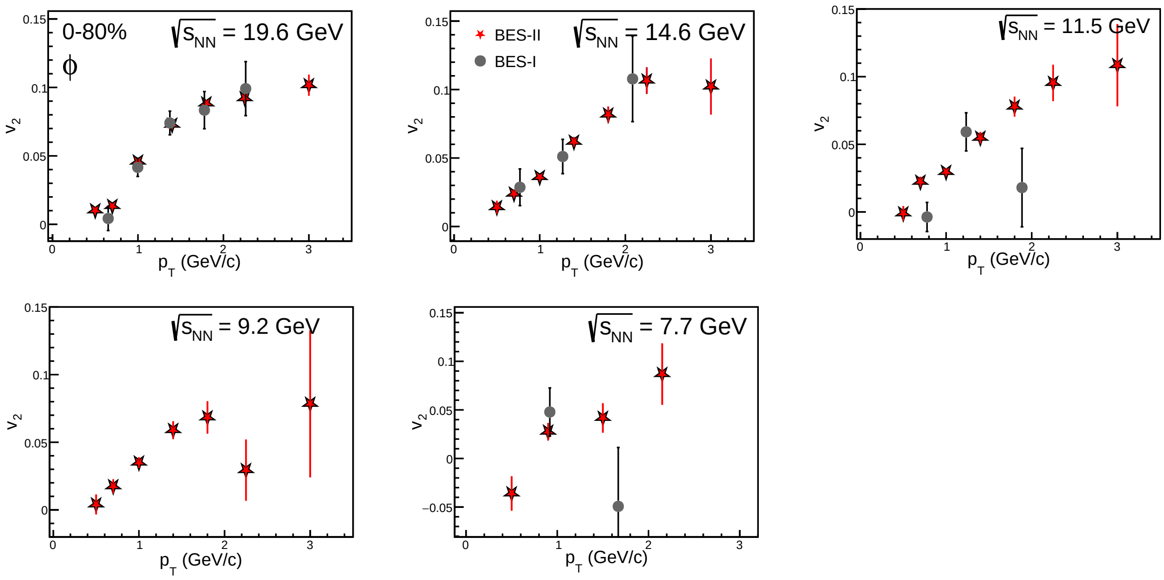

Figure 4.7: v_2 of ϕ mesons is plotted as a function of p_T in 0-80% centrality class events for $|y| < 1.0$ from $\sqrt{s_{NN}}$ = 7.7 to 19.6 GeV. The result is compared to BES-I results for ϕ mesons. Only statistical error bars are shown.

compared to baryons, while the difference in v_2 between mesons and their anti-particles remains minimal. Consequently, at lower energies, anti-baryons' v_2 values converge with those of mesons, leading to a disappearance of the baryon-meson splitting. The differences between v_2 for baryons and anti-baryons will be discussed in a later section. Such an observation holds true for v_3 also as shown in Fig. 4.10 and Fig. 4.11.

4.8.3 Test of the NCQ scaling

Figure 4.12 and 4.13 show the NCQ scaled v_2 of identified hadrons for particles and anti-particles respectively. The NCQ scaling holds for both particles and anti-particles at $\sqrt{s_{NN}}$ = 7.7 to 200 GeV indicating the partonic collectivity in the initial state of the produced medium.

In case of a perfect NCQ scaling for v_2, we have $v_2(B)/v_2(M) = 1.5$. Where $v_2(B)$ is the v_2 of baryons and $v_2(M)$ is the v_2 of mesons. To calculate $v_2(B)$, a simultaneous fit by Eq. 4.1 is performed to all the baryon data points as a function of $m_T - m_0$ as shown in Fig. 4.8 and 4.9. In the fitting function a, b, c, and d are free parameters. n is the number of constituent quarks for baryons and mesons. At any $m_T - m_0$, $v_2(B)$ is calculated by interpolating the fitting function. Same fitting function is used to fit the mesons and interpolated at $(m_T - m_0) \times 2/3$ for $v_2(M)$. The ratio of $v_2(B)/v_2(M)$ is shown in Fig. 4.14.

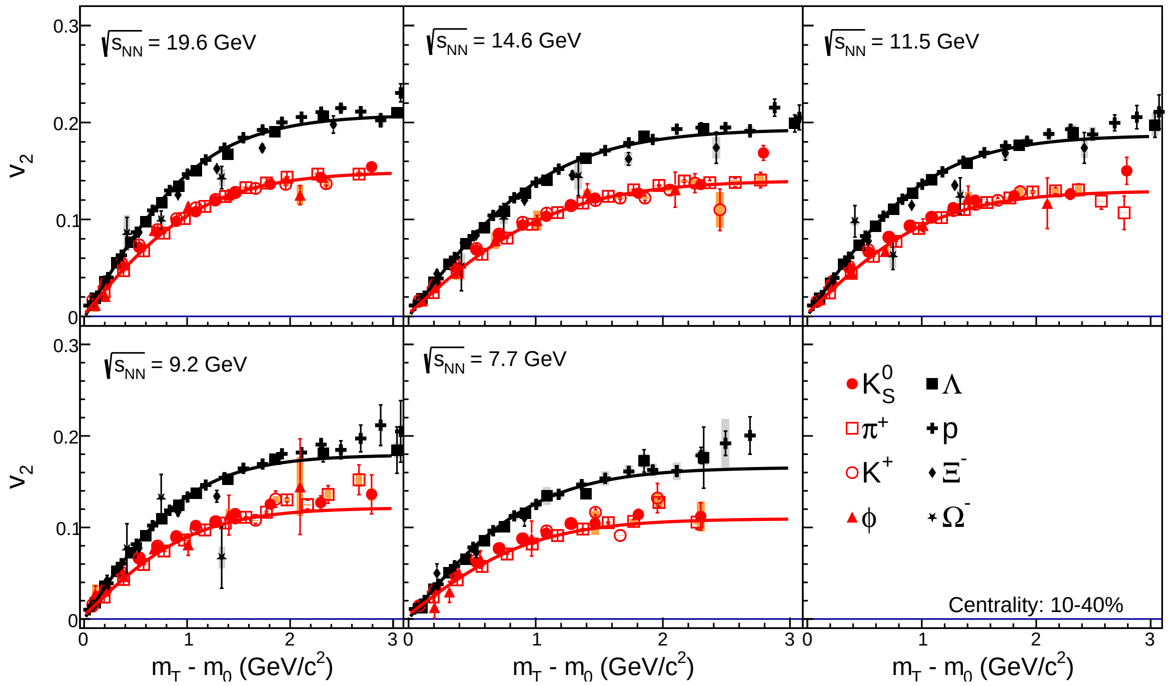

Figure 4.8: v_2 is plotted as a function of $m_T - m_0$ for identified hadrons in 10-40% centrality at $|y|$ <1.0 for collision energies $\sqrt{s_{NN}}$ = 7.7 to 19.6 GeV for particles. The solid black and red lines show the simultaneous fitting to baryons and mesons data points by Eq. 4.6 respectively.

$$f_{v_2}(m_T - m_0, n) = \frac{an}{1 + e^{-(m_T - m_0/(n-b))/c}} - dn \tag{4.6}$$

At $m_T - m_0$ = 2.0 GeV/c^2, NCQ scaling holds within 10% for anti-particles and within 15% for particles. This better agreement for anti-particles occurs because they are composed of produced quarks from the collisions, while particles may be affected by transported quarks. Transported quarks are part of the colliding system, and experience the whole system evolution. Where as produced quarks can be produced at any stage of the system evolution. Since transported quarks interact for a longer time with the system they can increase the magnitude of v_2 of the particles making them deviate from the NCQ scaling. At $m_T - m_0$ = 1.5 GeV/c^2, the NCQ scaling for particles deviate more compared to that at 2.0 GeV/c^2. This indicated that the transported quark affect might be dominant at low p_T. More phenomenological studies needed to understand this effect. The presence of NCQ scaling at $\sqrt{s_{NN}}$ = 7.7-19.6 GeV indicates the presence of partonic collectivity in the initial state of the medium and supports the quark coalescence model of hadronization.

Under the hydrodynamical assumption $v_n \propto v_2^{n/2}$, v_3 should follow a modified NCQ

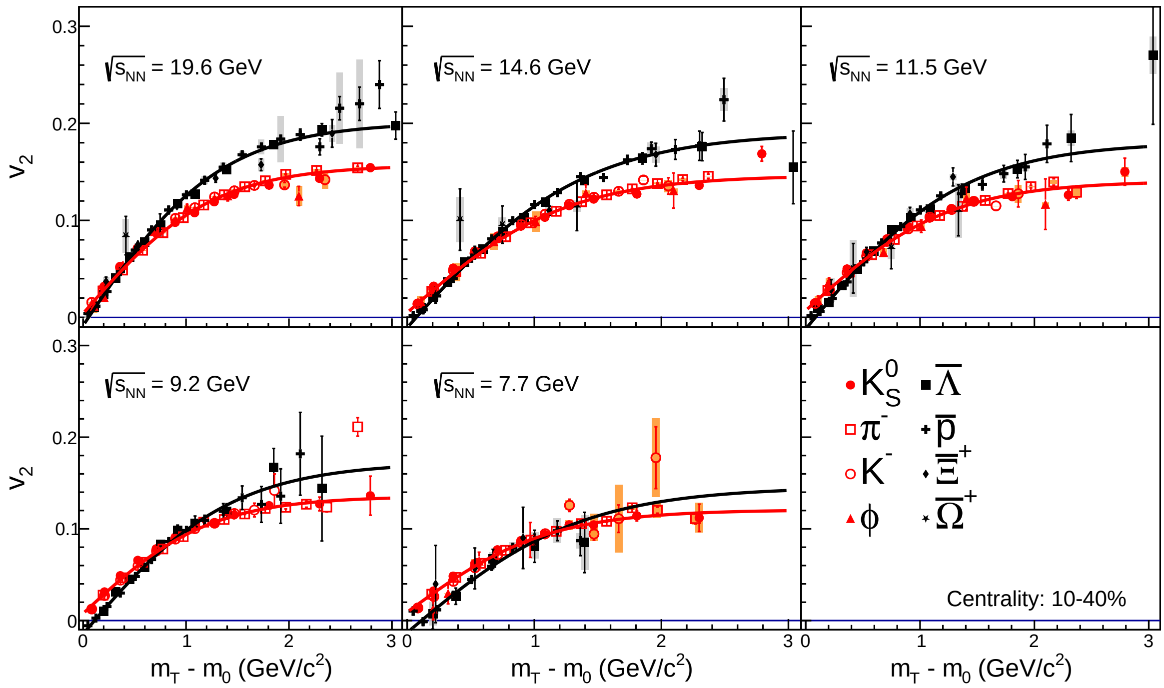

Figure 4.9: v_2 is plotted as a function of $m_T - m_0$ for identified hadrons in 10-40% centrality at $|y| < 1.0$ for collision energies $\sqrt{s_{NN}}$ = 7.7 to 19.6 GeV for anti-particles. The solid black and red lines show the simultaneous fitting to baryons and mesons data points by Eq. 4.6 respectively.

scaling when $v_3/n_q^{3/2}$ is plotted as a function of $(m_T - m_0)/n_q$. Such a scaling is tested at $\sqrt{s_{NN}}$ = 7.7-19.6 GeV. The modified NCQ scaling for v_3 for particles and anti-particles are shown in Fig. 4.15 and 4.16. The scaling holds approximately for both particles and anti-particle at all energies indicating the presence of collectivity in the initial state.

4.9 Difference between particles and anti-particles v_n

A p_T-differential particle-to-antiparticle v_2 ratio is shown in Fig.4.17. This ratio exhibits a clear energy dependence, with the relative difference in v_2 between particles and antiparticles increasing as collision energy decreases. The low p_T region contributes significantly to this difference. It is observed that the relative v_2 difference is larger for baryons than for mesons. For pions, π^- has a larger v_2 than π^+, in contrast, K^+ exhibits a larger v_2 than K^- at $p_T < 1.5$ GeV, while at higher p_T there is a hint of a reversed trend. In the case of protons and lambdas, particles show a significantly larger v_2 than their antiparticles.

Various model studies have attempted to explain this pronounced v_2 difference be-

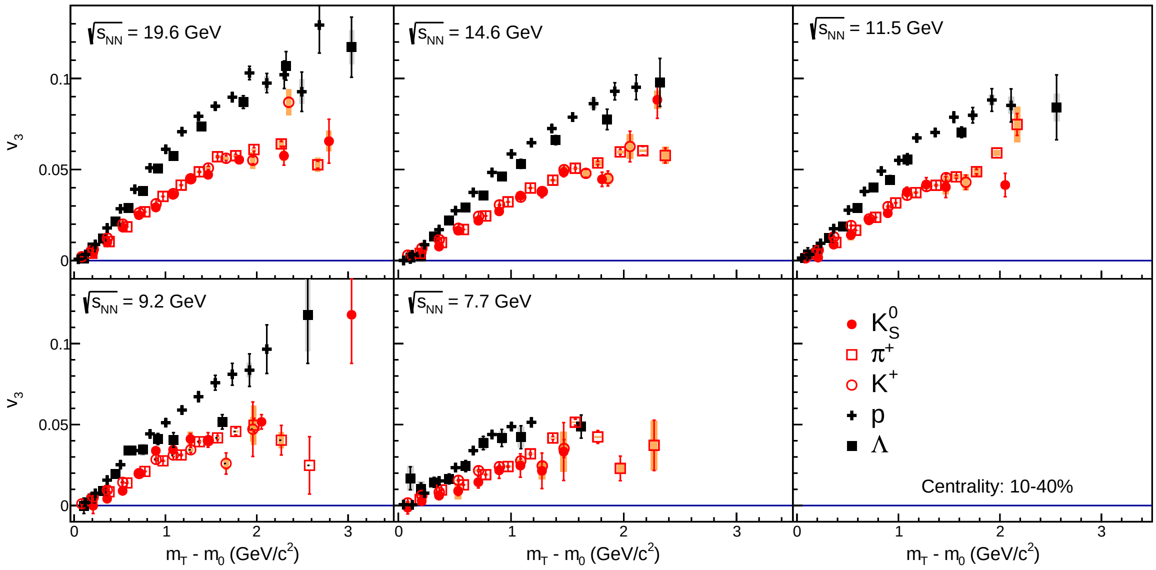

Figure 4.10: v_3 is plotted as a function of $m_T - m_0$ for identified hadrons in 10-40% centrality at $|y|$ <1.0 for collision energies $\sqrt{s_{NN}}$ = 7.7 to 19.6 GeV for particles. All the results in the figure are not yet published or STAR preliminary accepted. These are under collaboration review.

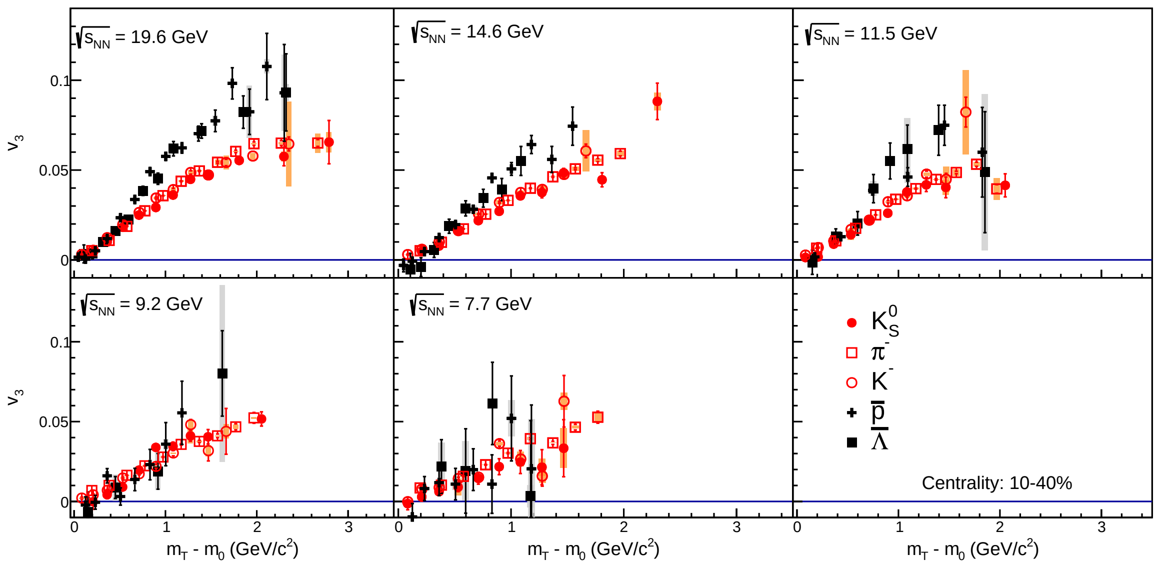

Figure 4.11: v_3 is plotted as a function of $m_T - m_0$ for identified hadrons in 10-40% centrality at $|y|$ <1.0 for collision energies $\sqrt{s_{NN}}$ = 7.7 to 19.6 GeV for anti-particles. All the results in the figure are not yet published or STAR preliminary accepted. These are under collaboration review.

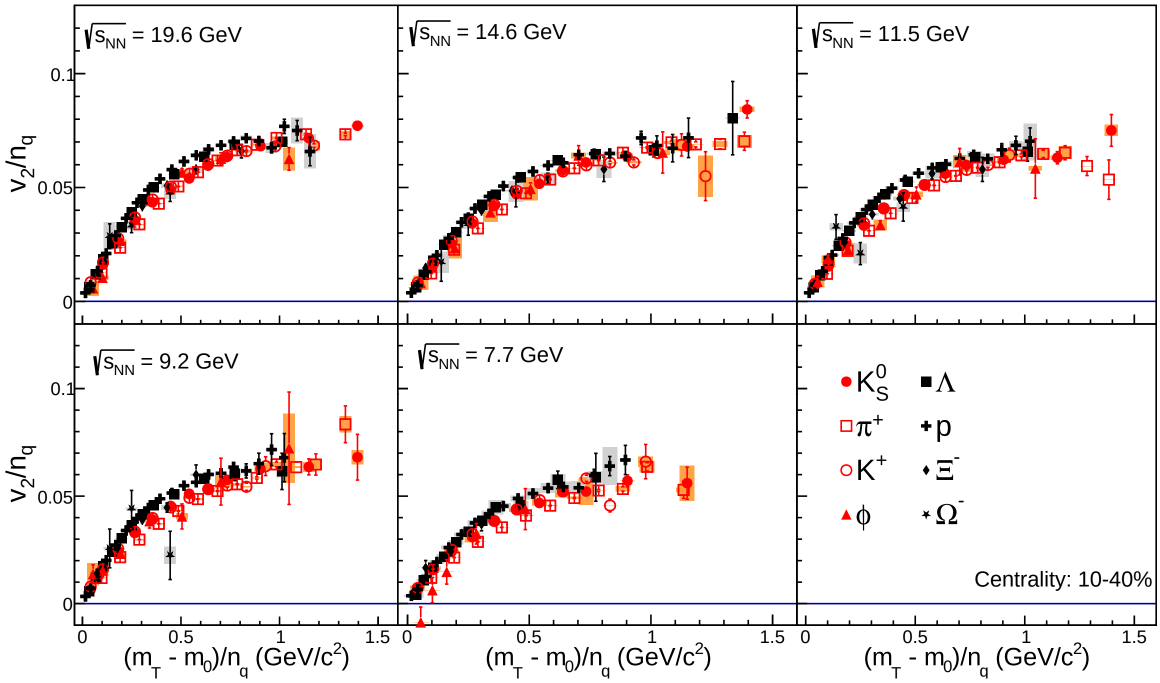

Figure 4.12: NCQ scaled v_2 is plotted as a function of NCQ scaled $m_T - m_0$ for particles at $\sqrt{s_{NN}}$ = 7.7 to 19.6 GeV. All the results in the figure are not yet published or STAR preliminary accepted. These are under collaboration review.

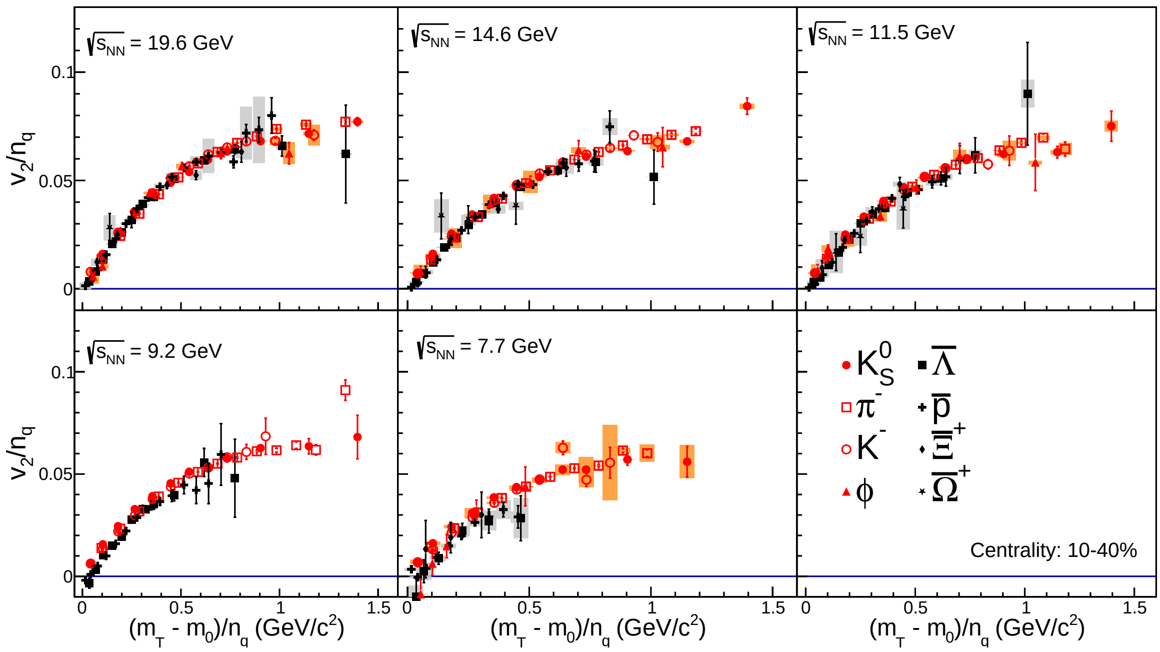

Figure 4.13: NCQ scaled v_2 is plotted as a function of NCQ scaled $m_T - m_0$ for anti-particles at $\sqrt{s_{NN}}$ = 7.7 to 19.6 GeV. All the results in the figure are not yet published or STAR preliminary accepted. These are under collaboration review.

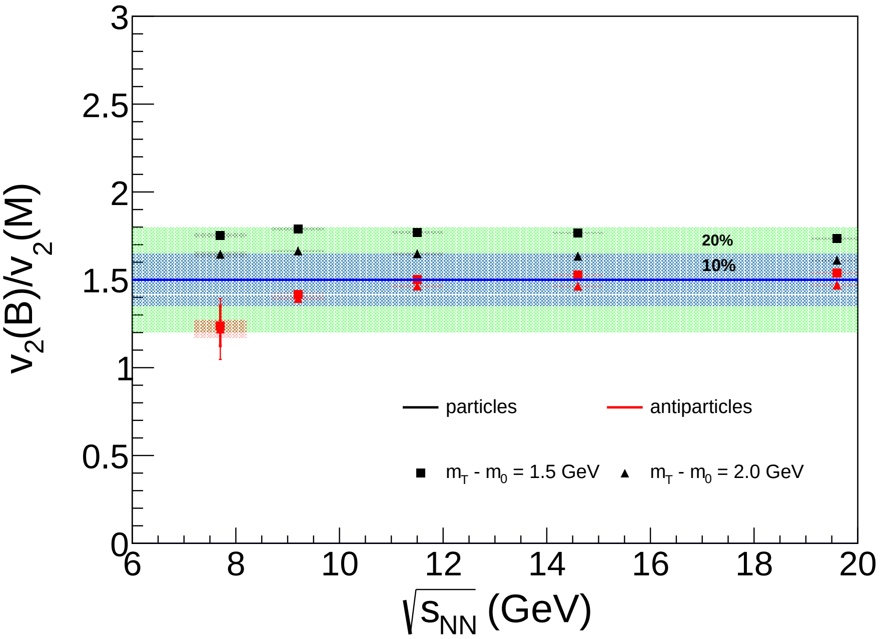

Figure 4.14: ratio of $v_2(B)/v_2(M)$ is shown as a function of collision energies. The blue shaded band and the green shaded bands are 10% and 20% deviations from 1.5. The plot is not yet published or STAR preliminary accepted. This is under review.

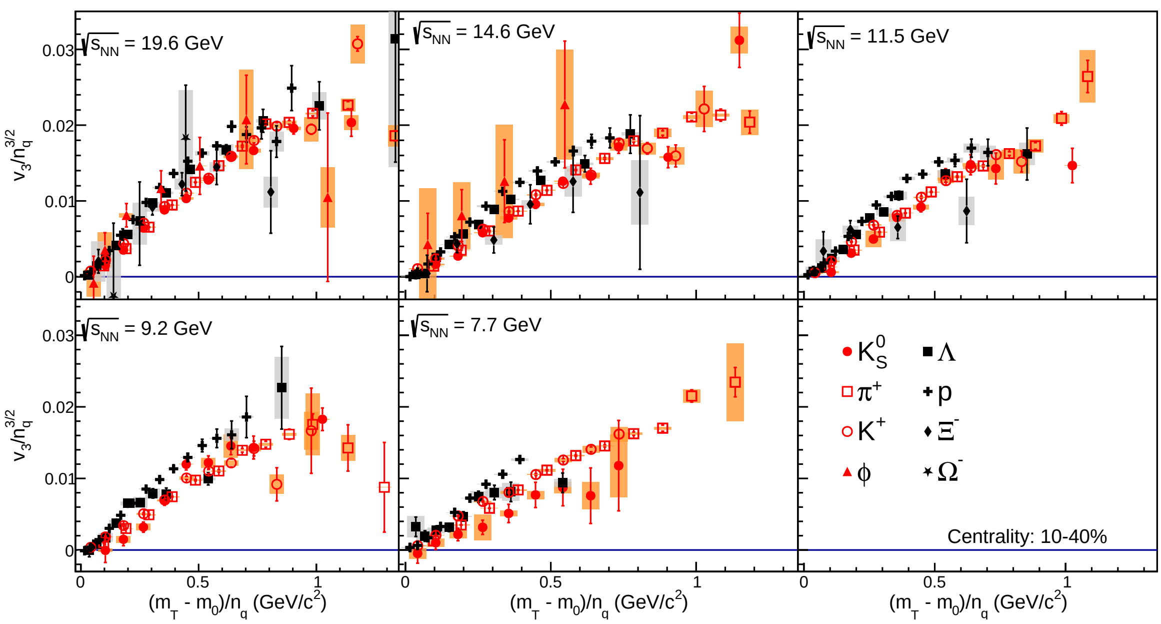

Figure 4.15: The modified NCQ scaling in v_3, $v_3/n_q^{3/2}$, for particles is plotted as a function of NCQ scaled transverse kinetic energy, $(m_T - m_0)/n_q$. The plot is not yet published or STAR preliminary accepted. This is under review.

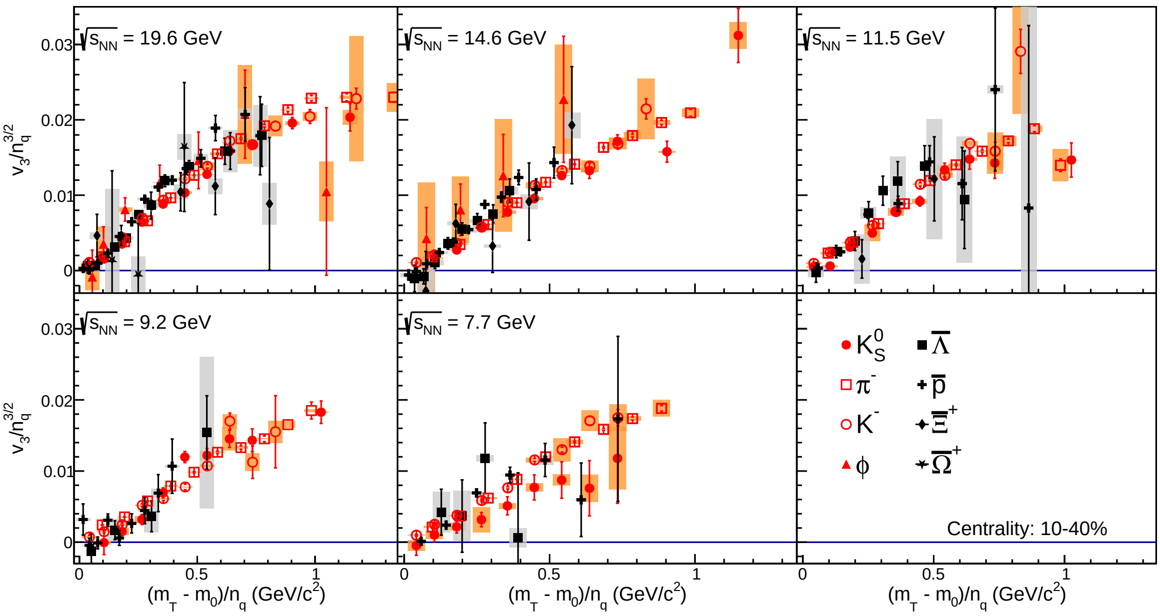

Figure 4.16: The modified NCQ scaling in v_3, $v_3/n_q^{3/2}$, for antiparticles is plotted as a function of NCQ scaled transverse kinetic energy, $(m_T - m_0)/n_q$. The plot is not yet published or STAR preliminary accepted. This is under review.

tween particles and antiparticles in past. The difference between π^+ and π^- v_2 initially explained by models with quadrupole deformation induced by chiral magnetic waves (CMW) [126] but later with models incorporating transported quarks have also predicted such a v_2 difference between π^+ and π^- [127]. The large difference in baryon-antibaryon v_2 also can be qualitatively explained by these transported quark models. At lower collision energies, baryon stopping may further amplify the transport quark effect at mid-rapidity, resulting in a greater v_2 difference between baryons and antibaryons. Models that include hadronic and partonic mean field potentials[128–130] also provide qualitative explanations for the v_2 splitting between particles and antiparticles. In Ref. [131], it was also pointed out that the induced electromagnetic field produced by the spectator nucleons could generate the difference in flow magnitude between positively and negatively charged particles.

Figure 4.18 illustrates the relative difference in the integrated v_n between particles and their corresponding antiparticles for pions, kaons, and protons in the 10–40% centrality range. The integrated v_n for each particle species is obtained by weighting its p_T-differential v_2 with the corresponding p_T spectra, as defined in Eq. 4.7. The p_T spectra for $\pi^{+(-)}$, $K^{+(-)}$ and $p(\bar{p})$ are taken from Ref. [132]. The integration range is 0.2–2.0 GeV/c for $\pi^{+(-)}$ and $K^{+(-)}$, and 0.5–2.0 GeV/c for $p(\bar{p})$.

The relative difference in v_n is observed to increase as the collision energy decreases for all particle species. For protons and kaons, the relative differences in both v_2 and v_3 are consistent within uncertainties. However, for pions, the difference in v_3 between π^+ and π^- is notably larger than that of v_2, particularly at lower collision energies ($\sqrt{s_{NN}}$ = 11.5 and 7.7 GeV). Further phenomenological studies are required to understand the origin of this significant difference in v_3 between π^+ and π^-.

$$\langle v_2^{int} \rangle = \frac{\int dp_T f(p_T) v_2(p_T)}{\int dp_T f(p_T)} \tag{4.7}$$

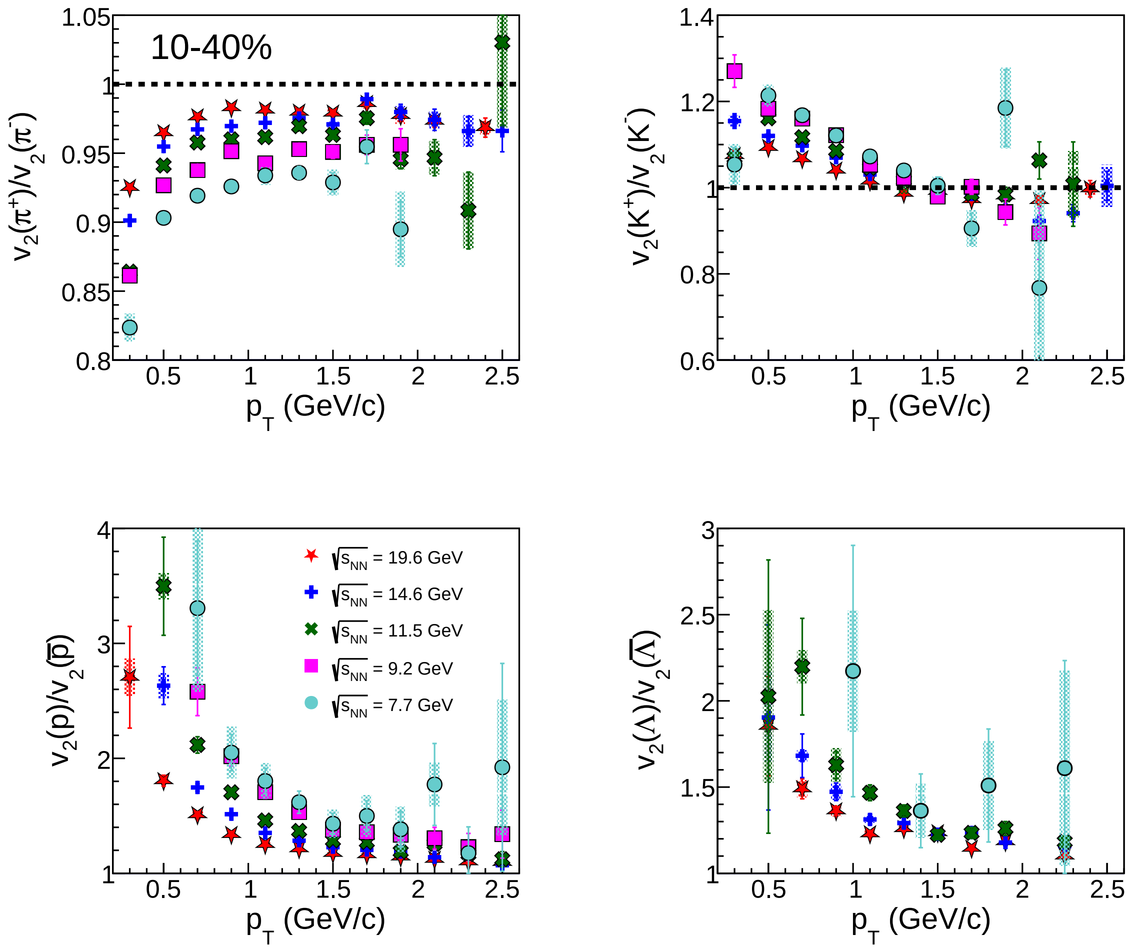

Figure 4.17: Particle to anti-particle v_2 ratio at $\sqrt{s_{NN}}$ = 7.7 to 19.6 GeV is plotted as a function of p_T for π, K, proton and Λ at 10-40% centrality. The plot is not yet published or STAR preliminary accepted. This is under review.

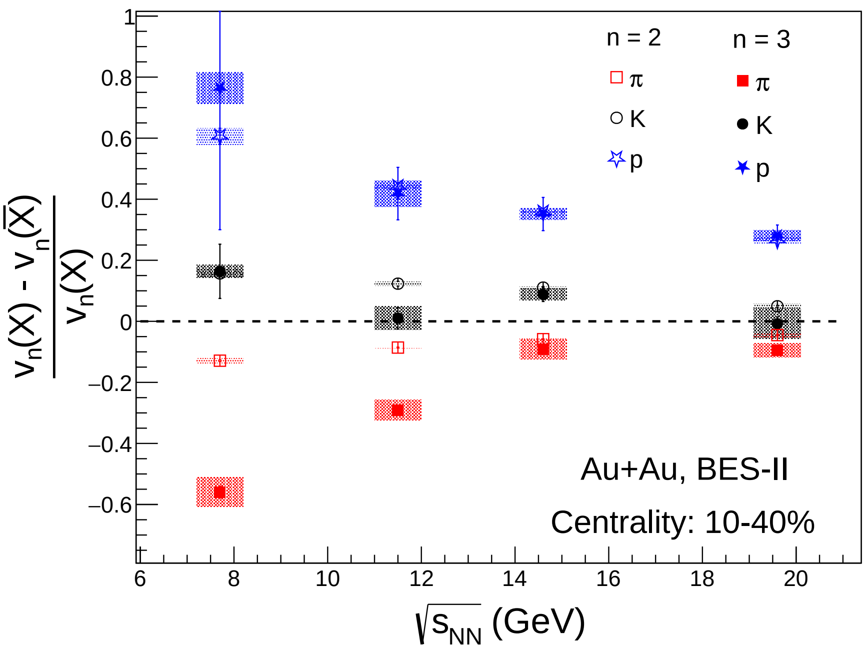

Figure 4.18: The relative difference between particle to anti-particle integrated v_n is plotted as a function of $\sqrt{s_{NN}}$ for π, K, and proton at 10-40% centrality. The plot is not yet published or STAR preliminary accepted. This is under review.

4.10 Summary

In this chapter we present the measurement of v_2 and v_3 of identified hadrons species at $\sqrt{s_{NN}}$ = 7.7 to 19.6 GeV using high statistics BES-II datasets. We observed that the v_2 of ϕ mesons follow the usual trend of v_2 unlike the BES-I results where its value seems to be suppressed at lower collision energies, $\sqrt{s_{NN}}$ < 14.6 GeV. This indicates that the earlier BES-I results are just statistical fluctuations due to small number of event samples. We observed that the $m_T - m_0$ splitting between baryons and mesons as well as NCQ scaling at $\sqrt{s_{NN}}$ = 7.7 to 19.6 GeV indicating the presence of a partonic dominant medium with collectivity. These scaling also hold approximately for v_3. The difference between particles and anti-particles v_2 increases with decreasing collision energy and this difference has major contribution from the low p_T particles. Similarly we studied the v_3 difference between particles and anti-particles. These differences in particle to anti-particle v_n could be due to transported quark affects and/or mean field potential affect in the lower collision energy regimes.

CHAPTER 5

Insight from the anisotropic flow of identified hadrons measured in relativistic heavy-ion collisions

5.1 Chapter introduction

In this chapter, we have calculated the v_2 and v_3 of the quarks from the available data of various hadron species at STAR experiment. We observed a new purely empirical scaling in the v_2 of light and strange quarks when plotted as a function of transverse kinetic energy. This chapter is based on Ref. [133].

5.2 Method of calculation for v_2 of quarks

Within the framework of coalescence mechanism [112, 134–137], v_2 of a quark is given by,

$$v_2^q(p_T/n_q) = \frac{v_2^h(p_T)}{n_q}. \tag{5.1}$$

Where v_2^q is the v_2 of the constituent quark of a hadron. v_2^h is the v_2 of the hadron species. n_q is the number of the constituent quarks inside the hadrons. v_2 of u and d quarks can be calculated by using proton assuming both u and d have nearly equal mass from Eq. 5.2.

$$v_2^{u/d}(p_T/n_q) = \frac{v_2^p(p_T)}{n_q}. \tag{5.2}$$

v_2 of u quarks can also be calculated from measured v_2 of Λ and Ξ using Eq. 5.3 [138, 139].

$$v_2^u(p_T) = \frac{1}{3}[2v_2^{\Lambda}((2+r)p_T) - v_2^{\Xi}((1+2r)p_T)] \tag{5.3}$$

Here $r = \frac{m_s}{m_u}$, is the ratio of constituent quarks masses of s and u quarks which is equal to 1.667. One can calculate the v_2 of strange quarks by using measured v_2 data for ϕ mesons or Ω using Eq. 5.4.

$$v_2^s(p_T/n_q) = \frac{v_2^{\phi/\Omega}(p_T)}{n_q}. \tag{5.4}$$

5.3 Results

5.3.1 Transverse momentum dependence

Figure 5.1 presents the v_2 of quarks as a function of their transverse momentum (p_T^q) in Au+Au collisions at $\sqrt{s_{NN}}$ = 200 GeV [53], where p_T^q is determined by dividing the p_T of the hadron by its number of constituent quarks. The results indicate that $v_2^{u/d}$, calculated using Eq.5.2 and Eq. 5.3, are consistent with each other. Similarly, the v_2 values of strange quarks, derived from ϕ mesons and Ω, are also in agreement. This consistency suggests that coalescence is the dominant hadronization process for the production of these strange hadrons.

Moreover, light quarks exhibit a larger magnitude of v_2 compared to strange quarks. This difference can be attributed to the radial flow of the initially produced medium, which propels low-p_T quarks to higher momentum, thereby reducing the anisotropy in their flow. This effect is more pronounced for heavier particles than for lighter ones.

5.3.2 An empirical scaling

NCQ scaling in v_2 of identified hadrons is a well-established observable where v_2/n_q is plotted as a function of $(m_T - m_0)/n_q$, the NCQ-scaled transverse kinetic energy. When v_2/n_q values from different hadron species converge to a similar magnitude, it indicates the presence of partonic collectivity in the medium and supports the coalescence model of hadronization.

In this study, instead of examining the scaling as a function of $(m_T - m_0)/n_q$, we calculate it as a function of the transverse kinetic energy of the quark, defined as $KE_T^q = m_T^q - m_q$,

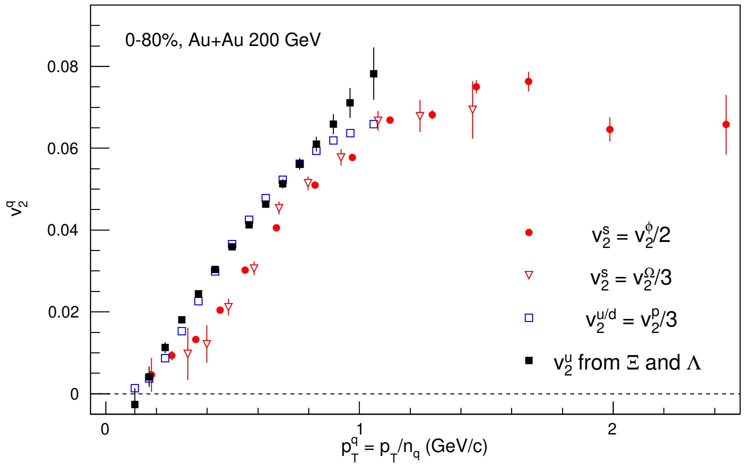

Figure 5.1: v_2 of u and s quarks are plotted as a function of transverse momentum p_T^q in Au+Au collisions at $\sqrt{s_{NN}}$ = 200 GeV in 0-80% centrality. The data points for $\sqrt{s_{NN}}$ = 200 GeV are taken from Ref. [53].

where m_q is the bare quark mass. Panel (b) of Fig.5.2 depicts the v_2 of u quarks, obtained using Eq.5.2 and Eq. 5.3, as a function of KE_T^q.

The v_2 values of u and s quarks exhibit similar magnitudes when plotted as a function of KE_T^q. To further quantify this scaling, the v_2 of u quarks is fitted with the functional form shown in Eq. 5.5.

$$v_2(x) = \frac{an}{1 + \exp(-(xn - b)/c)} - dn, \tag{5.5}$$

In Eq.5.5, a, b, c, d, and n are the fit parameters. Panels (d), (e), and (f) of Fig.5.2 display the ratio of the s quark's v_2 to the fitting function derived from u quarks. These ratios are further fitted with a constant polynomial to determine the average deviation (p_0) from the scaling.

The results show that the scaling holds within 3% when m_s is taken as 100 MeV/c^2 and within 1% when m_s is set to 140 MeV/c^2 in Au+Au collisions at $\sqrt{s_{NN}}$ = 200 GeV.

In this calculation, the bare mass of the u quark, m_u, is taken as 4 MeV/c^2. The bare mass of the s quark is varied from 90 MeV/c^2 to 180 MeV/c^2, and a better match between the v_2 of u and s quarks is observed when m_s is in the range of 130 to 140 MeV/c^2. The best match is quantified using χ^2/NDF as shown in Fig. 5.3.

For this study we considered two specific cases where m_s is 100 MeV/c^2, which falls within the PDG mass limit [140], and 140 MeV/c^2, which provides the best agreement between the v_2 values of u and s quarks.

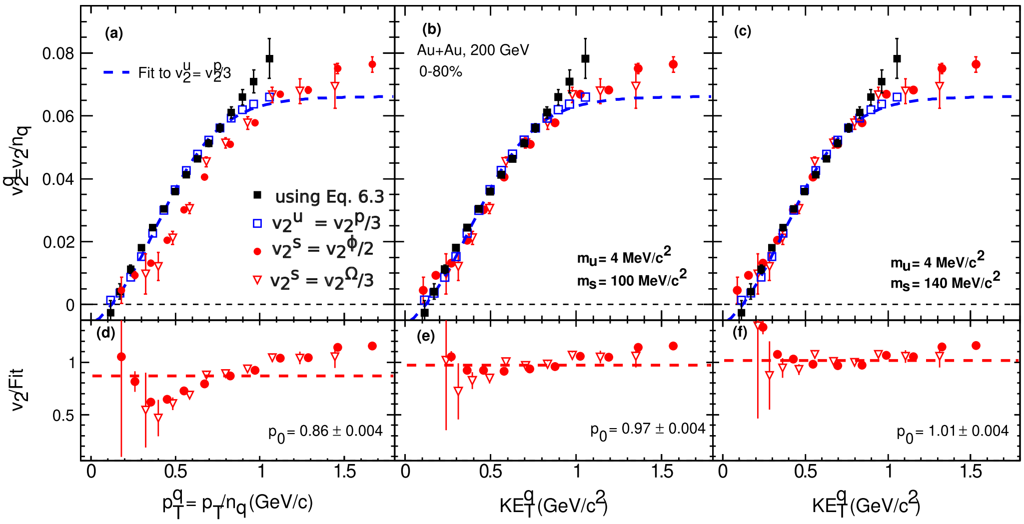

Figure 5.2: Panel (a) shows the v_2^q as a function of p_T/n_q. Panel (b) shows the v_2^q as a function of KE_T^q taking $m_u = 4$ MeV/c^2 and $m_s = 100$ MeV/c^2. Panel (c) shows the same as panel (b) but with $m_s = 140$ MeV/c^2. The blue dashed line in all the panels is the fitting to light quark v_2 obtained from protons with Eq. Panel (d), (e) and (f) shows the ratio of the strange quark v_2 to the fitting function. The dashed red line in all the lower panel is a zeroth order polynomial fitting to the ratios.

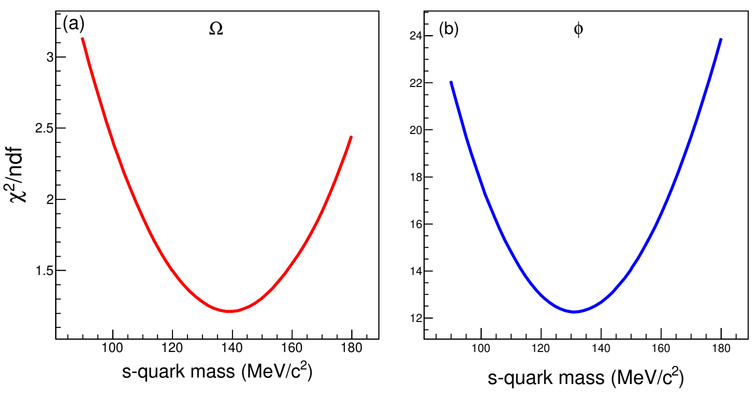

Figure 5.3: The χ^2/ndf values for different s-quark masses represent the best match between the v_2 of strange and light quarks as a function of transverse kinetic energy. This analysis is for Au+Au collisions at $\sqrt{s_{NN}} = 200$ GeV. Panel (a) shows the results where the v_2 of s quarks is derived from the Ω, while Panel (b) presents the results where the v_2 of s quarks is derived from the ϕ.

5.3.3 Test of the scaling at smaller RHIC energies

The scaling is testes using the RHIC data at lower collision energies. For smaller collision energy $\sqrt{s_{NN}}$ <19.6 GeV, we have used BES-II data for better precession results. At these energies we have used anti-particles to calculate the v_2 of the anti-quarks to avoid the affect of transported quarks. We observed that the newly proposed scaling performs equally well for both 39 and 19.6 GeV, as well as for 11.5 GeV.

5.3.4 Test of the scaling at LHC energy

We tested the scaling behavior at LHC energies using the latest measurements of the v_2 of ϕ mesons and protons at $\sqrt{s_{NN}}$ = 5.02 TeV from the ALICE experiment [141]. However, data for Ω and Ξ are not available at this energy. Figure 5.5 presents v_2/n_q as a function of p_T/n_q and KE_T^q in 20-30% Pb+Pb collisions at $\sqrt{s_{NN}}$ = 5.02 TeV.

We observe that in the low-p_T region, v_2/n_q for the ϕ meson is lower than that for protons when plotted against p_T/n_q. In contrast, when v_2/n_q is plotted as a function of KE_T^q, the values for protons and ϕ mesons converge and show similar behavior.

It is noteworthy that the empirical scaling of v_2/n_q as a function of KE_T^q holds consistently across both RHIC and LHC energies, despite the substantial difference in their center-of-mass energies, with the LHC being approximately 100 times higher than the RHIC BES energies. This intriguing observation calls for further theoretical investigation to uncover the underlying mechanisms responsible for the scaling observed in the v_2 of measured hadrons.

5.3.5 Test of the scaling for higher order flow harmonics

We conducted a systematic check using the triangular flow harmonic (v_3). Previous studies have shown that scaling in v_3 requires dividing it by $n_q^{3/2}$ [142]. Figure 5.6(a) illustrates $v_3/n_q^{3/2}$ as a function of p_T/n_q for protons and ϕ mesons measured by the STAR experiment in Au+Au collisions at $\sqrt{s_{NN}}$ = 200 GeV [54]. Similar to v_2, the scaled v_3 of the ϕ meson is observed to be lower than that of protons in the low p_T region. However, when $v_3/n_q^{3/2}$ is plotted as a function of KE_T^q, a good consistency between protons and ϕ mesons is observed, akin to the behavior seen for v_2.

5.4 Summary

In summary, we present a compilation of available data on the elliptic flow (v_2) and triangular flow (v_3) of identified hadrons at RHIC and LHC energies. Within the framework of the quark recombination model, the v_2 of light and strange quarks is extracted from the measured v_2 of identified hadrons. Our observations indicate that the v_2 of strange quarks derived from the ϕ-meson v_2 is consistent with that obtained from Ω v_2 in Au+Au collisions at $\sqrt{s_{NN}}$ = 200 GeV, suggesting that both ϕ and Ω are produced through quark recombination at top RHIC energy. However, at low transverse momentum, the v_2 of strange quarks is consistently smaller than that of light quarks. We have demonstrated an empirical relation between the v_2 of light and strange quarks, where v_2 scales as a function of the transverse kinetic energy of quarks. The transverse kinetic energy is calculated using the bare quark mass, and this relation holds true at both RHIC and LHC energies. Additionally, we show that the v_3 of measured hadrons follows a similar scaling behavior. This new scaling observed in flow measurements is purely empirical and warrants further theoretical investigation to understand the underlying mechanisms.

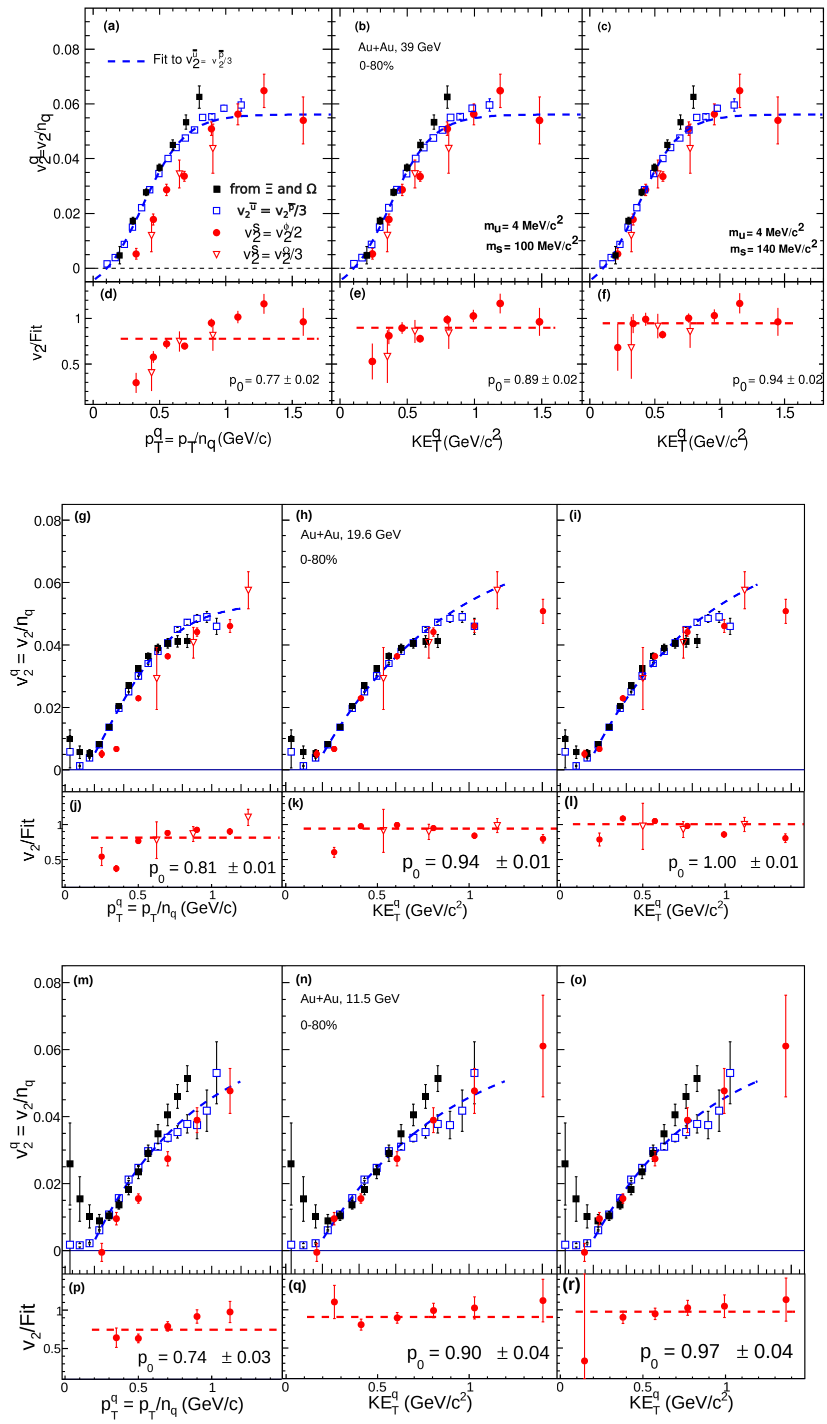

Figure 5.4: The v_2 values of light and strange quarks, obtained from $\bar{p}$ and ϕ (and from Ω, $\bar{\Lambda}$, and $\bar{\Xi}$ for 39 and 11.5 GeV only), are shown as a function of p_T/n_q in 0–80% central Au+Au collisions at $\sqrt{s_{NN}}$ = 39, 19.6, and 11.5 GeV. The middle panel presents the v_2 of quarks as a function of $KE_T^q = \sqrt{(p_T/n_q)^2 + m_q^2} - m_q$, where p_T is the transverse momentum of the hadron. For this calculation, the quark masses are assumed to be m_q = 4 MeV/c^2 for light quarks and m_q = 100 MeV/c^2 for strange quarks. The right panel shows the same analysis as the middle panel but assumes m_q = 140 MeV/c^2 for strange quarks. The blue dashed curves represent the fits to the v_2 of light quarks using Eq. 5.5, while the red dashed lines correspond to the constant polynomial fits applied to the ratios shown in the respective bottom panels. The data points for 39 GeV are taken from Ref. [45]. 11.5 and 19.6 GeV data are from BES-II analysis.

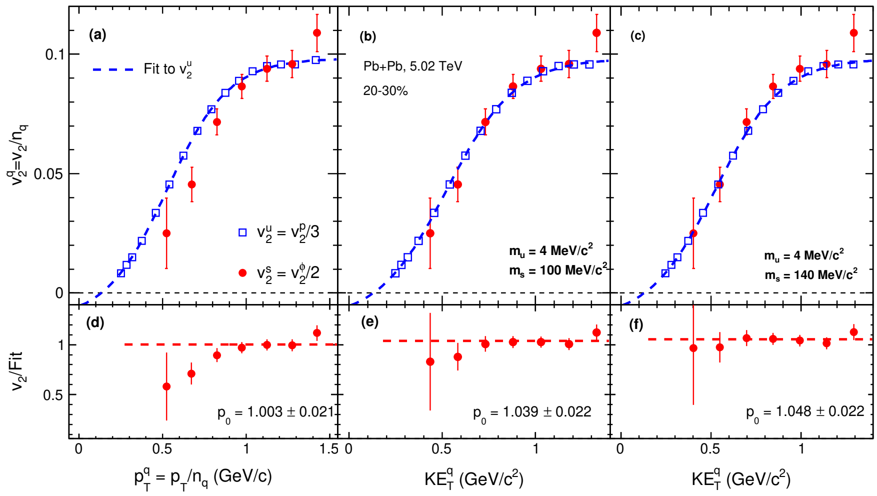

Figure 5.5: Panel (a) shows the v_2 of light and strange quarks obtained from protons and ϕ mesons as a function of p_T/n_q in 20–30% central Pb+Pb collisions at $\sqrt{s_{NN}}$ = 5.02 TeV [141]. Panel (b) presents the v_2 of quarks as a function of $KE_T^q = \sqrt{(p_T/n_q)^2 + m_q^2} - m_q$, where p_T is the transverse momentum of the hadron. Here, the quark masses are taken as m_q = 4 MeV/c^2 for light quarks and m_q = 100 MeV/c^2 for strange quarks. Panel (c) depicts the same as panel (b), but with the mass of strange quarks set to m_q = 140 MeV/c^2. The blue dashed curves represent the fit to the v_2 of light quarks using Eq. 5.5, while the red dashed lines indicate the constant polynomial fit to the ratios shown in the corresponding bottom panels.

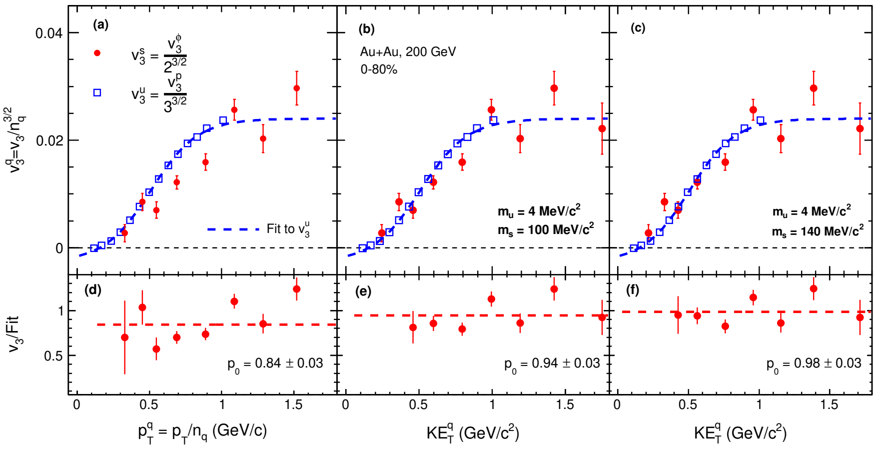

Figure 5.6: Panel (a): The $v_3/n_q^{3/2}$ of protons and ϕ mesons as a function of p_T/n_q in Au+Au collisions at $\sqrt{s_{NN}}$ = 200 GeV [54]. Panel (b): The $v_3/n_q^{3/2}$ of protons and ϕ mesons as a function of $KE_T^q = \sqrt{(p_T/n_q)^2 + m_q^2} - m_q$, where p_T represents the transverse momentum of the hadron. Here, the quark masses are taken as $m_q = 4$ MeV/c^2 for light quarks and m_q = 100 MeV/c^2 for strange quarks. Panel (c): Same as panel (b), but with m_q = 140 MeV/c^2 for strange quarks. The blue dashed curves represent the fits to the v_3 of light quarks using Eq. 5.5, while the red dashed lines correspond to a constant polynomial fit to the ratios shown in the respective bottom panels.

CHAPTER 6

Longitudinal flow decorrelation in heavy-ion collisions using AMPT model

6.1 Chapter introduction

In ultra-relativistic heavy-ion collisions at the LHC and top RHIC energies, a phenomenon known as longitudinal boost invariance is anticipated, meaning that the dynamics at mid-rapidity should be the same as those observed in forward and backward rapidity regions. However, at lower collision energies, this boost invariance may be broken, potentially leading to distinct dynamics along the longitudinal or rapidity direction.

One manifestation of this phenomenon is the fluctuation in the magnitude of flow and the event plane angle at forward and backward pseudorapidity windows compared to the mid-rapidity region, as illustrated in Fig.6.1. This variation in the flow vector along pseudorapidity is known as flow decorrelation. Flow decorrelation is thought to stem from event-by-event fluctuations in the initial energy density distribution along the longitudinal direction. Extensive experimental studies of flow decorrelation have been conducted in A+A collisions at $\sqrt{s_{NN}}$ = 200 GeV and LHC energies[143–148]. Additionally, various hydrodynamic and transport model studies have been undertaken to understand this phenomenon [149–157]. However, these studies are largely focused on LHC or top RHIC energies.

Given that boost symmetry breaking is more pronounced at lower energies, studying longitudinal flow decorrelation at intermediate and lower RHIC energies becomes essential. In this chapter, we measure longitudinal flow decorrelation using the A Multi Phase

Transport (AMPT) model for Au+Au collisions at $\sqrt{s_{NN}}$ = 11.5 to 200 GeV.

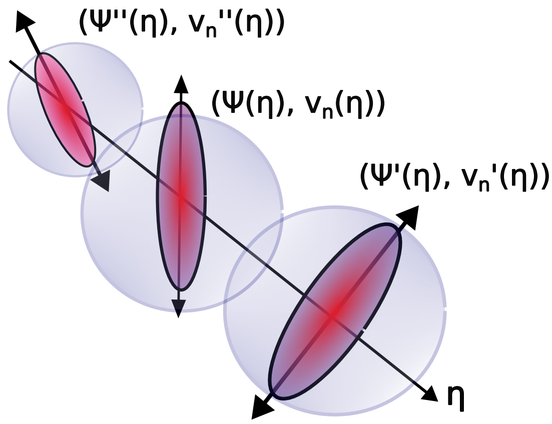

Figure 6.1: Illustration of the flow magnitude and flow angle fluctuation at different pseudorapidty window.

6.2 Second (r_2) and third order (r_3) factorization ratio

The observable used to measure the longitudinal flow vector decorrelation is first given by CMS collaboration [143], defined as follows.

$$r_n(\eta_a,\eta_b) = \frac{\langle V_n(-\eta_a)V_n^*(\eta_b)\rangle\rangle}{\langle V_n(+\eta_a)V_n^*(\eta_b)\rangle\rangle} \tag{6.1}$$

$$= \frac{\langle v_n(-\eta_a)v_n(\eta_b)\cos n(\Psi_n(-\eta_a)-\Psi_n(\eta_b))\rangle}{\langle v_n(\eta_a)v_n(\eta_b)\cos n(\Psi_n(\eta_a)-\Psi_n(\eta_b))\rangle}. \tag{6.2}$$

The angular bracket represents the event average. $V_n(-\eta_a)$ represents the flow vector at pseudorapidity η_a, while $V_n(-\eta_b)$ serves as a reference window at η_b. The positioning of these η windows is shown in Fig. 6.2. For our analysis, we select η_a within the range of -1.5 to 1.5, which aligns with the acceptance range of the STAR Time Projection Chamber (TPC) in experiments. The reference window η_b is chosen in the range $2.5 < \eta_b < 5.1$, corresponding to the acceptance of the Event Plane Detector (EPD) in the STAR detector system.

The observable in our study measures the correlation ratio between η_a and $-\eta_a$ relative to the reference window η_b; this ratio is termed the "factorization ratio." In the absence of fluctuations in flow vectors along the rapidity direction, this ratio would equal unity, as the flow vectors at η_a and $-\eta_a$ would be identical. However, when decorrelation is present, this ratio drops below unity, given that η_a is kinematically closer to the reference window η_b.

The second-order factorization ratio, r_2, quantifies the decorrelation in the magnitude of elliptic flow and fluctuations in the second-order event plane along pseudorapidity. Similarly, r_3 measures the decorrelation in triangular flow and fluctuations in the third-order event plane.

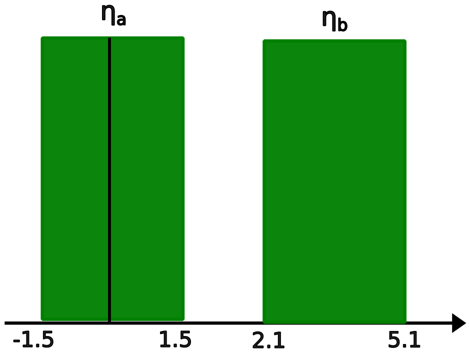

Figure 6.2: Illustration of η acceptance windows used in the analysis.

6.3 Model description

We have used A Multiphase Transport Model (AMPT) model [158] to study r_2 and r_3. This model is composed of four phases, providing a detailed simulation of the entire evolution of a heavy-ion collision, from the initial conditions to the late-stage hadronic interactions. The initial conditions are derived from the HIJING model [159–161], which generates the phase-space distribution of minijet partons. Interactions among these partons are then described by Zhang's Parton Cascade (ZPC) [162–165]. The differential cross-section for parton-parton interactions in this phase is given by

$$\frac{d\sigma}{dt} = \frac{9\pi\alpha^2}{2(t-\mu^2)^2}. \tag{6.3}$$

Here, σ represents the parton-parton scattering cross-section, t is the Mandelstam variable indicating four-momentum transfer, α is the strong interaction coupling constant, and μ denotes the Debye screening mass. For this study, we used AMPT version v1.26t9b, with $\alpha = 0.33$ and $\mu = 2.256, \text{fm}^{-1}$ across all energies, yielding a parton-parton cross-section of 3 mb. Using these parameters, we measured the transverse momentum and pseudorapidity dependence of elliptic flow (v_2) and triangular flow (v_3) at $\sqrt{s_{NN}} = 11.5$ and 200 GeV, as shown in Fig.6.3. These measurements were compared to experimental data from RHIC[49, 53, 106, 122, 166], and we observed a reasonable agreement between the data and the AMPT model.

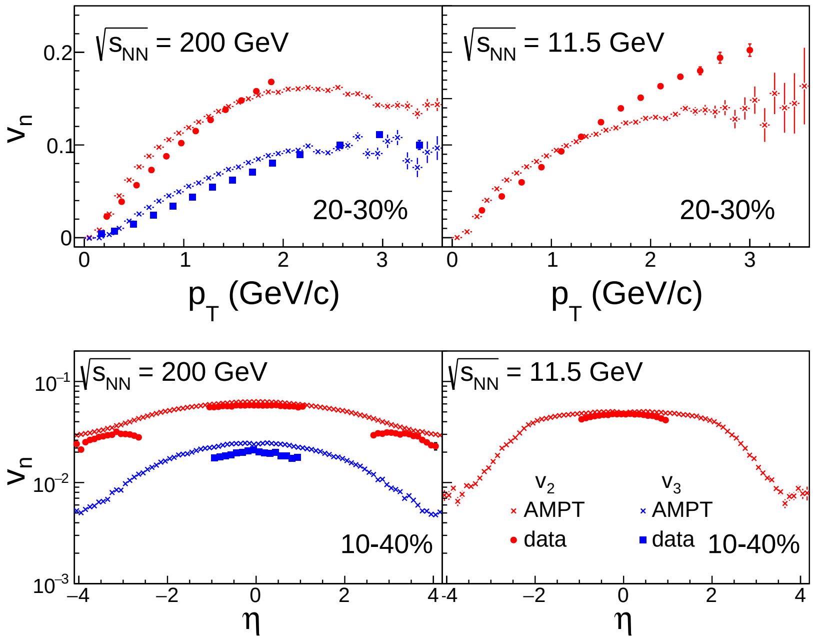

Figure 6.3: Panel (a) and (b) show the transverse momentum dependent v_2 and v_3 in Au+Au collisions from AMPT model and its comparison with the data. Panel (c) and (d) show the pseudorapidty dependence of v_2 and v_3 compared with data.

To further examine the impact of parton-parton scattering cross-section on the observables r_2 and r_3, we also generated data with an increased cross-section of 10 mb.

Regarding hadronization, the AMPT model offers two modes: the default mode and the string-melting mode. In the default mode, hadronization occurs via the Lund string fragmentation model [167]. In the string-melting mode [168–170], however, a quark coalescence model is used, where quarks close in both spatial and momentum space combine to form hadrons. For this study, we utilized the string-melting mode for hadronization.

6.4 Results

6.4.1 Centrality dependence of r_2 and r_3

Figure 6.4 and Figure 6.5 present r_2 and r_3, respectively, as functions of η_a/y_{beam} for Au+Au collisions at six different center-of-mass collision energies: $\sqrt{s_{NN}}$ = 11.5, 19.6, 27, 39, and 200 GeV, measured over the p_T range of 0.2 - 4.0 GeV/c in 0-10%, 10-40%, and 40-80% centrality events. Both r_2 and r_3 show values below one, decreasing as η_a/y_{beam} increases, indicating a stronger decorrelation with increasing distance from mid-rapidity. A significant

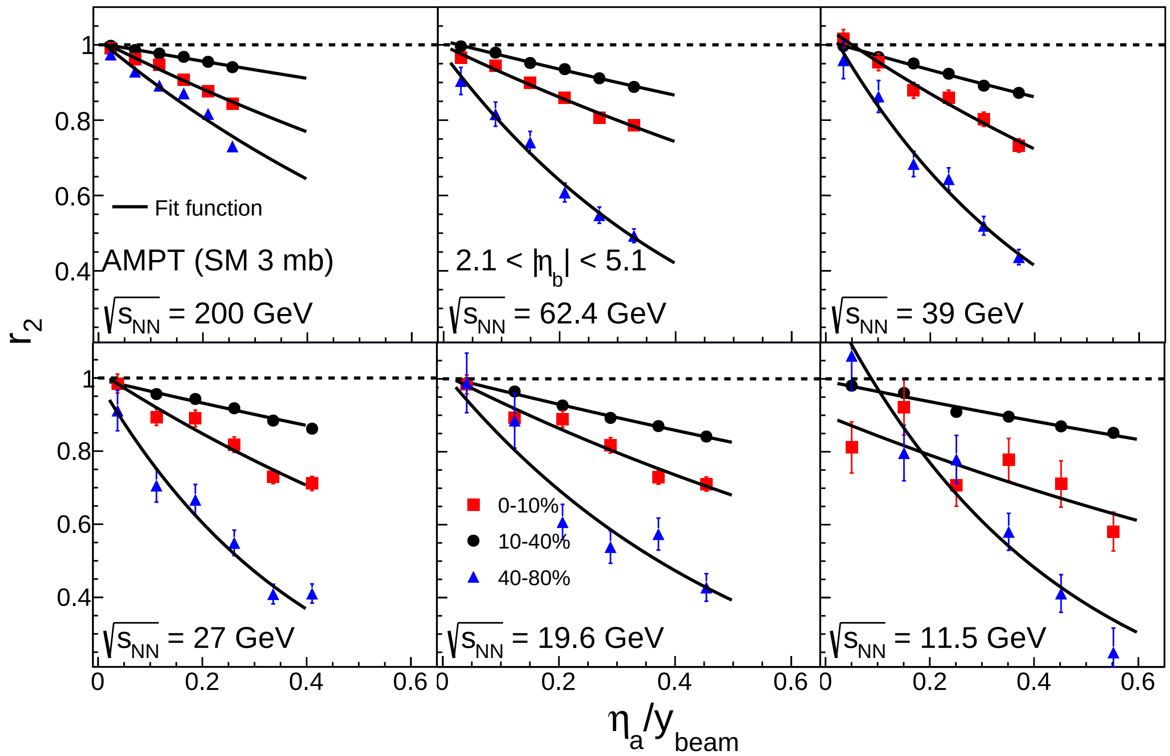

Figure 6.4: r_2 is plotted as a function of η_a/y_{beam} for Au+Au collisions in three centrality classes, 0-10%, 10-40%, and 40-80% at six energies ranging from 11.5 to 200 GeV. The black solid line represents the fitting function: $e^{-2F_2\eta/y_{beam}}$. The vertical lines on the points represent the statistical uncertainty.

centrality dependence is observed in r_2, with its magnitude being smallest in mid-central collisions and largest in peripheral collisions.

This observation aligns with the fact that in mid-central collisions, the initial elliptic geometry dominates over the longitudinal fluctuations in eccentricity, resulting in a smaller flow decorrelation. In central and peripheral collisions, however, the elliptic flow is primarily driven by fluctuations, leading to stronger decorrelation at these centralities. Conversely, r_3 shows a weak centrality dependence, as fluctuations predominantly drive the triangular distribution of energy density. This trend remains consistent across all collision energies.

6.5 Collision energy dependence of r_2 and r_3

To quantify the energy dependence of the decorrelation, we fit r_2 and r_3 with the function $e^{-2F_n\eta_a/y_{beam}}$, as shown in Figures 6.4 and 6.5. From these fits, we extract the slope parameters, F_2 and F_3, and plot them as a function of the center-of-mass energy in Figure 6.6. Our

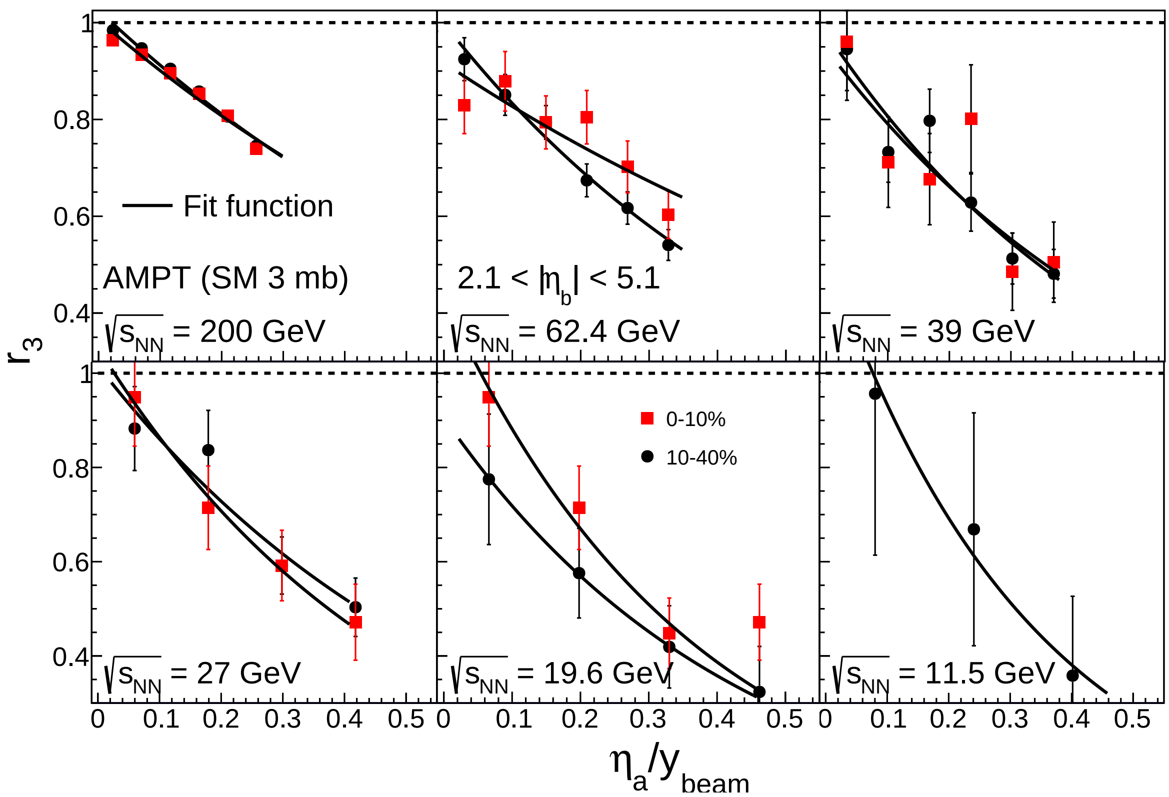

Figure 6.5: r_3 is plotted as a function of η_a/y_{beam} for Au+Au collisions in two centrality classes, 0-10% and 10-40% at six energies ranging from 11.5 to 200 GeV. The black solid line represents the fitting function: $e^{-2F_3\eta/y_{beam}}$. The vertical lines on the points represent the statistical uncertainty.

findings show that F_3 consistently exceeds F_2 across all energies. In the 10-40% centrality range, the average ratio F_3/F_2 is 5.2±0.3. Both r_2 and r_3 increases with increasing collision energy indicating larger decorrelation at lower collision.

6.6 Parton cross section dependence of r_2 and r_3

In AMPT model, the effective shear viscosity to entropy density (η_s/s) is estimated by the following equation [171].

$$\eta_s/s \approx \frac{3\pi}{40\alpha^2}\frac{1}{(9+\frac{\mu^2}{T^2})\ln(\frac{18+\mu^2/T^2}{\mu^2/T^2})-18} \tag{6.4}$$

Where α represent the coupling constant of the strong interaction, μ the Debye screening mass, and T the initial temperature of the quark-gluon plasma (QGP) created in a heavy-ion collision. The temperature T is estimated from the average energy density of mid-rapidity

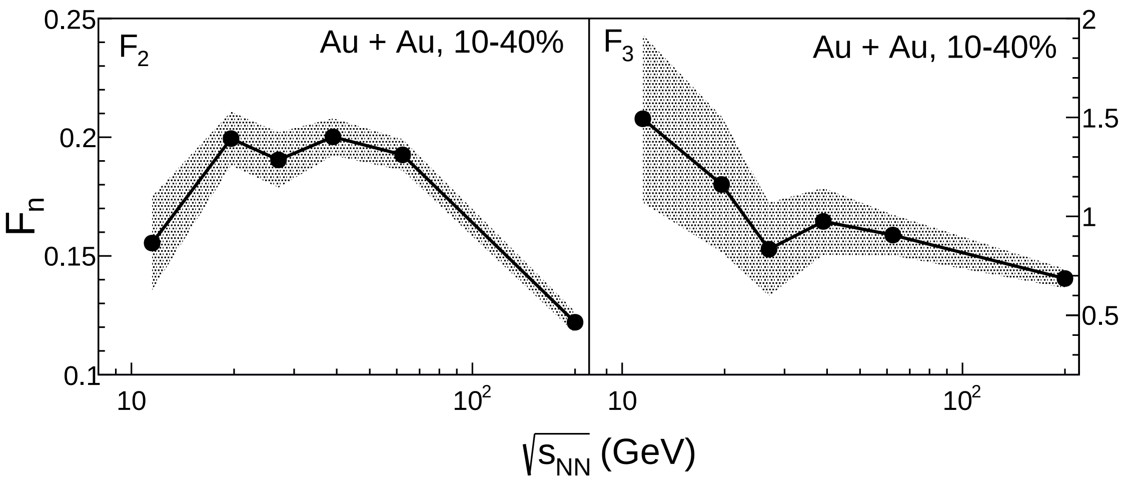

Figure 6.6: Left panel shows F_2 as a function of $\sqrt{s_{NN}}$ in 10-40% centrality events. The right panel shows the same for F_3. The shaded band represents the statistical uncertainty in the data.

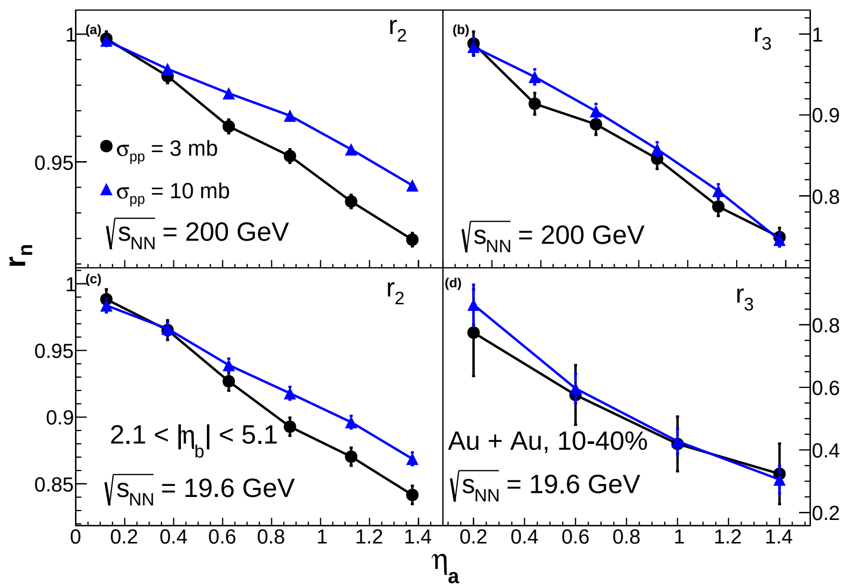

Figure 6.7: Panel (a) and (b) show r_2 and r_3 as a function of η at $\sqrt{s_{NN}}$ = 200 GeV. with parton-parton cross section 3 mb and 10 mb. Panel (c) and (d) show the same at $\sqrt{s_{NN}}$ = 19.6 GeV with parton-parton cross section 3 mb, and 10 mb.

partons at their typical formation time, with values of approximately 468 MeV at the LHC and 378 MeV at the top RHIC energy [171]. At $\sqrt{s_{NN}}$ = 19.6 GeV, the QGP medium temperature is assumed to be 278 MeV, following recent STAR measurements of dilepton production at finite baryon chemical potential [172]. By adjusting α and μ, we can control the shear viscosity to entropy density ratio (η_s/s) and the parton-parton cross section of the medium, as given in Eq. 6.3. Table 6.1 summarizes the variations in α and μ used to obtain different values of σ_{pp} and η_s/s. Notably, as the cross section σ_{pp} increases, η_s/s decreases.

The dependence of the parton-parton cross section on the observables r_2 and r_3 at $\sqrt{s_{NN}}$ = 19.6 and 200 GeV is illustrated in Fig.6.7. For a 3 mb cross section, r_2 is found to be greater compared to the 10 mb case. But r_3 is found to be independent of parton-parton cross section. Therefore, studying flow decorrelation could be a potential observable to constrain the η_s/s of the medium.

Table 6.1: Values of σ_{pp} and η_s/s for different values of α and μ in Au+Au collisions at $\sqrt{s_{NN}}$ = 200 and 19.6 GeV.

α	μ (fm^1)	σ_{pp} (mb)	η_s/s (200 GeV)	η_s/s (19.6 GeV)
0.33	2.256	3	0.229	0.355
0.47	1.8	10	0.086	0.126

6.7 Contribution from flow angle and flow magnitude decorrelation

To explore the factors contributing to flow decorrelation, we separately analyze the effects of flow magnitude and flow angle. The flow magnitude decorrelation is quantified by Equation 6.5, where both $v_n(\eta_a)$ and $v_n(-\eta_a)$ are obtained using the same event plane, determined within the pseudorapidity range $-0.5 < \eta < 0.5$. Similarly, flow angle decorrelation is evaluated using Equation 6.6. Figures 6.8 and 6.9 display the values of r_n^v and r_n^ψ alongside the total decorrelation r_n. The results indicate that the primary contribution to longitudinal flow decorrelation comes from flow angle decorrelation, which closely approximates the total decorrelation r_n. In contrast, the contribution from flow magnitude decorrelation is negligible. This pattern remains consistent across all energies from 11.5 to 200 GeV.

$$r_n^v = \frac{\langle v_n(-\eta_a) v_n(\eta_b)\rangle}{\langle v_n(\eta_a) v_n(\eta_b)\rangle}. \tag{6.5}$$

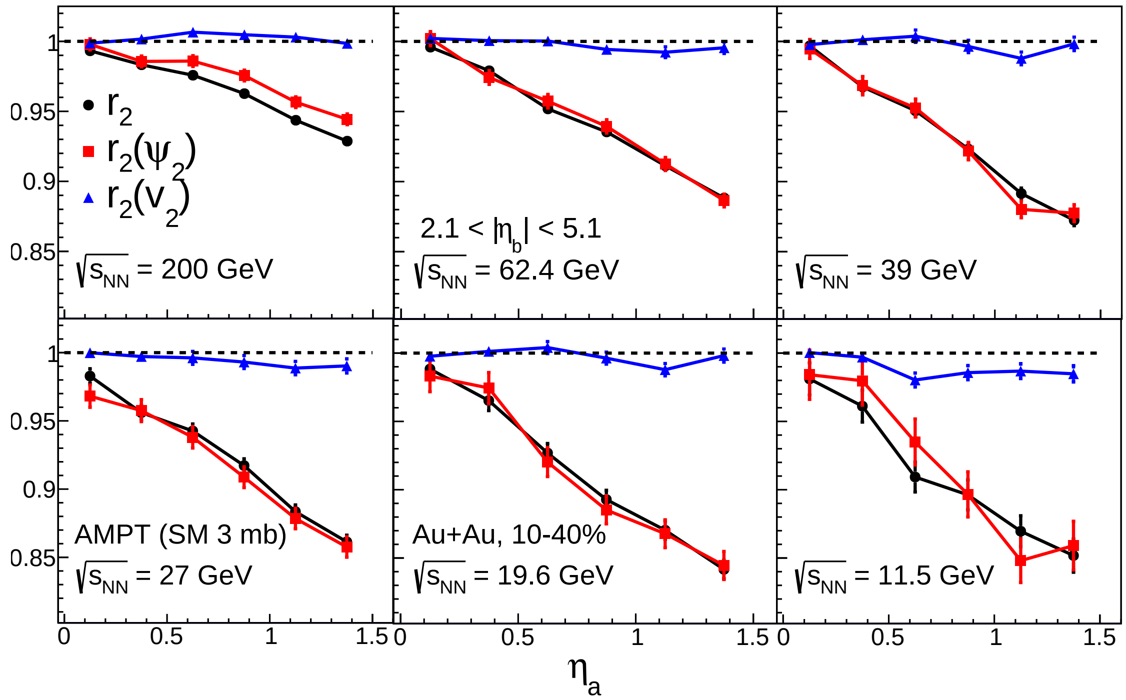

Figure 6.8: The flow magnitude decorrelation (r_2^v), flow angle decorrelation (r_2^{ψ}) and the total decorrelation (r_2) is plotted as a function of η_a for 10-40% centrality in Au+Au collisions at 11.5 to 200 GeV.

$$r_n^{\psi} = \frac{\langle \cos n(\Psi_n(-\eta_a) - \Psi_n(\eta_b)) \rangle}{\langle \cos n(\Psi_n(\eta_a) - \Psi_n(\eta_b)) \rangle}. \tag{6.6}$$

6.8 Summary

In summary, we have presented the measurement of longitudinal flow decorrelation parameters, r_2 and r_3, in Au+Au collisions at RHIC BES energies, ranging from $\sqrt{s_{NN}}$ = 11.5 to 200 GeV using the AMPT model. The decorrelation at the lower collision energy regimes are found to be larger compared to top RHIC energy. We observed that the second order factorization ratio, r_2 is sensitive to the effective η/s whereas r_3 shows weak sensitivity to η/s therefore, measuring both r_2 and r_3 can put constraint on the η/s of the produced medium.

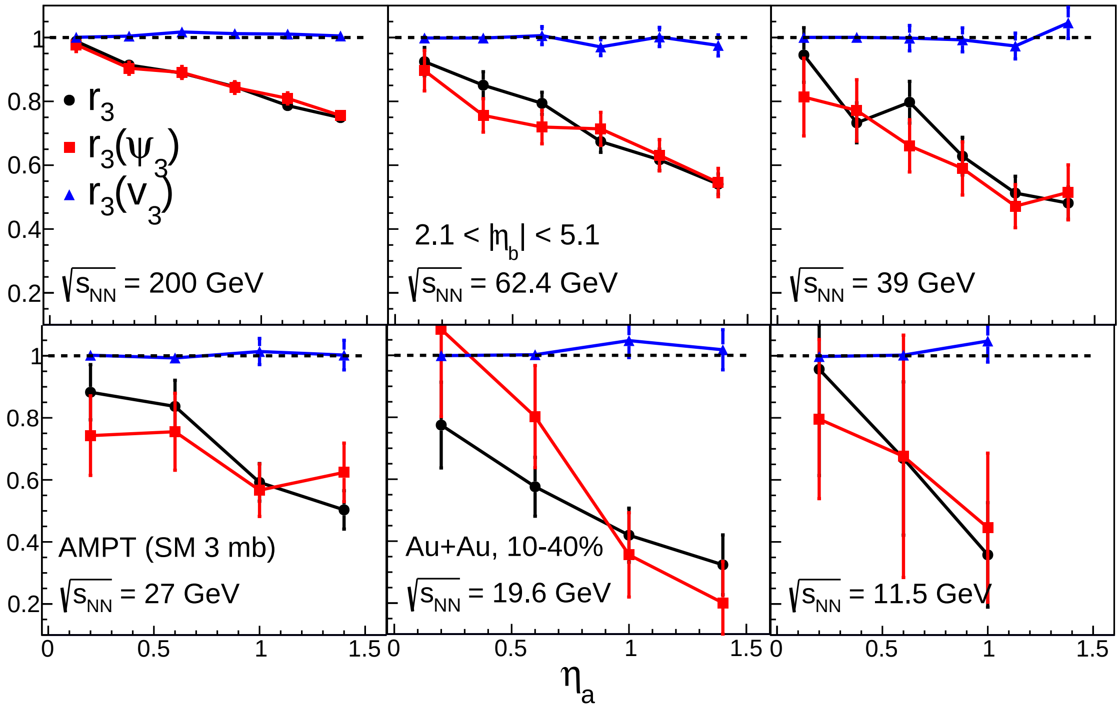

Figure 6.9: The flow magnitude decorrelation (r_3^v), flow angle decorrelation (r_3^ψ) and the total decorrelation (r_3) is plotted as a function of η_a for 10-40% centrality in Au+Au collisions at 11.5 to 200 GeV.

CHAPTER 7

Summary and outlook

7.1 Summary

The main objective of this thesis was to explore the phase diagram in the context of partonic collectivity by measuring v_2 and v_3 of identified hadrons in Au+Au collisions at $\sqrt{s_{NN}}$ = 7.7–54.4 GeV. This measurement aims to provide insights into the nature of the medium formed in lower collision energy systems and to investigate how the medium at lower collision energies differs from that at the top RHIC energy.

In Chapter 3, we present the measurement of v_2 and v_3 for strange and multi-strange hadrons in Au+Au collisions at $\sqrt{s_{NN}}$ = 54.4 GeV. Our observations show that the NCQ scaling at this energy holds within 10%, indicating the presence of partonic collectivity and supports quark coalescence model of hadronization. Furthermore, the hydrodynamics-motivated ratio, $v_3/v_2^{3/2}$, suggests the formation of a strongly interacting, fluid-like medium at this energy.

In Chapter 4, we delve further into lower collision energies, presenting the measurement of v_2 and v_3 for identified hadrons in Au+Au collisions at $\sqrt{s_{NN}}$ = 7.7, 9.2, 11.5, 14.6, and 19.6 GeV. These measurements utilize high-statistics data from the BES-II program, benefiting from improved detector conditions and enhanced acceptance. The observed baryon-meson splitting and NCQ scaling at all these energies indicate the presence of a partonic medium exhibiting collective flow. Additionally, the observed particle-to-antiparticle splitting, which increases with decreasing collision energy, suggests that the finite baryon chemical potential at these lower energies plays a significant role. Further theoretical and phenomenological studies are needed to understand this v_n difference between particles and antiparticles. Our measurement with model predication will play an important role in constraining temperature dependence η/s.

In Chapter 5, we found a new empirical scaling in flow coefficients when plotted as a function of transverse kinetic energy of quarks, calculated using their bare mass. This study needs further theoretical investigation for better understanding.

In Chapter 6, we have presented the measurement of the longitudinal decorrelation using AMPT model which is important to understand the longitudinal dynamics in heavy-ion collision and could be a sensitive observable for constraining η/s. This model calculation can be compared to the upcoming experimental data from STAR collaboration for better understanding of longitudinal decorrelation in heavy-ion collisions.

7.2 Outlook

To investigate the complete disappearance of partonic collectivity, we can explore even lower collision energies. The STAR experiment has completed data collection for fixed-target experiments at $\sqrt{s_{NN}}$ = 3.0–7.2 GeV. This fixed-target data will provide access to the high baryon density region of the QCD phase diagram. Measuring anisotropic flow coefficients at these low collision energies will offer valuable insights into the properties of the medium created under such conditions. Also upcoming experiments like Compressed Baryonic Matter (CBM) experiment at Facility for Antiproton and Ion Research (FAIR) could further probe into the properties of the medium produced at very high baryon density region of the phase diagram.

APPENDIX A

Appendix A - List of bad runs in BES-II

Bad runs at $\sqrt{s_{NN}}$ = 19.6 GeV

20057007, 20057025, 20057026, 20057050, 20058001, 20058002, 20058003, 20058004, 20058005, 20060012, 20060022, 20060025, 20060060, 20060061, 20060062, 20062010, 20062011, 20062012, 20062036, 20063011, 20063034, 20063035, 20063036, 20063039, 20064008, 20064009, 20064011, 20064012, 20064040, 20065018, 20067014, 20067023, 20067024, 20067029, 20067030, 20067045, 20067046, 20069030, 20069032, 20069054, 20070042, 20070043, 20070044, 20070047, 20071001, 20071004, 20071005, 20071006, 20071027, 20071037, 20072034, 20072035, 20072036, 20072039, 20072041, 20072045, 20072047, 20073071, 20073072, 20073076, 20074001, 20074003, 20074004, 20074005, 20074007, 20074008, 20074009, 20074012, 20074014, 20074017, 20074018, 20074020, 20074021, 20074026, 20074027, 20074029, 20074032, 20074033, 20074034, 20074044, 20074045, 20075001, 20075002, 20075006, 20075007, 20075009, 20075011, 20075013, 20081002, 20081014, 20082060, 20082065, 20083024, 20086012, 20087007, 20089008, 20090024, 20091011, 20092054

Bad runs at $\sqrt{s_{NN}}$ = 14.6 GeV

20094053, 20094054, 20096025, 20099032, 20099033, 20099034, 20099044, 20099048, 20099052, 20101002, 20102001, 20102002, 20102003, 20102013, 20102014, 20102035, 20102036, 20102053, 20103002, 20103003, 20103005, 20103006, 20104016, 20108010, 20108012, 20108013, 20110001, 20110022, 20111020, 20111047, 20113055, 20113063, 20113066, 20113067, 20113068, 20113069, 20113070, 20113081, 20113088, 20114025, 20114026, 20114031, 20117013, 20117055, 20119005, 20119053, 20120047, 20123015, 20123016, 20123018, 20123038, 20124001, 20124037, 20124051, 20124058, 20124059, 20124060, 20124062, 20124064, 20124066, 20124068, 20124070, 20124072, 20124074, 20124077, 20124079, 20125003, 20125005, 20125007, 20125008, 20125010, 20125011, 20125013, 20125015, 20125016, 20125018, 20125020, 20125023, 20125025, 20125027, 20125028, 20125029, 20125030, 20125031, 20125033, 20125034, 20125035, 20125036, 20125038, 20125039, 20125041, 20125044, 20125047, 20125048, 20125049, 20125050, 20125053, 20125055, 20125057, 20125058, 20125059, 20126004, 20126005, 20126006, 20126007, 20126008, 20126010, 20126013, 20126014, 20126015, 20126017, 20126019, 20126021, 20126025, 20126027, 20126029, 20127006, 20127007, 20127010, 20127012, 20128043, 20131015, 20131028, 20132002, 20132012, 20134024, 20136001, 20136003, 20136006, 20136008, 20137005, 20137011, 20137013, 20137015, 20137017, 20138002, 20138015, 20138039, 20139033, 20141002, 20143007, 20144038, 20147022, 20148007, 20148031, 20150004, 20151003, 20151006, 20151012, 20152026, 20152028, 20152029, 20152030

Bad runs at $\sqrt{s_{NN}}$ = 11.5 GeV

20344004, 20344006, 20344007, 20344008, 20344009, 20344013, 20344014, 20344015, 20347037, 20347035, 20347036, 20347038, 20347039, 20348023, 20351062, 20351067, 20354051, 20354053, 20355004, 20356005, 20356007, 20356020, 20356022, 20356023, 20357022, 20361014, 20361017, 20363010, 21003011, 21004021, 21005039, 21005040, 21005041, 21006008, 21006029, 21006031, 21007034, 21010036, 21011001, 21011004, 21012034, 21012035, 21013016, 21014027, 21015031, 21015029, 21017048, 21019016, 21019020, 21019069, 21019073, 21021009, 21021010, 21021011, 21025042, 21041025, 21041026, 21050043, 21045044, 21046005, 21046045, 21046046, 21046047, 21046048, 21048061, 21050044, 21050045, 21050046, 21050047, 21050048, 21050049, 21050050, 21050052, 21050053, 21050054, 21050055, 21050056, 21050057, 21050058, 21052039, 21053060, 21053061, 21053062, 21053063, 21053064

Bad runs at $\sqrt{s_{NN}}$ = 9.2 GeV

21036025, 21036028, 21036032, 21037025, 21037030, 21037031, 21037047, 21037052, 21038020, 21038021, 21038029, 21038031, 21038033, 21038035, 21038039, 21038042, 21038046, 21039025, 21039029, 21040007, 21056032, 21058027, 21058028, 21058029, 21058030, 21060015, 21060016, 21060021, 21060026, 21062015, 21062020, 21062021, 21064004, 21064024, 21064041, 21064047, 21065026, 21065042, 21066027, 21066028, 21067020, 21068024, 21068027, 21068030, 21069005, 21069006, 21069014, 21069017, 21069035, 21069038, 21069040, 21069042, 21069043, 21070011, 21071002, 21072016, 21073007, 21073008, 21073032, 21076004, 21076029, 21077024, 21078001, 21078002, 21078006, 21078020, 21080027, 21169035, 21169036, 21169037, 21169038, 21169039, 21170018, 21171007, 21171031, 21171032, 21171033, 21172032, 21174049, 21174050, 21175009, 21176020, 21176024, 21176029, 21177019, 21177020, 21177021, 21177022, 21177032, 21178013, 21179001, 21179018, 21179020, 21179026, 21180008, 21180025, 21180027, 21181024, 21181025, 21181026, 21181033, 21182037, 21182038, 21182041, 21184025, 21184026, 21186026, 21186027, 21187032, 21188017, 21188027, 21189039, 21189040, 21190053, 21191008, 21192018, 21193009, 21193027, 21194002, 21196004, 21197005, 21198002, 21203001, 21203002, 21203003, 21203017, 21205002, 21205020, 21205023, 21206002, 21206005, 21206007, 21206008, 21208027, 21209009, 21210009, 21210046, 21211004, 21211009, 21213004, 21213005, 21213006, 21213013, 21213014, 21213016, 21213017, 21213018, 21213019, 21213020, 21217001, 21217010, 21217020, 21218001, 21218002, 21218003, 21218004, 21218005, 21218006, 21218007, 21218013, 21218014, 21218015, 21218016, 21218017, 21219007, 21219008, 21219009, 21219010, 21220015, 21222026, 21223030, 21225035, 21225040, 21225041, 21225042, 21225045, 21226003, 21227007, 21227008, 21227021, 21228020, 21229006, 21229041, 21233002, 21233010, 21235015, 21235033, 21235035, 21237014, 21237021, 21237022, 21237023, 21239010, 21241015, 21241016, 21242028, 21243007, 21243008, 21243033, 21243038, 21244023, 21244024, 21245003

At $\sqrt{s_{NN}}$ = 9.2 GeV, there are some run IDs with distorted azimuthal angle (ϕ) distributions as show in Fig. Those Run IDs are rejected from the analysis

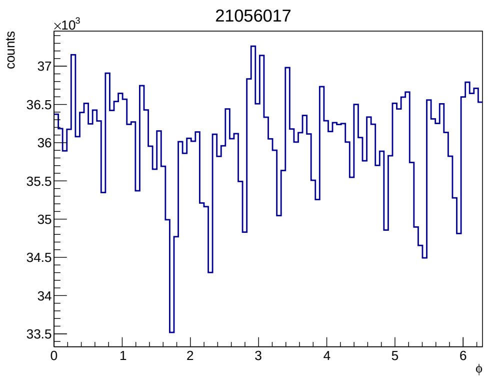

((a)) Distribution of ϕ in good run.

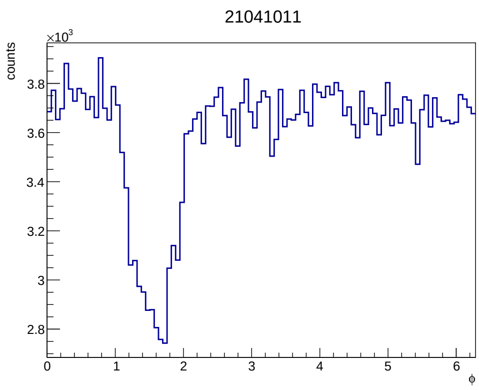

((b)) Distorted distribution of ϕ in some run IDs

There are 592 such run IDs in the $\sqrt{s_{NN}}$ = 9.2 GeV.

Bad runs at $\sqrt{s_{NN}}$ = 7.7 GeV

22031054 22033001 22035002 22038009 22039010 22039013 22039028 22042004 22043046 22043047 22044003 22044004 22044005 22046006 22046007 22046012 22047008 22048002 22048007 22048040 22048042 22049026 22049027 22049029 22050003 22050006 22050016 22050038 22050040 22050044 22050045 22051014 22052032 22052033 22052035 22052036 22052048 22053022 22054007 22054022 22054028 22054030 22054042 22055023 22057010 22058037 22059005 22061012 22061015 22062034 22062035 22062036 22063014 22064025 22064038 22065014 22065015 22067039 22068012 22068041 22069030 22069032 22069033 22069034 22069040 22070001 22070002 22070003 22070004 22070005 22070006 22070007 22070008 22070009 22070010 22070011 22070012 22070014 22070040 22070041 22071036

22074009 22074042 22076033 22076034 22077050 22078016 22078032 22079027 22084029 22084035 22085009 22085021 22086027 22087027 22088034 22091018 22091022 22091025 22093029 22094046 22095027 22096003 22096037 22097016 22097030 22098054 22099024 22099042 22100045 22101016 22101017 22101018 22101022 22102034 22103027 22103032 22104027 22105030 22106032 22108050 22109032 22110025 22111047 22112021 22113001 22113029 22114030 22115004 22115008 22115019 22115032 22116007 22116008 22116025 22116026 22116030 22117023 22118058

APPENDIX B

Appendix B - Derivation of the shift correction formula

In shift correction method our goal is to transform a variable Ψ_n having non-uniform distribution to another variable $\Psi_n^s = \Psi_n + \Delta\Psi_n$ which has a uniform distribution as illustrated in Fig. B.1.

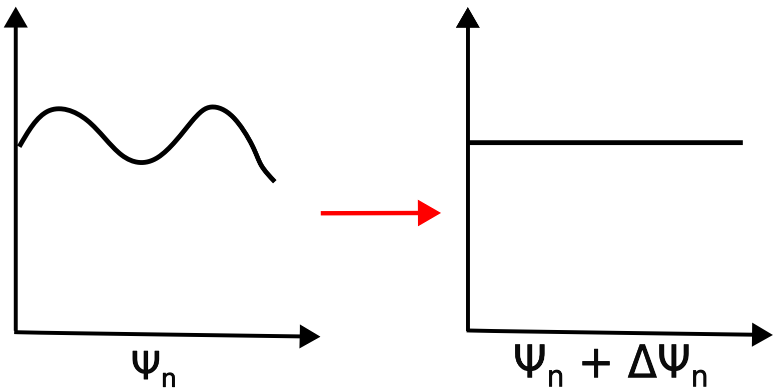

Figure B.1: Illustration of the shift correction method.

Here we treat Ψ_n as a random variable having some unknown distribution function which gets transformed into another random variable $\Psi_n + \Delta\Psi_n$ which has a uniform distribution function. From the properties of the transformation of the random variable we have

$$f(\Psi_n)d\Psi_n = g(\Psi_n + \Delta\Psi_n)d(\Psi_n + \Delta\Psi_n) \tag{B.1}$$

Simplifying Eq. B.1, we get

$$g(\Psi_n + \Delta\Psi_n) = f(\Psi_n) \times \frac{1}{1 + \frac{d(\Delta\Psi_n)}{d\Psi_n}} \tag{B.2}$$

The correction factor $\Delta\Psi_n$ can have any distribution function but it can be written in terms of sine and cosine series as follows

$$\Delta\Psi_n = \sum_n A_n \cos n\Psi_n + \sum_n B_n \sin n\Psi_n \tag{B.3}$$

Taking the derivative of $\Delta\Psi_n$ and substituting in Eq. B.2 we get,

$$\left(1 + \sum_n (-nA_n) \sin n\Psi_n + \sum_n B_n \cos n\Psi_n\right) g(\Psi_n + \Delta\Psi_n) = f(\Psi_n) \tag{B.4}$$

The R.H.S of Eq. B.4 has distribution of non-uniform Ψ_n which can be expanded in a Fourier series as follows.

$$\left(1 + \sum_n (-nA_n) \sin n\Psi_n + \sum_n B_n \cos n\Psi_n\right) g(\Psi_n + \Delta\Psi_n) = a_0 + \sum_n A_n^{'} \cos n\Psi_n + \sum_n B_n^{'} \sin n\Psi_n \tag{B.5}$$

Where a_0 is a constant, $a_0 = \int f(\Psi_n) d\Psi_n$ =1 (Since total probability =1). The factor $A_n^{'}$ and $B_n^{'}$ are given by

$$A_n^{'} = \int f(\Psi_n)(\cos n\Psi_n) d\Psi_n = \langle \cos n\Psi_n \rangle \tag{B.6}$$

$$B_n^{'} = \int f(\Psi_n)(\sin n\Psi_n) d\Psi_n = \langle \sin n\Psi_n \rangle \tag{B.7}$$

Now comparing coefficients of cosine and sine term on both sides of the Eq. B.5 we get,

$$A_n = \frac{-2}{n} \langle \sin n\Psi_n \rangle \tag{B.8}$$

$$B_n = \frac{2}{n} \langle \cos n\Psi_n \rangle \tag{B.9}$$

Now substuting Eq. B.8 and B.9 in Eq. B.3 we get,

$$\Delta\Psi_n = \sum_n \frac{-2}{n} \langle \sin n\Psi_n \rangle \cos n\Psi_n + \sum_n \frac{2}{n} \langle \cos n\Psi_n \rangle \sin n\Psi_n \tag{B.10}$$

Equation B.10 is the required shift correction factor.

APPENDIX C

Appendix C - Analysis plots

C.1 Analysis plots for π, K, and p

The 1D projection of $X(n\sigma_{\pi}, m^2)$ showing the peaks of π^+, K^+, and p in some of the p_T and in all $\phi - \Psi_n$ bins in Au+Au collisions at $\sqrt{s_{NN}}$ = 19.6 GeV are shown in Fig. C.1 - C.6. For π^-, K^-, and $\bar{p}$, the distribution also looks same(Not shown). Same distribution can also be obtained by projecting in various $\phi - \Psi_3$ bins while doing v_3 calculation.

The raw yield is calculated for each p_T and $\phi - \Psi_n$ bins. The raw yield distribution for π^+, π^-, K^+, and K^- as a function of $\phi - \Psi_n$ are shown in Fig. C.7 to Fig. C.14.

C.2 Analysis plot for multi-strange hadrons

For multi-strange hadrons invariant mass method and event plane method are used for measurement of v_2 and v_3. Figure C.15 to Fig. C.36 shows the intermediate analysis plots for K_S^0, Λ, $\bar{\Lambda}$, Ξ^-, $\bar{\Xi}^+$, ϕ, Ω^-, and $\bar{\Omega}^+$.

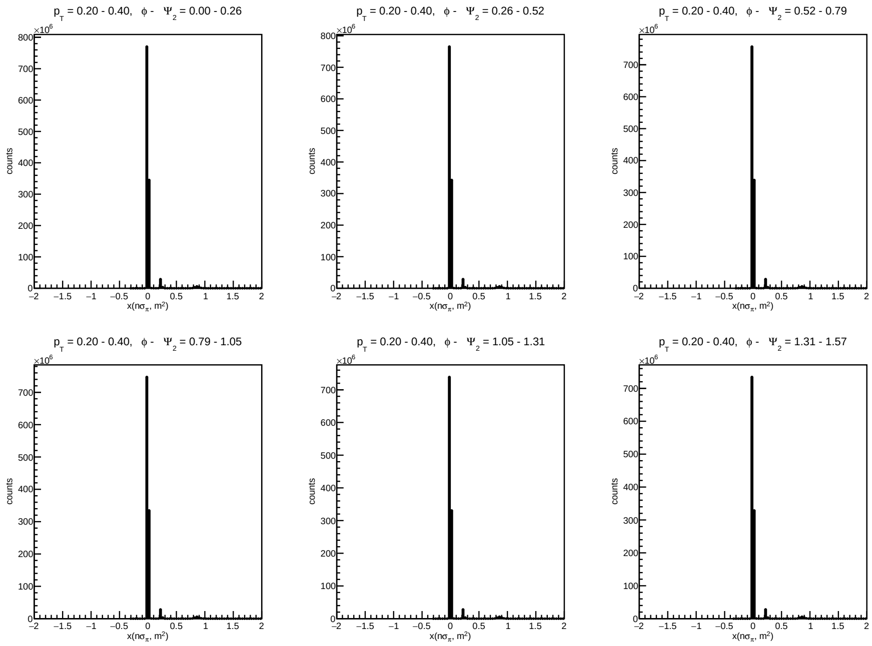

Figure C.1: 1D projection of $X(n\sigma_\pi, m^2)$ showing the peaks of π^+, K^+, and p in various $\phi - \Psi_2$ bins for p_T = 0.2-0.4 GeV/c in Au+Au collisions at $\sqrt{s_{NN}}$ = 19.6 GeV/c in 10-40% centrality.

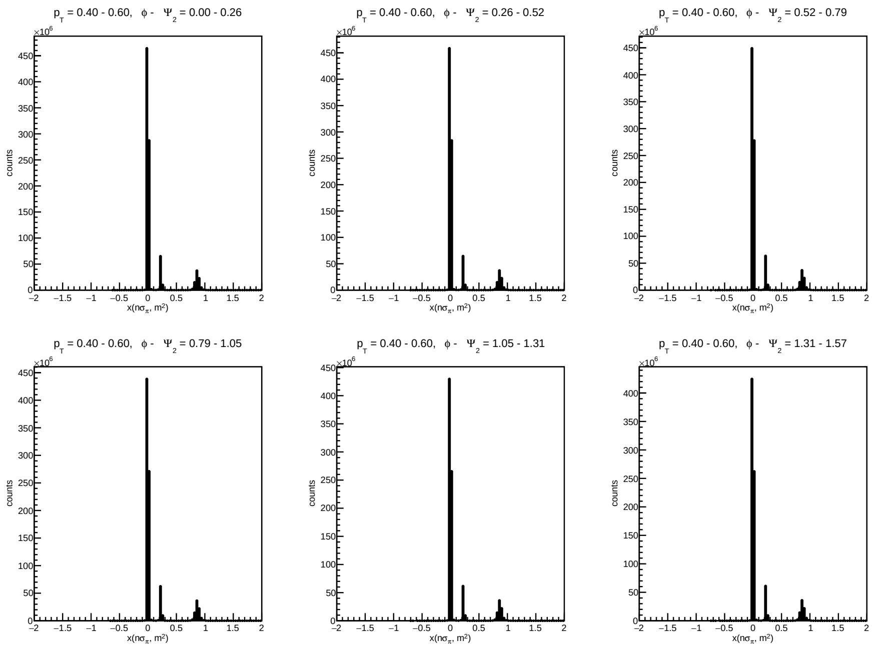

Figure C.2: 1D projection of $X(n\sigma_\pi, m^2)$ showing the peaks of π^+, K^+, and p in various $\phi - \Psi_2$ bins for p_T = 0.4-0.6 GeV/c in Au+Au collisions at $\sqrt{s_{NN}}$ = 19.6 GeV/c in 10-40% centrality.

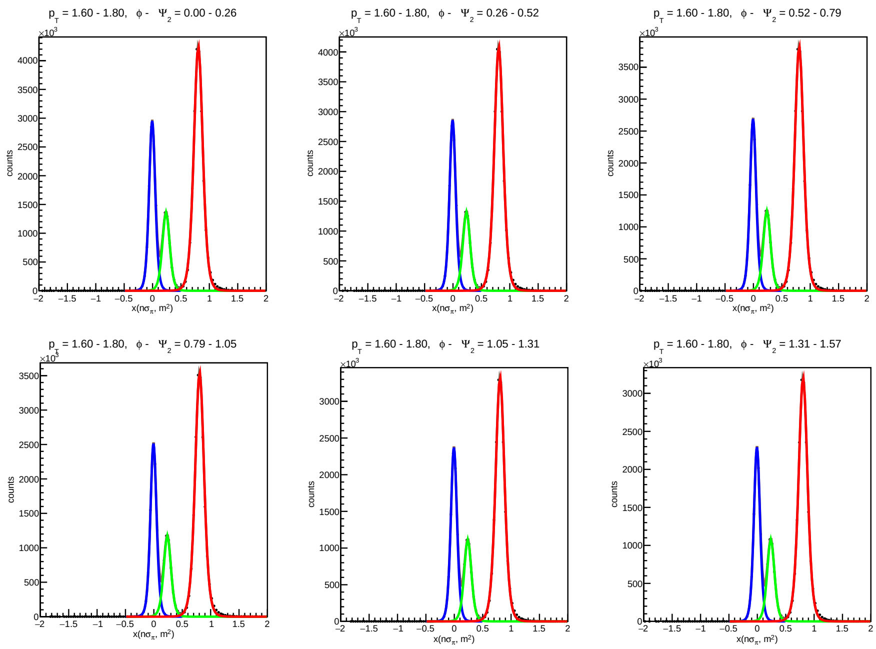

Figure C.3: 1D projection of $X(n\sigma_\pi, m^2)$ showing the peaks of π^+, K^+, and p in various $\phi - \Psi_2$ bins for p_T = 1.6-1.8 GeV/c in Au+Au collisions at $\sqrt{s_{NN}}$ = 19.6 GeV/c. The solid lines represent the student-t function for each peak in 10-40% centrality.

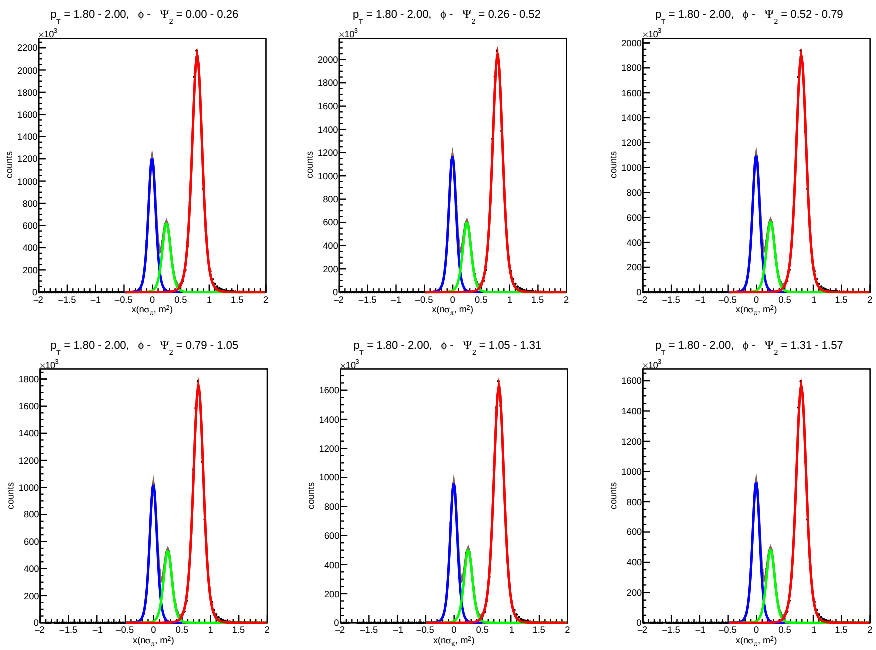

Figure C.4: 1D projection of $X(n\sigma_\pi, m^2)$ showing the peaks of π^+, K^+, and p in various $\phi - \Psi_2$ bins for p_T = 1.8-2.0 GeV/c in Au+Au collisions at $\sqrt{s_{NN}}$ = 19.6 GeV/c in 10-40% centrality.. The solid lines represent the student-t function for each peak.

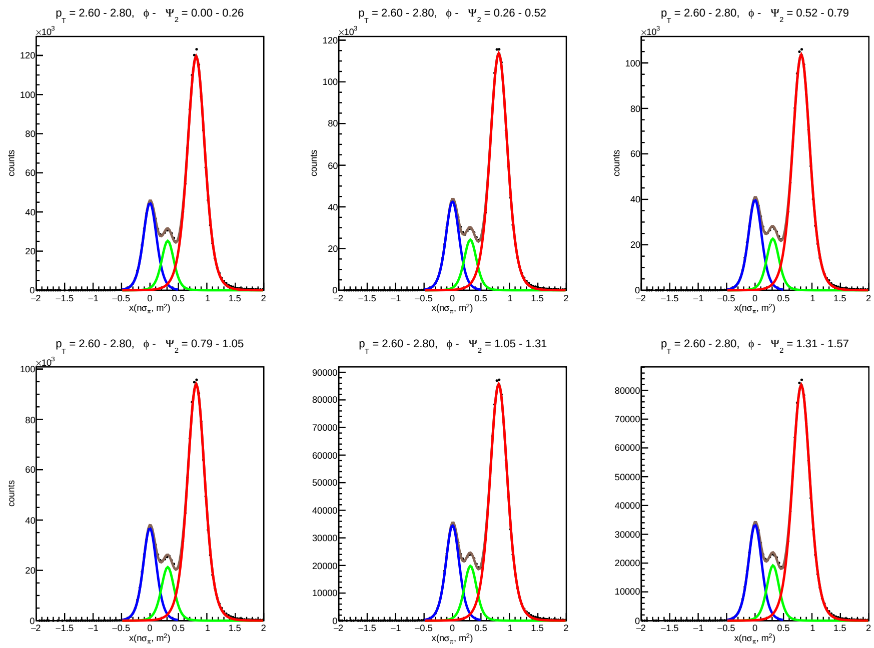

Figure C.5: 1D projection of $X(n\sigma_\pi, m^2)$ showing the peaks of π^+, K^+, and p in various $\phi - \Psi_2$ bins for p_T = 2.6-2.8 GeV/c in Au+Au collisions at $\sqrt{s_{NN}}$ = 19.6 GeV/c in 10-40% centrality.. The solid lines represent the student-t function for each peak.

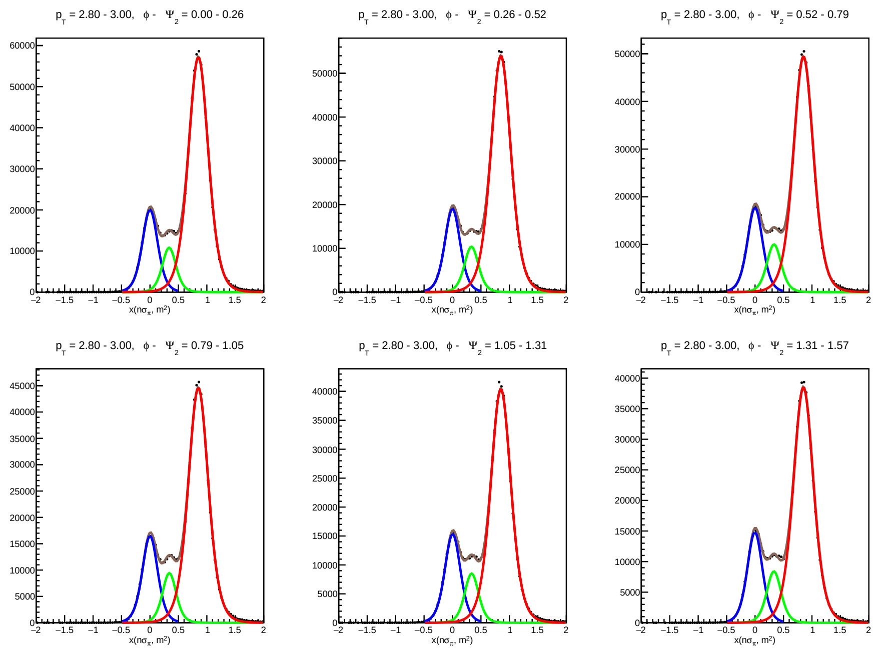

Figure C.6: 1D projection of $X(n\sigma_\pi, m^2)$ showing the peaks of π^+, K^+, and p in various $\phi - \Psi_2$ bins for p_T = 2.8-3.0 GeV/c in Au+Au collisions at $\sqrt{s_{NN}}$ = 19.6 GeV/c in 10-40% centrality.. The solid lines represent the student-t function for each peak.

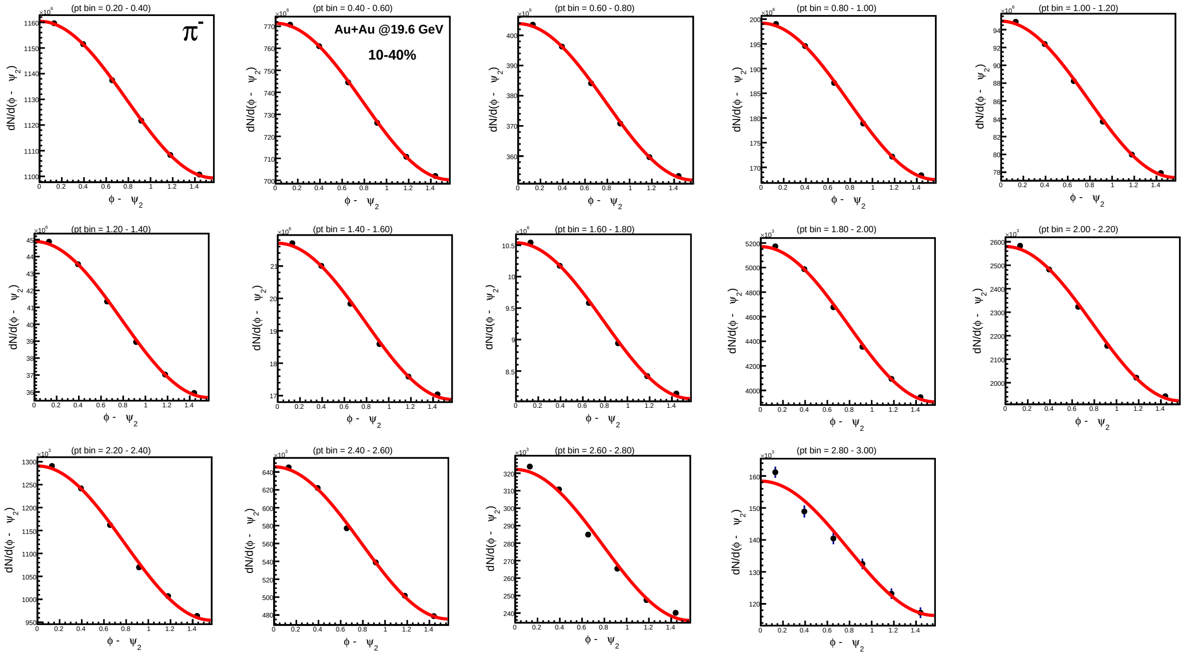

Figure C.7: The raw yield of π^- is plotted as a function of $\phi - \Psi_2$ in Au+Au collisions at $\sqrt{s_{NN}}$ = 19.6 GeV in 10-40% centrality. The red line represents the fitting function with Eq. 3.15 to calculate v_2.

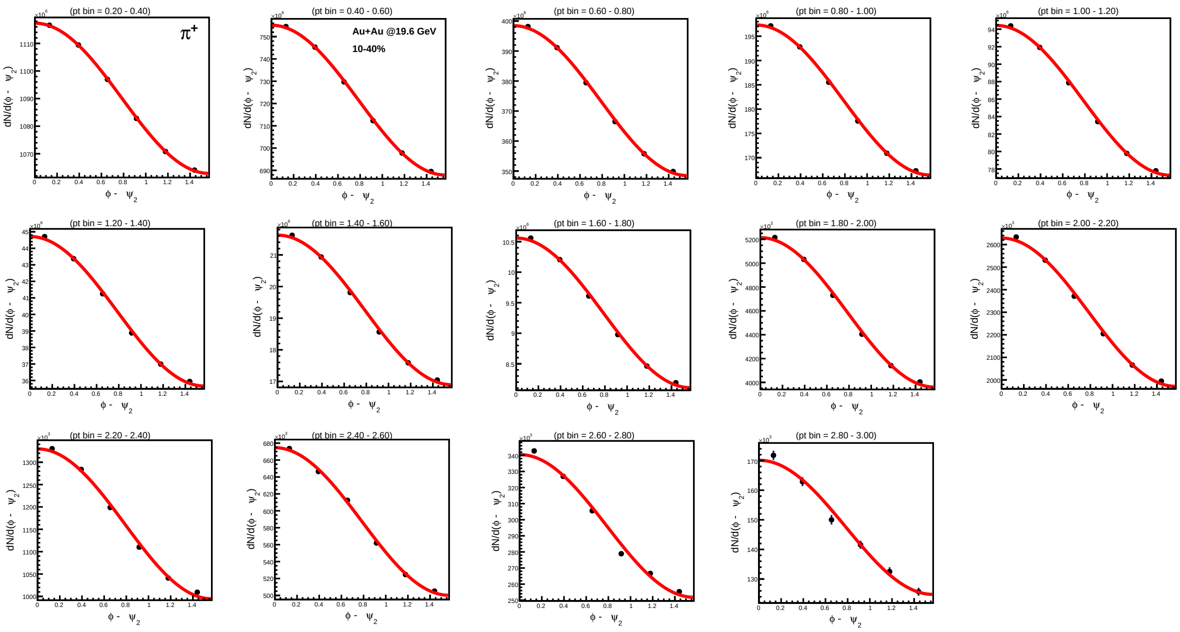

Figure C.8: The raw yield of π^+ is plotted as a function of $\phi - \Psi_2$ in Au+Au collisions at $\sqrt{s_{NN}}$ = 19.6 GeV in 10-40% centrality. The red line represents the fitting function with Eq. 3.15 to calculate v_2.

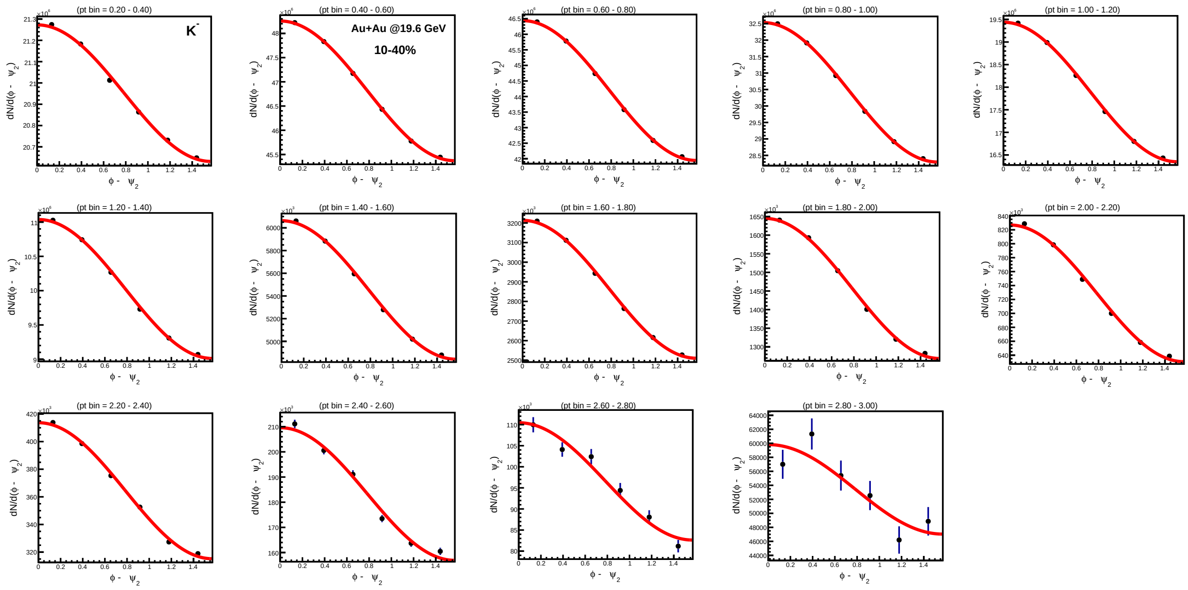

Figure C.9: The raw yield of K^- is plotted as a function of $\phi - \Psi_2$ in Au+Au collisions at $\sqrt{s_{NN}}$ = 19.6 GeV in 10-40% centrality. The red line represents the fitting function with Eq. 3.15 to calculate v_2.

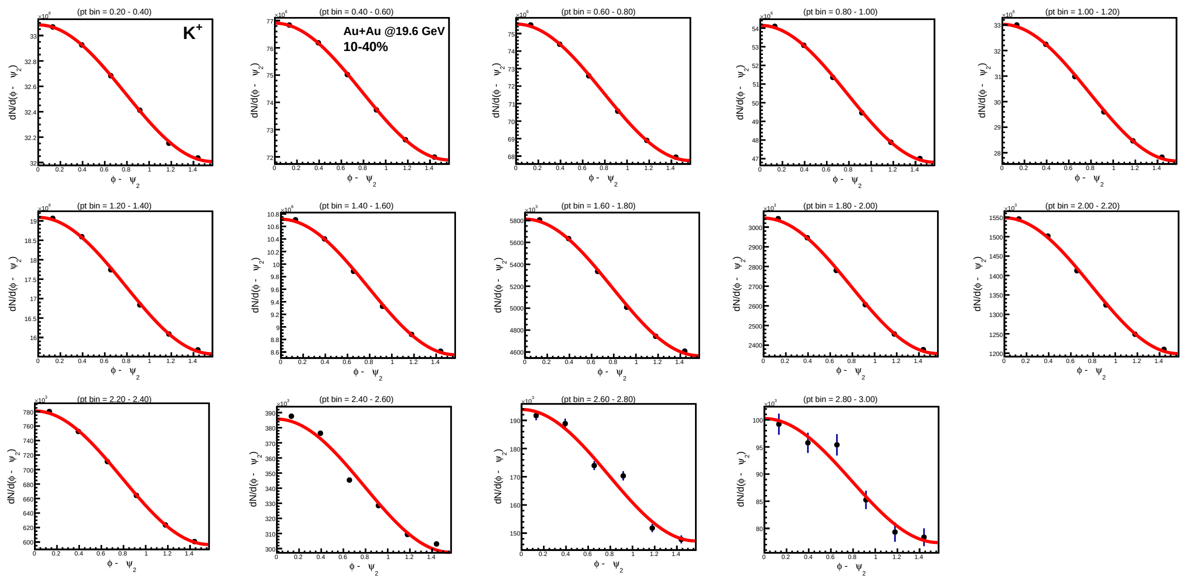

Figure C.10: The raw yield of K^+ is plotted as a function of $\phi - \Psi_2$ in Au+Au collisions at $\sqrt{s_{NN}}$ = 19.6 GeV in 10-40% centrality. The red line represents the fitting function with Eq. 3.15 to calculate v_2.

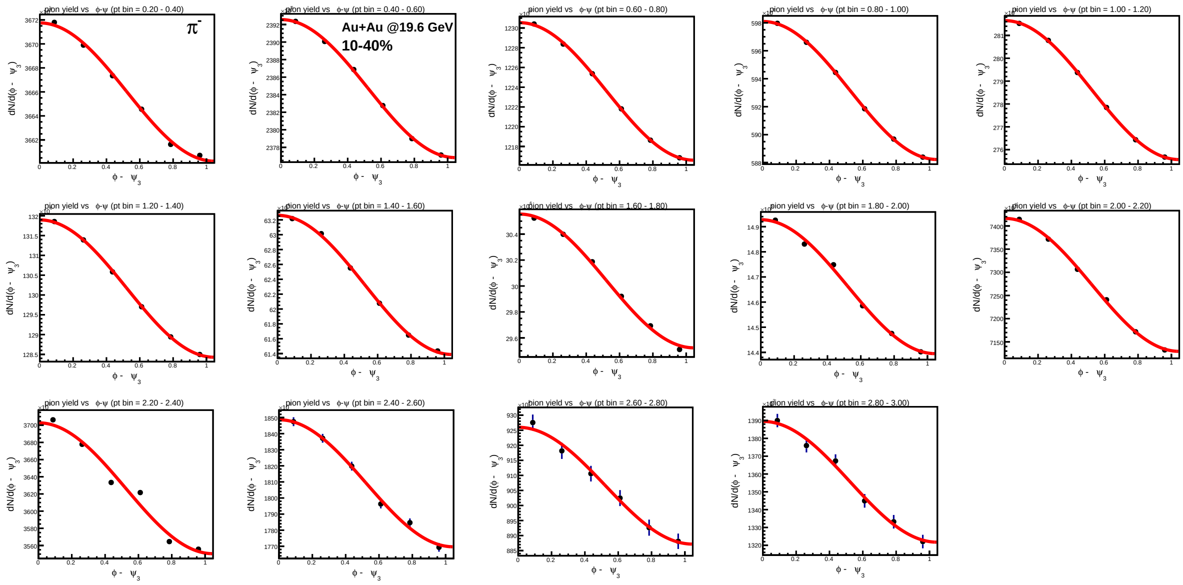

Figure C.11: The raw yield of π^- is plotted as a function of $\phi - \Psi_3$ in Au+Au collisions at $\sqrt{s_{NN}}$ = 19.6 GeV in 10-40% centrality. The red line represents the fitting function with Eq. 3.15 to calculate v_2.

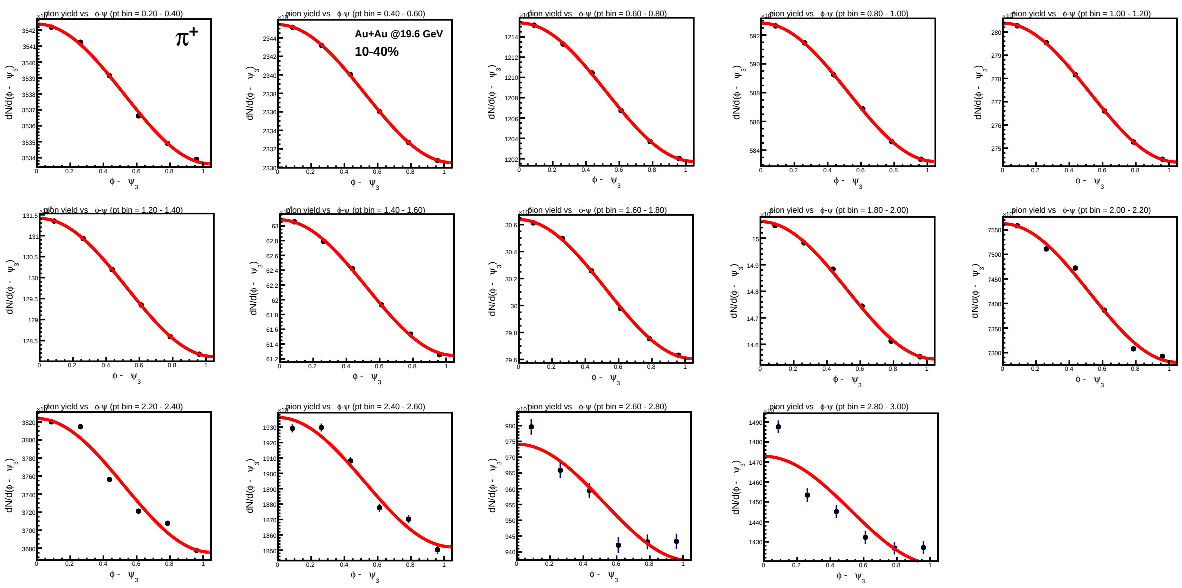

Figure C.12: The raw yield of π^+ is plotted as a function of $\phi - \Psi_3$ in Au+Au collisions at $\sqrt{s_{NN}}$ = 19.6 GeV in 10-40% centrality. The red line represents the fitting function with Eq. 3.15 to calculate v_3.

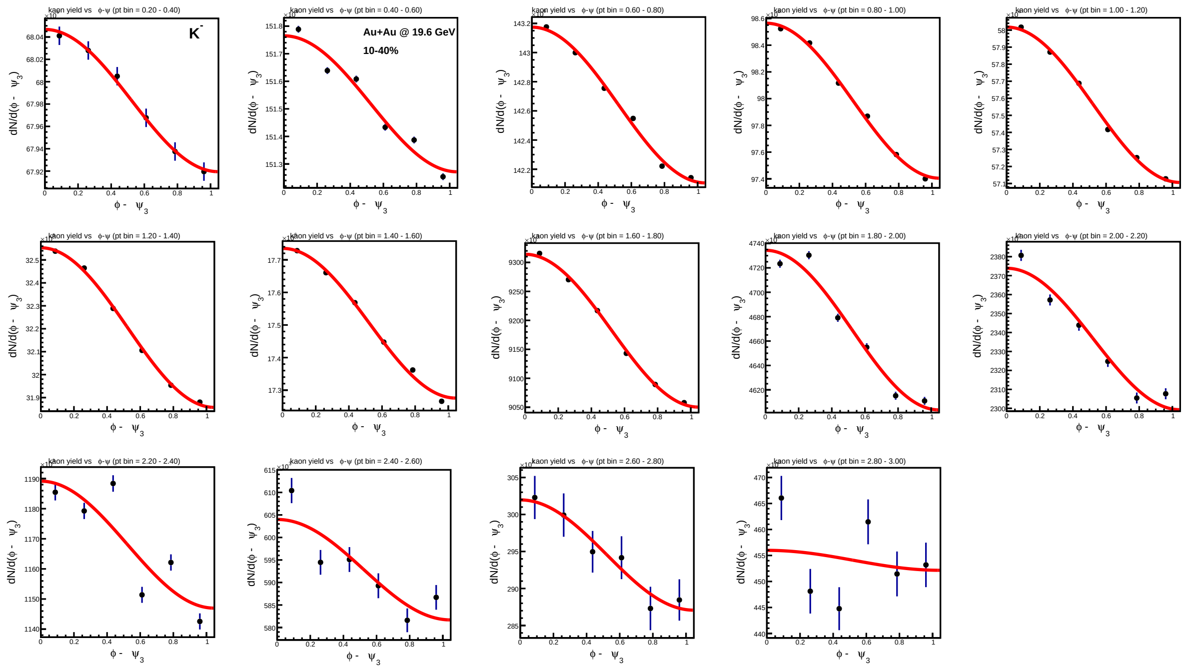

Figure C.13: The raw yield of K^- is plotted as a function of $\phi - \Psi_3$ in Au+Au collisions at $\sqrt{s_{NN}}$ = 19.6 GeV in 10-40% centrality. The red line represents the fitting function with Eq. 3.15 to calculate v_2. The red line represents the fitting function with Eq. 3.15 to calculate v_3.

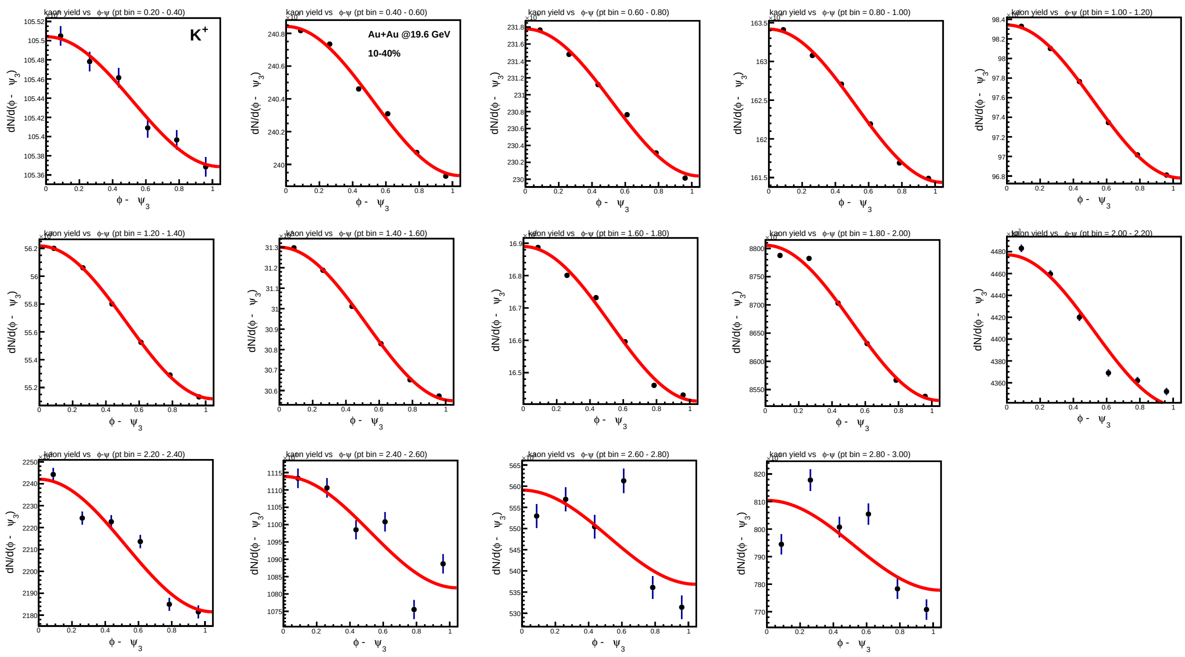

Figure C.14: The raw yield of K^+ is plotted as a function of $\phi - \Psi_3$ in Au+Au collisions at $\sqrt{s_{NN}}$ = 19.6 GeV in 10-40% centrality. The red line represents the fitting function with Eq. 3.15 to calculate v_3.

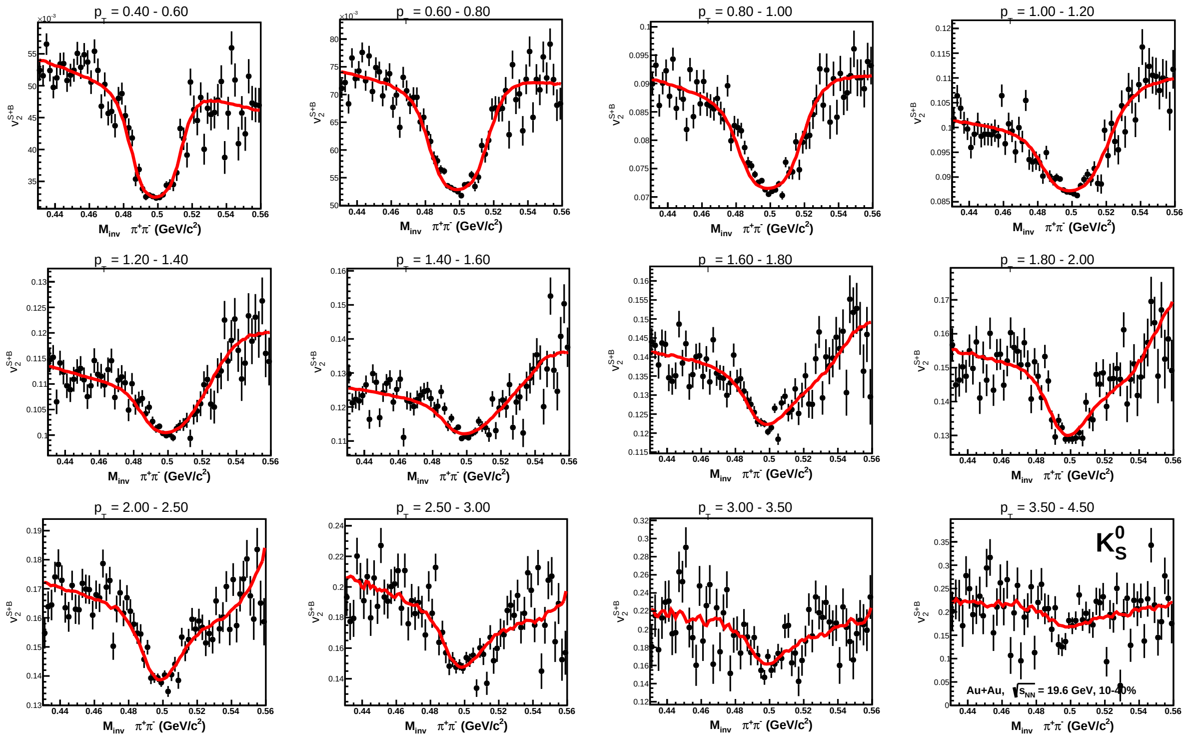

Figure C.15: v_2^{S+B} is plotted as a function of invariant mass of decay daughters of K_S^0 in Au+Au collisions at $\sqrt{s_{NN}}$ = 19.6 GeV in 10-40% centrality. The distribution is fitted with Eq. 3.13 to obtain v_2 of the signal.

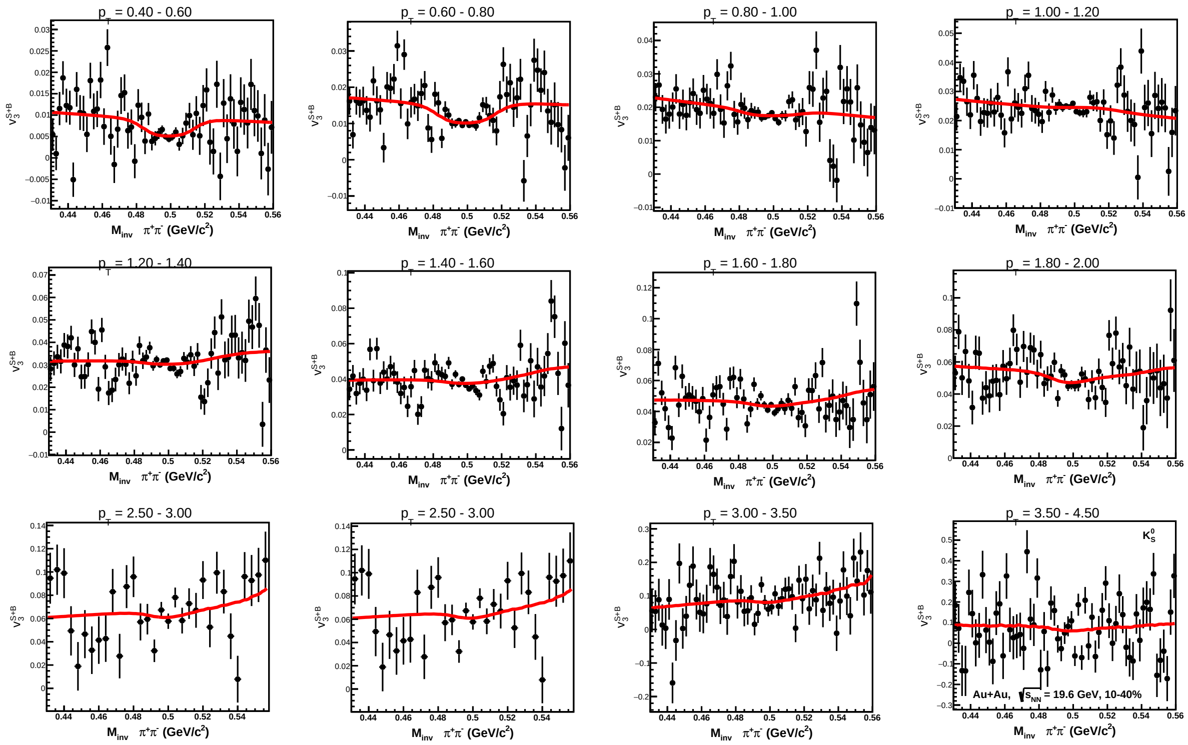

Figure C.16: v_3^{S+B} is plotted as a function of invariant mass of decay daughters of K_S^0 in Au+Au collisions at $\sqrt{s_{NN}}$ = 19.6 GeV in 10-40% centrality. The distribution is fitted with Eq. 3.13 to obtain v_3 of the signal.

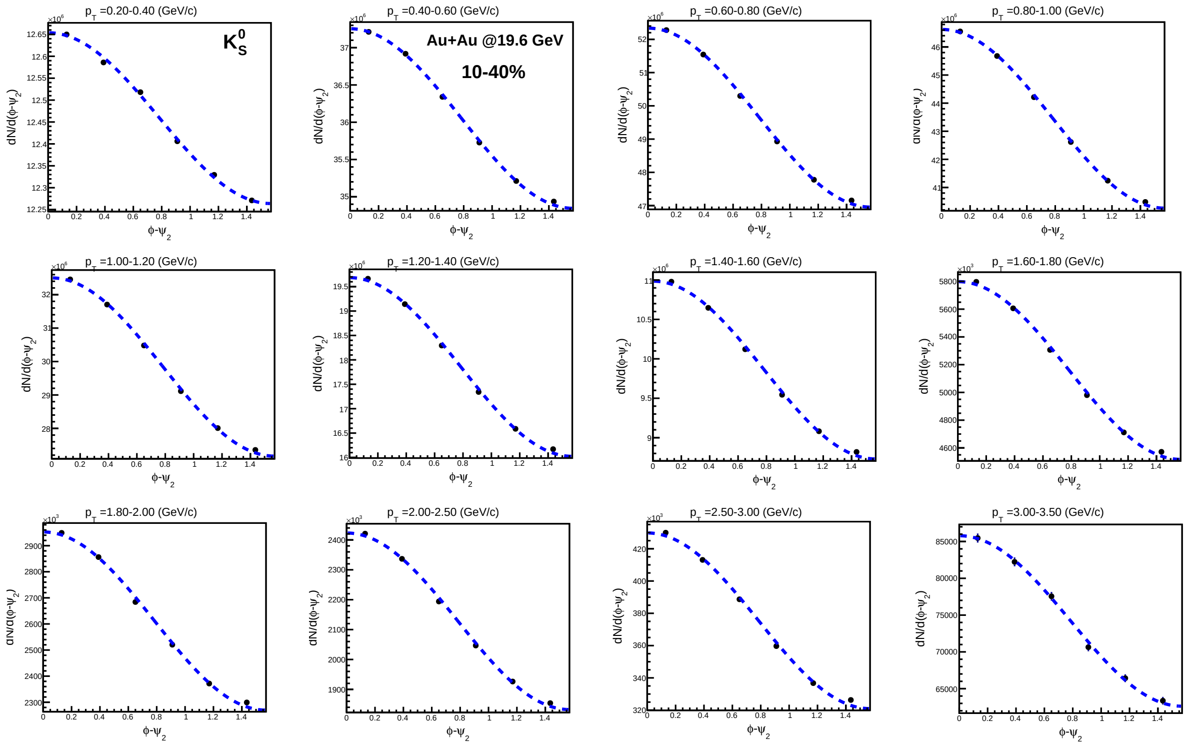

Figure C.17: Distribution of the raw yield of K_S^0 in $\phi - \Psi_2$ bin are plotted in Au+Au collisions at $\sqrt{s_{NN}}$ = 19.6 GeV in 10-40% centrality. The distribution is fitted with Eq. 3.15 to get v_2 of K_S^0.

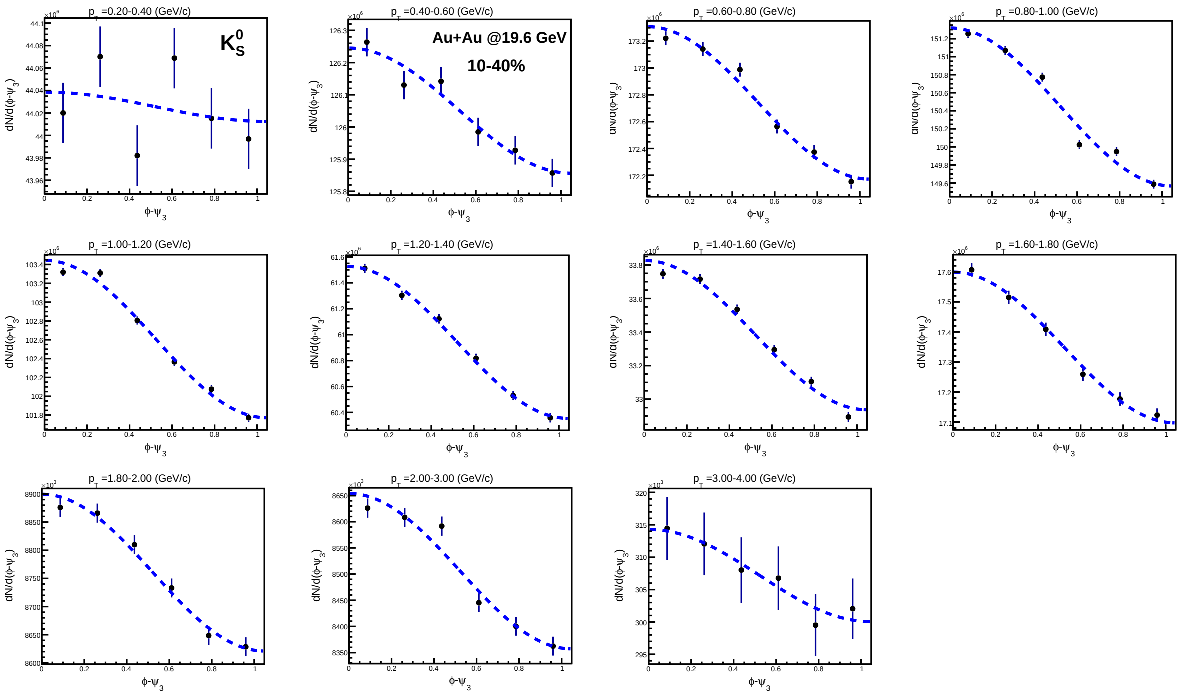

Figure C.18: Distribution of the raw yield of K_S^0 in $\phi-\Psi_3$ bin are plotted in Au+Au collisions at $\sqrt{s_{NN}}$ = 19.6 GeV in 10-40% centrality. The distribution is fitted with Eq. 3.15 to get v_3 of K_S^0.

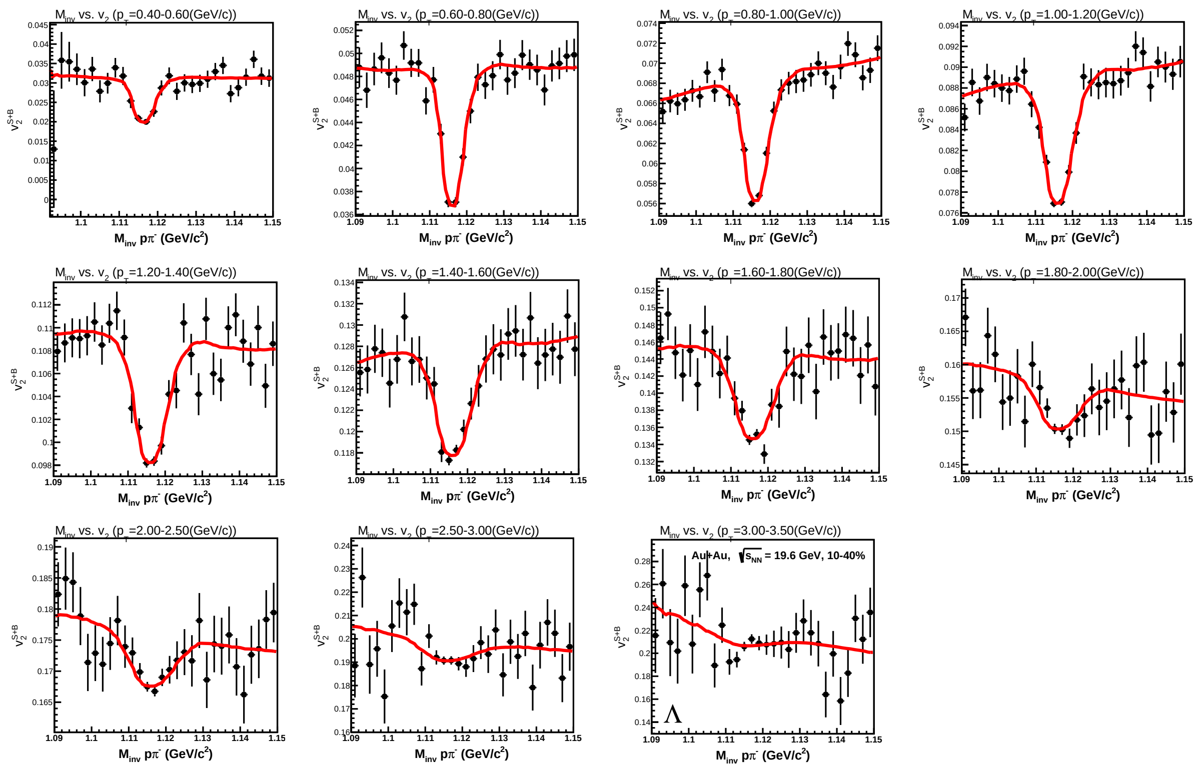

Figure C.19: v_2^{S+B} is plotted as a function of invariant mass of decay daughters of Λ in Au+Au collisions at $\sqrt{s_{NN}}$ = 19.6 GeV in 10-40% centrality. The distribution is fitted with Eq. 3.13 to obtain v_2 of the signal.

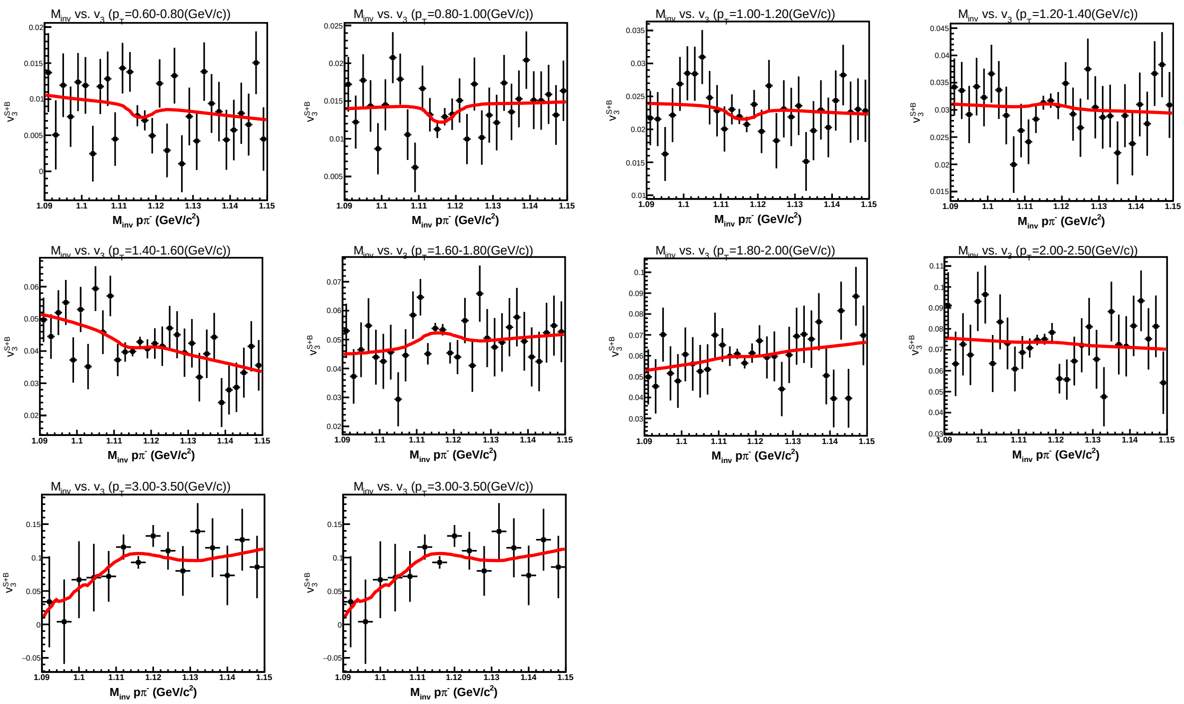

Figure C.20: v_3^{S+B} is plotted as a function of invariant mass of decay daughters of Λ in Au+Au collisions at $\sqrt{s_{NN}}$ = 19.6 GeV in 10-40% centrality. The distribution is fitted with Eq. 3.13 to obtain v_3 of the signal.

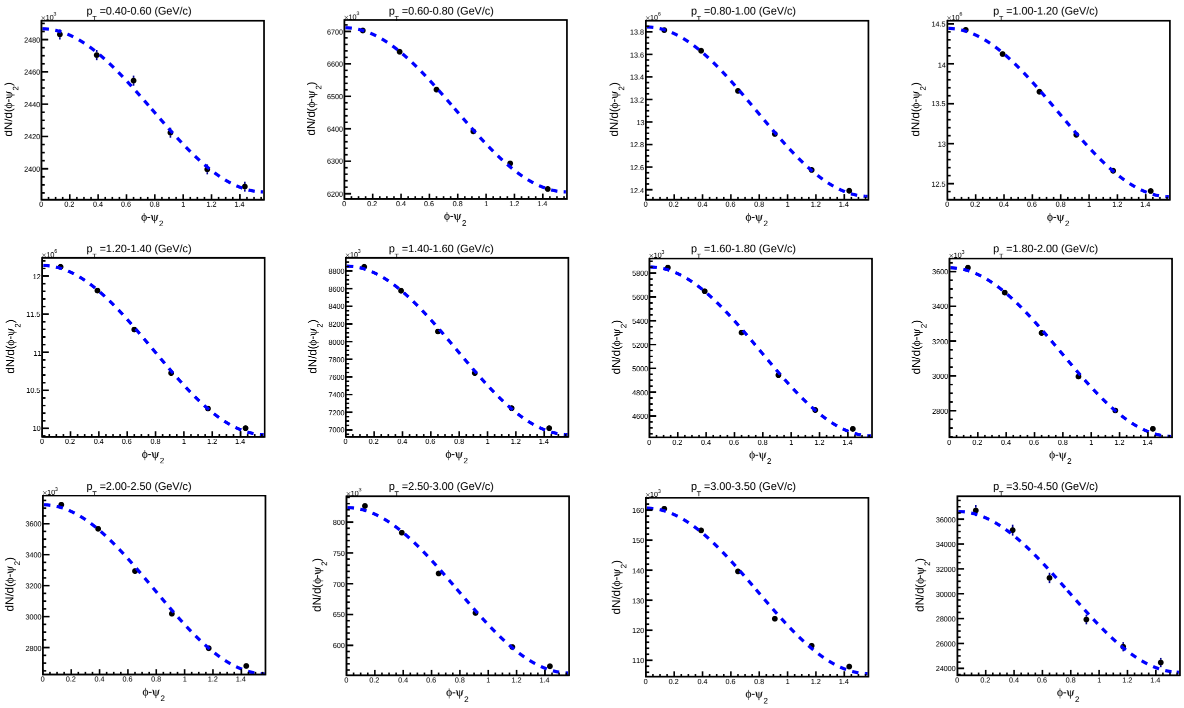

Figure C.21: Distribution of the raw yield of Λ in $\phi - \Psi_2$ bin are plotted in Au+Au collisions at $\sqrt{s_{NN}}$ = 19.6 GeV in 10-40% centrality. The distribution is fitted with Eq. 3.15 to get v_2 of Λ.

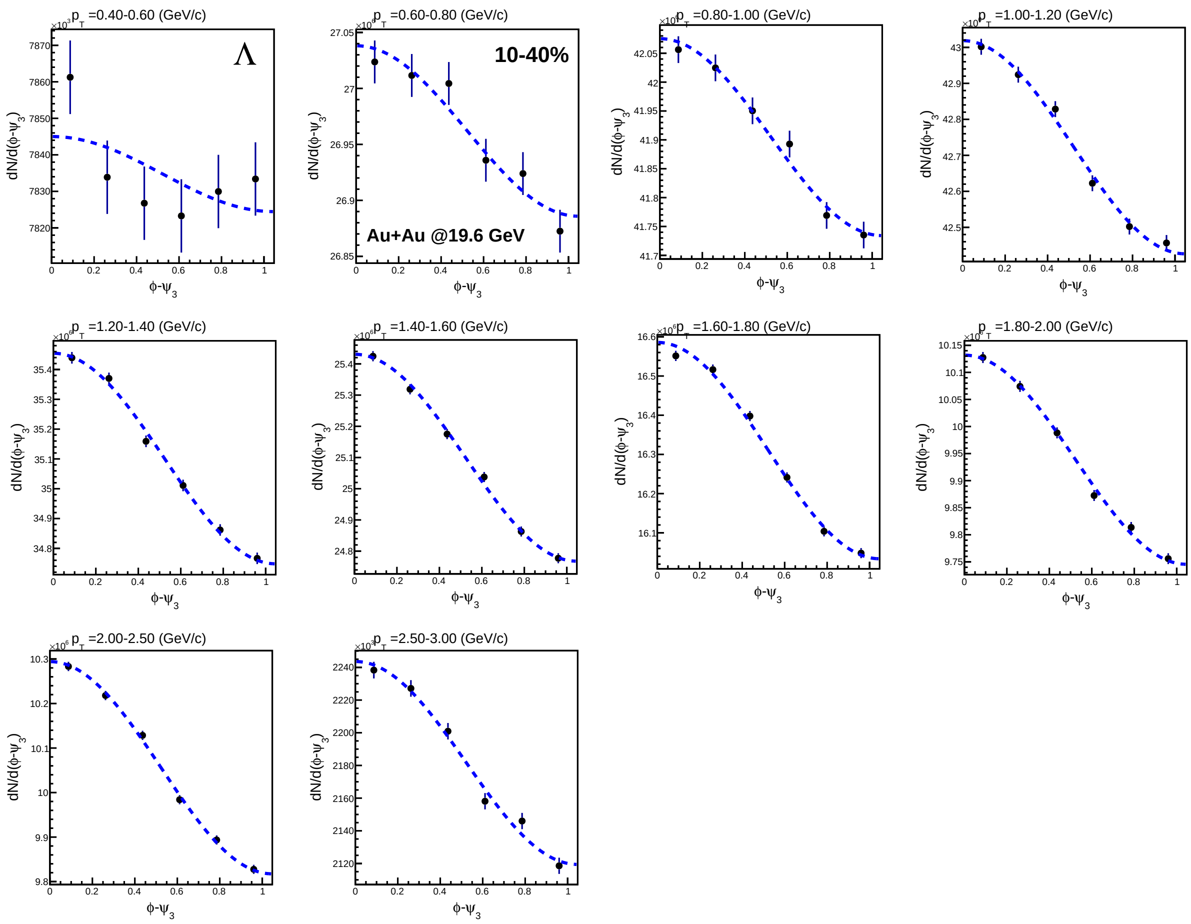

Figure C.22: Distribution of the raw yield of Λ in $\phi - \Psi_3$ bin are plotted in Au+Au collisions at $\sqrt{s_{NN}}$ = 19.6 GeV in 10-40% centrality. The distribution is fitted with Eq. 3.15 to get v_3 of Λ.

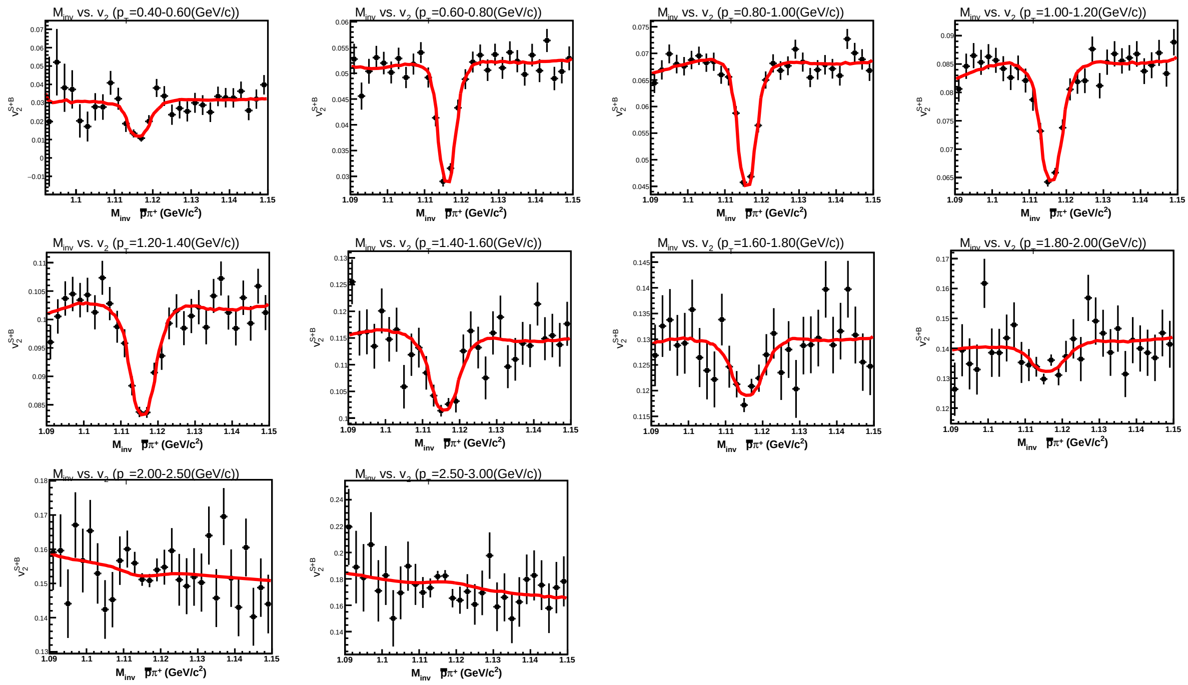

Figure C.23: v_2^{S+B} is plotted as a function of invariant mass of decay daughters of $\bar{\Lambda}$ in Au+Au collisions at $\sqrt{s_{NN}}$ = 19.6 GeV in 10-40% centrality. The distribution is fitted with Eq. 3.13 to obtain v_2 of the signal.

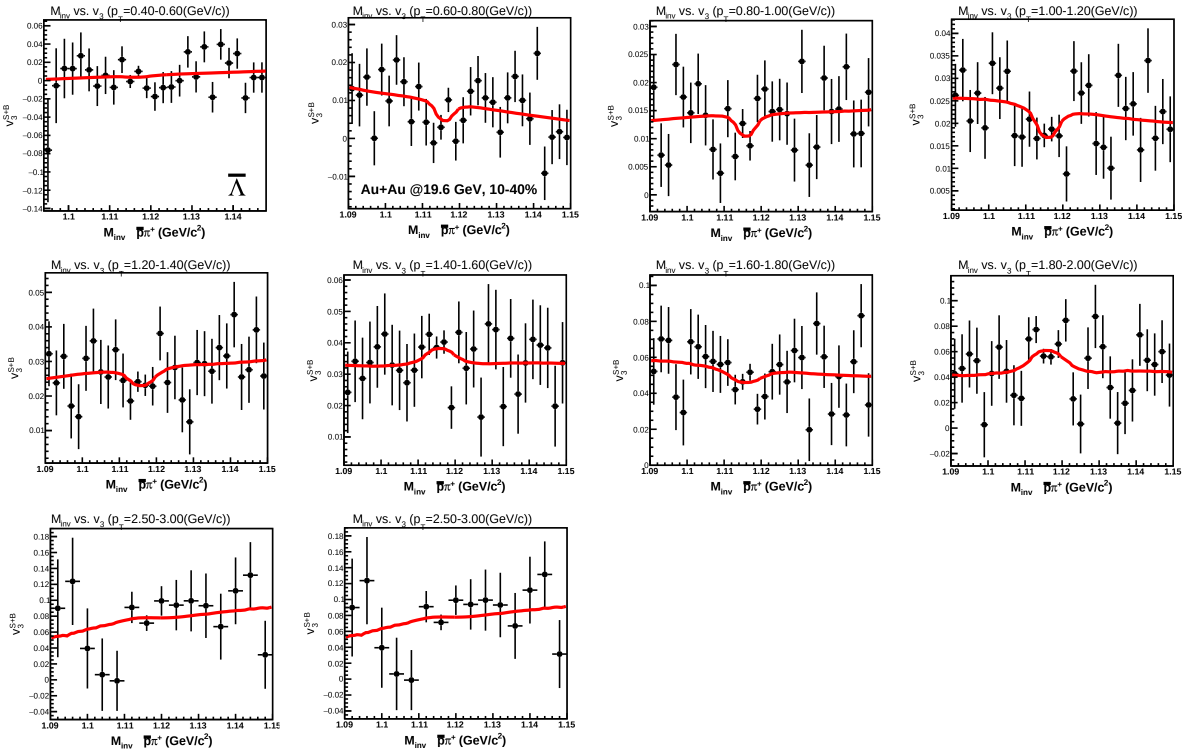

Figure C.24: v_3^{S+B} is plotted as a function of invariant mass of decay daughters of $\bar{\Lambda}$ in Au+Au collisions at $\sqrt{s_{NN}}$ = 19.6 GeV in 10-40% centrality. The distribution is fitted with Eq. 3.13 to obtain v_3 of the signal.

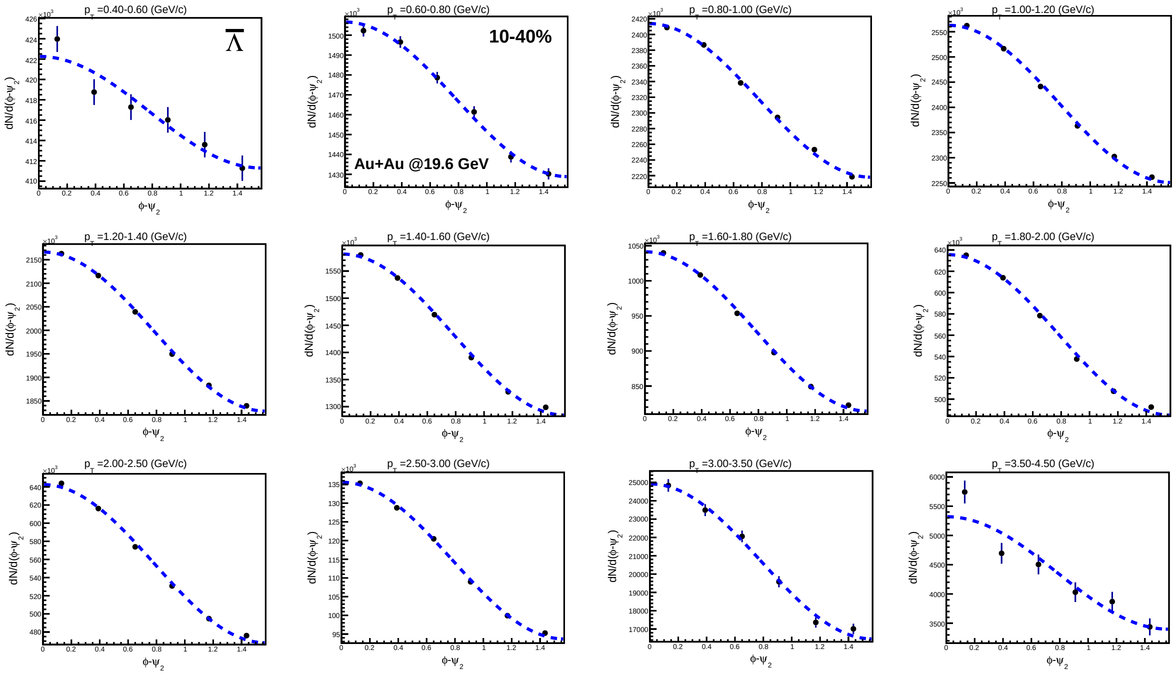

Figure C.25: Distribution of the raw yield of $\bar{\Lambda}$ in $\phi - \Psi_2$ bin are plotted in Au+Au collisions at $\sqrt{s_{NN}}$ = 19.6 GeV in 10-40% centrality. The distribution is fitted with Eq. 3.15 to get v_2 of $\bar{\Lambda}$.

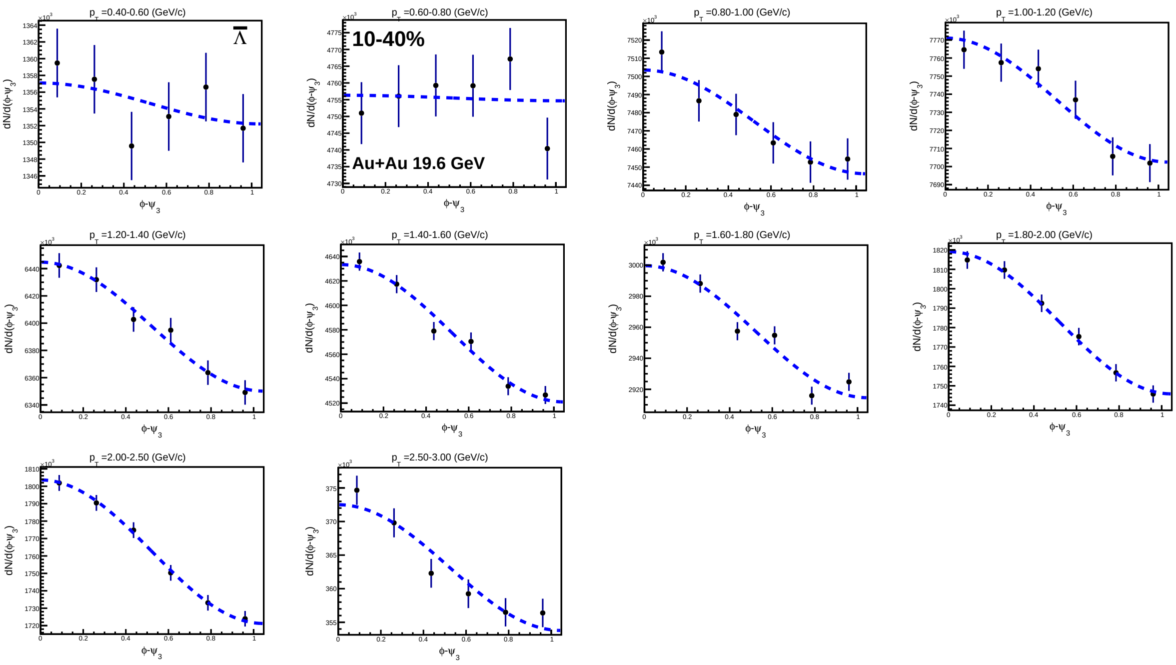

Figure C.26: Distribution of the raw yield of $\bar{\Lambda}$ in $\phi - \Psi_3$ bin are plotted in Au+Au collisions at $\sqrt{s_{NN}}$ = 19.6 GeV in 10-40% centrality. The distribution is fitted with Eq. 3.15 to get v_3 of Λ.

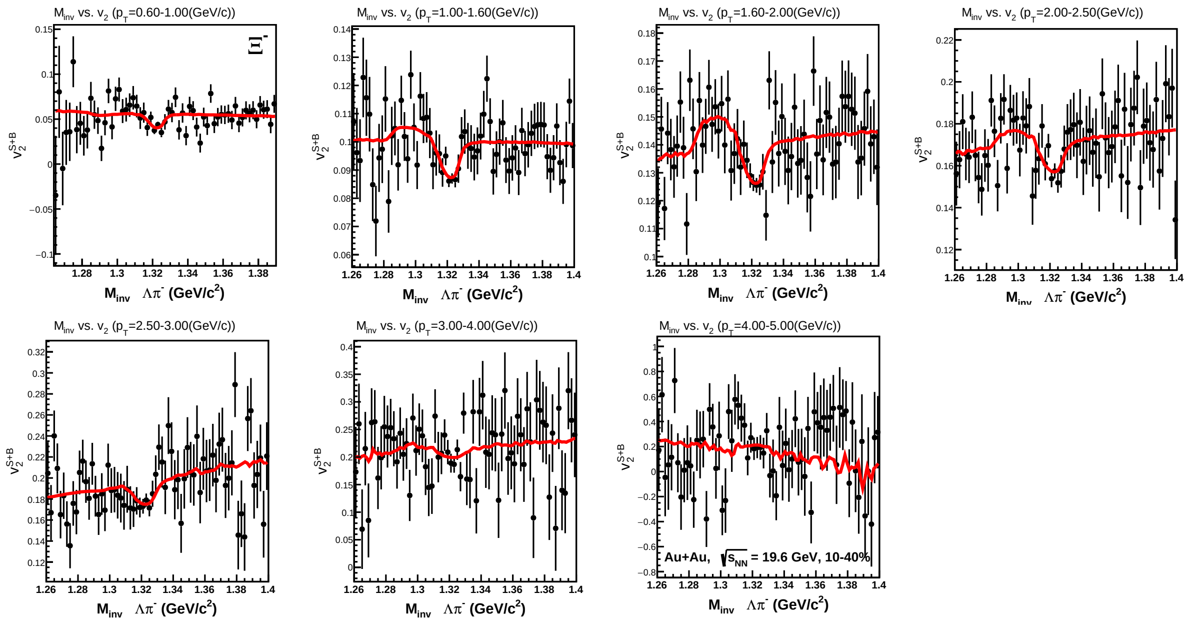

Figure C.27: v_2^{S+B} is plotted as a function of invariant mass of decay daughters of Ξ^- in Au+Au collisions at $\sqrt{s_{NN}}$ = 19.6 GeV in 10-40% centrality. The distribution is fitted with Eq. 3.13 to obtain v_2 of the signal.

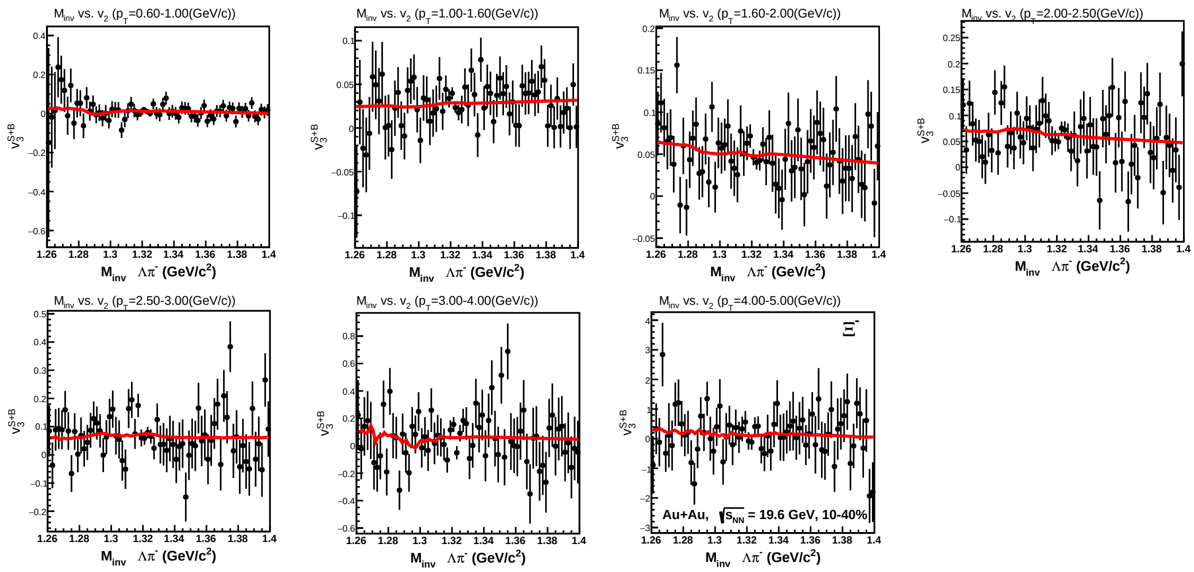

Figure C.28: v_3^{S+B} is plotted as a function of invariant mass of decay daughters of Ξ^- in Au+Au collisions at $\sqrt{s_{NN}}$ = 19.6 GeV in 10-40% centrality. The distribution is fitted with Eq. 3.13 to obtain v_3 of the signal.

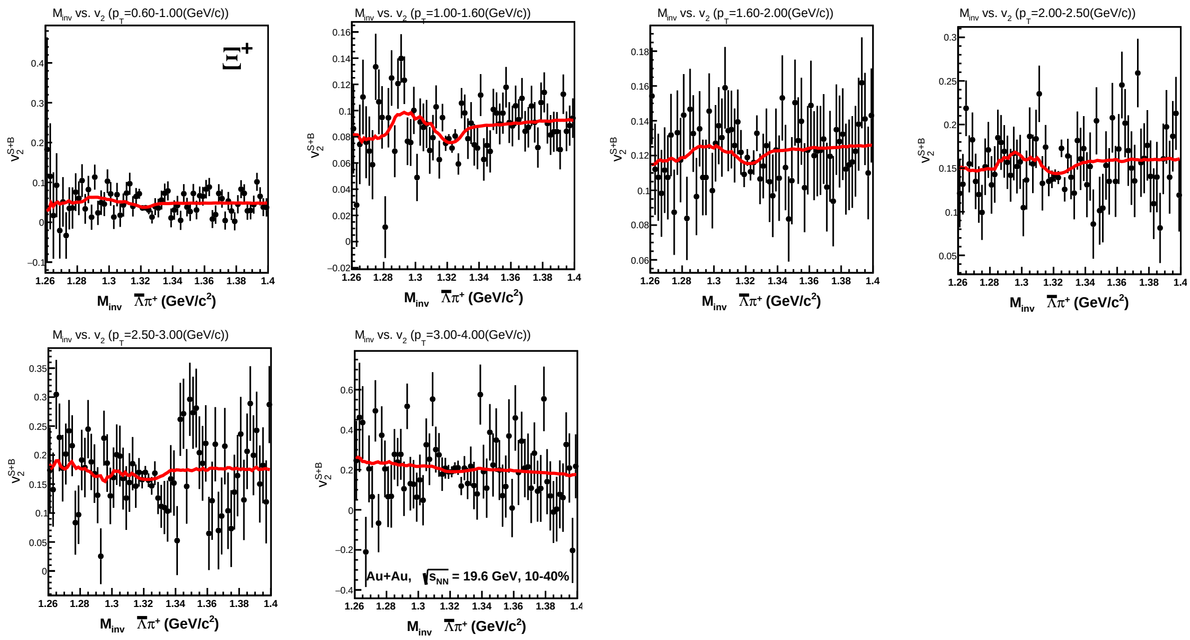

Figure C.29: v_2^{S+B} is plotted as a function of invariant mass of decay daughters of $\bar{\Xi}^+$ in Au+Au collisions at $\sqrt{s_{NN}}$ = 19.6 GeV in 10-40% centrality. The distribution is fitted with Eq. 3.13 to obtain v_2 of the signal.

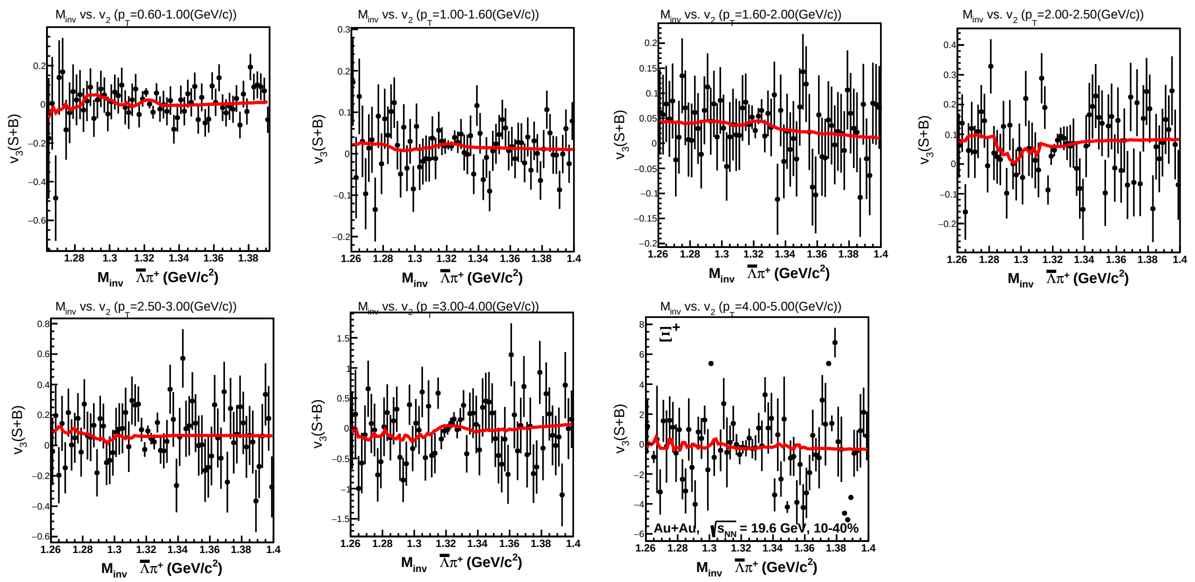

Figure C.30: v_3^{S+B} is plotted as a function of invariant mass of decay daughters of $\bar{\Xi}^+$ in Au+Au collisions at $\sqrt{s_{NN}}$ = 19.6 GeV in 10-40% centrality. The distribution is fitted with Eq. 3.13 to obtain v_3 of the signal.

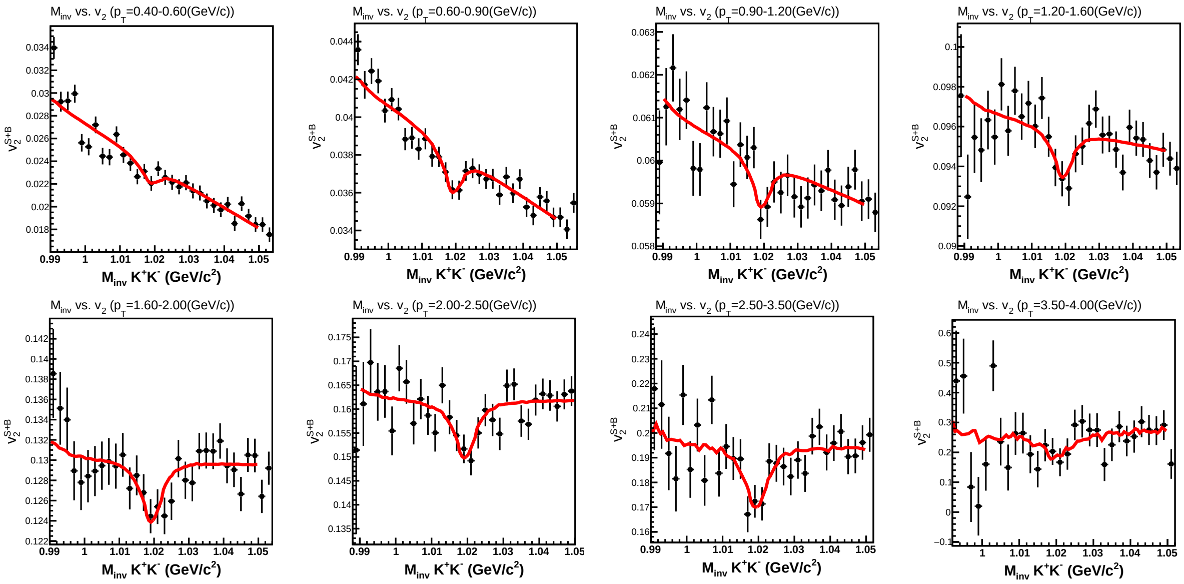

Figure C.31: v_2^{S+B} is plotted as a function of invariant mass of decay daughters of ϕ in Au+Au collisions at $\sqrt{s_{NN}}$ = 19.6 GeV in 10-40% centrality. The distribution is fitted with Eq. 3.13 to obtain v_2 of the signal.

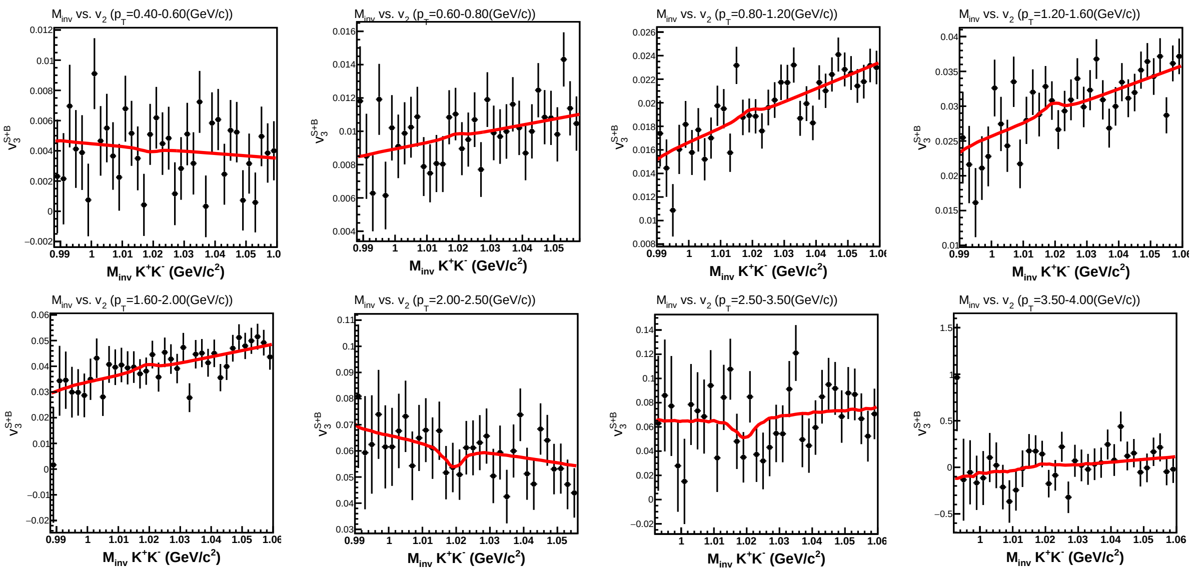

Figure C.32: v_3^{S+B} is plotted as a function of invariant mass of decay daughters of ϕ in Au+Au collisions at $\sqrt{s_{NN}}$ = 19.6 GeV in 10-40% centrality. The distribution is fitted with Eq. 3.13 to obtain v_3 of the signal.

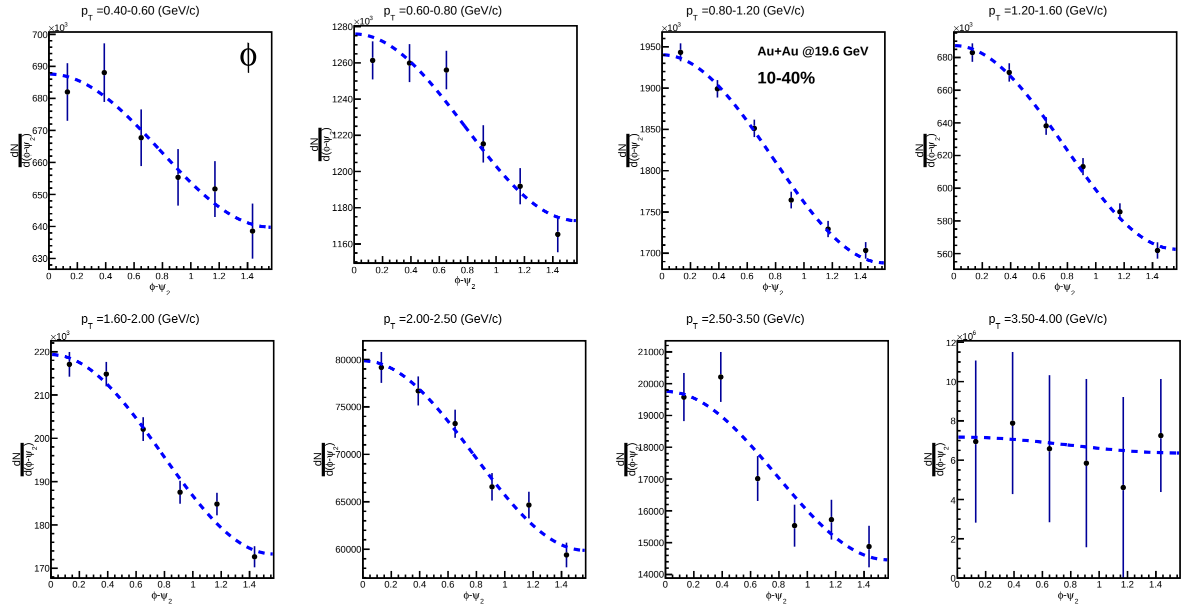

Figure C.33: Distribution of the raw yield of ϕ in $\phi-\Psi_2$ bin are plotted in Au+Au collisions at $\sqrt{s_{NN}}$ = 19.6 GeV in 10-40% centrality. The distribution is fitted with Eq. 3.15 to get v_2 of ϕ.

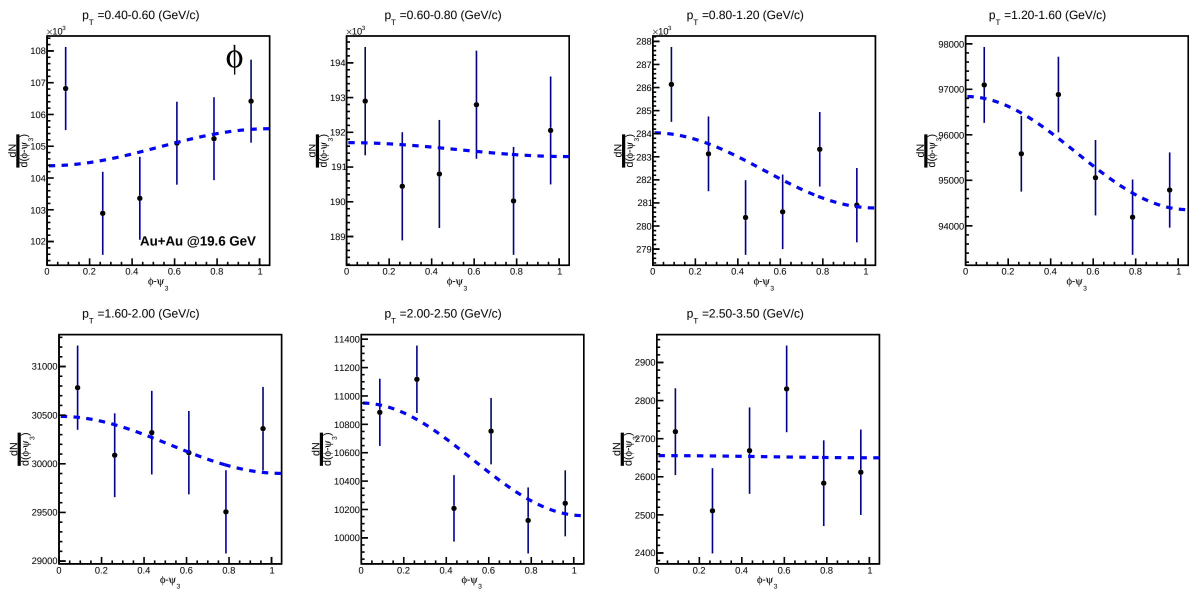

Figure C.34: Distribution of the raw yield of ϕ in $\phi-\Psi_3$ bin are plotted in Au+Au collisions at $\sqrt{s_{NN}}$ = 19.6 GeV in 10-40% centrality. The distribution is fitted with Eq. 3.15 to get v_3 of ϕ.

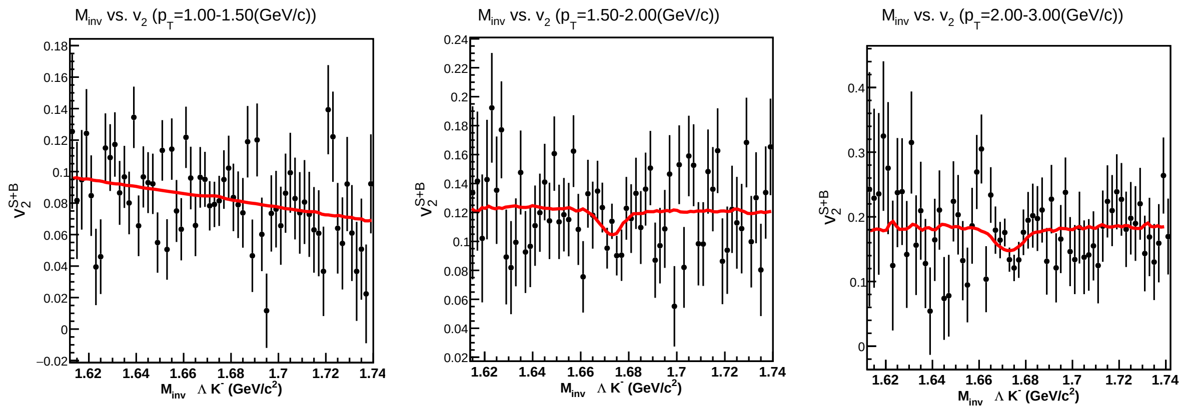

Figure C.35: v_2^{S+B} is plotted as a function of invariant mass of decay daughters of Ω^- in Au+Au collisions at $\sqrt{s_{NN}}$ = 19.6 GeV in 10-40% centrality. The distribution is fitted with Eq. 3.13 to obtain v_2 of the signal.

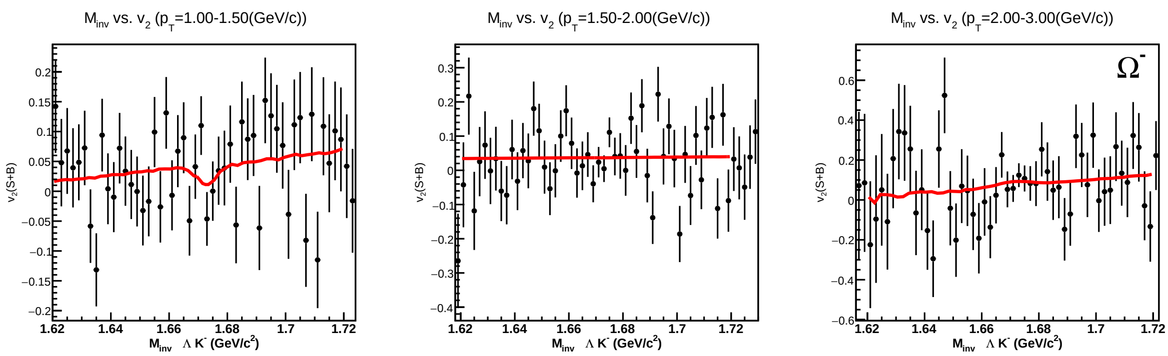

Figure C.36: v_3^{S+B} is plotted as a function of invariant mass of decay daughters of Ω^- in Au+Au collisions at $\sqrt{s_{NN}}$ = 19.6 GeV in 10-40% centrality. The distribution is fitted with Eq. 3.13 to obtain v_3 of the signal.

Bibliography

[1] Wikipedia contributors.
Standard Model — Wikipedia, the free encyclopedia.
2024.
URL: https://en.wikipedia.org/wiki/Standard_Model.

[2] David J. Gross and Frank Wilczek.
"Ultraviolet behavior of non-abelian gauge theories".
In: *Physical Review Letters* 30.26 (1973), pp. 1343–1346.
DOI: 10.1103/PhysRevLett.30.1343.

[3] H David Politzer.
"Asymptotic freedom: An approach to strong interactions".
In: *Physics Reports* 14.4 (1974), pp. 129–180.
ISSN: 0370-1573.
DOI: https://doi.org/10.1016/0370-1573(74)90014-3.
URL: https://www.sciencedirect.com/science/article/pii/0370157374900143.

[4] S. Bethke.
"Experimental tests of asymptotic freedom".
In: *Progress in Particle and Nuclear Physics* 58.2 (2007), pp. 351–386.
ISSN: 0146-6410.
DOI: https://doi.org/10.1016/j.ppnp.2006.06.001.
URL: https://www.sciencedirect.com/science/article/pii/S0146641006000615.

[5] Eemeli Annala et al.
"Evidence for quark-matter cores in massive neutron stars".
In: *Nature Physics* 16.9 (June 2020), pp. 907–910.
ISSN: 1745-2481.
DOI: 10.1038/s41567-020-0914-9.
URL: http://dx.doi.org/10.1038/s41567-020-0914-9.

[6] Y. Aoki et al.

"The QCD transition temperature: Results with physical masses in the continuum limit".
In: *Physics Letters B* 643.1 (2006), pp. 46–54.
ISSN: 0370-2693.
DOI: `https://doi.org/10.1016/j.physletb.2006.10.021`.
URL: `https://www.sciencedirect.com/science/article/pii/S0370269306012755`.

[7] Szabolcs Borsányi et al.
"Is there still any Tc mystery in lattice QCD? Results with physical masses in the continuum limit III".
In: *Journal of High Energy Physics* 2010.9 (2010), p. 73.
ISSN: 1029-8479.
DOI: `10.1007/JHEP09(2010)073`.
URL: `https://doi.org/10.1007/JHEP09(2010)073`.

[8] A. Bazavov et al.
"Chiral and deconfinement aspects of the QCD transition".
In: *Phys. Rev. D* 85 (5 Mar. 2012), p. 054503.
DOI: `10.1103/PhysRevD.85.054503`.
URL: `https://link.aps.org/doi/10.1103/PhysRevD.85.054503`.

[9] Yasumichi Aoki et al.
"The QCD transition temperature: results with physical masses in the continuum limit II".
In: *Journal of High Energy Physics* 2009.06 (June 2009), p. 088.
DOI: `10.1088/1126-6708/2009/06/088`.
URL: `https://dx.doi.org/10.1088/1126-6708/2009/06/088`.

[10] P. Braun-Munzinger and J. Wambach.
The Phase Diagram of Strongly-Interacting Matter.
2009.
arXiv: `0801.4256 [hep-ph]`.
URL: `https://arxiv.org/abs/0801.4256`.

[11] Peter Braun-Munzinger et al.
"Properties of hot and dense matter from relativistic heavy ion collisions".
In: *Physics Reports* 621 (Mar. 2016), pp. 76–126.
ISSN: 0370-1573.
DOI: `10.1016/j.physrep.2015.12.003`.

URL: http://dx.doi.org/10.1016/j.physrep.2015.12.003.

[12] M. A. Stephanov.
"QCD PHASE DIAGRAM AND THE CRITICAL POINT".
In: *International Journal of Modern Physics A* 20.19 (July 2005), pp. 4387–4392.
ISSN: 1793-656X.
DOI: 10.1142/s0217751x05027965.
URL: http://dx.doi.org/10.1142/S0217751X05027965.

[13] M. A. Stephanov.
QCD phase diagram: an overview.
2006.
arXiv: hep-lat/0701002 [hep-lat].
URL: https://arxiv.org/abs/hep-lat/0701002.

[14] Kenji Fukushima and Chihiro Sasaki.
The phase diagram of nuclear and quark matter at high baryon density.
2013.
arXiv: 1301.6377 [hep-ph].
URL: https://arxiv.org/abs/1301.6377.

[15] Gordon Baym et al.
"From hadrons to quarks in neutron stars: a review".
In: *Reports on Progress in Physics* 81.5 (Mar. 2018), p. 056902.
ISSN: 1361-6633.
DOI: 10.1088/1361-6633/aaae14.
URL: http://dx.doi.org/10.1088/1361-6633/aaae14.

[16] Wenkai Fan.
Multi-Stage Heavy Quark Transport in Ultra-relativistic Heavy-ion Collisions.
2022.
arXiv: 2207.12452 [nucl-th].
URL: https://arxiv.org/abs/2207.12452.

[17] Adam Bzdak et al.
"Mapping the phases of quantum chromodynamics with beam energy scan".
In: *Physics Reports* 853 (2020). Mapping the phases of quantum chromodynamics with beam energy scan, pp. 1–87.
ISSN: 0370-1573.
DOI: https://doi.org/10.1016/j.physrep.2020.01.005.

URL: https://www.sciencedirect.com/science/article/pii/S0370157320300156.

[18] *Sketch of Relativistic Heavy-Ion Collisions.*
https://u.osu.edu/vishnu/2014/08/06/sketch-of-relativistic-heavy-ion-collisions/.

[19] Jean Letessier, Johann Rafelski, and Ahmed Tounsi.
"Strange antibaryons from QGP".
In: *Nucl. Phys. A* 590.1 (1995), pp. 613–616.
ISSN: 0375-9474.
DOI: https://doi.org/10.1016/0375-9474(95)00290-H.
URL: https://www.sciencedirect.com/science/article/pii/037594749500290H.

[20] Johann Rafelski and Berndt Müller.
"Strangeness Production in the Quark-Gluon Plasma".
In: *Phys. Rev. Lett.* 48 (16 Apr. 1982), pp. 1066–1069.
DOI: 10.1103/PhysRevLett.48.1066.
URL: https://link.aps.org/doi/10.1103/PhysRevLett.48.1066.

[21] Johann Rafelski.
"Discovery of Quark-Gluon Plasma: Strangeness Diaries".
In: *The European Physical Journal Special Topics* 229.1 (2020), pp. 1–140.
ISSN: 1951-6401.
DOI: 10.1140/epjst/e2019-900263-x.
URL: https://doi.org/10.1140/epjst/e2019-900263-x.

[22] P. Koch and J. Rafelski.
"Time evolution of strange-particle densities in hot hadronic matter".
In: *Nucl. Phys. A* 444.4 (1985), pp. 678–691.
ISSN: 0375-9474.
DOI: https://doi.org/10.1016/0375-9474(85)90112-5.
URL: https://www.sciencedirect.com/science/article/pii/0375947485901125.

[23] Jaroslav Adam et al.
"Enhanced production of multi-strange hadrons in high-multiplicity proton-proton collisions".
In: *Nature Phys.* 13 (2017), pp. 535–539.
DOI: 10.1038/nphys4111.
arXiv: 1606.07424 [nucl-ex].

[24] B.I. Abelev et al.

"Energy and system size dependence of meson production in Cu+Cu and Au+Au collisions".
In: *Physics Letters B* 673.3 (2009), pp. 183–191.
ISSN: 0370-2693.
DOI: `https://doi.org/10.1016/j.physletb.2009.02.037`.
URL: `https://www.sciencedirect.com/science/article/pii/S0370269309002159`.

[25] Megan Connors et al.
"Jet measurements in heavy ion physics".
In: *Rev. Mod. Phys.* 90 (2 June 2018), p. 025005.
DOI: `10.1103/RevModPhys.90.025005`.
URL: `https://link.aps.org/doi/10.1103/RevModPhys.90.025005`.

[26] Guang-You Qin and Xin-Nian Wang.
"Jet quenching in high-energy heavy-ion collisions".
In: *International Journal of Modern Physics E* 24.11 (2015), p. 1530014.
DOI: `10.1142/S0218301315300143`.

[27] Leticia Cunqueiro and Anne M. Sickles.
"Studying the QGP with Jets at the LHC and RHIC".
In: *Progress in Particle and Nuclear Physics* 124 (2022), p. 103940.
ISSN: 0146-6410.
DOI: `https://doi.org/10.1016/j.ppnp.2022.103940`.
URL: `https://www.sciencedirect.com/science/article/pii/S0146641022000011`.

[28] Karen M. Burke et al.
"Extracting the jet transport coefficient from jet quenching in high-energy heavy-ion collisions".
In: *Phys. Rev. C* 90 (1 July 2014), p. 014909.
DOI: `10.1103/PhysRevC.90.014909`.
URL: `https://link.aps.org/doi/10.1103/PhysRevC.90.014909`.

[29] J. Adams et al.
"Experimental and theoretical challenges in the search for the quark–gluon plasma: The STAR Collaboration's critical assessment of the evidence from RHIC collisions".
In: *Nucl. Phys. A* 757.1–2 (Aug. 2005), pp. 102–183.
ISSN: 0375-9474.
DOI: `10.1016/j.nuclphysa.2005.03.085`.
URL: `http://dx.doi.org/10.1016/j.nuclphysa.2005.03.085`.

[30] J. J. Aubert et al.
"Experimental Observation of a Heavy Particle J".
In: *Phys. Rev. Lett.* 33 (23 Dec. 1974), pp. 1404–1406.
DOI: 10.1103/PhysRevLett.33.1404.
URL: https://link.aps.org/doi/10.1103/PhysRevLett.33.1404.

[31] J. -E. Augustin et al.
"Discovery of a Narrow Resonance in e^+e^- Annihilation".
In: *Phys. Rev. Lett.* 33 (23 Dec. 1974), pp. 1406–1408.
DOI: 10.1103/PhysRevLett.33.1406.
URL: https://link.aps.org/doi/10.1103/PhysRevLett.33.1406.

[32] T. Matsui and H. Satz.
"J/ suppression by quark-gluon plasma formation".
In: *Physics Letters B* 178.4 (1986), pp. 416–422.
ISSN: 0370-2693.
DOI: https://doi.org/10.1016/0370-2693(86)91404-8.
URL: https://www.sciencedirect.com/science/article/pii/0370269386914048.

[33] M. C. Abreu et al.
"J / psi and psi-prime production in p, O and S induced reactions at SPS energies".
In: *Phys. Lett. B* 466 (1999), pp. 408–414.
DOI: 10.1016/S0370-2693(99)01108-9.

[34] M. C. Abreu et al.
"Evidence for deconfinement of quarks and gluons from the J / psi suppression pattern measured in Pb + Pb collisions at the CERN SPS".
In: *Phys. Lett. B* 477 (2000), pp. 28–36.
DOI: 10.1016/S0370-2693(00)00237-9.

[35] R. Arnaldi et al.
"J/ψ Production in Indium-Indium Collisions at 158 GeV/Nucleon".
In: *Phys. Rev. Lett.* 99 (13 Sept. 2007), p. 132302.
DOI: 10.1103/PhysRevLett.99.132302.
URL: https://link.aps.org/doi/10.1103/PhysRevLett.99.132302.

[36] A. Adare et al.
"J/ψ Production versus Centrality, Transverse Momentum, andRapidity in Au + Au Collisions at $\sqrt{s_{NN}} = 200$ GeV".
In: *Phys. Rev. Lett.* 98 (23 June 2007), p. 232301.

DOI: 10.1103/PhysRevLett.98.232301.
URL: https://link.aps.org/doi/10.1103/PhysRevLett.98.232301.

[37] L. Adamczyk et al.
"J/ψ production at low p_T in Au + Au and Cu + Cu collisions at $\sqrt{s_{NN}} = 200$ GeV with the STAR detector".
In: *Phys. Rev. C* 90 (2 Aug. 2014), p. 024906.
DOI: 10.1103/PhysRevC.90.024906.
URL: https://link.aps.org/doi/10.1103/PhysRevC.90.024906.

[38] Jaroslav Adam et al.
"Measurement of inclusive J/ψ suppression in Au+Au collisions at $\sqrt{s_{NN}} = 200$ GeV through the dimuon channel at STAR".
In: *Phys. Lett. B* 797 (2019), p. 134917.
DOI: 10.1016/j.physletb.2019.134917.
arXiv: 1905.13669 [nucl-ex].

[39] Jaroslav Adam et al.
"Inclusive, prompt and non-prompt J/ψ production at mid-rapidity in Pb-Pb collisions at $\sqrt{s_{NN}} = 2.76$ TeV".
In: *JHEP* 07 (2015), p. 051.
DOI: 10.1007/JHEP07(2015)051.
arXiv: 1504.07151 [nucl-ex].

[40] J. Adam et al.
"J/ suppression at forward rapidity in Pb–Pb collisions at sNN=5.02 TeV".
In: *Physics Letters B* 766 (2017), pp. 212–224.
ISSN: 0370-2693.
DOI: https://doi.org/10.1016/j.physletb.2016.12.064.
URL: https://www.sciencedirect.com/science/article/pii/S0370269317300102.

[41] Arthur M. Poskanzer and S. A. Voloshin.
"Methods for analyzing anisotropic flow in relativistic nuclear collisions".
In: *Phys. Rev. C* 58 (1998), pp. 1671–1678.
DOI: 10.1103/PhysRevC.58.1671.
arXiv: nucl-ex/9805001.

[42] K. H. Ackermann et al.
"Elliptic Flow in $Au + Au$ Collisions at $\sqrt{s_{\rm NN}} = 130$GeV".
In: *Phys. Rev. Lett.* 86 (3 Jan. 2001), pp. 402–407.

DOI: 10.1103/PhysRevLett.86.402.
URL: https://link.aps.org/doi/10.1103/PhysRevLett.86.402.

[43] Paul Romatschke and Ulrike Romatschke.
"Viscosity Information from Relativistic Nuclear Collisions: How Perfect is the Fluid Observed at RHIC?"
In: *Phys. Rev. Lett.* 99 (17 Oct. 2007), p. 172301.
DOI: 10.1103/PhysRevLett.99.172301.
URL: https://link.aps.org/doi/10.1103/PhysRevLett.99.172301.

[44] Matthew Luzum and Paul Romatschke.
"Conformal relativistic viscous hydrodynamics: Applications to RHIC results at $\sqrt{s_{NN}}$ = 200 GeV".
In: *Phys. Rev. C* 78 (3 Sept. 2008), p. 034915.
DOI: 10.1103/PhysRevC.78.034915.
URL: https://link.aps.org/doi/10.1103/PhysRevC.78.034915.

[45] L. Adamczyk et al.
"Inclusive charged hadron elliptic flow in Au + Au collisions at $\sqrt{s_{NN}}$ = 7.7 - 39 GeV".
In: *Phys. Rev. C* 86 (2012), p. 054908.
DOI: 10.1103/PhysRevC.86.054908.
arXiv: 1206.5528 [nucl-ex].

[46] Bjoern Schenke, Sangyong Jeon, and Charles Gale.
"(3+1)D hydrodynamic simulation of relativistic heavy-ion collisions".
In: *Phys. Rev. C* 82 (2010), p. 014903.
DOI: 10.1103/PhysRevC.82.014903.
arXiv: 1004.1408 [hep-ph].

[47] B. Alver and G. Roland.
"Collision-geometry fluctuations and triangular flow in heavy-ion collisions".
In: *Phys. Rev. C* 81 (5 May 2010), p. 054905.
DOI: 10.1103/PhysRevC.81.054905.
URL: https://link.aps.org/doi/10.1103/PhysRevC.81.054905.

[48] A. Adare et al.
"Measurements of Higher Order Flow Harmonics in Au + Au Collisions at $\sqrt{s_{NN}}$ = 200 GeV".
In: *Phys. Rev. Lett.* 107 (25 Dec. 2011), p. 252301.
DOI: 10.1103/PhysRevLett.107.252301.

URL: `https://link.aps.org/doi/10.1103/PhysRevLett.107.252301`.

[49] L. Adamczyk et al.
"Third Harmonic Flow of Charged Particles in Au+Au Collisions at sqrtsNN = 200 GeV".
In: *Phys. Rev. C* 88.1 (2013), p. 014904.
DOI: `10.1103/PhysRevC.88.014904`.
arXiv: `1301.2187 [nucl-ex]`.

[50] Bjorn Schenke, Sangyong Jeon, and Charles Gale.
"Higher flow harmonics from (3+1)D event-by-event viscous hydrodynamics".
In: *Phys. Rev. C* 85 (2012), p. 024901.
DOI: `10.1103/PhysRevC.85.024901`.
arXiv: `1109.6289 [hep-ph]`.

[51] Rainer J. Fries, Vincenzo Greco, and Paul Sorensen.
"Coalescence Models For Hadron Formation From Quark Gluon Plasma".
In: *Ann. Rev. Nucl. Part. Sci.* 58 (2008), pp. 177–205.
DOI: `10.1146/annurev.nucl.58.110707.171134`.
arXiv: `0807.4939 [nucl-th]`.

[52] Amir Goudarzi, Gang Wang, and Huan Zhong Huang.
"Evidence of coalescence sum rule in elliptic flow of identified particles in high-energy heavy-ion collisions".
In: *Phys. Lett. B* 811 (2020), p. 135974.
DOI: `10.1016/j.physletb.2020.135974`.
arXiv: `2007.11617 [nucl-ex]`.

[53] L. Adamczyk et al.
"Centrality and Transverse Momentum Dependence of Elliptic Flow of Multistrange Hadrons and ϕ Meson in Au + Au Collisions at $\sqrt{s_{NN}} = 200$ GeV".
In: *Phys. Rev. Lett.* 116 (6 Feb. 2016), p. 062301.
DOI: `10.1103/PhysRevLett.116.062301`.
URL: `https://link.aps.org/doi/10.1103/PhysRevLett.116.062301`.

[54] M. S. Abdallah et al.
"Centrality and transverse-momentum dependence of higher-order flow harmonics of identified hadrons in Au+Au collisions at $\sqrt{s_{NN}} = 200$ GeV".
In: *Phys. Rev. C* 105 (6 June 2022), p. 064911.
DOI: `10.1103/PhysRevC.105.064911`.

URL: https://link.aps.org/doi/10.1103/PhysRevC.105.064911.

[55] L. Adamczyk et al.
"Azimuthal anisotropy in Cu+Au collisions at $\sqrt{s_{NN}} = 200$ GeV".
In: *Phys. Rev. C* 98 (1 July 2018), p. 014915.
DOI: 10.1103/PhysRevC.98.014915.
URL: https://link.aps.org/doi/10.1103/PhysRevC.98.014915.

[56] A. Adare et al.
"Scaling Properties of Azimuthal Anisotropy in Au + Au and Cu + Cu Collisions at $\sqrt{s_{\mathrm{NN}}} = 200$ GeV".
In: *Phys. Rev. Lett.* 98 (16 Apr. 2007), p. 162301.
DOI: 10.1103/PhysRevLett.98.162301.
URL: https://link.aps.org/doi/10.1103/PhysRevLett.98.162301.

[57] L. Adamczyk et al.
"Elliptic flow of identified hadrons in Au+Au collisions at $\sqrt{s_{NN}} = 7.7$–62.4 GeV".
In: *Phys. Rev. C* 88 (1 July 2013), p. 014902.
DOI: 10.1103/PhysRevC.88.014902.
URL: https://link.aps.org/doi/10.1103/PhysRevC.88.014902.

[58] Asher Shor.
"φ-Meson Production as a Probe of the Quark-Gluon Plasma".
In: *Phys. Rev. Lett.* 54 (11 Mar. 1985), pp. 1122–1125.
DOI: 10.1103/PhysRevLett.54.1122.
URL: https://link.aps.org/doi/10.1103/PhysRevLett.54.1122.

[59] B Mohanty and N Xu.
"Probe of the QCD phase diagram with -mesons in high-energy nuclear collisions".
In: *Journal of Physics G: Nuclear and Particle Physics* 36.6 (May 2009), p. 064022.
DOI: 10.1088/0954-3899/36/6/064022.
URL: https://dx.doi.org/10.1088/0954-3899/36/6/064022.

[60] J. H. Chen et al.
"Elliptic flow of ϕ mesons and strange quark collectivity".
In: *Phys. Rev. C* 74 (6 Dec. 2006), p. 064902.
DOI: 10.1103/PhysRevC.74.064902.
URL: https://link.aps.org/doi/10.1103/PhysRevC.74.064902.

[61] Md. Nasim, Bedangadas Mohanty, and Nu Xu.

"Elliptic flow of ϕ mesons as a sensitive probe for the onset of the deconfinement transition in high energy heavy-ion collisions".
In: *Phys. Rev. C* 87 (1 Jan. 2013), p. 014903.
DOI: 10.1103/PhysRevC.87.014903.
URL: https://link.aps.org/doi/10.1103/PhysRevC.87.014903.

[62] Rosi Reed.
"STAR Overview".
In: *EPJ Web Conf.* 296 (2024), p. 01005.
DOI: 10.1051/epjconf/202429601005.

[63] M Adamczyk et al.
"The BRAHMS experiment at RHIC".
In: *Nucl. Instr. Meth. A* 499.2 (2003). The Relativistic Heavy Ion Collider Project: RHIC and its Detectors, pp. 437–468.
ISSN: 0168-9002.
DOI: https://doi.org/10.1016/S0168-9002(02)01949-6.
URL: https://www.sciencedirect.com/science/article/pii/S0168900202019496.

[64] Jay N. Marx.
"The STAR Experiment at RHIC".
In:
Advances in Nuclear Dynamics 2.
Ed. by Wolfgang Bauer and Gary D. Westfall.
Boston, MA: Springer US, 1996,
Pp. 233–237.
ISBN: 978-1-4757-9086-3.
DOI: 10.1007/978-1-4757-9086-3_32.
URL: https://doi.org/10.1007/978-1-4757-9086-3_32.

[65] K. F. Read.
"The Phenix Experiment".
In:
Advances in Nuclear Dynamics 5.
Ed. by Wolfgang Bauer and Gary D. Westfall.
Boston, MA: Springer US, 1999,
Pp. 91–99.
ISBN: 978-1-4615-4719-8.

DOI: 10.1007/978-1-4615-4719-8_9.
URL: https://doi.org/10.1007/978-1-4615-4719-8_9.

[66] Judith M. Katzy et al.
"The PHOBOS experiment at the RHIC collider".
In: *Nucl. Phys. A* 661.1 (1999), pp. 690–693.
ISSN: 0375-9474.
DOI: https://doi.org/10.1016/S0375-9474(99)85119-7.
URL: https://www.sciencedirect.com/science/article/pii/S0375947499851197.

[67] Brookhaven National Laboratory.
Brookhaven Lab Flickr.
Accessed: 13 March 2025.
2025.
URL: https://www.flickr.com/photos/brookhavenlab/.

[68] K.H. Ackermann others.
"STAR detector overview".
In: *Nucl. Instr. Meth. A* 499.2 (2003), pp. 624–632.
ISSN: 0168-9002.
DOI: https://doi.org/10.1016/S0168-9002(02)01960-5.
URL: https://www.sciencedirect.com/science/article/pii/S0168900202019605.

[69] F. Bergsma et al.
"The STAR detector magnet subsystem".
In: *Nucl. Instr. Meth. A* 499.2 (2003), pp. 633–639.
ISSN: 0168-9002.
DOI: https://doi.org/10.1016/S0168-9002(02)01961-7.
URL: https://www.sciencedirect.com/science/article/pii/S0168900202019617.

[70] STAR Collaboration.
STAR Public Images.
Accessed: 2024-12-24.
n.d.
URL: https://drupal.star.bnl.gov/STAR/public/img/.

[71] M. Anderson et al.
"The STAR time projection chamber: a unique tool for studying high multiplicity events at RHIC".
In: *Nucl. Instr. Meth. A* 499.2 (2003), pp. 659–678.

ISSN: 0168-9002.
DOI: https://doi.org/10.1016/S0168-9002(02)01964-2.
URL: https://www.sciencedirect.com/science/article/pii/S0168900202019642.

[72] Qian Yang.
"The STAR BES-II and Forward Rapidity Physics and Upgrades".
In: *Nucl. Phys. A* 982 (2019), pp. 951–954.
ISSN: 0375-9474.
DOI: https://doi.org/10.1016/j.nuclphysa.2018.10.029.
URL: https://www.sciencedirect.com/science/article/pii/S0375947418303105.

[73] L. Kotchenda et al.
"STAR TPC gas system".
In: *Nucl. Instr. Meth. A* 499.2 (2003), pp. 703–712.
ISSN: 0168-9002.
DOI: https://doi.org/10.1016/S0168-9002(02)01967-8.
URL: https://www.sciencedirect.com/science/article/pii/S0168900202019678.

[74] Ming Shao et al.
"Extensive particle identification with TPC and TOF at the STAR experiment".
In: *Nucl. Instr. Meth. A* 558.2 (2006), pp. 419–429.
ISSN: 0168-9002.
DOI: https://doi.org/10.1016/j.nima.2005.11.251.
URL: https://www.sciencedirect.com/science/article/pii/S0168900205024411.

[75] W.J Llope et al.
"The TOFp/pVPD time-of-flight system for STAR".
In: *Nucl.Instr.Meth* 522.3 (2004), pp. 252–273.
ISSN: 0168-9002.
DOI: https://doi.org/10.1016/j.nima.2003.11.414.
URL: https://www.sciencedirect.com/science/article/pii/S016890020303393X.

[76] Yichun Xu et al.
"Improvement of resonance reconstruction with time-of-flight detector at STAR experiment".
In: *Nucl. Instr. Meth. A* 596.2 (2008), pp. 186–189.
ISSN: 0168-9002.
DOI: https://doi.org/10.1016/j.nima.2008.07.147.
URL: https://www.sciencedirect.com/science/article/pii/S0168900208011327.

[77] W.J. Llope et al.
"The STAR Vertex Position Detector".
In: *Nucl. Instr. Meth. A* 759 (2014), pp. 23–28.
ISSN: 0168-9002.
DOI: https://doi.org/10.1016/j.nima.2014.04.080.
URL: https://www.sciencedirect.com/science/article/pii/S0168900214004938.

[78] W.J. Llope.
"The large-area time-of-flight upgrade for STAR".
In: *Nucl. Instr. Meth. B* 241.1 (2005). The Application of Accelerators in Research and Industry, pp. 306–310.
ISSN: 0168-583X.
DOI: https://doi.org/10.1016/j.nimb.2005.07.089.
URL: https://www.sciencedirect.com/science/article/pii/S0168583X05012267.

[79] M. C. S. Williams.
"The Time-of-flight detector for the ALICE experiment".
In: *Nucl. Phys. A* 698 (2002). Ed. by T. J. Hallman et al., pp. 464–467.
DOI: 10.1016/S0375-9474(01)01405-1.

[80] F.S. Bieser et al.
"The STAR trigger".
In: *Nucl. Instr. Meth. A* 499.2 (2003), pp. 766–777.
ISSN: 0168-9002.
DOI: https://doi.org/10.1016/S0168-9002(02)01974-5.
URL: https://www.sciencedirect.com/science/article/pii/S0168900202019745.

[81] Clemens Adler et al.
"The RHIC zero degree calorimeter".
In: *Nucl. Instr. Meth. A* 470 (2001), pp. 488–499.
DOI: 10.1016/S0168-9002(01)00627-1.
arXiv: nucl-ex/0008005.

[82] Anthony J Baltz, Chellis Chasman, and Sebastian N White.
"Correlated forward–backward dissociation and neutron spectra as a luminosity monitor in heavy-ion colliders".
In: *Nucl. Instr. Meth* 417.1 (Nov. 1998), pp. 1–8.
ISSN: 0168-9002.
DOI: 10.1016/s0168-9002(98)00575-0.

URL: http://dx.doi.org/10.1016/S0168-9002(98)00575-0.

[83] J. KIRYLUK.
"LOCAL POLARIMETRY FOR PROTON BEAMS WITH THE STAR BEAM BEAM COUNTERS".
In: *Spin 2004*.
WORLD SCIENTIFIC, Aug. 2005,
Pp. 718–721.
DOI: 10.1142/9789812701909_0152.
URL: http://dx.doi.org/10.1142/9789812701909_0152.

[84] C.E. Allgower et al.
"The STAR endcap electromagnetic calorimeter".
In: *Nucl. Instr. Meth.* 499.2 (2003), pp. 740–750.
ISSN: 0168-9002.
DOI: https://doi.org/10.1016/S0168-9002(02)01971-X.
URL: https://www.sciencedirect.com/science/article/pii/S016890020201971X.

[85] M. Beddo et al.
"The STAR Barrel Electromagnetic Calorimeter".
In: *Nucl. Instr. Meth.* 499.2 (2003), pp. 725–739.
ISSN: 0168-9002.
DOI: https://doi.org/10.1016/S0168-9002(02)01970-8.
URL: https://www.sciencedirect.com/science/article/pii/S0168900202019708.

[86] L. Adamczyk et al.
"Inclusive charged hadron elliptic flow in Au + Au collisions at $\sqrt{s_{NN}} = 7.7$–39 GeV".
In: *Phys. Rev. C* 86 (5 Nov. 2012), p. 054908.
DOI: 10.1103/PhysRevC.86.054908.
URL: https://link.aps.org/doi/10.1103/PhysRevC.86.054908.

[87] B. I. Abelev et al.
"Identified particle production, azimuthal anisotropy, and interferometry measurements in Au + Au collisions at $\sqrt{s_{NN}} = 9.2$ GeV".
In: *Phys. Rev. C* 81 (2 Feb. 2010), p. 024911.
DOI: 10.1103/PhysRevC.81.024911.
URL: https://link.aps.org/doi/10.1103/PhysRevC.81.024911.

[88] D. Drijard, H. G. Fischer, and T. Nakada.
"Study of Event Mixing and Its Application to the Extraction of Resonance Signals".

In: *Nucl. Instr. Meth. A* 225 (1984), p. 367.
DOI: 10.1016/0167-5087(84)90275-8.

[89] C. Adler et al.
"Azimuthal Anisotropy of K_S^0 and $\Lambda+\overline{\Lambda}$ Production at Midrapidity from Au+Au Collisions at $\sqrt{s_{NN}} = 130$ GeV".
In: *Phys. Rev. Lett.* 89 (2002). [Erratum: Phys.Rev.Lett. 127, 089901 (2021)], p. 132301.
DOI: 10.1103/PhysRevLett.89.132301.
arXiv: hep-ex/0205072.

[90] Mohamed Abdallah et al.
"Azimuthal anisotropy measurements of strange and multistrange hadrons in $U+U$ collisions at $\sqrt{s_{NN}}$ =193 GeV at the BNL Relativistic Heavy Ion Collider".
In: *Phys. Rev. C* 103.6 (2021), p. 064907.
DOI: 10.1103/PhysRevC.103.064907.
arXiv: 2103.09451 [nucl-ex].

[91] Mohamed Abdallah and et al. (STAR).
"Azimuthal anisotropy measurement of (multi)strange hadrons in Au+Au collisions at $\sqrt{S_{NN}} = 54.4 GeV$".
In: *Phys. Rev. C* 107.2 (2023), p. 024912.
DOI: 10.1103/PhysRevC.107.024912.
arXiv: 2205.11073 [nucl-ex].

[92] J. Adams and et al. (STAR).
"Multistrange Baryon El liptic Flow in Au + Au Collisions at $\sqrt{s_{NN}} = 200$ GeV".
In: *Phys. Rev. Lett.* 95 (12 Sept. 2005), p. 122301.
DOI: 10.1103/PhysRevLett.95.122301.
URL: https://link.aps.org/doi/10.1103/PhysRevLett.95.122301.

[93] N. Borghini and J.-Y. Ollitrault.
"Azimuthally sensitive correlations in nucleus-nucleus collisions".
In: *Phys. Rev. C* 70 (6 Dec. 2004), p. 064905.
DOI: 10.1103/PhysRevC.70.064905.
URL: https://link.aps.org/doi/10.1103/PhysRevC.70.064905.

[94] Hiroshi Masui, Alexander Schmah, and A.M. Poskanzer.
"Event plane resolution correction for azimuthal anisotropy in wide centrality bins".
In: *Nucl. Instr. Meth. A* 833 (2016), pp. 181–185.
ISSN: 0168-9002.

DOI: https://doi.org/10.1016/j.nima.2016.07.037.
URL: https://www.sciencedirect.com/science/article/pii/S0168900216307781.

[95] Roger Barlow.
Systematic Errors: facts and fictions.
2002.
arXiv: hep-ex/0207026 [hep-ex].
URL: https://arxiv.org/abs/hep-ex/0207026.

[96] K. Dusling and D. Teaney.
"Simulating elliptic flow with viscous hydrodynamics".
In: *Phys. Rev. C* 77 (3 Mar. 2008), p. 034905.
DOI: 10.1103/PhysRevC.77.034905.
URL: https://link.aps.org/doi/10.1103/PhysRevC.77.034905.

[97] Paul Romatschke and Ulrike Romatschke.
"Viscosity Information from Relativistic Nuclear Collisions: How Perfect is the Fluid Observed at RHIC?"
In: *Phys. Rev. Lett.* 99 (17 Oct. 2007), p. 172301.
DOI: 10.1103/PhysRevLett.99.172301.
URL: https://link.aps.org/doi/10.1103/PhysRevLett.99.172301.

[98] Chun Shen and Ulrich Heinz.
"Collision Energy Dependence of Viscous Hydrodynamic Flow in Relativistic Heavy-Ion Collisions".
In: *Phys. Rev. C* 85 (2012). [Erratum: Phys.Rev.C 86, 049903 (2012)], p. 054902.
DOI: 10.1103/PhysRevC.85.054902.
arXiv: 1202.6620 [nucl-th].

[99] Chun Shen et al.
"The QGP shear viscosity: Elusive goal or just around the corner?"
In: *J. Phys. G* 38 (2011). Ed. by Yves Schutz and Urs Achim Wiedemann, p. 124045.
DOI: 10.1088/0954-3899/38/12/124045.
arXiv: 1106.6350 [nucl-th].

[100] P. Huovinen et al.
"Radial and elliptic flow at RHIC: further predictions".
In: *Physics Letters B* 503.1 (2001), pp. 58–64.
ISSN: 0370-2693.
DOI: https://doi.org/10.1016/S0370-2693(01)00219-2.

URL: https://www.sciencedirect.com/science/article/pii/S0370269301002192.

[101] Tetsufumi Hirano et al.
"Mass ordering of differential elliptic flow and its violation for ϕ mesons".
In: *Phys. Rev. C* 77 (4 Apr. 2008), p. 044909.
DOI: 10.1103/PhysRevC.77.044909.
URL: https://link.aps.org/doi/10.1103/PhysRevC.77.044909.

[102] L. Adamczyk et al.
"Observation of an Energy-Dependent Difference in Elliptic Flow between Particles and Antiparticles in Relativistic Heavy Ion Collisions".
In: *Phys. Rev. Lett.* 110.14 ().
ISSN: 1079-7114.
DOI: 10.1103/physrevlett.110.142301.
URL: http://dx.doi.org/10.1103/PhysRevLett.110.142301.

[103] C M Ko and G Q Li.
"Medium effects in high energy heavy-ion collisions".
In: *Journal of Physics G: Nuclear and Particle Physics* 22.12 (Dec. 1996), p. 1673.
DOI: 10.1088/0954-3899/22/12/002.
URL: https://dx.doi.org/10.1088/0954-3899/22/12/002.

[104] Jun Xu et al.
"Elliptic Flow Splitting as a Probe of the QCD Phase Structure at Finite Baryon Chemical Potential".
In: *Phys. Rev. Lett.* 112 (1 Jan. 2014), p. 012301.
DOI: 10.1103/PhysRevLett.112.012301.
URL: https://link.aps.org/doi/10.1103/PhysRevLett.112.012301.

[105] Jun Xu and Che Ming Ko.
"Collision energy dependence of elliptic flow splitting between particles and their antiparticles from an extended multiphase transport model".
In: *Phys. Rev. C* 94 (5 Nov. 2016), p. 054909.
DOI: 10.1103/PhysRevC.94.054909.
URL: https://link.aps.org/doi/10.1103/PhysRevC.94.054909.

[106] L. Adamczyk et al.
"Centrality dependence of identified particle elliptic flow in relativistic heavy ion collisions at $\sqrt{s_{NN}} = 7.7--62.4$ GeV".
In: *Phys. Rev. C* 93 (1 Jan. 2016), p. 014907.

DOI: 10.1103/PhysRevC.93.014907.
URL: https://link.aps.org/doi/10.1103/PhysRevC.93.014907.

[107] Ekaterina Retinskaya, Matthew Luzum, and Jean-Yves Ollitrault.
"Constraining models of initial conditions with elliptic and triangular flow data".
In: *Phys. Rev. C* 89 (1 Jan. 2014), p. 014902.
DOI: 10.1103/PhysRevC.89.014902.
URL: https://link.aps.org/doi/10.1103/PhysRevC.89.014902.

[108] Ekaterina Retinskaya, Matthew Luzum, and Jean-Yves Ollitrault.
"Constraining models of initial state with v2 and v3 data from LHC and RHIC".
In: *Nucl. Phys. A* 926 (2014). IS2013, pp. 152–158.
ISSN: 0375-9474.
DOI: https://doi.org/10.1016/j.nuclphysa.2014.03.015.
URL: https://www.sciencedirect.com/science/article/pii/S0375947414000736.

[109] Christian Lang and Nicolas Borghini.
"Dissipative corrections to particle spectra and anisotropic flow from a saddle-point approximation to kinetic freeze out".
In: *The European Physical Journal C* 74.7 (July 2014).
ISSN: 1434-6052.
DOI: 10.1140/epjc/s10052-014-2955-7.
URL: http://dx.doi.org/10.1140/epjc/s10052-014-2955-7.

[110] Clément Gombeaud and Jean-Yves Ollitrault.
"Effects of flow fluctuations and partial thermalization on v_4".
In: *Phys. Rev. C* 81 (1 Jan. 2010), p. 014901.
DOI: 10.1103/PhysRevC.81.014901.
URL: https://link.aps.org/doi/10.1103/PhysRevC.81.014901.

[111] J. Tian et al.
"Breaking of the number-of-constituent-quark scaling for identified-particle elliptic flow as a signal of phase change in low-energy data taken at the BNL Relativistic Heavy Ion Collider (RHIC)".
In: *Phys. Rev. C* 79 (6 June 2009), p. 067901.
DOI: 10.1103/PhysRevC.79.067901.
URL: https://link.aps.org/doi/10.1103/PhysRevC.79.067901.

[112] R. J. Fries et al.

"Hadron production in heavy ion collisions: Fragmentation and recombination from a dense parton phase".
In: *Phys. Rev. C* 68 (4 Oct. 2003), p. 044902.
DOI: 10.1103/PhysRevC.68.044902.
URL: https://link.aps.org/doi/10.1103/PhysRevC.68.044902.

[113] Meng Wang et al.
"Number-of-constituent-quark scaling of elliptic flow: a quantitative study".
In: *Nucl. Sci. Tech.* 33.3 (2022), p. 37.
DOI: 10.1007/s41365-022-01019-9.
arXiv: 2203.10353 [hep-ph].

[114] Subhash Singha and Md. Nasim.
"Scaling of elliptic flow in heavy-ion collisions with the number of constituent quarks in a transport model".
In: *Phys. Rev. C* 93 (3 Mar. 2016), p. 034908.
DOI: 10.1103/PhysRevC.93.034908.
URL: https://link.aps.org/doi/10.1103/PhysRevC.93.034908.

[115] Wenbin Zhao et al.
"Number of constituent quark scaling of elliptic flows in high multiplicity p-Pb collisions at sNN=5.02TeV".
In: *Nucl. Phys. A* 1005 (2021). The 28th International Conference on Ultra-relativistic Nucleus-Nucleus Collisions: Quark Matter 2019, p. 121876.
ISSN: 0375-9474.
DOI: https://doi.org/10.1016/j.nuclphysa.2020.121876.
URL: https://www.sciencedirect.com/science/article/pii/S037594742030186X.

[116] Qi-Ye Shou et al.
"Properties of the QCD Matter: A Review of Selected Results from the ALICE Experiment".
In:
Sept. 2024.
arXiv: 2409.17964 [nucl-ex].

[117] Leszek Adamczyk et al.
"Azimuthal anisotropy in Cu+Au collisions at $\sqrt{s_{NN}} = 200$ GeV".
In: *Phys. Rev. C* 98.1 (2018), p. 014915.
DOI: 10.1103/PhysRevC.98.014915.

arXiv: 1712.01332 [nucl-ex].

[118] Liang Zheng et al.
"Investigating the NCQ scaling of elliptic flow at LHC with a multiphase transport model".
In: *Eur. Phys. J. A* 53.6 (2017), p. 124.
DOI: 10.1140/epja/i2017-12312-8.
arXiv: 1611.05185 [nucl-th].

[119] J. Tian et al.
"Breaking of the number-of-constituent-quark scaling for identified-particle elliptic flow as a signal of phase change in low-energy data taken at the BNL Relativistic Heavy Ion Collider (RHIC)".
In: *Phys. Rev. C* 79 (2009), p. 067901.
DOI: 10.1103/PhysRevC.79.067901.
arXiv: 0906.5287 [nucl-th].

[120] M. Bleicher and X. Zhu.
"Is constituent quark scaling a unique sign of parton recombination?"
In: *Eur. Phys. J. C* 49 (2007). Ed. by F. Antinori et al., pp. 303–308.
DOI: 10.1140/epjc/s10052-006-0125-2.

[121] Y. Lu et al.
"Anisotropic flow at RHIC: How unique is the number-of-constituent-quark scaling?"
In: *J. Phys. G* 32 (2006), pp. 1121–1130.
DOI: 10.1088/0954-3899/32/8/004.
arXiv: nucl-th/0602009.

[122] L. Adamczyk et al.
"Elliptic flow of identified hadrons in Au+Au collisions at $\sqrt{s_{NN}} = 7.7$–62.4 GeV".
In: *Phys. Rev. C* 88 (1 July 2013), p. 014902.
DOI: 10.1103/PhysRevC.88.014902.
URL: https://link.aps.org/doi/10.1103/PhysRevC.88.014902.

[123] Xin-Yue Ju et al.
"Applying the Kalman filter particle method to strange and open charm hadron reconstruction in the STAR experiment".
In: *Nucl. Sci. Tech.* 34.10 (2023), p. 158.
DOI: 10.1007/s41365-023-01320-1.

[124] Maksym Zyzak.
"Online selection of short-lived particles on many-core computer architectures in the CBM experiment at FAIR".
doctoralthesis. Universitätsbibliothek Johann Christian Senckenberg, 2016,
P. 165.

[125] Sergey Gorbunov.
"On-line reconstruction algorithms for the CBM and ALICE experiments".
doctoralthesis. Universitätsbibliothek Johann Christian Senckenberg, 2013,
Pp. 104, 9.

[126] Yannis Burnier et al.
"Chiral Magnetic Wave at Finite Baryon Density and the Electric Quadrupole Moment of the Quark-Gluon Plasma".
In: *Phys. Rev. Lett.* 107 (5 July 2011), p. 052303.
DOI: 10.1103/PhysRevLett.107.052303.
URL: https://link.aps.org/doi/10.1103/PhysRevLett.107.052303.

[127] J. C. Dunlop, M. A. Lisa, and P. Sorensen.
"Constituent quark scaling violation due to baryon number transport".
In: *Phys. Rev. C* 84.4 (Oct. 2011).
ISSN: 1089-490X.
DOI: 10.1103/physrevc.84.044914.
URL: http://dx.doi.org/10.1103/PhysRevC.84.044914.

[128] Che Ming Ko et al.
"Partonic mean-field effects on matter and antimatter elliptic flows".
In: *Nucl. Phys. A* 928 (2014). Special Issue Dedicated to the Memory of Gerald E Brown (1926-2013), pp. 234–246.
ISSN: 0375-9474.
DOI: https://doi.org/10.1016/j.nuclphysa.2014.05.016.
URL: https://www.sciencedirect.com/science/article/pii/S037594741400150X.

[129] Jun Xu et al.
"Effects of hadronic potentials on elliptic flows in relativistic heavy ion collisions".
In: *Phys. Rev. C* 85 (4 Apr. 2012), p. 041901.
DOI: 10.1103/PhysRevC.85.041901.
URL: https://link.aps.org/doi/10.1103/PhysRevC.85.041901.

[130] Jun Xu and Che Ming Ko.

"Collision energy dependence of elliptic flow splitting between particles and their antiparticles from an extended multiphase transport model".
In: *Phys. Rev. C* 94 (5 Nov. 2016), p. 054909.
DOI: `10.1103/PhysRevC.94.054909`.
URL: `https://link.aps.org/doi/10.1103/PhysRevC.94.054909`.

[131] Umut Gürsoy et al.
"Charge-dependent Flow Induced by Magnetic and Electric Fields in Heavy Ion Collisions".
In: *Phys. Rev. C* 98.5 (2018), p. 055201.
DOI: `10.1103/PhysRevC.98.055201`.
arXiv: `1806.05288 [hep-ph]`.

[132] L. Adamczyk et al.
"Bulk properties of the medium produced in relativistic heavy-ion collisions from the beam energy scan program".
In: *Phys. Rev. C* 96 (4 Oct. 2017), p. 044904.
DOI: `10.1103/PhysRevC.96.044904`.
URL: `https://link.aps.org/doi/10.1103/PhysRevC.96.044904`.

[133] Prabhupada Dixit and Md. Nasim.
"Insight from the elliptic flow of identified hadrons measured in relativistic heavy-ion collisions".
In: *Int. J. Mod. Phys. E* 31.06 (2022), p. 2250059.
DOI: `10.1142/S0218301322500598`.
arXiv: `2110.08573 [nucl-ex]`.

[134] Peter F. Kolb et al.
"Momentum anisotropies in the quark coalescence model".
In: *Phys. Rev. C* 69 (5 May 2004), p. 051901.
DOI: `10.1103/PhysRevC.69.051901`.
URL: `https://link.aps.org/doi/10.1103/PhysRevC.69.051901`.

[135] Denes Molnar and Sergei A. Voloshin.
"Elliptic flow at large transverse momenta from quark coalescence".
In: *Phys. Rev. Lett.* 91 (2003), p. 092301.
DOI: `10.1103/PhysRevLett.91.092301`.
arXiv: `nucl-th/0302014`.

[136] Lie-Wen Chen and Che Ming Ko.

"phi and omega production from relativistic heavy ion collisions in a dynamical quark coalescence model".
In: *Phys. Rev. C* 73 (2006), p. 044903.
DOI: 10.1103/PhysRevC.73.044903.
arXiv: nucl-th/0602025.

[137] Subikash Choudhury, Debojit Sarkar, and Subhasis Chattopadhyay.
"Elliptic flow of ϕ mesons at intermediate p_T: Influence of mass versus quark number".
In: *Phys. Rev. C* 95.2 (2017), p. 024904.
DOI: 10.1103/PhysRevC.95.024904.
arXiv: 1702.03540 [nucl-th].

[138] Jun Song et al.
"Strange hadron production in a quark combination model in Au+Au collisions at energies available at the BNL Relativistic Heavy Ion Collider".
In: *Phys. Rev. C* 103.3 (2021), p. 034907.
DOI: 10.1103/PhysRevC.103.034907.
arXiv: 2007.14588 [nucl-th].

[139] Jun Song, Hai-hong Li, and Feng-lan Shao.
"Elliptic flow of hadrons in equal-velocity quark combination mechanism in relativistic heavy-ion collisions".
In: *Eur. Phys. J. C* 81.1 (2021), p. 5.
DOI: 10.1140/epjc/s10052-020-08760-8.
arXiv: 2008.03017 [nucl-th].

[140] P.A. Zyla et al.
"Review of Particle Physics".
In: *PTEP* 2020.8 (2020). and 2021 update, p. 083C01.
DOI: 10.1093/ptep/ptaa104.

[141] S. Acharya et al.
"Anisotropic flow of identified particles in Pb-Pb collisions at $\sqrt{s}_{\mathrm{NN}} = 5.02$ TeV".
In: *JHEP* 09 (2018), p. 006.
DOI: 10.1007/JHEP09(2018)006.
arXiv: 1805.04390 [nucl-ex].

[142] Xu Sun.

"Triangular flow of identified hadrons in Au + Au collisions at $\sqrt{s_{NN}}$ = 39 and 200 GeV".
In: *Nucl. Phys. A* 931 (2014). Ed. by Peter Braun-Munzinger, Bengt Friman, and Johanna Stachel, pp. 1194–1198.
DOI: 10.1016/j.nuclphysa.2014.09.058.

[143] V. Khachatryan et al.
"Evidence for transverse-momentum- and pseudorapidity-dependent event-plane fluctuations in PbPb and pPb collisions".
In: *Phys. Rev. C* 92 (3 Sept. 2015), p. 034911.
DOI: 10.1103/PhysRevC.92.034911.
URL: https://link.aps.org/doi/10.1103/PhysRevC.92.034911.

[144] Morad Aaboud et al.
"Measurement of longitudinal flow decorrelations in Pb+Pb collisions at $\sqrt{s_{\mathrm{NN}}}$ = 2.76 and 5.02 TeV with the ATLAS detector".
In: *Eur. Phys. J. C* 78.2 (2018), p. 142.
DOI: 10.1140/epjc/s10052-018-5605-7.
arXiv: 1709.02301 [nucl-ex].

[145] Georges Aad et al.
"Longitudinal Flow Decorrelations in Xe+Xe Collisions at $\sqrt{s_{\mathrm{NN}}}$ = 5.44 TeV with the ATLAS Detector".
In: *Phys. Rev. Lett.* 126.12 (2021), p. 122301.
DOI: 10.1103/PhysRevLett.126.122301.
arXiv: 2001.04201 [nucl-ex].

[146] Maowu Nie.
"Energy dependence of longitudinal flow decorrelation from STAR".
In: *Nucl. Phys. A* 1005 (2021). Ed. by Feng Liu et al., p. 121783.
DOI: 10.1016/j.nuclphysa.2020.121783.
arXiv: 2005.03252 [nucl-ex].

[147] Shreyasi Acharya et al.
"Pseudorapidity dependence of anisotropic flow and its decorrelations using long-range multiparticle correlations in Pb–Pb and Xe–Xe collisions".
In: *Phys. Lett. B* 850 (2024). [Erratum: Phys.Lett.B 853, 138659 (2024)], p. 138477.
DOI: 10.1016/j.physletb.2024.138477.
arXiv: 2307.11116 [nucl-ex].

[148] Georges Aad et al.
"Longitudinal Flow Decorrelations in Xe+Xe Collisions at $\sqrt{s_{\mathrm{NN}}} = 5.44$ TeV with the ATLAS Detector".
In: *Phys. Rev. Lett.* 126.12 (2021), p. 122301.
DOI: 10.1103/PhysRevLett.126.122301.
arXiv: 2001.04201 [nucl-ex].

[149] Long-Gang Pang et al.
"Longitudinal decorrelation of anisotropic flows in heavy-ion collisions at the CERN Large Hadron Collider".
In: *Phys. Rev. C* 91.4 (2015), p. 044904.
DOI: 10.1103/PhysRevC.91.044904.
arXiv: 1410.8690 [nucl-th].

[150] Long-Gang Pang et al.
"Decorrelation of anisotropic flow along the longitudinal direction".
In: *Eur. Phys. J. A* 52.4 (2016), p. 97.
DOI: 10.1140/epja/i2016-16097-x.
arXiv: 1511.04131 [nucl-th].

[151] Wenbin Zhao et al.
"3D structure of anisotropic flow in small collision systems at energies available at the BNL Relativistic Heavy Ion Collider".
In: *Phys. Rev. C* 107.1 (2023), p. 014904.
DOI: 10.1103/PhysRevC.107.014904.
arXiv: 2211.16376 [nucl-th].

[152] Pingal Dasgupta, Han-Sheng Wang, and Guo-Liang Ma.
"Effect of global momentum conservation on longitudinal flow decorrelation".
In: *Phys. Rev. C* 107.1 (2023), p. 014905.
DOI: 10.1103/PhysRevC.107.014905.
arXiv: 2208.00468 [nucl-th].

[153] Azumi Sakai, Koichi Murase, and Tetsufumi Hirano.
"Effects of hydrodynamic and initial longitudinal fluctuations on rapidity decorrelation of collective flow".
In: *Phys. Lett. B* 829 (2022), p. 137053.
DOI: 10.1016/j.physletb.2022.137053.
arXiv: 2111.08963 [nucl-th].

[154] Azumi Sakai, Koichi Murase, and Tetsufumi Hirano.
"Rapidity decorrelation of anisotropic flow caused by hydrodynamic fluctuations".
In: *Phys. Rev. C* 102.6 (2020), p. 064903.
DOI: `10.1103/PhysRevC.102.064903`.
arXiv: `2003.13496 [nucl-th]`.

[155] Arabinda Behera, Maowu Nie, and Jiangyong Jia.
"Longitudinal eccentricity decorrelations in heavy ion collisions".
In: *Phys. Rev. Res.* 2.2 (2020), p. 023362.
DOI: `10.1103/PhysRevResearch.2.023362`.
arXiv: `2003.04340 [nucl-th]`.

[156] Xiang-Yu Wu et al.
"Longitudinal fluctuations and decorrelations of anisotropic flows at energies available at the CERN Large Hadron Collider and at the BNL Relativistic Heavy Ion Collider".
In: *Phys. Rev. C* 98.2 (2018), p. 024913.
DOI: `10.1103/PhysRevC.98.024913`.
arXiv: `1805.03762 [nucl-th]`.

[157] Piotr Bozek and Wojciech Broniowski.
"The torque effect and fluctuations of entropy deposition in rapidity in ultra-relativistic nuclear collisions".
In: *Phys. Lett. B* 752 (2016), pp. 206–211.
DOI: `10.1016/j.physletb.2015.11.054`.
arXiv: `1506.02817 [nucl-th]`.

[158] Zi-Wei Lin et al.
"A Multi-phase transport model for relativistic heavy ion collisions".
In: *Phys. Rev. C* 72 (2005), p. 064901.
DOI: `10.1103/PhysRevC.72.064901`.
arXiv: `nucl-th/0411110`.

[159] Xin-Nian Wang.
"Role of multiple mini - jets in high-energy hadronic reactions".
In: *Phys. Rev. D* 43 (1991), pp. 104–112.
DOI: `10.1103/PhysRevD.43.104`.

[160] Xin-Nian Wang and Miklos Gyulassy.

"HIJING: A Monte Carlo model for multiple jet production in p p, p A and A A collisions".
In: *Phys. Rev. D* 44 (1991), pp. 3501–3516.
DOI: 10.1103/PhysRevD.44.3501.

[161] Xin-Nian Wang and Miklos Gyulassy.
"A Systematic study of particle production in $p+p$ (anti-p) collisions via the HIJING model".
In: *Phys. Rev. D* 45 (1992), pp. 844–856.
DOI: 10.1103/PhysRevD.45.844.

[162] G. C. Rossi and G. Veneziano.
"A Possible Description of Baryon Dynamics in Dual and Gauge Theories".
In: *Nucl. Phys. B* 123 (1977), pp. 507–545.
DOI: 10.1016/0550-3213(77)90178-X.

[163] L. Montanet, G. C. Rossi, and G. Veneziano.
"Baryonium Physics".
In: *Phys. Rept.* 63 (1980), pp. 149–222.
DOI: 10.1016/0370-1573(80)90161-1.

[164] D. Kharzeev.
"Can gluons trace baryon number?"
In: *Phys. Lett. B* 378 (1996), pp. 238–246.
DOI: 10.1016/0370-2693(96)00435-2.
arXiv: nucl-th/9602027.

[165] V. Topor Pop et al.
"Baryon junction loops in HIJING / B anti-B v2.0 and the baryon /meson anomaly at RHIC".
In: *Phys. Rev. C* 70 (2004), p. 064906.
DOI: 10.1103/PhysRevC.70.064906.
arXiv: nucl-th/0407095.

[166] B. I. Abelev et al.
"Centrality dependence of charged hadron and strange hadron elliptic flow from s(NN)**(1/2) = 200-GeV Au + Au collisions".
In: *Phys. Rev. C* 77 (2008), p. 054901.
DOI: 10.1103/PhysRevC.77.054901.
arXiv: 0801.3466 [nucl-ex].

[167] Bo Andersson, G. Gustafson, and B. Soderberg.
"A General Model for Jet Fragmentation".
In: *Z. Phys. C* 20 (1983), p. 317.
DOI: 10.1007/BF01407824.

[168] Zi-wei Lin and C. M. Ko.
"Partonic effects on the elliptic flow at RHIC".
In: *Phys. Rev. C* 65 (2002), p. 034904.
DOI: 10.1103/PhysRevC.65.034904.
arXiv: nucl-th/0108039.

[169] Zi-wei Lin, C. M. Ko, and Subrata Pal.
"Partonic effects on pion interferometry at RHIC".
In: *Phys. Rev. Lett.* 89 (2002), p. 152301.
DOI: 10.1103/PhysRevLett.89.152301.
arXiv: nucl-th/0204054.

[170] Zi-wei Lin and C. M. Ko.
"Kaon interferometry at RHIC from AMPT model".
In: *J. Phys. G* 30 (2004). Ed. by S. A. Bass et al., S263–S270.
DOI: 10.1088/0954-3899/30/1/031.
arXiv: nucl-th/0305069.

[171] Jun Xu and Che Ming Ko.
"Pb-Pb collisions at $\sqrt{s_{NN}} = 2.76$ TeV in a multiphase transport model".
In: *Phys. Rev. C* 83 (2011), p. 034904.
DOI: 10.1103/PhysRevC.83.034904.
arXiv: 1101.2231 [nucl-th].

[172] STAR Collaboration.
Temperature Measurement of Quark-Gluon Plasma at Different Stages.
2024.
arXiv: 2402.01998 [nucl-ex].
URL: https://arxiv.org/abs/2402.01998.